UNIVERSITY OF CATANIA

DEPARTMENT OF CHEMICAL SCIENCES

INTERNATIONAL Ph.D. IN CHEMICAL SCIENCES – XXXVI Cycle

Giuseppina Domenica Giovanna Santonoceta

Stimuli-Responsive Metal-Coordinated Assemblies as Drug Delivery Platforms

Ph.D. Thesis

SUPERVISOR

Prof. Carmelo Sgarlata

COORDINATOR

Prof. Salvatore Sortino

Table of contents

Chapter III: Metal-coordinated assemblies containing methotrexate 122

Abstract

Drug delivery systems (DDSs) are widely used to overcome the intrinsic limitations (low solubility, poor permeability, and short biological half-life) of several drugs which can affect their efficacy and/or induce toxicity.

Polymer-based systems gained particular attention for the efficient delivery of bioactive compounds. The unique features of the polymers (flexibility, variety of composition and properties, easy functionalization to respond to specific stimuli) along with the presence of multiple functional groups in their chains ensure the efficient binding of the therapeutic agents to achieve the target-oriented delivery of payloads.

Smart polymers can change their structural and conformational features as well as their properties in response to external and/or physiological signals. These “on-demand” processes account for the tailored site- and time-controlled release of therapeutics avoiding/reducing their leaking into the healthy physiological environment.

pH-responsive carriers are among the most explored compounds and their development is extensively pursued for the construction of stimuli-responsive drug delivery platforms. These systems exploit the localized pH changes occurring between healthy and pathological tissues (due to cancer, infection, and inflammation processes) or intracellular compartments.

Despite the plenty of efforts made towards the design of effective pH-responsive delivery systems, a quantitative analysis of the strength and nature of the interactions occurring between the drug and the carrier, which are of paramount significance for the success of the releasing systems, was rarely reported.

In this PhD thesis, the study of multiple equilibria in solution is proposed as a valuable strategy for the design and development of delivery platforms obtained by the non-covalent assembling of poly(acrylic acid) (PAA), a biocompatible and pH-responsive polymer, metal ions of biological interest (Cu(II), Zn(II) or Co(II)) and quercetin (Que) or methotrexate (MTX), selected as model active principles, with the aim of optimizing the stability and the drug loading and release capability of the resulting assemblies.

It is well known that the application of quercetin, a flavonoid with a broad spectrum of physiological activities, is severely confined due to its low water solubility, short half-life and *in vivo* bioavailability. The efficacy of methotrexate, a chemotherapy agent, is strongly affected by its poor solubility, short half-life in the bloodstream and drug resistance by targeted cells. Moreover, this drug shows a lack of selectivity toward neoplastic cells causing severe side effects.

Metal-coordinated assemblies containing quercetin are described in *Chapter II*. The flavonoid ability to complex metal ions and the PAA polymer as well as the formation of the metal-coordinated assemblies were investigated in aqueous solution at pH 7.4 and 25 °C by both UV-Vis spectroscopy and isothermal titration calorimetry (ITC). Speciation models showed that Que can form an ML species with all metal ions and an additional ML_2 species with Cu(II) and Co(II). ITC measurements allowed for the determination of the thermodynamic parameters that drive the formation of the metal-complex species formed by the flavonoid. Interestingly, although Que and PAA are unable to interact, the presence of the metal ions allowed for their binding and thus its peculiar features resulted to be crucial for the formation of the assemblies. The carboxyl groups of PAA are able to complex the metal(II) ions forming the M(PAA) and $M(PAA)_2$ species through an entropically favoured and driven process. ITC and UV-Vis measurements mutually confirmed the species and their stability for the Que-M(II)-PAA systems in solution. Que_2CuPAA formation occurs through an entropically favoured and driven process; the formation of $QueZn(PAA)_2$ is enthalpically favoured and driven whilst for $QueCo(PAA)_2$ the enthalpic and entropic contributions are almost comparable.

The formation of the cobalt(II)-coordinated assembly was also investigated at the solid-liquid interface through the quartz-crystal microbalance with dissipation monitoring (QCM-D) technique. The measurements confirmed the ability of the flavonoid to be adsorbed onto the metal-polymer complex and released under pH control.

The kinetic stability of the copper(II)- and zinc(II)-based assemblies were investigated by UV-Vis to evaluate if the formation of the assemblies would increase the stability of quercetin, which undergoes degradation in aqueous solution when alone. The developed systems exhibited a longer half-life than that of the free flavonoid emphasizing that the formation of the three-component architecture improves the quercetin kinetic stability.

The ability of the metal-coordinated carriers to release quercetin in a localized acidic environment was investigated under different pH conditions using dialysis and UV Vis spectroscopy for the copper(II)- and zinc(II)-based systems and by QCM-D experiments for the cobalt(II)-based one. These studies proved that the developed delivery systems permit the release of the loaded drug under pH control.

In *Chapter III*, metal-coordinated assemblies containing methotrexate are designed and prepared. The quantitative analysis of the species, binding affinity and thermodynamic signature of all the formation equilibria involving the chemotherapy agent, metal ions and poly(acrylic acid) was carried out in aqueous solution at 25 °C and physiological pH by ITC. Methotrexate forms ML complex species with both Cu(II) and Zn(II) ions and an MTXM(PAA)$_2$ complex species when in the presence of poly(acrylic acid). Entropically favoured and driven processes mainly due to desolvation and conformational changes of the metal(II)-polymer complex are responsible for the formation of the metal-coordinated assemblies.

The binding ability of MTX toward the polymer-metal complexes was also examined at the solid-liquid interface by QCM-D. MTX was found to be adsorbed onto the polymer-metal layer confirming their ability to interact as well as to release the drug under different pH values.

Dynamic light scattering (DLS), ζ-potential and scanning electron microscopy (SEM) measurements provided a thorough characterization of the size, charge, and morphology of the MTX-based assemblies. The *in vitro* cytotoxicity of the assemblies was assessed in the U87 glioblastoma cell line through the Alamar Blue assay; the results highlighted the most efficient anticancer activity of the three-component complexes compared to the free chemotherapy drug. A flow cytometry analysis of samples treated with the metal-based assemblies allowed us to assess the role of reactive oxygen species generation in the mechanism of cell death. Finally, the internalization of the assemblies in glioblastoma cancer cells was observed by confocal microscopy.

The affinities of the polymeric systems toward human serum albumin (HSA) were investigated both in solution and at the interface. The strength of these interactions resides in the electrostatic forces occurring between the two interacting systems as suggested by the energetics of the binding process.

A poly-lysine-based system containing MTX was also developed and the affinity of the drug towards this positively charged polymer was investigated in aqueous solution at 25 °C and pH 7.4 by UV-Vis, ITC and QCM-D experiments. Methotrexate interacts with the pH-responsive poly-lysine forming a stable complex thanks to an enthalpically favoured and driven process. The pH-sensitive release of the drug was investigated in solution and at the interface; both studies indicate that the polymeric system is not able to undergo a controlled release of the drug thus emphasizing the importance of metal ions in the assembly structure.

In *Chapter IV*, copper(II)-coordinated assemblies with and without methotrexate were integrated with the *layer-by-layer* approach to develop multilayer polymeric systems to promote a pH-sensitive release of the chemotherapy drug. The fabricated polymeric nanoparticles were thoroughly characterized by ζ-potential, scanning electron microscopy (SEM) and transmission electron microscopy (TEM) measurements which revealed the surface charge, size and morphology of the different systems. Further studies will examine their ability to release the drug in a pH-controlled fashion.

In *Chapter V*, the binding features of a new class of negatively charged water-soluble macrocyclic hosts (prismarene, PrS[5]^{carboxy} and PrS[6]^{carboxy}), which may be employed as a potential drug carrier, were investigated. Species, stability constants and forces driving the interaction of the host with guests having different sizes, shapes and charge in buffered aqueous solution at neutral pH were determined by ITC experiments. The guests were selected as model molecules for examining the recognition processes by containers potentially exploitable for the encapsulation/transport of charged species of biological relevance. Results highlighted the capabilities of the prismarene to encapsulate mono and dicationic molecules and provide crucial information about the role played by the guest size and charge in the encapsulation process. The stability of the host-guest complexes formed by PrS[5]^{carboxy} with the ammonium cations is significantly affected by the structural features of the differently charged guests, while the affinity values determined for PrS[6]^{carboxy} are quite comparable for all the cations investigated regardless of the properties of the guests. The inclusion of ammonium cations into PrS[5]^{carboxy} is driven by enthalpically favourable attractive forces whilst, in the case of PrS[6]^{carboxy}, the inclusion of monocations is an entropically favoured and driven process while enthalpy drives the complexation of the doubly charged guests.

Overall, this doctoral thesis provides a detailed picture of the formation of metal-coordinated assemblies containing suitable drugs as well as of the solution thermodynamics and mechanisms involving multiple non-covalent, weak interactions. This information was revealed to be essential for the rational design and efficient application of the metal-based systems and macrocyclic receptors in solution. The strategy of examining multiple solution equilibria including different species resulted very helpful in designing a variety of efficient drug delivery platforms able to simultaneously enhance the loading and the site- and time-controlled release of proper drugs as well as to increase their efficacy.

Chapter I:
Introduction

1. Drug delivery systems

The past decades have witnessed many efforts in developing nanocarriers to deliver many and varied classes of payloads, including anticancer, antimicrobial and antiviral drugs, commonly employed for treating several diseases.[1] Many of these drugs are characterized by several drawbacks which can somehow affect their efficacy and/or induce toxicity.[2]

Because of their size, drugs can rapidly diffuse through biological fluids, across many biological barriers and through cell membranes thus interacting with nearly all tissues and cell types in the body. However, the diffusion process requires that these molecules must be freely soluble in biological fluids; hence, this limits or hampers the therapeutic use of poorly soluble molecules.[3] For example, extremely low solubility in water is characteristic of chemotherapy drugs whose use is still nowadays the most promising approach to treat cancer.[4] Many drugs are also characterized by inadequate chemical and physical stability which, along with poor solubility, determines also an insufficient bioavailability of the therapeutic agent. Consequently, very high-dose concentrations of drugs should be necessary to achieve the desired therapeutic effect. However, this could lead to the onset of undesirable severe side effects since the lack of targeting of free drugs determines a not site-specific action. Moreover, the effectiveness of some drugs is often altered by nonspecific cellular and tissue biodistribution due to their rapid metabolization or excretion from the body.[5]

To overcome the great variety of drug-related drawbacks which became one of the most troublesome questions of the pharmaceutical field, the development of drug delivery systems (DDSs) was proposed as a strategy to properly transport drugs in the body and safely achieve the desired therapeutic response. Thus, to meet this need, these systems were ideally designed to improve the aqueous solubility and stability of active agents, increase pharmacological activity, and reduce side effects. Moreover, the DDSs should be able to direct the drug to its target and maintain its concentration at the site for a sufficient period for therapeutic action to take effect.

DDS includes two main components, a carrier and a drug, and its optimal properties are controlled by the careful selection of these components. To be successfully used in controlled drug delivery formulations, a carrier must be chemically inert and biodegradable. Furthermore, the suitability and efficacy of delivery systems depend on a variety of characteristics of the material employed, including size and porosity.

Nanotechnology paved the way for the design and development of these carriers. A broad range of DDSs such as polymeric systems,[6,7] micelles,[8-10] liposomes,[11] inorganic nanoparticles (gold, silica, etc.),[12] dendrimers,[13] macrocyclic hosts,[14] polymer-drug conjugates,[15] protein-based nanocarriers,[16] MOFs,[17] (*Figure 1*) was proposed.

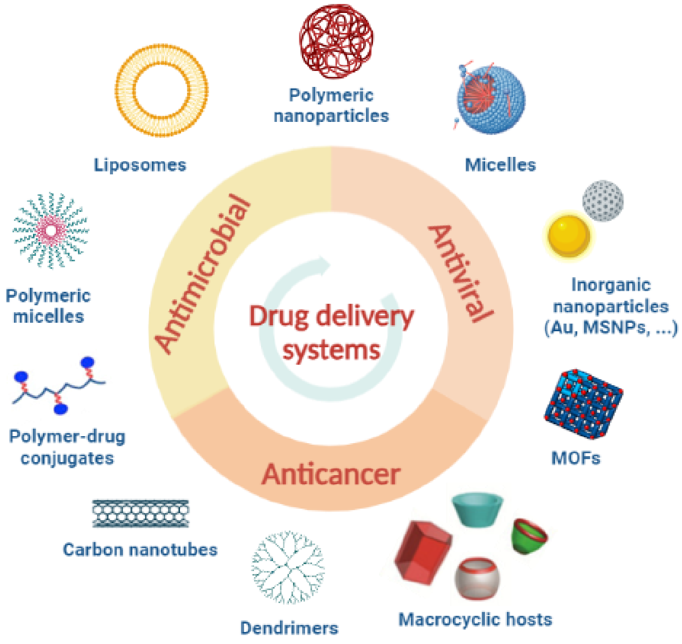

Figure 1. Examples of proposed DDSs.

Polymer-based DSSs are made up of a repeating unit of specific biocompatible and biodegradable polymers. The polymeric systems can be obtained through different strategies such as the inclusion of the drugs in the core of polymeric nanoparticles or the conjugation of the therapeutics to the polymer chains; accordingly, their size is between a few nm to several microns.[18] Micelles are usually formed through the self-assembly of a monolayer of lipid molecules in the aqueous environment into a nano-vesicle of between 5 and 50 nm. They permit the successful transport of hydrophobic molecules, trapped in the hydrophobic core, at concentrations above their inherent water solubility. Liposomes are bilayer vesicles similar to the cell membrane with sizes ranging from 10 nm to several microns. The hydrophilic phospholipids of the outer layer are exposed to the aqueous environment, while those of the inner layer enclose the aqueous core. Consequently, the hydrophobic tails of the bilayer lie above each other and are often used to trap hydrophobic drugs while the aqueous core is used to entrap hydrophilic drugs. Lipid nanoparticles were proposed to effectively deliver nucleic acid-based therapeutics to target cells. They can be engineered to include a variety of lipids, including cationic lipids, neutral lipids, and cholesterol, to optimize their stability, encapsulation efficiency, and cellular uptake. Additionally, they can be functionalized with targeting ligands to improve specificity for certain cell types or tissues.

Inorganic nanoparticles (dendrimers, silica and gold carriers) gained particular interest thanks to their tunable properties. Silica nanocarriers, for example, can be functionalized with targeting moieties or with a coating that protects the drug from degradation. Gold nanocarriers have unique optical properties that can be used for imaging and photothermal therapy, making them useful for the treatment of cancer. One of the main advantages of dendrimers is their ability to encapsulate a large amount of drug in their interior or on their surface thus allowing a controlled and sustained release of the drug. Taking advantage of their biocompatibility, nontoxicity and biodegradability, they were used as promising platforms for the delivery of a wide range of drugs, including small molecules, proteins, and nucleic acids.[19,20]

The above-mentioned nanocarriers are characterized by various sizes, architectures, and surface properties which are mainly responsible for their capabilities. In general, because of both their small size and large surface area to volume ratio, they possess unique features that allow them to carry drugs with high loading efficiency.[21] These transporters also improve drug solubility and stability, increase its biocompatibility, protect the drug from *in vivo* conditions and reduce its toxicity.[22] In general, the strategic use of suitable nanocarriers may reduce both the distribution volume of the drugs *in vivo*, thus avoiding indiscriminate exposure of healthy tissues, and unwanted side effects observed in systemic delivery of free drugs. Indeed, DDSs modify the pharmacokinetics of the carried medicine allowing for a more favourable/advantageous distribution in tissues.[23] Since drug carriers have sizes in the nanometric range and their surfaces are usually modified by hydrophilic molecules, they can avoid renal clearance and rapid uptake by the cells of the reticuloendothelial system (RES) thus maximizing blood circulation time. Accordingly, passive accumulation mechanisms can occur leading to high drug concentration in suitable tissues.[24] For example, in certain tumour regions, inflammation and sites of bacterial infection, the enhanced permeation and retention (EPR) process allows different intravenously injected drug carriers to extravasate and later accumulate in tissues with leaky vasculature and poor lymphatic drainage. As a result, drug delivery systems enhance the therapeutic potential of the drug while reducing systemic side effects.[25-28]

Macrocyclic hosts are another class of extensively studied drug-transporting systems as they exhibit a variety of adaptable conformations and structures that make them excellent molecular carriers. They are characterized by hydrophobic cavities which can entrap drugs by forming host-guest complexes mainly through hydrophobic interactions. Drug encapsulation in the host cavity potentially enhances its solubility, bioavailability and stability (*Figure 2*).

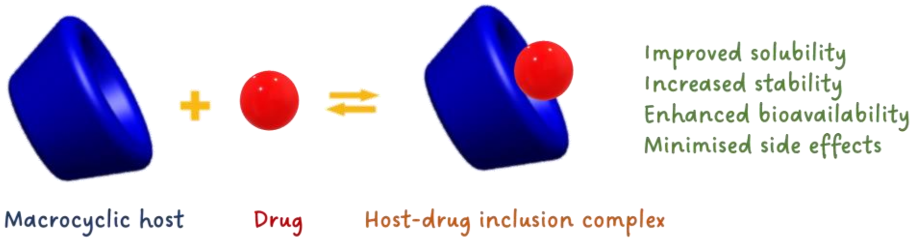

Figure 2. Modification of the inherent properties of a drug through host-guest complexation.

Host molecules can be properly modified with different functional groups to change their properties such as solubility and degree of hydrophobicity and to enhance either their affinity or selectivity for a given guest. Macrocyclic receptors include cyclodextrins (α-, β-, and γ-CD),[29] cucurbit[n]urils (CB[n]),[30] calix[n]arenes,[31] and pillar[n]arenes.[32] Their intriguing supramolecular functions and molecular recognition properties were exploited for the efficient delivery of different chemotherapeutic agents.[33,34]

CDs are cylinder-shaped cyclic oligosaccharides composed of D-glucose units linked by α-(1,4)-glucosidic bonds, which can be produced from enzyme-triggered starch degradation. The most commonly used CDs are α-, β-, and γ-CDs containing 6, 7, and 8 glucose units, respectively. The cyclodextrin is a truncated cone with an inner hydrophobic pocket and an outer hydrophilic exterior. CDs are the most widely studied and extensively applied receptors in the field of biomedicine as they exhibit good water solubility, good biocompatibility, and nontoxicity toward biological systems. CDs are known to form inclusion complexes with various hydrophobic drugs, such as quercetin, camptothecin, methotrexate and doxorubicin.[35,36] For example, it was demonstrated that the aqueous solubility and chemical stability of quercetin (at alkaline pH) can be substantially augmented via complexation with β-CDs (*Figure 3*).[37]

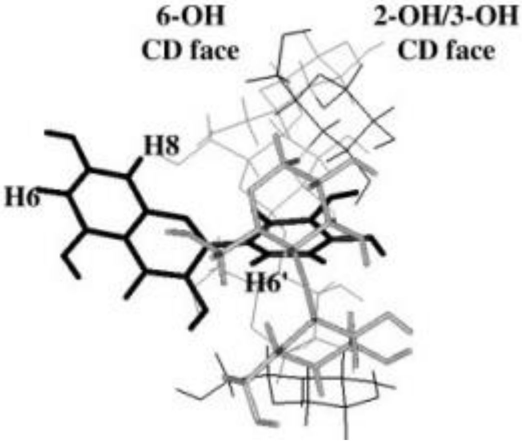

Figure 3. Molecular dynamics simulation of the quercetin/β-CD complex.[37]

Cucurbit[n]urils are a family of barrel-shaped macrocycles consisting of *n* glycoluril units (primarily with *n* = 6, 7, and 8) linked in a ring-like arrangement by 2*n* methylene groups at each side. The most commonly used CB in drug recognition is CB[7] because of its relatively high water solubility compared to CB[6] and CB[8]. CB[7] can form complexes with many cationic or neutral drugs such as doxorubicin, oxaliplatin, cisplatin, memantine, and temozolomide.[38,39] In particular, the host-guest complexation of cucurbit[6]uril with a bifunctional guest compound (DTA) possessing one alkyl head and two ammonium tails was exploited to construct a drug delivery system able to encapsulate both a hydrophobic dye as molecular probe and doxorubicin in its internal microenvironment (*Figure 4*). The proposed doxorubicin-loaded nanoparticles exhibited better anticancer activity toward tumour cells.[40]

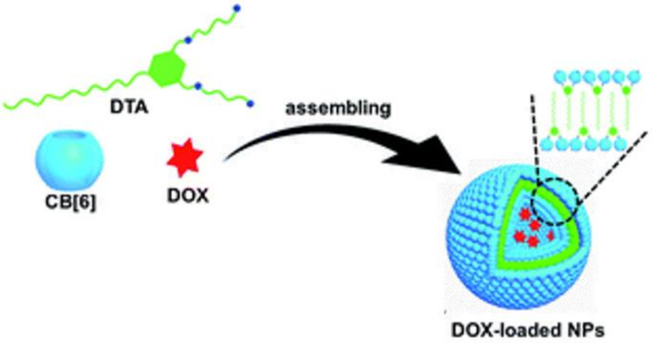

Figure 4. Graphical representation of the doxorubicin-loaded nanoparticles.[40]

Calix[n]arenes are basket-like-shaped macrocyclic hosts composed of *n* (generally *n* = 4, 5, 6, or 8) phenolic units linked by methylene bridges at the *ortho* positions of their constituent hydroxyl group. They can exist in several conformations and usually exhibit a higher affinity for guests in their cone conformation.[38] Due to the very limited solubility in aqueous media, different functional groups, such as sulfonate, carboxylate, phosphonate and ammonium moieties, have been introduced into the calixarene molecules to confer water solubility.[41] Water-soluble calixarene derivatives show good biocompatibility and non-cytotoxicity, which are important prerequisites for practical application as DDSs. Calixarenes can encapsulate further classes of anticancer drugs such as doxorubicin, temozolomide, carboplatin, docetaxel and paclitaxel.[31] For example, the inclusion of temozolomide in the hydrophobic cavity of *p*-sulfonatocalix[4]arene protects the drug by preventing its rapid hydrolysis (*Figure 5*), and it was observed a significant reduction in the growth of glioblastoma cells when treated with the inclusion complex rather than with free drug.[42]

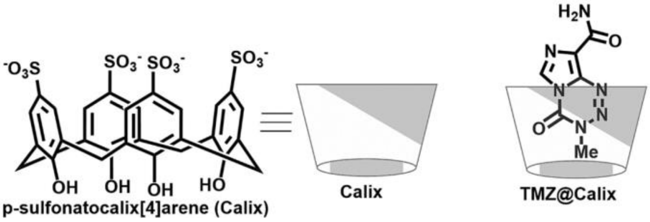

Figure 5. Schematic representations of *p*-sulfonatocalix[4]arene and its inclusion complex with temozolomide.[42]

More recently, an amphiphilic derivative of *p*-sulfonatocalix[4]arene able to form micellar nanoparticles was proposed for the co-entrapment of temozolomide and curcumin (*Figure 6*). The encapsulation into the calixarene-based nanocontainer enhanced the solubility and half-life of both drugs, whose therapeutic efficacy is affected by low solubility and rapid degradation.[8]

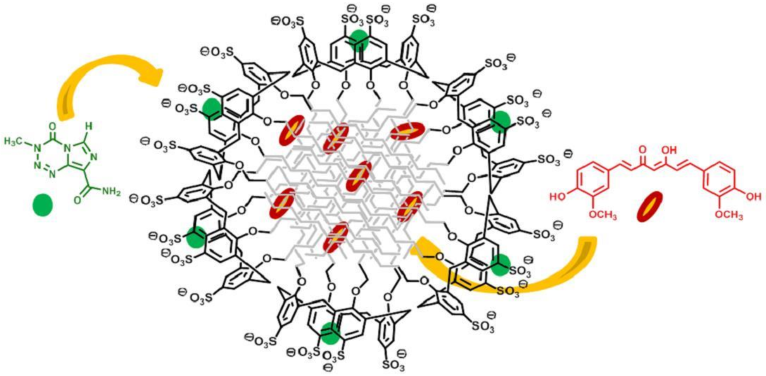

Figure 6. Graphical representation of the *p*-sulfonatocalix[4]arene-based micellar aggregate with the loaded drugs.[8]

Pillar[n]arenes are a class of pillar-shaped macrocyclic hosts composed of n (mainly $n = 5$ or 6) hydroquinone units linked by methylene bridges at their respective *para* positions. Like calixarenes, pillar[n]arenes can be easily functionalised through the incorporation of sulfonate, carboxylate, ammonium, or guanidinium subunits. They can bind drugs such as amikacin, norharmane and oxaliplatin.[43]

Inspired by the shape and supramolecular performances of pillar[n]arenes,[44,45] a novel class of macrocycles, the prism[n]arenes (*Figure 7*), were recently proposed.

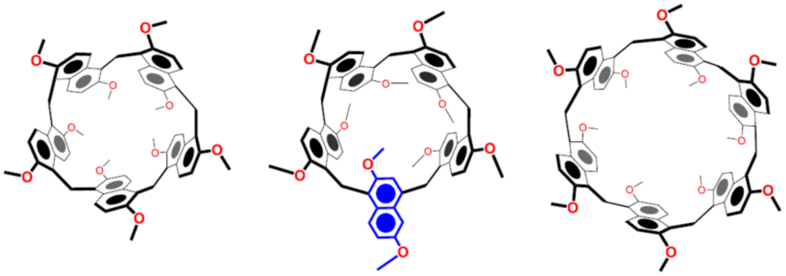

Prism[5]arene

1,4-C-prism[5]arene

Prism[6]arene

Figure 7. Structures of prism[n]arenes.

The prism[n]arenes are cyclo-structures based on methylene-bridged 1,5-naphthalene units. They have an electron-rich cavity with conformational flexibility as they can tilt the naphthalene walls.[46] Their ability to complex cations in organic solvents was accurately studied highlighting interesting binding properties. Although the high affinity towards model molecules would suggest their potential use as DDSs, their solubility in solely organic solvents represents a great limit for their application as drug-transporting systems. For this reason, more recently, prism[n]arenes were suitably functionalized with carboxylate groups to obtain new and completely water-soluble macrocyclic receptors (hereafter named $PrS[n]^{carboxy}$, $n = 5$ or 6, *Figure 8*) which may be employed as potential drug containers and carriers.[47]

Studies of the molecular recognition properties of these macrocycles in aqueous solution to evaluate their ability to encapsulate small molecules by forming discrete host-guest complexes are needed.

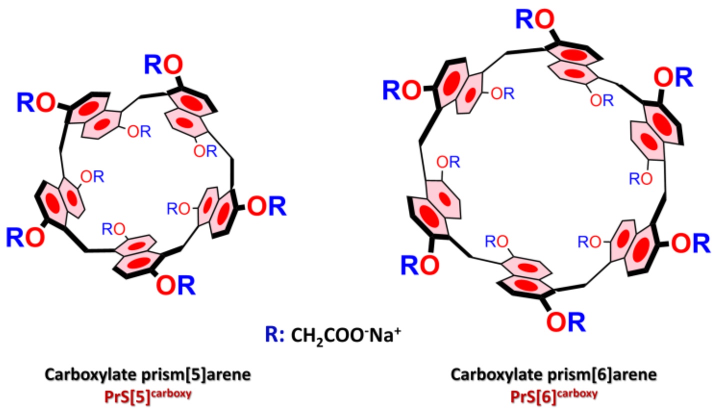

Carboxylate prism[5]arene
PrS[5]^{carboxy}

Carboxylate prism[6]arene
PrS[6]^{carboxy}

Figure 8. Structures of PrS[n]^{carboxy}.

2. *Polymer-based carriers*

Polymer-based DDSs are extensively described in the literature. They gained particular attention for their potential to efficiently deliver bioactive compounds, including drugs, proteins, genes and nucleic acids, thus becoming a promising tool in pharmaceutical and biomedical applications.

Polymers are macromolecules characterized by flexibility and diversity in composition and property and can be easily functionalized. Unique features, including nontoxicity, water solubility and biocompatibility, made polymers an advantageous "building block" for developing nanocarrier structures. The presence of multiple functional groups ensures the efficient incorporation attachment of the therapeutics to achieve target-oriented delivery of payloads. These features, along with the relatively high abundance in nature, are responsible for the great interest in natural polymers such as chitosan, alginate, and hyaluronic acid. Once introduced into the organism, they do not require removal or additional manipulation and their degradation products are normal metabolites of the body or products that can be metabolized and easily cleared from the body. However, synthetically polymers (*i.e.* poly(ethylene glycol), poly(glycolic acid), poly(lactic acid), poly(lactic-co-glycolic acid), poly(acrylic acid)) with biocompatibility, degradability and other properties similar to those of natural polymers, are widely used for the development of new DDSs with specific features (chemical, interfacial, mechanical and biological) for suitable applications.[48] Various classes of polymeric nanostructures such as nanoparticles, liposomes, micelles, and nanogels were proposed.

Depending on the processes used for the preparation, polymeric nanoparticles can be distinguished into nanospheres or nanocapsules (*Figure 9*). Nanospheres are matrix systems in which the drug is dispersed throughout the structure or adsorbed onto the surface, whereas nanocapsules are systems in which the drug is contained within the core surrounded by a polymeric shell.[49]

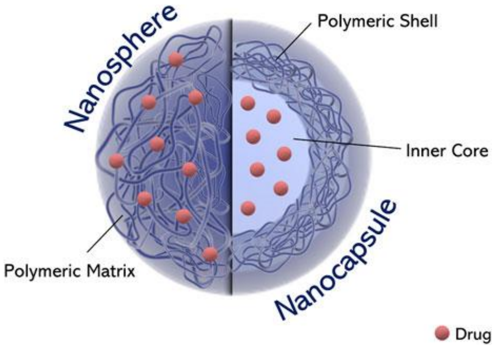

Figure 9. Schematic representation of polymeric nanoparticles as a function of their morphology.[49]

Polymeric micelles are self-assembled structures of amphiphilic polymers that contain both connected hydrophobic and hydrophilic moieties. The self-aggregation processes form a structure with a hydrophobic core with hydrophilic side chains in the outer shell. This structure hinders the encapsulation of hydrophilic drugs allowing instead the inclusion of hydrophobic drugs into the micelle core. Polymeric micelles prepared with a hydrophobic core and poly(ethylene glycol) shells exhibit improved permeability and retention properties for the delivery of anticancer drugs in malignant tissues.[7]

Nanogels are physically or chemically cross-linked polymeric networks exhibiting attributes such as biocompatibility, mechanical strength, high water absorption capacity, good dispersion stability, and structural permeability. These properties, along with high drug-loading capability, make nanogels suitable for drug delivery applications.[50] For example, a polysaccharide-based nanogel was proposed for the successful delivery of curcumin and simvastatin.[51]

Generally, polymeric carriers can be obtained by exploiting different development strategies: (1) physical encapsulation/inclusion, (2) complexation of drugs with donor atoms of the polymer chains, and (3) conjugation of drugs with a polymeric carrier via a linker.[52] The chosen method will somehow influence the performance of the developed system (loading and release capacity, physico-chemical properties).

2.1 Layer-by-layer based polymeric nanoparticles

The *layer-by-layer* (LbL) approach can be used as a potent tool to develop advantageous polymeric and hybrid micro- and nanoplatforms displaying multifunctional properties (*Figure 10*).

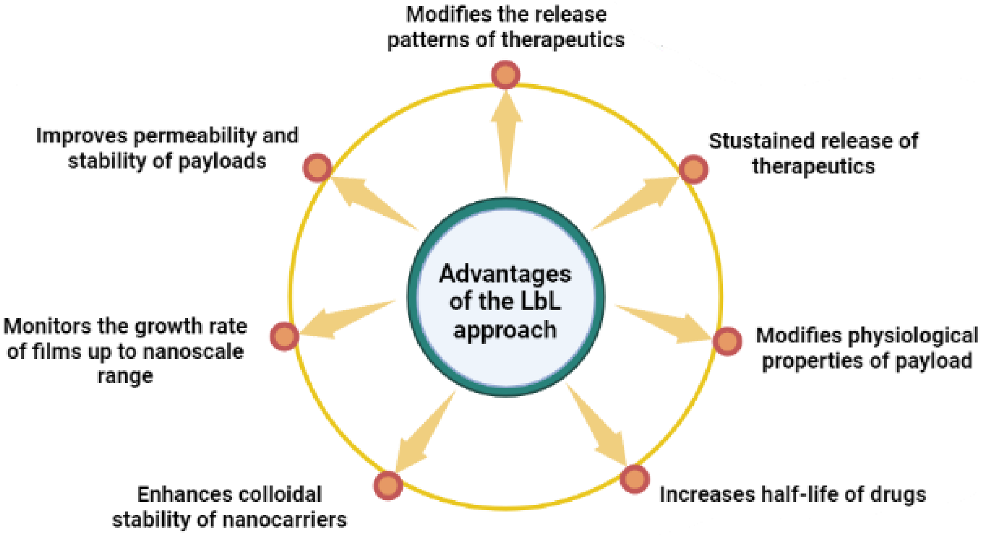

Figure 10. Advantages of the LbL approach.

Initially, the LbL approach was based on the alternate deposition of charged polyelectrolytes onto planar substrates to create self-assembled multilayer films through electrostatic interactions. Once they are attached to the substrate, the net charge (usually negative) on the substrate surface switches because of the adsorption of polyelectrolytes with opposite charges. The films are consequently rinsed with pure water to remove the loosely adsorbed polyelectrolytes. To subsequently grow the LbL, the films are placed in the negatively charged polyelectrolyte solutions. With such cyclic depositions, multilayer films on the substrates with desired thicknesses, structures and charge can be obtained (*Figure 11*).

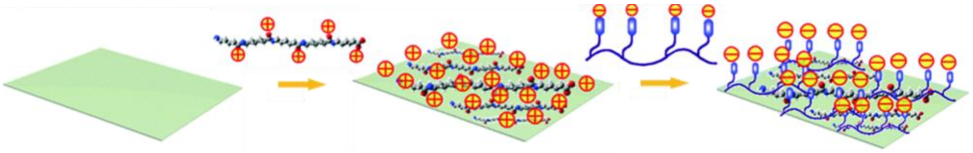

Figure 11. Scheme of the preparation of multilayer thin films using the LbL approach: deposition of positively charged polyelectrolytes and subsequent deposition of negatively charged ones.

The structure of the LbL film is influenced by different process parameters including pH, temperature, ionic strength, solvent and physicochemical properties of polyelectrolyte.[53,54] For example, the pH value of polyelectrolyte solution influences the charge density and degree of ionization of weak polyelectrolyte thus altering the composition, crosslinking and structure of the polymeric coating.[55] The ionic strength affects the permeability of molecules, stability, mass, swellability, stiffness and growth of LbL coating. Since the major interaction between the polyelectrolytes is due to the presence of ionic charges on multilayers, a change in ionic strength leads to the conformational transition of polyelectrolytes (extended rod-like surface at low ionic strength or globular coil at larger ionic concentration) determining rough to multilayer structure instead of smooth ones. Also, the molecular weight and charge density affect the multilayer film. An increase in the molecular weight of a polycation provides a film with higher internal roughness, swelling and dissociation response. For example, molecular weight less than 65 kDa provides better stability while higher molecular weight leads to enhanced aggregation. The increase in charge density of polyelectrolytes enhances the thickness of multilayer thin film.[56]

Although LbL was originally developed for polyelectrolyte/polyelectrolyte systems, nowadays the versatile approach is applicable for almost any type of charged components, including inorganic clusters, nanoparticles, nanorods, dendrimers, polypeptides, DNA and proteins obtaining an exceptionally broad range of morphological characteristics and functional responses (*Figure 12*).

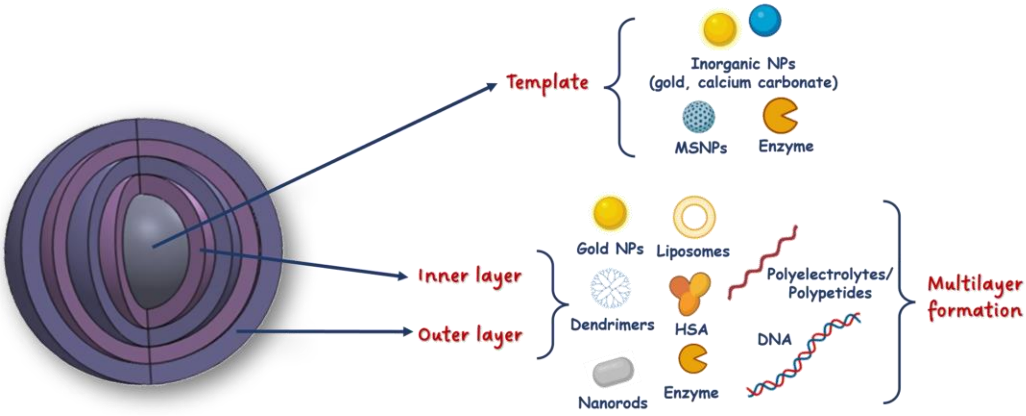

Figure 12. Structure of LbL-based nanoparticles.

The forces that promote the formation of LbL films are also not restricted to electrostatic interactions, but they also include ionic charge transfer, hydrogen bonding, covalent conjugation, biological recognition, and hydrophobic interactions.[57] Thanks to its versatility, the process was rapidly exploited to create multi-component films not only in planar substrates but also in a wide variety of (sacrificial) templates such as colloidal particles thus obtaining polymeric particles. The subsequent remotion of the core yields hollow polymer capsules.[58] The size and shape of the polymeric systems are affected by the template employed. The chosen substrate must be stable during the LbL process to ensure the proper deposition of the multiple layers and, at the same time, its remotion should be carried out in mild conditions, avoiding any damage to the multilayer assembly and their sensitive components. Drug or enzyme crystals can be used as a template in the LbL approach resulting in high loading capacity concerning other carriers. In particular, this allows for improving the stability and availability of hydrophobic and poor water-soluble compounds of bio/pharmaceutical interest.

The modulation of the membrane permeability by increasing the number of deposited layers (which increases the thickness of the membrane) or using polymers with peculiar conformation permits to control the kinetics of the release of the target molecule.[59] This approach was used for the encapsulation of doxorubicin within polymer capsules made out of tannic acid and poly(N-vinylpyrrolidone).[60] However, the use of these kinds of substrates does not allow the control of the shape, the polydispersity and the size of the polymeric platforms. A promising alternative is the use of highly porous templates such as mesoporous silica or calcium carbonate nanoparticles. The therapeutic payload (small drugs, genetic material, proteins, nanoparticles) can be included in the porous template by incubation or coprecipitation; the high surface area and controllable pore size will ensure a high loading capacity. The biocompatible template can be finally eliminated (using a suitable solvent) or not, obtaining polymer capsules or core-shell structures, respectively.

Also, the polymeric layers can affect both the mechanical integrity and effectiveness of the resulting systems. The polymeric architecture shields the included cargo from the surrounding environment and is responsible for the structural stability of the systems to avoid disassembly before reaching the target site. LbL multilayer capsules were vastly studied for drug delivery applications predominantly using classical polyelectrolytes with a net surface charge such as sodium poly(styrenesulfonate) (PSS), poly(acrylic acid) (PAA), poly(methacrylic acid) (PMA), poly(allylamine) hydrochloride (PAH) as well as poly(ethylenimine) (PEI). Indeed, their robust structure enables the transfer of substrates across the polymeric membrane while protecting the active compound from the external environment. [61]

3. *Stimuli-responsive carries*

Despite their potential benefits, there are also some issues associated with the use of DSSs. The retention of the drug within the carrier should be strong enough to avoid premature leakage but, on the other hand, the drug should be easily released from the carrier once it has reached its target site. This is a significant challenge since the active targeting nanomaterials often suffer from inadequate delivery of therapeutics at targeted sites and/or an insufficient release of the cargo might hinder the therapeutic efficacy.[62] To overcome such shortcomings in the targeted delivery process, a promising alternative involves "on-demand" processes that account for the tailored site- and time-controlled release of therapeutics.[63] This requires the development of stimuli-responsive systems which nowadays are emerging platforms for numerous applications in the field of nanotechnology and therapy of diseases. The concept of stimuli-responsiveness is of great importance in nature, and its origin lies in the fundamental behaviours of natural systems, including communication and survival of living cells and organisms. In the field of drug delivery, this strategy was first applied in the late 1970s with the use of thermosensitive liposomes for the local release of drugs through hyperthermia.[64]

Stimuli-responsive nanosystems must "smartly" recognize the surrounding altered microenvironment typical of a specific pathology and react accordingly. Ideally, these systems should entrap the drug in such a way that no premature release occurs at undesirable places. Subsequently, properties changes in response to various stimuli will trigger the release of therapeutics directly at the desired site thereby reducing the effect in the surrounding healthy tissues.[65-67] This requires the use of biocompatible materials that can undergo a specific protonation, a hydrolytic cleavage, or a molecular or supramolecular conformational change upon the suitable stimulus.[68] For this reason, functional natural or synthetic molecules, belonging to the class of "soft materials", (such as polymers, lipids and peptides) able to respond to particular conditions are therefore employed.[69] Generally, their design foresees the presence of a hydrophobic inner core and a hydrophilic or amphiphilic outer shell. Inorganic nanocarriers were also developed providing stable structures able to host suitable drugs and to arrange effective stimuli-responsive systems.[70] Formulating drugs entrapped in liposomal carriers or micelles as well as in other nanoparticulate drug delivery systems showed successful results in terms of therapeutic efficacy and tolerability.[71-74] In addition, these nanocarriers sometimes contain other components such as a targeting ligand or adhesion ligand which is specific to its receptor on target cells or tissues.

A wide range of stimuli able to trigger the drug release at the right place and time were reported (*Figure 13*). They can mainly be categorized as endostimuli (internal or intrinsic) and exostimuli (external or extrinsic).

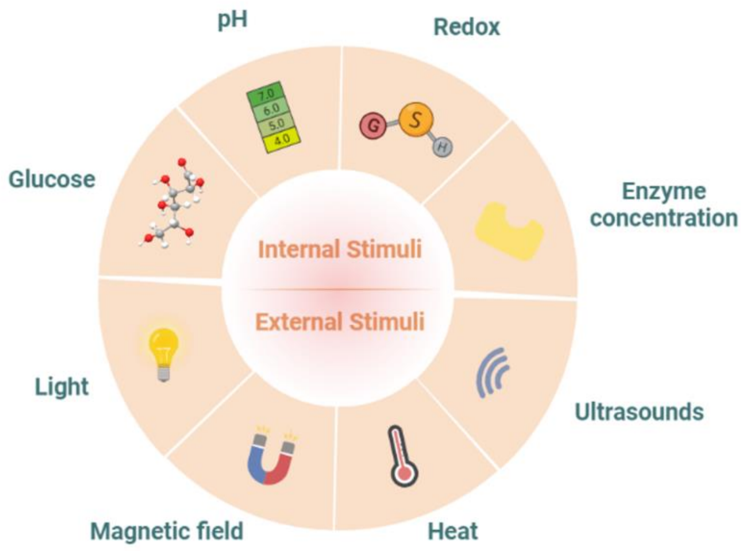

Figure 13. Illustration of internal and external stimuli.

Physiological signals such as pH, redox potential, and metabolite or enzyme concentration changes belong to the internal stimuli category.

pH-sensitive systems were widely used for the delivery of several drugs in specific organs characterized by pH changes due to pathological conditions including cancer and inflammation. pH-responsive nanocarriers decorated with a targeting moiety or ligand can bind to its target cell resulting in its internalization. After entering an acidic intracellular environment, pH-responsive carriers can dissociate and deliver the loaded therapeutics.

The release of therapeutics from nanocarriers can be triggered through a redox reaction by decorating the nanocarriers with redox-sensitive bonds (e.g. disulfide or diselenide bonds) and/or linker that is known to cleave by glutathione (GSH) which is known to be present in the intracellular compartments and tumour tissues at higher concentration (2-10 mM) than the normal ones (2-10 μM).[75] Many redox-sensitive carriers were developed including nanocapsules, mesoporous silica nanoparticles,[76] polymeric vesicles and micelles.[77] The conjugation or the inclusion of some bioactive drug to or into nanomaterials through disulfide bonds ensures the release of the payload inside the cells. Moreover, the redox sensitivity could also be applied to detach the surface shell and cross-link the core to increase the stability of the nanocarriers.[65] Another strategy to exploit the GSH-triggered release is based on the GSH-reduction of metal ions inside cancer cells. For example, cationic vesicles formed by chelation of Fe(III) with amphiphilic pillarene were investigated as a redox-responsive system: the reduction of Fe(III) to Fe(II) induced by GSH determined the collapse of the vesicles and, consequently, the release of the included drug (*Figure 14*).[78]

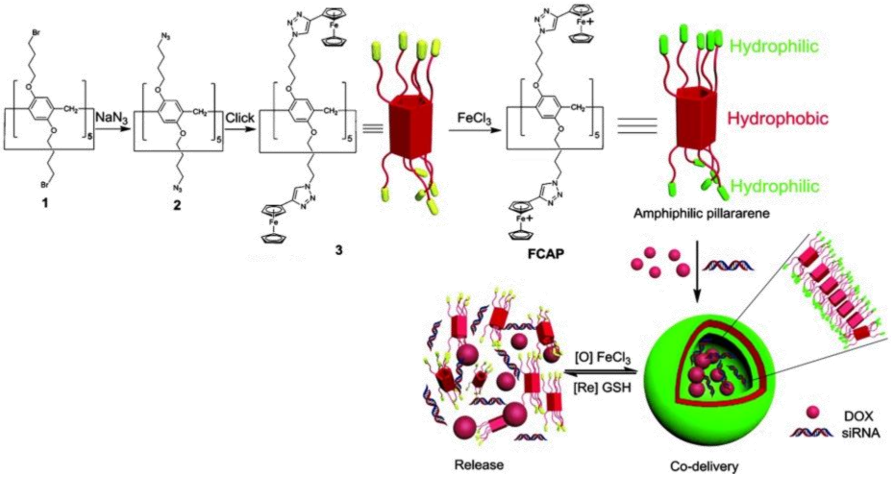

Figure 14. Illustration of the synthesis of ferrocenium-capped amphiphilic pillar[5]arene, formation of cationic vesicles, and redox-responsive drug/siRNA release.[78]

The morphology of redox-sensitive nanocarriers may affect the intracellular delivery of the therapeutics. Different redox-responsive reservoirs with different morphologies (spheres, vesicles, lamellae) were self-assembled with camptothecin and polymers through the disulfide bonds demonstrating that the lamellar structure permits more efficient cellular internalization than others.[79]

Enzymes play essential roles in systemic metabolism and cell regulation. Many of them such as proteases, phospholipases, and glycosidases are present at higher concentrations at disease sites or areas of enzymatic expression dysregulation, which can be associated with certain diseases (tumour or inflammatory tissues). Owing to these unique physical properties, enzyme-responsive platforms can be designed to achieve high specificity, stimulus-triggered drug release, and reduced side effects.[80]

Metalloproteinases (MMPs) are the most used triggers for drug-controlled release. They play complex roles in the promotion of tumourigenesis by degrading the extracellular matrices and activating growth factors and angiogenesis, while their expression and activation are increased in almost all tumours compared to normal tissue. For example, an MMP-sensitive based on polymer-coated mesoporous silica nanoparticles with therapeutics loaded into both core and shell domains was proposed.[81] Intracellular-specific enzymes (such as cathepsin B, elastase, or glycosidases) are also employed for controlled drug release. For example, cathepsin B (CaB), a lysosomal cysteine protease involved in cancer progression with specific peptide cleaving capability,[82] offers an attractive choice for triggering selective cancer therapy. This inspired the design of CaB-activatable nanocarriers for selective therapy.[83] Enzyme sensitivity can be also exploited for the treatment of bacterial infection. For example, a triple-layered nanogel, which contains a bacterial lipase-sensitive poly(ε-caprolactone) interlayer between the cross-linked polyphosphoester core and the shell of the poly(ethylene glycol), was proposed for the release of vancomycin allowing the significant inhibition of the growth of *S. aureus* and killing intracellular bacteria (*Figure 15*).[84]

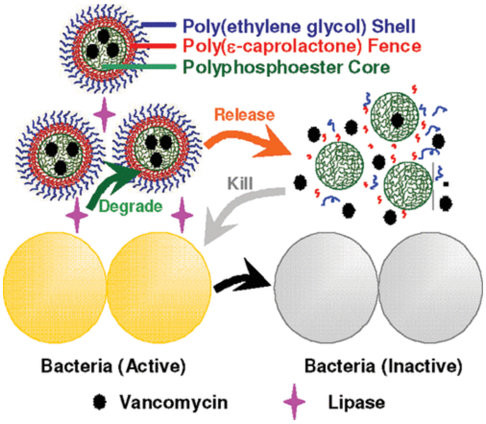

Figure 15. Schematic illustration of the on-demand drug delivery triggered by bacterial lipase to treat bacterial infections using a lipase-sensitive polymeric nanogel.[84]

Although the internal triggers are intrinsic to the pathological microenvironment, they could show poor specificity and heterogenetic distribution which may affect their efficacy. The use of external stimuli allows for enhancing the accumulation of the nanocarriers in a desired region thanks to strict control of the location and intensity of a given stimulus.

The release of therapeutics from carriers can be induced by various external stimuli such as temperature changes, light, magnetic fields or ultrasound. Such stimuli can be applied to a specific location or organ to trigger the release of therapeutics from the nanocarrier while it passes by the targeted location or organ. By applying heat or cold, a local temperature shift can be achieved in the target location or organ in the body to dissociate the nanocarriers at that site resulting in the delivery of the therapeutics. Similarly, nanocarriers can be formed that are sensitive to various radiations (ionizing radiation, microwaves, or radiowaves), light (ultraviolet, near- or far-infrared) and sound waves (ultrasound).

Thermoresponsiveness is among the most investigated stimuli-responsive approaches for the delivery of therapeutics. A thermoresponsive nanocarrier is usually made up of one component whose properties could be sharply changed by variations in temperature. Such sensitive material can trigger the release of the loaded drug in response to a variation in the surrounding temperature. Ideally, thermoresponsive carriers should be capable of holding their load at body temperature (~37 °C) and quickly deliver the loaded drug at sites of locally heated tissues which are usually observed where inflammation, injury, infection, and cancer occur (with a temperature of about ~40-42 °C).[85]

Thermoresponsiveness is also associated with a decrease in temperature phenomena. In this case, a local cooling effect can increase the porosity of the nanocarrier system leading to free diffusion of the loaded therapeutics at the target site. Thermoresponsive systems are generally liposomes, polymer micelles or nanoparticles. For liposomes, thermoresponsiveness usually arises from a phase transition of the constituent lipids and the associated conformational variations in the lipid bilayers. Thermosensitive liposomes are perhaps the most advanced thermoresponsive nanosystems, as shown by their use in several clinical trials. Temperature-responsive polymeric systems could show a negative or positive temperature sensitivity. In the first case, the polymers swell due to the formation of hydrogen bonds at temperatures lower than the lower critical state temperature (*LCST*) and collapse at temperatures above *LCST*.[86,87] In the latter, positive temperature-sensitive polymers swell at temperatures above the upper critical state temperature (*UCST*) and collapse at temperatures below it.[88] Temperature-responsive polymers display a transition from a sol-gel form with varying temperature changes; many hydrogels are capable of in situ gelation at body temperature. A typical example of a temperature-sensitive polymer is poly(N-isopropyl acrylamide) (PNIPAM) which exhibits a lower critical solution temperature (~33 °C).

Exploiting the temperature changes peculiar to certain pathologies can be challenging due to the narrow range in which they oscillate. Another strategy for achieving thermal sensitivity is to incorporate thermal-unstable materials inside nanocarriers. *In vivo,* heat is generally applied by using temperature-controlled water sacks, radiofrequency oscillators or microwave applicators. For example, NH_4HCO_3-incorporated liposomes allowed efficient intracellular drug delivery exploiting the ability to generate CO_2 after giving local hyperemia (42 °C) to make liposomes efficiently swollen and collapse (*Figure 16*).[89]

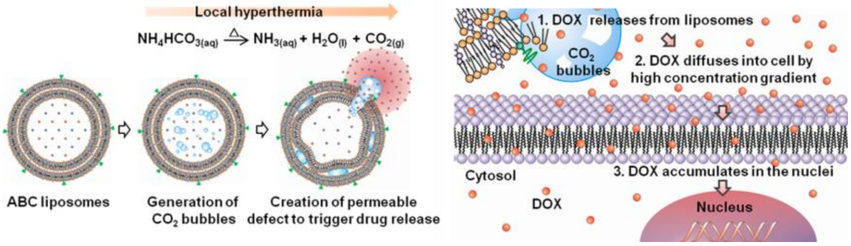

Figure 16. Schematic illustrations of the structure and functions of thermoresponsive, bubble-generating liposomes and the mechanism of localized extracellular drug release as triggered by heat.[89]

Magnetic carriers belong to the category of systems able to generate heat in response to a physical (magnetic) stimulation. These nanocarriers are composed of a magnetic core, where drugs are generally loaded, and a coating shell whose surface can be modified with targeting molecules.[90] Depending on the strength of the magnetic field, magnetic-sensitive systems can effectively generate thermal or mechanical effects applied in hyperthermia theranostics. Heat is generated by magnetic particles during magnetization reversal, and the therapeutic effects are increased by increasing the amplitude and frequency of an alternating magnetic field.[91] Hyaluronic acid-modified mesoporous silica-coated superparamagnetic Fe_3O_4 nanoparticles (HA-MSNs) are just an example of magnetic-sensitive carriers (*Figure 17*).[92]

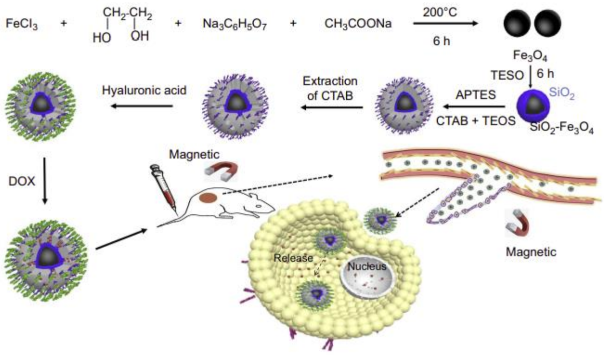

Figure 17. Schematic illustration of the fabrication of the HA-MSNs and their application for responsive drug release after specific binding with cancer cells, as well as targeted cancer therapy *in vivo*.[92]

The magnetic properties of the nanoparticles permitted the accumulation of the drug tumour tissues enhancing the EPR effect while the presence of hyaluronic acid allowed their uptake via CD44 receptor-mediated phagocytosis, as CD44 (which can specifically bind HA) is overexpressed in many cancer cells.[93] Accordingly, the use of magnetic-based systems represents an inspiring strategy that reduces the drug dose needed and the associated systemic toxicity.

Ultrasound-triggered drug delivery systems offer spatiotemporal control of therapeutic delivery at the specific site thereby reducing side effects to the normal tissues. The use of ultrasounds is also attractive because of their non-invasiveness, the absence of ionizing radiations, and the facile regulation of tissue penetration depth by tuning frequency, duty cycles and time of exposure. Ultrasound waves can trigger the release of the drug from a variety of nanocarriers through the thermal and/or physical forces generated by cavitation phenomena or radiation forces.[94-96] Indeed, the mechanical mechanisms associated with cavitation can induce nanocarrier destabilization, drug release and transient increase in vessel permeability, leading to the cellular uptake of therapeutic molecules. Ultrasound-responsive polymeric systems were extensively used to help in site-specific controlled drug delivery. Many novel nanodroplets, bubbles, micelles and gels have been developed as ultrasound-responsive, polymeric systems. For example, pluronic micelles loaded with doxorubicin were used as ultrasonically responsive polymeric DDSs allowing the maximum drug release by using a frequency of 20 kHz.[97] Other examples include an ultrasound-responsive chitosan doxorubicin nanobubble system which accounts for the release of almost twice the amount of drug compared to the non-ultrasound-responsive system.[98]

Light-responsive drug delivery systems are generally non-invasive, and they can be remotely controlled in a spatiotemporal manner. Owing to these features, several light-sensitive carriers were developed to deliver therapeutics at the target site in response to the application of specific wavelengths such as UV, visible or near-infrared (NIR).[99] Several light-responsive nanocarriers were developed by using nanoparticles,[100] polymeric micelles,[101] liposomes,[102] nanogels,[103] and nanorods.[104]

In general, light-sensitive systems show two drug-release pathways based on photochemical and photothermal mechanisms. They imply changes in the conformation of suitable molecules (azobenzene, spiropyran, diazonaphthoquinone etc.), the cleavage of the light-sensitive chemical bonds with subsequent nanocarrier dissociation and triggered release of therapeutics to diseased regions. The irradiation can induce either reversible or irreversible structural modifications of the nanocarriers; the range of irradiation can be properly tuned to preserve normal organs and tissues. For example, the UV-Vis reversible photoisomerization of the azobenzene group (and its derivatives), from trans to cis upon irradiation at 300-380 nm and from *cis* to *trans* by shining light in the visible region, enables photo-regulated control of drug release. In general, the photo-switching carriers demonstrated high potential for loading different bioactive compounds for UV-Vis triggered drug release, including paclitaxel, docetaxel and doxorubicin as well as for cancer therapy.[105] Light-responsive systems can also be used for light-activated imaging or imaging-guided therapy to generate reactive oxygen species (ROS) for photodynamic therapy (PDT) [106] and photothermal effect for tumour ablation by photothermal therapy (PTT). [107]

Although the use of external stimuli ensures the accumulation of the nanocarrier in a desired region thanks to the strict control of the location and intensity of a given stimulus, they could be impractical when the location of the pathological tissues is uncertain. [65]

To make more specific and effective nanocarrier systems, recently researchers have designed multi-stimuli responsive nanocarriers by combining two or more stimuli-responsive components in a single nanocarrier. This facilitates multistage drug delivery and achieves higher specificity and efficacy. Because of the coexistence of a pH gradient and an oxidative environment in certain pathological conditions, pH and redox responsiveness can be sometimes used in combination. For example, nanocarriers responding to both intracellular pH and GSH were developed for enhancing intracellular drug delivery.[108]

pH and temperature-sensitive nanoparticles comprised of a copolymer of poly(N-isopropylacrylamide) and carboxymethylchitosan as the shell and PLGA as the core of the nanosystem were proposed. This nanoparticle was loaded with a superparamagnetic iron oxide (SPIO) which showed the dual function of image contrast agent and inductor of temperature change by an external magnetic field. The temperature alternation caused the nanocarrier conformational change, allowing the drug to be released. Moreover, the pH-sensitive shell of the nanoparticles also facilitated drug release in the acidic pH environment.[109] Light sensitivity and pH responsiveness can also be associated by exploiting the resonance surface properties of palladium and silver.[110] Other systems have shown response to temperature and magnetic field,[111] to light and reducing environment to control the release kinetic from block copolymer micelles,[112] and to ultrasounds and enzymes to enhance drug release from liposomes.[113]

As for the LbL-based systems, the functionalization of the membrane can be achieved by using a wide variety of inorganic particles and/or therapeutic agents as building blocks in the assembly process. Alternatively, the building blocks can be functionalized before or after deposition on the template. The use of an “active agent” as a component of the polymeric membrane is one of the most employed strategies to provide functional properties to the multilayered capsules. The incorporation of inorganic nanoparticles such as magnetite (Fe_3O_4) or gold nanoparticles or nanorods between the layers endows the “smartness” of polymeric membranes. This allows the monitoring and/or the triggered drug release upon proper stimuli.[114,115] The cross-linking of the building blocks constituting the multilayer membrane can be also exploited to determine the mechanical integrity and/or responsiveness to the polymeric capsules. For example, the use of thiol-modified polyelectrolytes for the LbL deposition and its subsequent crosslinking to form disulfide bonds allows to obtain a redox-responsive platform able to release the included drug in response to the GSH concentration.[116] Polymeric capsules were also developed by employing polyelectrolytes that are sensitive to UV light or pH change.[117] Also, the conjugation of the therapeutics to a polyelectrolyte permits a better control of the release rate and an improvement in the targeting. For example, doxorubicin and paclitaxel were suitably conjugated to a wide variety of polyelectrolytes by exploiting the pH-responsive amine-bond formation or the inclusion of guest molecules into the CD hydrophobic cavity.[118]

4. pH-responsive carriers

The idea of pH responsiveness is one of the most explored and extensively pursued in the field of stimuli-responsive drug delivery platforms. The mode of action of these systems exploits the well-marked pH changes existing between healthy and pathological tissues (due to cancer, infection or inflammation process, ischemia), intracellular compartments (cytosol, endosomes and lysosomes), and organs (gastrointestinal tract or vagina).[68,69,119]

The development of pH-sensitive nanocarriers against tumours is still considered a charming attractive strategy in the field of cancer treatment. These kinds of systems were introduced in 1980 relying on a typical characteristic of cancer cells.[120] According to the *"Warburg Effect"*, cancer cells modify their metabolic pathway increasing the anaerobic glycolysis instead of the Krebs cycle, to support the biosynthetic requirements of uncontrolled proliferation. This leads to the accumulation of lactic acid and a decrease of the pH (from pH 7.4, typical of physiological conditions, to pH 5.7-6.0 depending on the tumour type).[121-123] Furthermore, the ischemic feature of tumour tissues and their low lymphatic supply contribute to accelerating the acidification of the tumour environment.[124] Hence, these features allow for enhancing the tumour-targeted drug delivery avoiding the leakage of chemotherapy agents into the healthy physiological environment and reducing the related adverse side effects.

The pH-responsive systems can also exploit the so-called *"endosomal effect"*. [125] The drug carriers taken up by cells through receptor-mediated endocytosis are trapped within the endosome (pH 5.0-6.5), which later matures to the lysosome (pH 4.5-5.0). Thus, the delivery systems can smartly respond to the severe acidic pH level by releasing the transported drug to the cytosol preventing its degradation and enhancing its bioavailability.[68,119]

Although pH-responsive delivery systems were extensively studied and proposed for cancer treatment, their use for the treatment of bacterial infections has recently emerged.[126-129] This heightening interest is owing to bacteria growth and metabolism: the production of acetic and lactic acid during glycolysis leads to localized acidification sites under anaerobic conditions.[130-132] Consequently, by exploiting the pH changes, the uncontrolled/untargeted release of antibiotics can be avoided thus promoting their accumulation and uptake at the infection sites level, reducing their toxicity and minimizing the undesired development of bacterial resistance.[133]

4.1 Strategies for the design of pH-responsive systems

pH-responsive systems must be designed to remain stable at physiological pH, but they need to undergo conformational changes under pathological acidic pH conditions.[134] Generally, the forces responsible for these dynamic responses are the formation or destruction of weak non-covalent bonds, such as electrostatic interactions, hydrogen bonds, or simple reactions involving molecule moieties and functional groups.

Two strategies are mainly applied in the design of pH-responsive carriers. The first strategy involves the use of acid-labile linkages. The acidic environment will induce the dissociation between the carrier and the drug, favouring its release. The formation and the cleavage of metal ion-ligand coordination bonds fall into this category. Metal ions and protons are Lewis acids and compete each other to bind the ligand, which is a Lewis base. At first, several “metal-based” drugs were investigated and proposed as anticancer agents (e.g. cisplatin complex) rather than stimuli-responsive systems as some of them can intercalate in DNA double-strands inducing tumour cell death.

Metal ions are present in living organisms where they play a key role in a variety of the processes necessary for life. Some of them, such as Cu, Fe, and Zn, called *essential elements*, have structural roles and are responsible for the stability of important biological molecules; in particular, they perform as a cofactor for certain enzymes involved in metabolism and cell growth and donate or accept electrons in redox reactions that are of primary importance in the generation and utilization of metabolic energy. Inspired by the mechanisms of biological processes involving metal ions (i.e., transferrin recycling in cells), biomimetic coordination-bonding processes were exploited to obtain a pH-responsive drug-delivery system. For example, *Xing et al.*[135] proposed pH-responsive systems based on coordination bonds between metal ions and drug and/or various host molecules for precise and sensitive release between pH 7.4 and 4.0 (*Figure 18*).

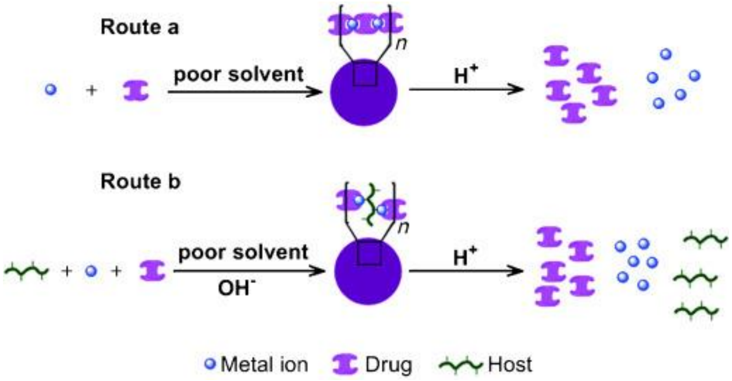

Figure 18. Schematic of a pH-responsive system based on coordination bond in nanoparticles.[135]

The second strategy is based on the use of pH-sensitive materials with ionizable (acidic or basic) functional groups. Owing to the pH differences occurring at the targeted acidic site, a protonation or deprotonation event will determine a charge shifting leading to conformational changes in the carrier. These events will trigger the release of the drug from a carrier in a pH-dependent fashion.

4.2 pH-responsive polymeric systems

Among the pH-responsive systems, polymeric ones aroused great interest thanks to their favourable physicochemical properties which made them ideal carriers for the delivery and controlled release of drugs. Indeed, these “smart polymers” can adapt their conformation (polymeric chains can shrink or expanse) in response to the internal stimulus ensuring the effective drug release at specific sites.[136] To date, a great variety of pH-sensitive nanocarriers have been designed to exploit pH changes. The drugs could be physically encapsulated or chemically conjugated to the carriers. Two different approaches can be exploited to prepare a pH-responsive polymeric system. It can be designed with acid-sensitive bonds whose cleavage allows the release of the molecules anchored at the polymeric backbone, the modification of the charge of the polymer or the exposure of the drug. Alternatively, polymers bearing ionizable groups (polyacid or polybases) can be directly employed to construct the nanocarriers.

Once reach the acidic target, the pH-sensitive carriers can accept protons and undergo a conformational change to their structures via three pathways to achieve drug release: (1) destabilisation, (2) precipitation/aggregation or (3) dissociation (disruption). This strictly depends on the pKa value of polymeric molecules functional groups and the microenvironmental pH.[137] This approach can be also applied to promote the internalization of the carriers into cells by achieving protonation of the functional groups on the surface of the nanocarriers at low pH, as the positively charged transporters may bind with the negatively charged cell surface via electrostatic interaction.[138] Hence, by properly choosing a polyacid or polybase moiety having a suitable pKa for the desired pH of action, it is possible to achieve targeted drug release or cellular uptake by the above-explained mechanisms.

The pH-responsive polymers can be classified (according to the pKa values of their functional groups) as anionic and cationic depending on their status at pH 7.4.

Anionic polymers with carboxylic acid functional groups are commonly used for targeting the acidic pH tissues, where they get protonated and become hydrophobic, causing shrinkage of the polymer chains (coil-to-globule transition) and leading to destabilization of the structure and payload release at either extracellular or intracellular sites. At physiological pH 7.4, their groups are deprotonated and hydrophilic and the negatively charged pendant groups determine the fusogenic properties of the polymer chains. Polyacids, such as poly(acrylic acid) (PAA), poly(methacrylic acid) (PMAA), and poly(glycolic acid) (PGA), are some examples of this class of compounds.[139]

Cationic polymers include polybases bearing amine moieties in the side chains. The amine functional groups remain neutral under basic conditions, but they get positively charged under acidic conditions by accepting protons. The positive charge induces cellular uptake via the negatively charged membranes of pathological tissues characterized by a lower pH value and can also facilitate endosomal effects. Poly(N,N′-diethylaminoethyl methacrylate) (PDEAEM) and poly(N,N′-dimethylaminoethyl methacrylate) (PDMAEMA) are examples of cationic polymers. Generally, cationic polymers are more toxic than the anionic ones. However, the negative charge of anionic polymers may compromise cell uptake and endosomal escape due to charge repulsion. Taking advantage of the aforementioned properties, several pH-responsive nanocarriers were developed using both natural anionic (hyaluronic acid, alginate)[140, 141] and cationic (chitosan)[142] polymers.

Poly(amino acid)s were widely employed for the development of pH-sensitive carriers thanks to their attractive biochemical properties including water solubility, biocompatibility and easy degradation by cells.[143] The ability of these natural polymers to respond to pH change is due to the presence of ionizable carboxylic or amino groups. Among these, poly-glutamic acid (PGlu) and poly-lysine (PLys) are mostly reported. PGlu is composed of repeated glutamate units and it belongs to the class of the anionic polymer as the pKa of the carboxyl group of its chains is about 4.5. This anionic poly(amino acid) was widely used in the controlled and targeted delivery of hydrophobic drugs. For example, conjugates of paclitaxel, doxorubicin and daunorubicin were proposed to increase the solubility and stability of the anticancer drugs.[144] The properties of the anionic poly(amino acid), such as retention, absorption and viscosity, are strictly influenced by its molecular weight.

PLys is a natural homopolymer of L-lysine which attracted particular attention for a variety of biomedical applications. pKa of the amino side chains of the biopolymer is about 9.0 and, therefore, poly-lysine is positively charged under physiological conditions because of the protonation of primary amino groups.[145] The cationic nature of poly-lysine allowed the delivery of negatively charged molecules exploiting electrostatic interactions. Furthermore, the positive charge promotes the internalization into the cells via electrostatically adsorptive endocytosis. However, the interactions between the cationic polylysine and the anionic membranes of red blood cells and vascular endothelial cells can frequently cause hemolysis and cytotoxicity. Generally, the high molecular-weight polypeptide is recognized as more cytotoxic than the low molecular weight due to the more deleterious effects on mitochondrial oxidative phosphorylation and glycolytic activity, which lead to significant intracellular ATP depletion and initiating necrotic-type cell death.[146] The amino pendants of poly-lysine side chains can be readily functionalized affording a wide variety of multifunctional biomaterials that can find several applications (antibacterial agents, delivery systems, bio-sensing, bio-imaging, and tissue engineering). The polypeptide can fold into different secondary structures (α-helical, β-sheet, and random coil) due to hydrogen bonding and electrostatic interactions between the backbone and the side chains. These interactions are frequently affected by environmental stimuli (pH, temperature, solvent, and surfactants). The different conformations display different hydrophilicity due to the influence of intramolecular hydrogen with neighbouring water molecules.[145]

Charged synthetic or natural polyelectrolytes (PSS or PGlu as negatively charged polymers, and PAH or PLys as positively charged ones) were widely employed for the development of pH-sensitive polymeric capsules through the LbL approach. For example, PSS/PAH-based capsules (synthesized by using $CaCO_3$ nanoparticles as template) were proposed for the delivery and the pH-triggered release of doxorubicin (*Figure 19*).[147,148] The pH-responsiveness of these kinds of systems may rely on the permeability of the capsule layers or the binding of the drug to the polymer chains. The latter approach seems to be more effective as drug molecules may be dissociated from the matrix and released from the capsules upon pH changes.

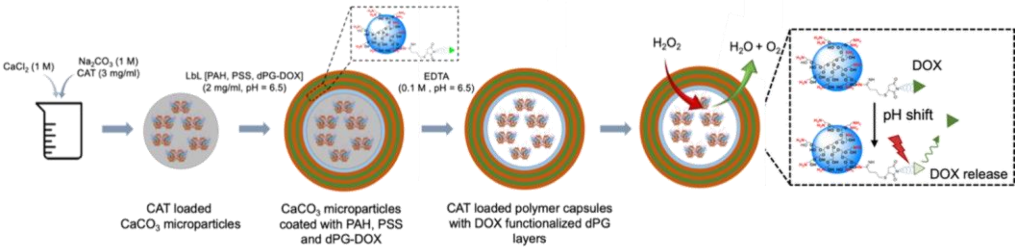

Figure 19. Schematic representation of the fabrication of multifunctional polymer capsules. Rearranged from *ref. 147*.

4.2.1 Poly(acrylic acid)-based systems

Among all polymers, poly(acrylic acid) (PAA) and its derivatives hold plenty of distinguishing properties, such as satisfactory biocompatibility, good stability, and sensitivity to pH and temperature, which are particularly attractive in DDS development.[149]

PAA is a linear polymer obtained by polymerization of acrylic acid, which is the simplest unsaturated carboxylic acid consisting of a vinyl group connected directly to a carboxylic acid terminus (*Figure 20*). The PAA chain bears carboxyl acid functional groups which have a pKa value ranging from 4.5 to 6.5 (depending on ionic strength, supporting electrolyte and PAA molecular weight).[150,151]

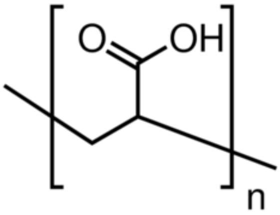

Figure 20. Structure of polyacrylic acid (PAA).

Generally, at pH higher than the pKa, the carboxyl groups are in a dissociated state and hydrophilic thus determining the fusogenic properties of the polymer chains. Conversely, at pH lower than pKa, they become protonated and hydrophobic, causing shrinkage of the polymer and leading to destabilization of the structure and payload release at either extracellular or intracellular sites. Both these features can be exploited to design a pH-sensitive carrier. Indeed, the negatively charged polymer at pH above pKa can be used for carrying a positively charged payload. Since the formation of the delivery system would be strictly guided by the electrostatic interaction between the ionic groups of the drug and the macromolecule, the protonation of carboxyl groups, favoured by a decrease in pH in the pathological tissue, will lead to the rapid release of the loaded drug. This strategy was proposed for the development of a PAA-based bioactive construct for the delivery of doxorubicin. The chemotherapy drug has an amino group (pKa 8.6) in its backbone which at neutral pH will be positively charged. The binding of the antitumour drug to the anionic PAA resulted in a complex/adduct stabilized by electrostatic and stacking interactions between doxorubicin and the polymer chain (*Figure 21*).[152]

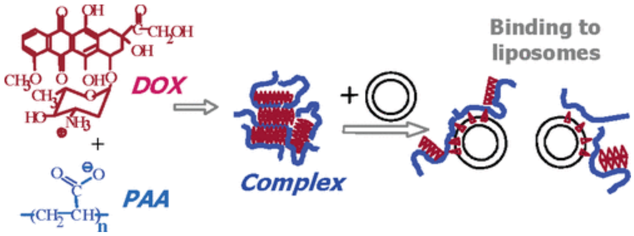

Figure 21. Complexation of doxorubicin with poly(acrylic acid) and subsequent interaction with liposomes.[152]

The moieties of PAA can undergo typical reactions of the carboxyl groups to be conjugated with other functional groups obtaining multifunctional acrylic derivatives and hence several nanocarriers (mostly nanoparticles) based on PAA and its derivatives were developed. PAA-based carriers ensure the transport of hydrophilic and hydrophobic drugs as well as biomolecules with high-loading efficacy while preserving their bioactivity, improving their pharmacokinetics and enhancing tumour-specific distribution. Indeed, the polymeric systems can respond to both or internal stimuli and some of them are capable of returning to their initial state after removing the stimuli, which is extremely helpful in drug loading and sustained release. This “on-off” drug release ensures enhanced drug efficacy and unnoticeable systemic toxicity allowing satisfactory therapeutic outcomes. [149,153,154]

Although most of the delivery systems based on PAA and its derivatives were designed for the loading and release of chemotherapy drugs, these polymers can also be used in the antimicrobial field. For example, a multifunctional grafted polymer bilayer obtained by chemically combining chitosan as an outer layer and PAA as an inner layer was proposed for tuning the uptake and the pH-controlled release of the antibiotic tobramycin (*Figure 22*).[155]

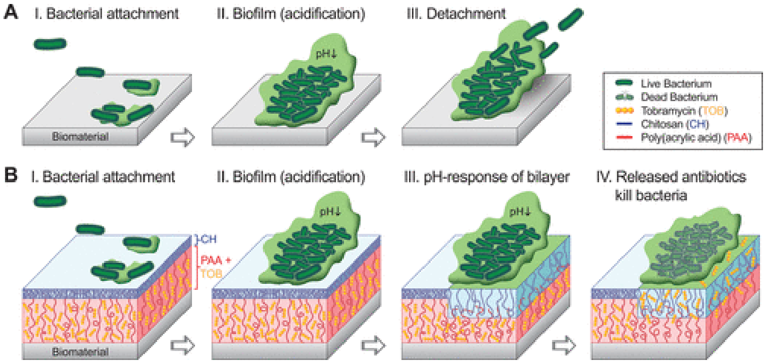

Figure 22. pH-responsive drug-release polymeric system made of an outer layer of chitosan and an inner layer of poly(acrylic acid).[155]

Moreover, polyelectrolyte multilayers fabricated using the LbL approach and based on PLL and PAA were proposed for the delivery of gentamicin.[156]

Within this framework, poly(acrylic acid) capabilities of promoting drug loading and release in a pH-controlled fashion were exploited in this doctoral research work for the development of delivery systems for model drugs (quercetin and methotrexate) with anticancer and/or antimicrobial applications.

5. Quercetin

In the search for new chemotherapy and/or antimicrobial agents with improved activity and a targeted mode of action, flavonoids, a class of natural compounds, gained particular interest. The chemical diversity makes flavonoids versatile molecules exhibiting many biologically and pharmacologically relevant properties including anti- or pro-oxidant, anti-inflammatory, anticancer and antimicrobial activity.[157,158] Quercetin (3,5,7,3’,4’-pentahydroxyflavone, Que, *Figure 23*) is one of the most popular and biologically active compounds among them.

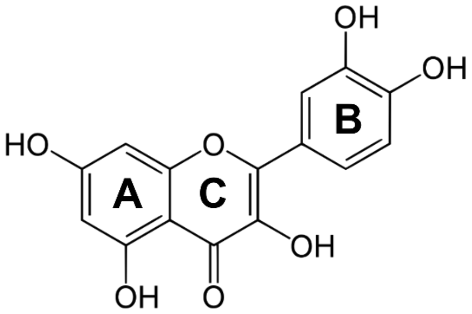

Figure 23. Structure of quercetin.

Que naturally occurs in many plants and consumed food items such as fruits, vegetables and teas, and displays a broad spectrum of physiological activities such as neuro/cardioprotective, anti/pro-oxidative, anti-inflammatory, anti-bacterial and anti-mutagenic and anticancer effects.[159-161]

Due to its multi-functionalities, this flavonoid became the subject of intense research activity to elucidate its molecular targets and mechanisms of action (*Figure 24*).

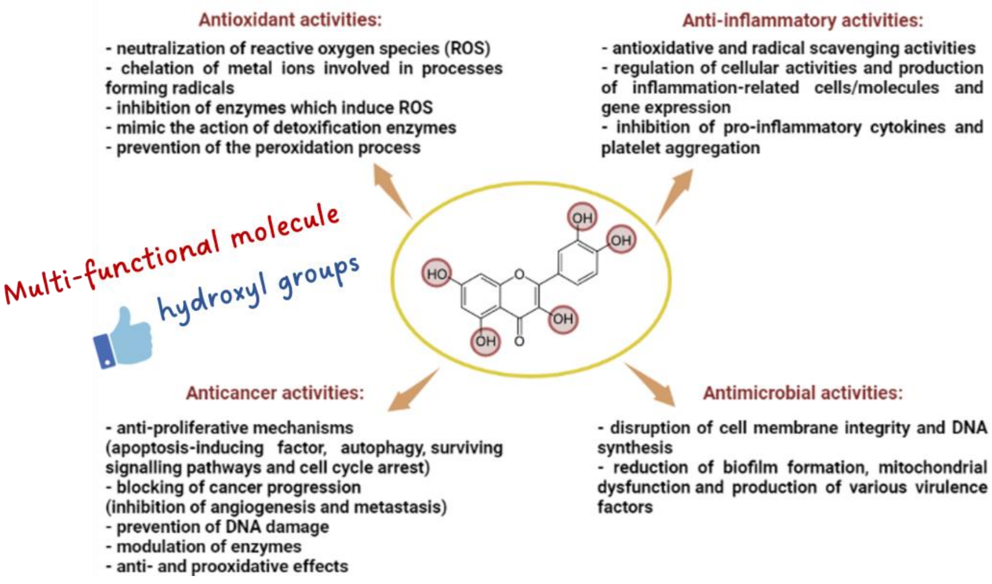

Figure 24. Examples of quercetin activities and properties.

The antioxidant properties can be due to different mechanisms of action. The flavonoid can directly neutralize ROS (reactive oxygen species), chelate metal ions which are involved in processes forming radicals, inhibit enzymes whose catalytic cycle induces ROS, mimic the action of detoxification enzymes (e.g. superoxide dismutase) and prevent the peroxidation process (by reducing alkoxyl and peroxyl radicals).[162] Many studies revealed that the antioxidant effectiveness of flavonoids depends on their structure. The *o*-dihydroxy moieties in the B ring are the most significant determinant of ROS scavenging as they induce higher stability to the radical form and participate in the delocalization of electrons. For example, they are responsible for the ability of quercetin to reduce the peroxyl radicals involved in lipids peroxidation preventing their damage.[163] Conversely, the double bond C-C in conjugation with 4-oxo function in the C ring and hydroxyl groups bound to ring A has little impact on superoxide anion radical scavenging rate constants. Quercetin antioxidant properties are not only due to direct radical scavenging but also to its ability to chelate metal ions, thus reducing their ability to interact with biomolecules and preventing the possibility of induced damage. Moreover, the chelation can prevent Fenton reactions. Under certain circumstances, the flavonoids can also behave as pro-oxidants promoting the oxidation of other compounds. For example, the reduction of Cu(II) and Fe(III) will generate Fe(II) and Cu(I) leading to the formation of ROS by a metal-mediated redox cycling mechanism. In general, the pro-oxidant activity of flavonoids is directly proportional to the total number of hydroxyl groups in their structure. Moreover, some of them may autoxidize in neutral or basic medium, generating ROS. Flavonoids with low reduction potentials may autoxidize, slowly under neutral conditions and faster in alkaline media, by transferring their electrons to O_2 to generate the superoxide anion.[164]

The anti-inflammatory activity of flavonoids is based on a series of mechanisms which involve their antioxidative and radical scavenging activities, the regulation of cellular activities of inflammation-related cells, the modulation of the activities of arachidonic acid metabolism enzymes (produced by macrophages during the inflammatory reaction), the modulation of the production of other pro-inflammatory molecules and gene expression. Specifically, quercetin significantly inhibits pro-inflammatory cytokines and platelet aggregation.

The anticancer activity can be expressed through anti-proliferative mechanisms (apoptosis-inducing factor, autophagy, surviving signalling pathways and cell cycle arrest), blocking of cancer progression (inhibition of angiogenesis and metastasis), prevention of DNA damage and modulation of enzymes, anti- and prooxidative effects.[165] Many studies showed that Que has anticancer activity against various cancer cells such as colon, prostate, skin, glioma and breast cancer cells. More specifically, it was demonstrated its antitumour effect through the induction of ROS-dependent pathway in MCF-7 cells and its role in impeding the mobility of breast cancer cells to contain tumour progression through the suppression of migration marker proteins, such as matrix metalloproteinases (e.g., MMP-2 and MMP-9) and vascular endothelial growth factor (VEGF).[166-168] Moreover, quercetin was employed as a chemosensitizer in co-administration with chemotherapeutic drugs to alleviate multidrug resistance of breast cancer cells through inhibition of P-glycoprotein (Pgp) expression.[169] Recent findings suggest that quercetin could trigger apoptosis in several tumour cells via its pro-oxidant properties due to the generation of reactive oxygen species.

The strong antimicrobial activity of quercetin against a variety of bacterial strains, particularly those affecting the gastrointestinal, respiratory, and urinary tracts was also demonstrated.[170] Quercetin antibacterial effect is based on its structural functionalities as the hydroxyl groups in the flavonoid backbone play a significant role in the interactions with the bacterial cell membrane.[171] The same evidence is reported for other flavonoids. [172-174] More specifically, they resulted to be effective agents against several Gram-positive (e.g. methicillin-resistant *S. aureu*s (MRSA), methicillin-sensitive *S. aureus* (MSSA) and Enterococcus)[175, 176] and Gram-negative bacteria (e.g. E. coli, *K. pneumoniae*, *P. aeruginosa*).[177] However, the difference in the cell membrane composition between the two types of bacteria determines a reduced bactericidal efficacy of the flavonoid towards the Gram-negative compared to the Gram-positive bacteria.[178] Diverse molecular mechanisms seem to be responsible for the antimicrobial activity,[179] such as the ability to disrupt cell membrane integrity and

DNA synthesis.[180] Recent studies reported that quercetin effectively decreases biofilm formation, mitochondrial dysfunction and production of various virulence factors.[181]

5.1 Quercetin-metal complexes

The antioxidant and anti-radical properties of quercetin can be attributed to its ability to chelate metal ions, particularly transition metal ions, involved in the processes of radical formation. Indeed, due to the presence of carbonyl and hydroxyl groups, Que can coordinate metal ions and form stable complexes with improved biological effects than the free flavonoid. The coordination of metal ions changes the redox potential of the ligand thus modifying its antioxidant activity. For example, the enhanced oxidation pathway of the quercetin-copper(II) complex by DPPH radical via semiquinone radical intermediate stabilized by the metal centre and by conjugation with the 3-hydroxyl group was described.[182] Moreover, the SOD-like activity of flavonoid complexes with iron and copper ions was demonstrated: the complexation process decreases the oxidation potential of the flavonoid/semiquinone redox pair determining a more favorable oxidation of the complexed flavonoid by the superoxide ion.[183]

Flavonoid complexes also exerted improved anti-cancer properties due to their ability to cause oxidative DNA damage or promote the cleavage of plasmid DNA via a hydrolytic pathway. An important mechanism of anticancer and apoptosis-inducing activities was reported for the quercetin-Cu(II) complex which can intercalate into DNA inducing oxidative damage.[184] The proposed mechanism induced by the quercetin-copper(II) complex is reported in *Figure 25*.

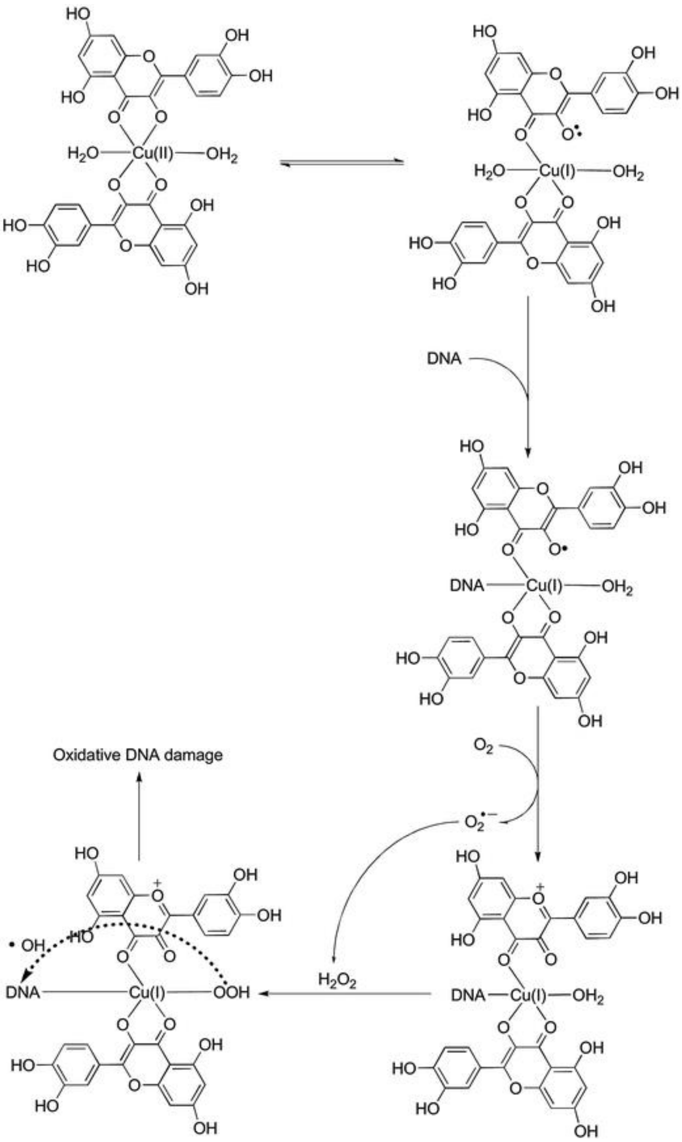

Figure 25. Scheme of the possible mechanism of oxidative DNA damage induced by the quercetin-copper(II) complex.[184]

Pro-oxidative effects and formation of single- and double-strand DNA breaks caused by quercetin-La(III),[185] as well as DNA cleavage activity of Ni(II), Mn(II) and Zn(II) complexes, were also reported.[168,186] Quercetin-metal complexes could bind DNA by electrostatic interaction and/or intercalation in the GC (guanine-cytosine)-rich regions.[187]

The antibacterial features of metal complexes containing flavonoids were widely investigated and their properties strongly depend on the metal ions and bacteria strain. Complexes of Hg(II), Mn(II), Co(II) and Cd(II) with quercetin showed remarkable properties against *S. aureus*, *B. cereus*, *P. aeruginosa*, *E. coli* and *K. pneuoniae*. The higher antibacterial activity of the metal ion complexes is due to the changes in flavonoid structure after complexation which increase their ability to interact with a different set of cellular components in the microorganism as well as the binding affinities to the various intracellular components.[165]

The quercetin ability to bind ions of biological interest (iron, copper, zinc, cobalt) was widely investigated and reported. Generally, metal ions can be coordinated by three different domains: the 3',4'-dihydroxy group on the B ring as well as the 3- or 5-hydroxy and the 4-carbonyl group in the C ring of the Que molecule (*Figure 26*). Que complex species with different stoichiometries were proposed.

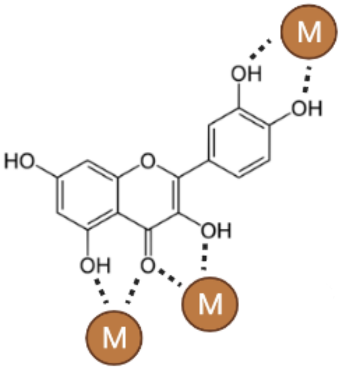

Figure 26. Possible chelation sites of quercetin.

For example, *Zhang et al.* investigated the complex formation between quercetin and copper(II) ions at 20 °C and two different pH values by combining spectroscopic measurements and a chemometric method.[188] They reported the formation of ML and ML_2 complex species of quercetin at pH 6.0, while at pH 7.4 they observed the formation of the ML complex species only. Instead, *Ni et al.* reported that the interaction of quercetin with copper at pH 7.4 leads to the formation of an ML_2 species.[189] *Hajji et al.* spectroscopically investigated the complex species formed by quercetin with copper(I)/(II) and iron (II)/(III) at 37 °C and pH 5 and 7.4. The analysis of the kinetic data allowed them to determine the formation of an ML species only. [190] *Bukhari et al.* claimed instead the presence of M_2L complex species.[182] *Cherrak et al.* examined the formation of quercetin-metal complexes at 25 °C and pH 7.4 (CH_3OH/H_2O 80/20 by weight). For Fe(III) and Zn(II) they found only an ML species whereas for Cu(II) both ML and ML_2 complexes are reported.[191] *Primikyri et al.* reported the formation of ML species for quercetin-zinc(II) interaction in DMSO. [192] More recently, *Corrente et al.* provided a speciation profile obtained by potentiometric titrations for quercetin complexation with Al(III), Cu(II) and Fe(III) at 37 °C in aqueous solution. They suggested the formation of ML species with Al(III) and Cu(II), and ML and ML_2 complexes with Fe(III).[193] ML complex species of quercetin with Co(II), Ni(II), Ca(II) and Mg(II) were also reported.[194,195]

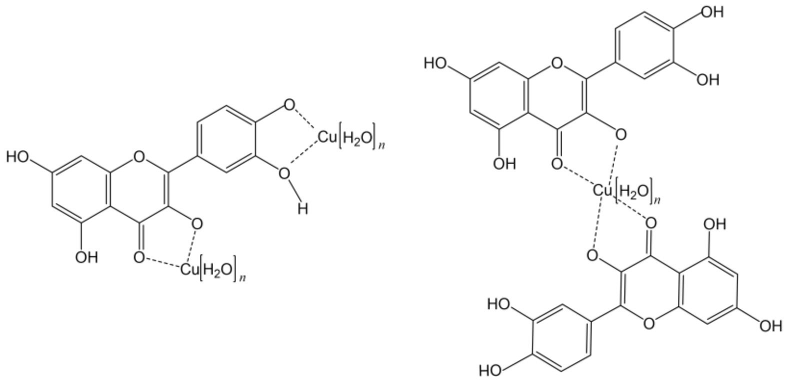

Figure 27. Example of some stoichiometries and structures proposed for quercetin-copper(II) complex.

It is noticeable the wide range of stoichiometries (often contradictory, *Figure 27*) reported for the quercetin complex species formed with the different metal ions and the binding constants accordingly reported (either directly determined or estimated). These differences could be explained by considering the solubility issues of quercetin. Indeed, most of the above-mentioned complexes were studied in organic solvent and only a few of them have been investigated in buffered aqueous solution still containing a large percentage of the organic component. Such differences should be also due to the different techniques and methods of data analysis employed.

5.2 Delivery systems for quercetin

Despite the promising broad spectrum of physiological activity, the pharmacological application of quercetin is severely confined due to its low *in vivo* bioavailability, poor water solubility, low stability and short half-life.[196] Various drug carriers were currently proposed to ameliorate the solubility and stability of Que and, consequently, to increase the beneficial biological activities and availability of the flavonoid to produce significant therapeutic effects. For example, *Rubini et al.* loaded quercetin on gelatin films to develop materials with tailored anti-oxidant, mechanical and stability properties.[197] They demonstrated the sustained flavonoid release which occurs through anchorage to gelatin nanoparticles and the relevant anti-oxidant properties which are comparable to that of pure quercetin.

Que-loaded chitosan nanoparticles, prepared using high molecular weight polyanion cross-linkers, were proposed as systems for improving Que absorption by *Kim et al.*[198] Mucoadhesion and cell permeation of the flavonoid were significantly increased by positively charged nanoparticles due to interactions with the negatively charged mucosal layer. This resulted in higher antioxidant activities of these systems after internalization into Caco-2 cells. *Ramasamy et al.* reported that a bioactive poly(l-phenylalanine)-b-poly(l-histidine)-b-poly(ethylene glycol) polypeptide nanovehicle may co-encapsulate doxorubicin and quercetin for synergistic chemotherapy.[199] The smart pH-sensitive carrier resulted in accelerated drug release with enhanced cytotoxic potential. In particular, the pro-oxidant activity of quercetin remarkably reduced the GSH/GSSG ratio, indicating high oxidative stress and damage to cellular components. Furthermore, *Samadi et al.* proposed hydrogel nanocomposite of agarose (AG)-polyvinylpyrrolidone (PVP)-hydroxyapatite (HAp) loaded with Que that improves the loading efficiency and displays a sustained-release (*Figure 28*).[200]

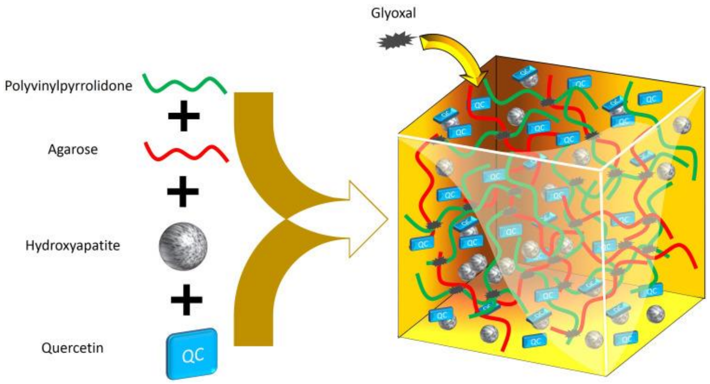

Figure 28. Formation of a quercetin-loaded hydrogel nanocomposite with non-covalent interaction of nanoparticles and hydrogel.[200]

The interactions between nanoparticle, drug, and hydrogel polymers rendered the nanocomposite pH-responsive at acidic conditions and controlled the burst release at neutral conditions. Moreover, this delivery platform showed an ameliorated anticancer activity by releasing the drug at an effective therapeutic level over a long period to induce apoptosis.

A series of troxerutin-based star-shaped systems made of poly(acrylic acid) or poly(2-dimethylaminoethyl methacrylate) with different chain lengths were presented by *Zaborniak et al.* as smart materials for the controlled release of quercetin.[201] The properties of the polyelectrolytes and the branched architecture allowed the proposed systems to exhibit pH-responsive release of the flavonoid, strongly correlated to the length of the polymer chains.

Darvishan et al. proposed a polyacrylic acid (PAA) based hydrogel coated with γ-alumina modified with polyvinyl pyrrolidone (PVP) for the delivery of quercetin. The PVP-modified PAA hydrogel allowed to increase the stability and the retention of Que as well as the pH-sensitive drug release.[202]

6. *Methotrexate*

Methotrexate (MTX) is a methylated derivative of folic acid characterized by a pteridine ring and dimethyl-p-aminobenzoic acid residue linked with glutamic acid (*Figure 29*).

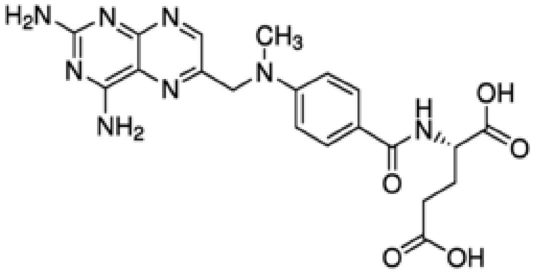

Figure 29. Structure of methotrexate.

Currently, MTX is considered a key drug widely employed in a broad spectrum of diseases. It is used as a major chemotherapeutic agent to treat various human malignancies, such as breast, lung, head, and neck cancers and also in acute lymphoblastic leukaemia, lymphoma, and osteosarcoma.[203-206] Moreover, it is recommended for the treatment of autoimmune disorders, rheumatoid arthritis, psoriasis, multiple sclerosis and Crohn's disease.[207-210] The cytotoxic action of MTX is due to its ability to inhibit DNA, RNA and protein synthesis and release of adenosine.[211] Specifically, MTX is an antimetabolite of folic acid that impedes folate metabolism by inhibiting the activity of dihydrofolate reductase responsible for the conversion of dihydrofolates to tetrahydrofolates. The depletion of tetrahydrofolates inhibits the synthesis of purine and pyrimidine and, consequently, the synthesis of DNA and RNA and other metabolic reactions. As many types of cancer cells are characterized by high levels of folate receptor expression, MTX itself could act as a specific targeting ligand due to its structural similarity to folic acid.[212-214] MTX also exerts its cytotoxic effects thanks to the production of reactive oxygen species (ROS) which causes oxidative damage to nuclear DNA.

6.1 Methotrexate-metal complexes

The pteridine ring and the glutamic acid in the MTX structure are responsible for its ability to coordinate metal ions. Although metal complexes of pteridines are rare due to the highly *p* electron-deficiency of the heterocyclic system, glutamic acid is well-known for its coordination properties towards metal ions. Indeed, a wide number of its metal complexes were reported. These features were thus exploited to obtain MTX coordination compounds with increased biological effects than the free drug. For example, *Chibber et al.* demonstrated the higher pro-oxidant potential of copper(II)-MTX complex. The exposure of the complex to white light determines the reduction of copper thus increasing the generation of ROS and the oxidative DNA breakage.[215]

Nagaj et al. investigated the coordination properties of MTX toward Cu(II) ions by potentiometric measurements; the drug forms three monomeric complexes with copper(II) in a wide pH range (*Figure 30*).[204]

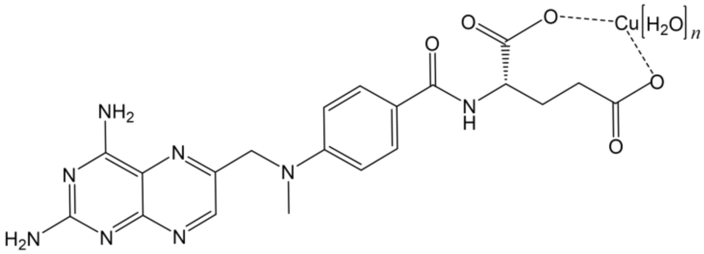

Figure 30. Proposed structure for methotrexate-copper(II) complex at pH 7.5

They demonstrated the nuclease activity of the copper complex which determines DNA cleavage, and its ability to generate ROS. The complex showed also a higher cytotoxicity against A459 and CT26 cell lines than the ligand and metal ion separately. *Notidi et al.* reported the synthesis of zinc(II)-MTX complex with an ML_2 stoichiometry.[205] Copper(II), zinc(II) and platinum(II) complexes of MTX were also synthesized and characterized by *Çeşme et al.* Elemental analysis data provided the stoichiometry (ML) of the metal-based compounds while electronic spectra suggested that carboxyl groups could be the site of complexation. Furthermore, they also investigated the ability of these compounds to interact with the fish sperm doublestranded DNA (FS-dsDNA) and their cytotoxicity in C6 and HeLa cell lines proving the better effectiveness of some metal-based compounds than other well-known anticancer drugs.[216] More recently, *Fernández-Villa et al.* developed MTX complexes with Sr(II), Zn(II), or Mg(II) for the treatment of rheumatoid arthritis. The detailed analysis demonstrated the involvement of carboxylate groups in the coordination geometry. The complexes showed an increased deposition of glycosaminoglycans and alternative anti-inflammatory capacities with respect to the free drug, without compromising the immunosuppressant properties of MTX on macrophages.[217]

Although the importance of metal-containing compounds is increasing due to their enhanced properties, only the few aforementioned papers deal with the study of MTX-metal complexes. Hence, a deep investigation of MTX binding features toward metal ions of biological interest is still required as this will provide the basis to understand and enhance the applications of these metal-drug complexes.

6.2 Delivery systems for methotrexate

The ability of the MTX to inhibit key cellular functions causes a lack of selectivity toward neoplastic cells which results in severe side effects. This, along with poor solubility, short half-life in the bloodstream and drug resistance by targeted cells, strongly affect its efficacy. Therefore, many studies are focused on the development of DDSs to overcome these limitations.

For example, *Cerra et al.* proposed the functionalization of gold nanoparticles with the antifolate drug via electrostatic interactions as a strategy to modify the pharmacodynamics and pharmacokinetics thus increasing drug efficacy.[218]

Abolmaali et al. developed a nanogel PEGylated poly ethyleneimine (L-histidine substituted) for the delivery and sustained release of MTX. The proposed systems showed superior specific cytotoxicity, a greater cell cycle arrest and a higher apoptotic response than the free drug solution in the MTX-resistant HepG2 cell line.[219] Moreover, *Bernaczek et al.* proposed water-soluble polymethacrylate-MTX conjugates for the targeted delivery of the drug. The amount of MTX released from the proposed systems depends on pH and can be controlled via the shape, topology, and composition of the polymeric carrier.[220]

Several nanocarriers for MTX based on PAA have been proposed and some of them have demonstrated great potential thanks to their efficient drug encapsulation, pH-sensitivity behaviour, and improved uptake capability.[221,222] Among these, a vesicle obtained through the self-assembly of PAA and α-tocopherol succinate properly linked thanks to cystamine was proposed by *Ding et. al* for the pH- and GSH-triggered release of MTX (*Figure 31*). [223]

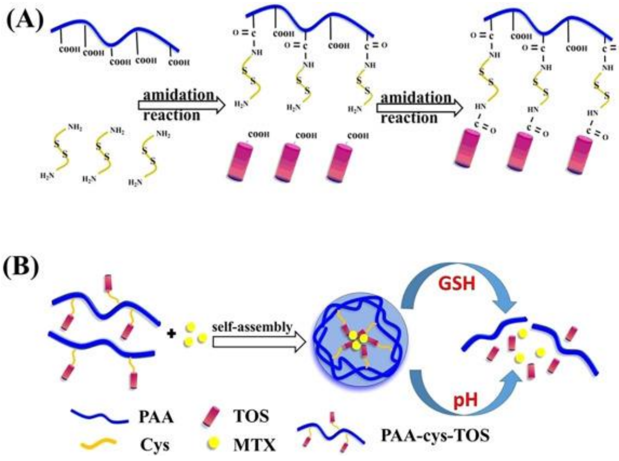

Figure 31. Schematic illustration showing the synthesis of PAA-cys-TOS via a two-step amidation, its self-assembly in an aqueous solution of MTX and the dual-stimuli responsive delivery of MTX.

The use of proper carriers was also exploited for the delivery of the MTX-metal complexes. They were loaded into spray-dried chitosan microparticles as a proof of concept that they can be encapsulated and further delivered in situ in rheumatoid arthritis-affected joints.[217]

Aim of the PhD Thesis

Nanocarriers and molecular containers/transporters are nowadays considered major tools for effective site- and time-controlled drug delivery though, despite they have been significantly improved over time, there are still significant issues and challenges in their design, performance and application to be overcome.

The affinity of a drug for a specific carrier plays a pivotal role in understanding its binding and release ability, while the thermodynamic fingerprint of this interaction provides fundamental insights on the mechanisms of the binding processes which are essential for developing successful drug delivery systems.[224]

Although the determination of the nature and the strength of these interactions is of paramount significance for the design and the efficiency of the resulting carrier systems, a quantitative analysis of the species, binding affinity and thermodynamic features of the molecular interactions among the various components was rarely considered.[225] A thorough knowledge of the binding forces which are mainly responsible for the biological activity of these drug carriers/containers can arise by the examination of the chemical equilibria involved in the recognition and release events; these information are essential for the rational design of the carriers, their characterization and their use for bio/medical and pharmaceutical applications.

This PhD project aims to take advantage of the detailed thermodynamic analysis of the equilibria occurring in solution as the key strategy for designing and developing stimuli-responsive drug delivery systems. This approach was used to prepare pH-responsive carriers by exploiting the non-covalent assembling of selected model drugs (quercetin, Que and methotrexate, MTX), pH-sensitive molecule (poly(acrylic acid), PAA) and metal ions of biological interest (Cu(II), Zn(II) and Co(II)) (*Figure 32*).

The use of the pH-sensitive polymer with ionizable moieties along with the ability of the drug as well as of the polymer to establish coordination bonds with metal ions is the strategy here used for the development of pH-responsive carriers. This approach strictly relies on the acid-base properties of the polymer and drug functional groups as well as their complexing ability towards metal ions, with all these (often simultaneous) processes that definitely depend on the pH conditions. The study of the multiple equilibria occurring in solution among the three components (drug, metal ion and polymer) is therefore essential to predict and perform a rational design of the final metal-coordinated assemblies. Indeed, the knowledge of the interactions and the binding affinities ensures an accurate control and optimization of the stability and drug loading capability of the resulting assemblies.

The non-covalent nature of these interactions is also responsible for the reversible "dynamic" binding under suitable conditions. This feature is of fundamental importance for the development of systems capable of releasing the drug in a site- and time-controlled way thus increasing the drug efficacy. Since the dynamic "behaviour" of the drug-loaded carrier depends on the nature and strength of the interactions involving the components of the system, the thermodynamics of the chemical equilibria still comes into play in the drug release process.

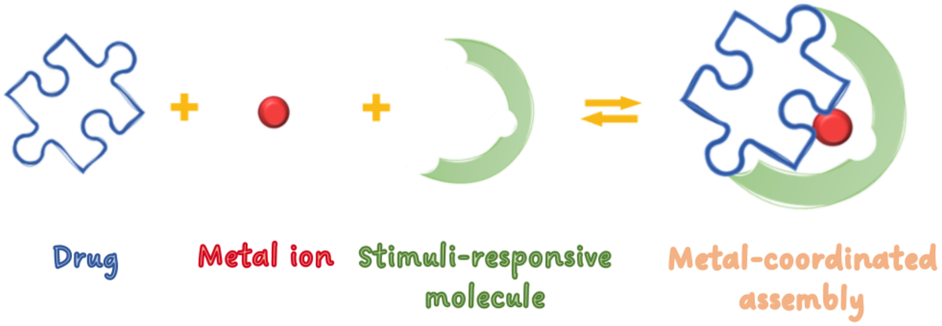

Figure 32. Schematic representation of a metal-coordinated assembly.

Within this framework, the study of the multiple equilibria occurring in solution was utilized for the design and development of stimuli-responsive metal-coordinated assemblies containing two model drugs. The accurate study of the assembly formation implies that all the equilibria involving the system components are considered. To this aim, the binding features and the thermodynamic parameters for the interaction of the drugs (Que or MTX) towards the metal ions and PAA as well as of the metal ions with PAA were investigated in aqueous solution at 25 °C and pH 7.4 through UV-Vis spectrophotometry and isothermal titration calorimetry (ITC) experiments. These information resulted to be crucial for the development of Que-based assemblies containing Cu(II), Zn(II) or Co(II) and PAA for anticancer and/or antimicrobial applications. The stabilization properties of these systems and the controlled release of the model drug under pH control were investigated in solution and at the solid-liquid interface through quartz-crystal microbalance with dissipation monitoring (QCM-D) experiments.

With the same approach, MTX-based assemblies containing Cu(II) or Zn(II) and PAA were developed for anticancer applications. Dynamic light scattering (DLS), ζ-potential and scanning electron microscopy (SEM) measurements provided a thorough physicochemical and morphological characterization of the MTX-based systems. The formation of the assemblies and their ability to release the drug under different pH values were examined at the interface by QCM-D measurements.

In vitro cellular studies proved the higher cytotoxicity of the metal-coordinated assemblies and the ability to generate reactive oxygen species (ROS) in glioblastoma cells as well as their internalization.

Envisaging a possible biological application of these delivery systems, the ability of the MTX-based assemblies to interact with human serum albumin (HSA) was explored in solution and at the interface by ITC and QCM-D experiments respectively.

To prove the importance of the metal ions in the assembly formation and structure, a poly-lysine-based system containing MTX was also developed. The affinity of the drug towards this positively charged polymer was investigated in aqueous solution at 25 °C and pH 7.4 by UV-Vis, ITC and QCM-D experiments. The pH-sensitive release of the drug was investigated in solution and at the interface.

Moreover, the assemblies containing MTX were employed for developing positively and negatively charged polymeric nanoparticles using the *layer-by-layer* (LbL) approach. The systems were physicochemically and morphologically characterized by ζ-potential measurements and scanning and transmission electron microscopy (TEM).

Finally, the recognition processes involving water-soluble macrocyclic containers potentially employable for the encapsulation/transport of charged species of biological relevance were examined. The interactions and the binding features of the negatively charged PrS[5]^{carboxy} or PrS[6]^{carboxy} hosts with mono- and dicationic guests having different sizes and shapes were investigated in neutral aqueous solution by isothermal titration calorimetry. Species, stability constants and thermodynamic parameters of the host-guest complex formation were essential to explore the supramolecular properties of the receptors, to understand the efficiency of these systems to encapsulate molecules with different properties and to unveil the role played by the guest charge in the complexation process.

Chapter II:

Metal-coordinated assemblies containing quercetin

The development of novel DDSs is essential to overcome the broad range of quercetin drawbacks which affect the biological activities of the flavonoid. In this chapter, DDSs based on pH-responsive copper(II)-, zinc(II)- or cobalt(II)-coordinated assembly containing quercetin and polyacrylic acid are proposed. These systems are suggested to ameliorate the stability of both quercetin and its metal complexes increasing the physiological properties and the availability of the flavonoid with significant therapeutic effects. Moreover, the metal(II)-based assemblies are proposed to trigger the release of the flavonoid in a pH-dependent mode by exploiting a localized acidic microenvironment.

The delivery systems were designed by accurately examining the species and the multiple equilibria occurring in solution among the assembly components. The formation of the quercetin-metal(II) complexes in the absence or presence of the pH-responsive polyacrylic acid was investigated in buffered aqueous solution at pH 7.4 using spectrophotometric (UV-Vis) and calorimetric (ITC) techniques. The determined binding affinities and thermodynamic parameters resulted essential for the development of DDSs with improved loading, stabilization, and release capabilities in a pH-dependent way. Furthermore, the affinity of the polymer-cobalt(II) complex toward the flavonoid was explored at the solid-liquid interface by quartz crystal microbalance (QCM-D) experiments, which provided marked evidence for drug loading and release under pH control.

1. RESULTS AND DISCUSSION

The metal(II)-based polymeric assemblies containing quercetin were developed in aqueous solution at neutral pH by exploiting the ability of the various components to establish multiple non-covalent interactions. An accurate design of the desired DDSs implies the investigation of the multiple equilibria occurring in solution among the elements of the system. Consequently, the binding affinities and thermodynamic parameters for the complexation of metal(II) ions with Que and poly(acrylic acid) as well as the overall formation of the Que-M(II)-PAA assembly were determined.

1.1 Quercetin solubility and stability in organic solvent and aqueous solution

Molecules or systems of biological interest are usually studied in buffered aqueous solutions to both mimic the physiological environment and avoid problems related to organic solvent toxicity. However, quercetin is insoluble in water and the use of an organic solvent is necessary to solubilize the flavonoid. DMSO was chosen as a solvent due to its miscibility in water and in line with its wide applicability in biological studies. Indeed, it was demonstrated that low concentrations of DMSO do not interfere with the functions of biological systems.[226] Preliminary tests were performed to evaluate the quercetin solubility and stability both in pure DMSO and when it is diluted/mixed in buffered aqueous solution (pH 7.4, MOPS 10 mM) before running complexation studies.

The spectrum of the flavonoid in pure DMSO shows two major absorption bands in the UV–Vis region at 380 nm (band I) and 260 nm (band II) (*Figure 33*) which are ascribable to the $\pi \rightarrow \pi^*$ transitions within the aromatic 3-ring system of the ligand molecule.[227] Specifically, band I is due to the absorption of the cinnamoyl system (ring B) while band II to that of the benzoyl moiety (ring A). The absorbance profile does not change over five days confirming the stability of Que in this solvent.

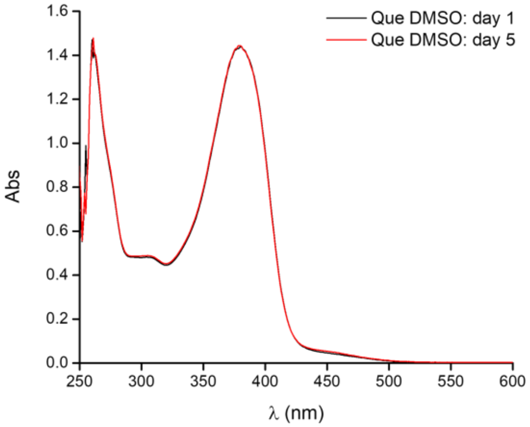

Figure 33. UV-Vis spectra of Que 0.06 mM at 25 °C in pure DMSO.

To overcome issues related to the use of organic solvents in biological/pharmaceutical applications, buffered aqueous solutions of quercetin were prepared in such a way as to minimize the % (v/v) of organic medium dissolved. Hence, aqueous solutions of Que containing different (small) concentrations of DMSO were prepared to ascertain the maximum concentration of Que that is possible to solubilize in the presence of the lowest % (v/v) of organic solvent. By decreasing the amount of organic solvent, the concentration of Que which can be maintained in solution decreases as precipitation occurs. To exclude any role/effect due to the buffering agent used, tests were also carried out in pure water and no significant differences were observed.

Best conditions were found preparing buffered aqueous solution of Que at a concentration of 0.15 mM containing 5% (v/v) DMSO. To date, this is one of the first attempts to prepare and use Que solutions containing such a high percentage of water; mixed solvents with larger amounts of organic media are commonly used due to flavonoid solubility and precipitation issues. Solution stability was checked for several hours and no precipitation was detected. The UV-Vis spectra of Que at 25 °C in water (5% v/v DMSO) and buffered aqueous solution (pH 7.4, MOPS 10 mM, 5% v/v DMSO) are shown in *Figure 34*.

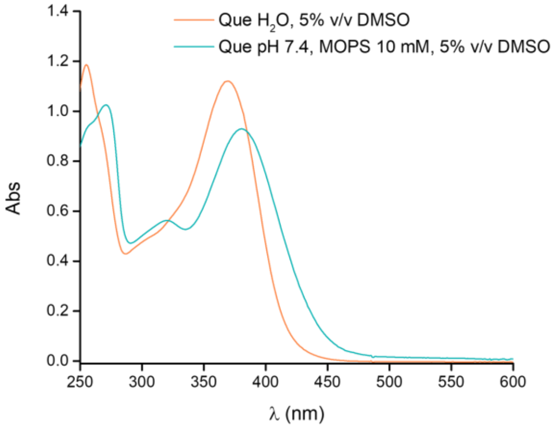

Figure 34. UV-Vis spectra of Que 0.06 mM at 25°C in water and pH 7.4, MOPS 10 mM 5% v/v DMSO.

Band I of the quercetin spectrum are at 368 nm and 379 nm in water and in buffered aqueous solution, respectively, both containing 5% v/v DMSO. Band II absorb at 255 nm and 269 nm in water and in buffered aqueous solution, respectively, both containing 5% v/v DMSO. Hereafter, all solutions and experiments involving quercetin are prepared and carried out at pH 7.4, MOPS 10 mM, 5% v/v DMSO.

1.2 Quercetin-metal(II) complexes

A fundamental step for the development of metal(II)-coordinated assemblies containing quercetin is the study of the complex species that the flavonoid can form with metal ions. Complex species of Que with copper(II), zinc(II) and cobalt(II) were reported in the literature; however, the stoichiometry as well as the different proposed binding constants for the quercetin complex species strongly depends on the experimental conditions employed (polarity of the solvent, the strength, pH, buffering agent). Hence, we decided to study the formation of metal(II)-Que complexes in a buffered aqueous solution at pH 7.4 (MOPS 10 mM). The experimental conditions were chosen to mimic the physiological environment. Indeed, a drug delivery system must not degrade and/or disassemble in these conditions to prevent drug alteration and/or release before it can reach its target organ/tissue. Generally, DDSs stability studies are conducted in phosphate buffer as it perfectly simulates the plasma buffer components and is non-toxic to most cells. However, it was widely demonstrated that phosphates complex polyvalent cations. Consequently, MOPS, an N-substituted aminosulfonic acid with a morpholine ring, was chosen as a buffering agent as it does not bind metals and is commonly used for the study of metal complexes in solution.[228] Species, binding affinities, and thermodynamic parameters of quercetin–metal(II) complexes were determined using UV-Vis and ITC calorimetric measurements. Typical UV-Vis titrations are shown in *Figure 35*.

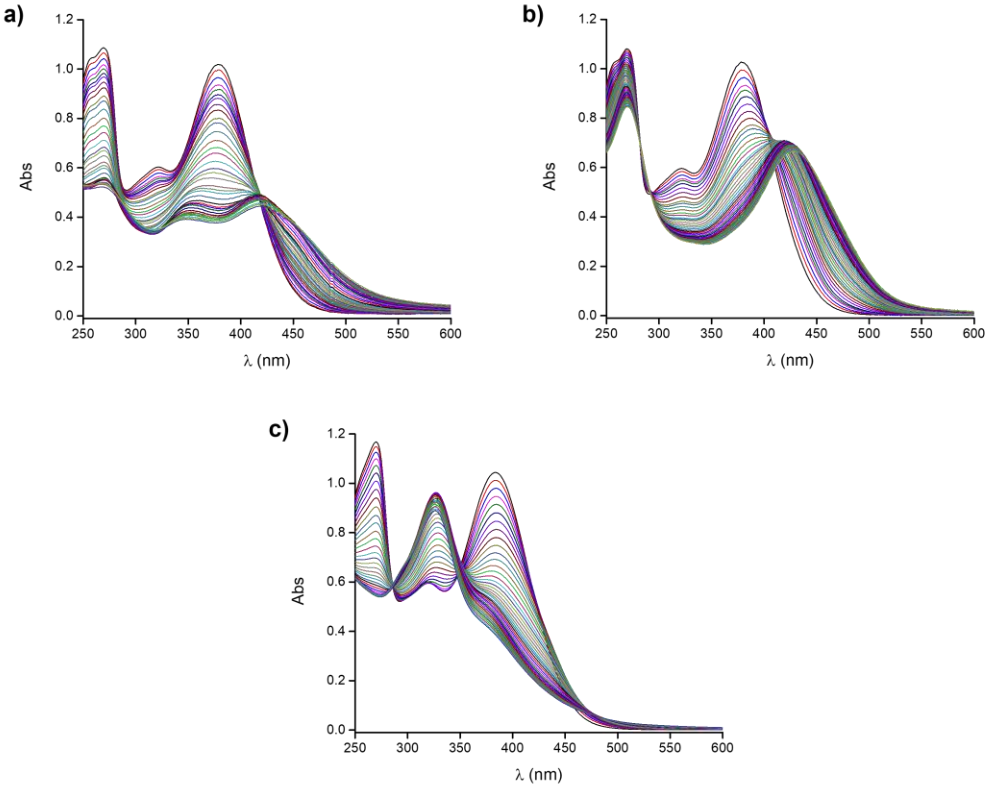

Figure 35. Typical UV-Vis titration of *a)* Cu(II) (0.30 mM), *b)* Zn(II) (0.87 mM) and *c)* Co(II) (0.60 mM) into Que (0.06 mM) solution at 25 °C and pH 7.4; the correspondent molar ratio plots are shown in the *Supplementary materials - Chapter II, Figure S1*.

In agreement with previous studies, both bands of Que show a decrease in absorbance upon the stepwise addition of metal ions to the ligand solution. Moreover, for all metal ions, the extension of the conjugated system as a consequence of the metal-ligand complexation process determines a concomitant red-shift of the band I of the ligand.[229] This shift is slight in the case of cobalt(II), while a new absorption band at 420 nm and 436 nm can be observed for copper(II)- and zinc(II)-quercetin systems. The two isosbestic points at 285 and 418 nm for the copper(II) system and 282 and 410 nm for the zinc(II) system further confirm the formation of the complex species of Que with these metal ions.[189] No changes in the position of band II are observed suggesting that complexation does not affect the ring A. Indeed, it was reported that the 5-hydroxyl group (ring A) of flavonoids is not involved in the complexation process due to its smaller proton acidity.[182] The comparison with the literature reports along with the reported chelation power of the 3-hydroxyl group due to the delocalization of the π electrons [157,230,231] prompted us to suppose that, at our experimental conditions, the 3-hydroxyl and 4-oxo groups of quercetin are the sites involved in the complexation process. Preliminary indications on the stoichiometry of the main complex species were obtained by the molar ratio method. The plots of the absorbance versus the equivalents of metal(II) added (*Supplementary materials - Chapter II, Figure S1*) show an inflection at about M:L = 0.5 for the copper(II)-quercetin systems, a gentle decrease for the zinc(II) system and an inflection at about M:L = 1 for the cobalt(II) system. In the case of copper, it was not possible to add more than 1 equivalent of metal ion solution due to precipitation which began at about M:L = 0.7-0.8. For the zinc(II) and cobalt(II) titrations, the addition of more than 2 equivalents of metal solution did not cause any relevant effect on the absorption spectra.

The multi-wavelength analysis of the spectroscopic data in the 315-445 nm, 320-455 nm and 240-480 nm range for copper(II)-, zinc(II)- and cobalt(II)-based systems, respectively, allowed for the accurate determination of the metal(II) complex species and their conditional stability constants at pH 7.4. Different species and their combinations were tested with the program, but the data analysis consistently converged to the results shown in *Table 1*.

Table 1. Overall conditional stability constant values[a,b] for the formation of quercetin (L) - metal (M) complexes at 25 °C and pH 7.4 (MOPS 10 mM).

Metal ion	**Species**	**Log β**
Cu(II)	ML	4.80 (2)
	ML_2	11.19 (4)
Zn(II)	ML	4.35 (1)
Co(II)	ML	5.66 (2)
	ML_2	10.18 (8)

[a] refers to the equilibrium pM + qL ⇄ M_pL_q where charges are omitted for simplicity; [b] σ in parenthesis.

To our knowledge, a detailed study on the quercetin binding ability toward copper(II), zinc(II) and cobalt(II) in water at pH 7.4 has not yet been reported. In agreement with the stoichiometry reported for several flavonoid complexes, quercetin forms quite stable ML species with all metal ions and an additional ML_2 species with copper(II) and cobalt(II). The conditional stability constant of the zinc(II)-quercetin complex species is lower than that of copper(II), in agreement with the classical Irving-Williams order of stability.[232] Due to the very low solubility in aqueous solution, in most cases the complex stability was determined in organic solvent or water/organic solvent mixtures and, consequently, this makes the data comparison rather difficult. Indeed, the polarity of the solvent and its capability of forming hydrogen bonds significantly affect the metal ion-ligand interactions. The results obtained are however in line with stoichiometry and binding constants already reported in the literature for the same systems in different experimental conditions and they are also comparable with those reported for the complex formed by copper(II) and zinc(II) with other flavonoids such as apigenin and luteolin.[233] The stability constant value for the formation of the ML species with cobalt(II) at pH 7.4 is quite similar to those reported for the complexes with quercetin and rutin at pH 5.[234]

The formation of quercetin-metal(II) complexes was also examined by calorimetric titrations to obtain a complete thermodynamic characterization of the investigated systems. Typical ITC titrations are shown in *Figure 36* and the overall thermodynamic parameters are listed in *Table 2*.

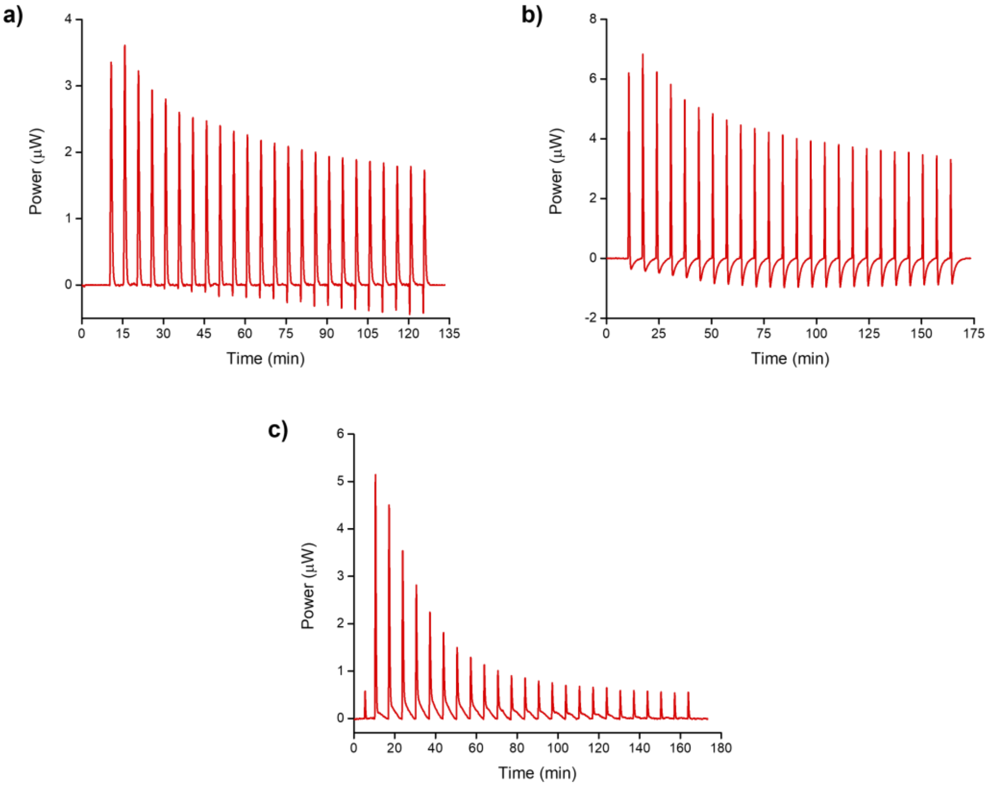

Figure 36. Typical ITC titration of *a)* Cu(II) (0.56 mM) into Que (0.15 mM), *b)* Zn(II) (1.40 mM) into Que (0.13 mM) and *c)* Co(II) (0.55 mM) into Que (0.12 mM) solution at 25 °C and pH 7.4; the integrated heat data are shown in *Supplementary materials - Chapter II, Figure S2*.

Table 2. Overall thermodynamic parameters[a,b,c] for the formation of quercetin (L) - metal (M) complexes at 25 °C and pH 7.4 (MOPS 10 mM).

Metal ion	**Species**	**$-\Delta G^0$**	**ΔH^0**	**$T\Delta S^0$**
Cu(II)	ML	27.40	-17 (2)	10
	ML_2	63.87	-6.9 (4)	57.0
Zn(II)	ML	24.83	1.7 (3)	26.5
Co(II)	ML	32.3	-11.45 (2)	21.1
	ML_2	51.4	-35.78 (4)	15.6

[a] refer to the equilibrium pM + qL ⇄ M_pL_q where charged are omitted for simplicity;

[b] σ in parenthesis; [c] in kJ mol $^{-1}$.

To better understand the driving forces for the formation of quercetin-metal(II) complexes, the stepwise values of the thermodynamic parameters were calculated and graphically represented in *Figure 37*.

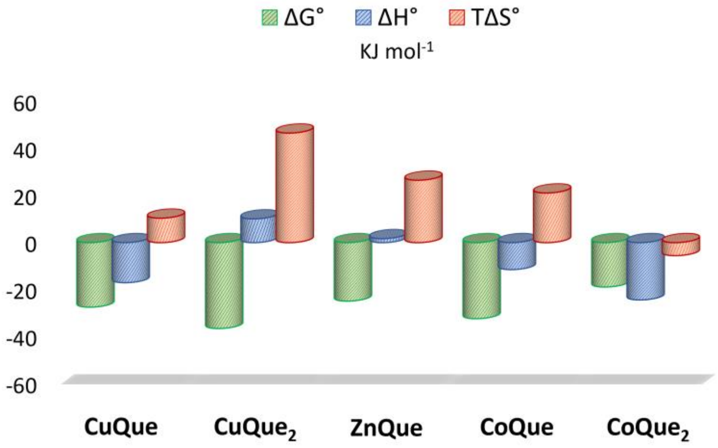

Figure 37. Stepwise thermodynamic parameters for the formation of quercetin-metal(II) complexes at 25 °C and pH 7.4.

For copper(II), enthalpy favours and drives the formation of the ML complex species with quercetin; there is also a favourable entropic contribution. The formation of ML_2 complex species is entropically favoured and driven, due to metal and ligand desolvation upon complexation, and enthalpically unfavoured. This unfavourable contribution could be due to the higher enthalpic cost of the desolvation needed for the binding of a second ligand molecule (ML_2 species).

The ML species formed by zinc(II) with Que is entropically favoured and driven but slightly enthalpically unfavoured. This finding is somehow in agreement with that described in the literature for the quercetin-zinc(II) system in pure DMSO, which is the only data reported for these systems.[192] The differences can be due to the different reaction environments as the solvation of ions and molecules strictly depends on the properties of the solvent which significantly affect the nature and driving forces of the complexation processes.[235-237]

For cobalt(II), the complexation process is enthalpically favoured; the formation of the ML species is driven by entropy due to desolvation. Unlike what was observed for copper(II), the binding of a second ligand molecule (ML_2 species) is driven by enthalpy with an unfavourable entropic contribution ascribable to the loss of degrees of freedom of the system as a result of the complexation event.

1.3 Quercetin-poly(acrylic acid) interactions

The ability of the polymer to interact with free Que was investigated by both UV-Vis and calorimetric titrations performed at different experimental conditions to explore different polymer/quercetin ratios (up to 25). A typical UV-Vis titration and the corresponding molar ratio curve are shown in *Figure 38*; titrations at different polymer/Que ratios are shown in *Supplementary materials - Chapter II, Figure S3* and *Figure S4.* The changes in the UV-Vis titration are solely due to the dilution of the flavonoid upon the addition of the polymer solution. Indeed, no curvature can be detected in any of the molar ratio plots regardless of the wavelength used. The ITC titrations (*Figure 39*) confirmed that no associative process happens as the calorimetric curves and the quite negligible heat values recorded indicated that no detectable reaction occurred in the calorimetric vessel upon titration. Overall, these studies proved that PAA and quercetin are not able to interact. This can be attributable to the electrostatic repulsion that occurs between the anionic moieties of the two molecules at pH 7.4, namely the carboxylic acid groups and the hydroxyl group on PAA and quercetin, which prevents any form of interaction.[150]

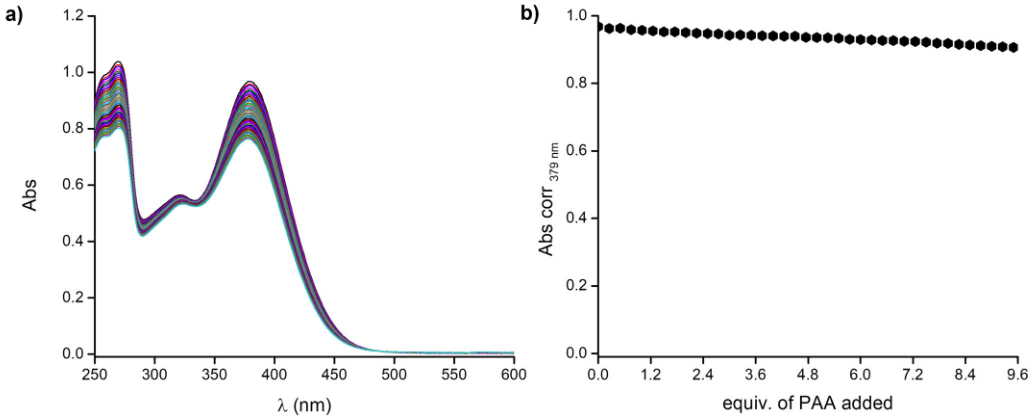

Figure 38. *a)* Typical UV-Vis titration of PAA (3.00 mM) into Que (0.06 mM) solution at 25 °C and pH 7.4; *b)* molar ratio curve at 379 nm.

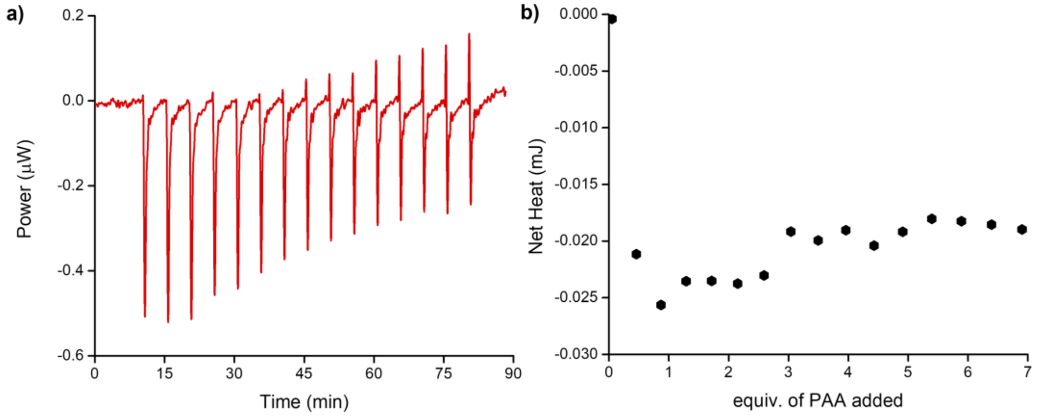

Figure 39. *a)* Typical ITC titration of PAA (3.70 mM) into Que (0.15 mM) solution at 25 °C and pH 7.4; *b)* integrated heat data for the PAA/Que system.

1.4 *Poly(acrylic acid)-metal(II) complexes*

The binding properties of water-soluble chelating polymers and the ability of their functional groups to bind metal ions were extensively studied. Based on literature reports, water-soluble polymers bearing ionizable moieties bind metal ions forming complex species that can be stabilized through electrostatic, donor-acceptor and hydrophobic interactions.[238] The stability and the features of these complexes depend on several factors (nature of the polymer backbone, distance of the pendant binding sites from the backbone, nature of the metal ions, pH, ionic strength).[239-241] The mechanism of complexation as well as the stoichiometry of the complex that is formed are still open questions. The metal(II)-polymer complex species formation was investigated by ITC calorimetric titrations (*Figure 40*) and the resulting species, binding constants and thermodynamic parameters are listed in *Table 3*.

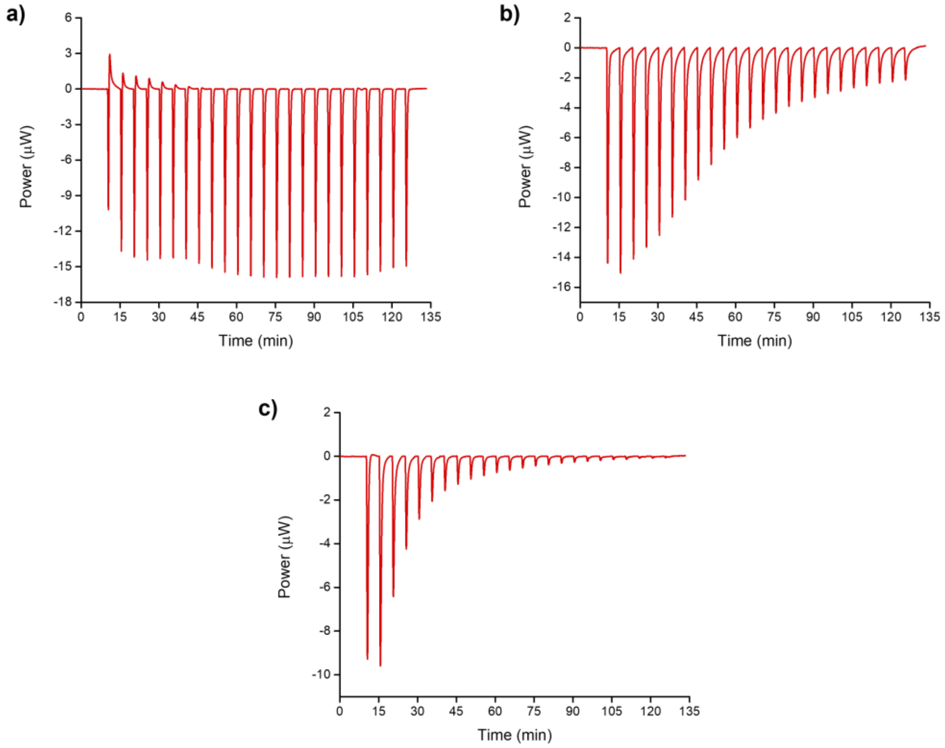

Figure 40. Typical ITC titration of *a)* Cu(II) (3.00 mM) into PAA (0.50 mM), *b)* Zn(II) (3.00 mM) into PAA (0.60 mM) and *c)* Co(II) (3.50 mM) into PAA (0.50 mM) solution

at 25 °C and pH 7.4; the integrated heat data are shown in *Supplementary materials - Chapter II, Figure S5*.

Table 3. Overall conditional stability constant values[a,b] and thermodynamic parameters[a,b,c] for the formation of polymer (PAA) - metal (M) complexes at 25 °C and pH 7.4 (MOPS 10 mM).

Metal ion	**Species**	**Log β**	**-ΔG⁰**	**ΔH⁰**	**TΔS⁰**
Cu(II)	M(PAA)	4.3 (4)	24.5	-3.15 (5)	21.4
	$M(PAA)_2$	8.3 (4) 11.14 [d]	47.4	-9.15 (6)	38.2
Zn(II)	M(PAA)	4.1 (3)	23.4	12.9 (1)	36.3
	$M(PAA)_2$	8.5 (3) 9.31[d]	48.5	10.27 (3)	58.8
Co(II)	M(PAA)	4.3 (2)	24.5	7.39 (6)	31.9
	$M(PAA)_2$	8.1 (1) 9.76 [d]	47.4	6.16 (2)	52.4

[a] refers to the equilibrium pM + qPAA ⇄ M_pPAA_q where charges are omitted for simplicity; [b] σ in parenthesis; [c] in kJ mol $^{-1}$; [d] calculated using the values from ref. *242*.

Poly(acrylic acid) forms M(PAA) and $M(PAA)_2$ complex species with all metal ions, which show similar binding affinities for the polymer. For the sake of comparison, *Table 3* also displays the values for the overall conditional stability constants of the $M(PAA)_2$ complexes calculated at pH 7.4 by using values reported elsewhere.[151] The determined binding constants are lower than those calculated at pH 7.4 in the absence of a supporting electrolyte. This highlights the effect of the ionic strength on the formation of polyelectrolyte-metal complexes: the buffering salt causes an increase in the ionic strength of the solution and weakens the formation of these complexes due to the screening of the electrostatic interactions.[243] Based on the literature reporting possible binding modes with similar ligands, we can suppose that the coordination features of the metal ion are satisfied by two carboxyl anions of the polymer chain or by the oxygen atoms of one carboxyl group and one carboxyl anion of a nearby acidic function of the polymer chain. A tentative structure for the metal(II)-polymer complexes is shown in *Figure 41*.

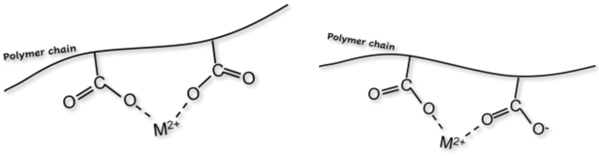

Figure 41. Schematic structures assumed for the metal(II)-PAA complexes.

Insights for the complexation processes can be obtained by calculating the stepwise thermodynamic parameters, graphically represented in *Figure 42*. For all metal ions, the formation of both the M(PAA) and $M(PAA)_2$ species is entropically favoured and driven due to the orientation disorder of hydration water molecules upon complexation and conformational changes of the polymer backbone. Both complexes formed by PAA with copper(II) have a favourable enthalpic contribution that can be ascribable to the attractive electrostatic interactions between the negatively charged groups of the polymer chain and the metal cation. For the zinc(II) complexes, enthalpy is unfavourable for the M(PAA) species due to the cost of energy needed for desolvation. For cobalt(II), the formation of M(PAA) is also enthalpically unfavoured, while a slightly favourable enthalpic contribution is observed for $M(PAA)_2$ as in the case of the zinc(II) homologous species (the binding of a second carboxyl unit to the metal ion is likely to compensate for the cost of desolvation).

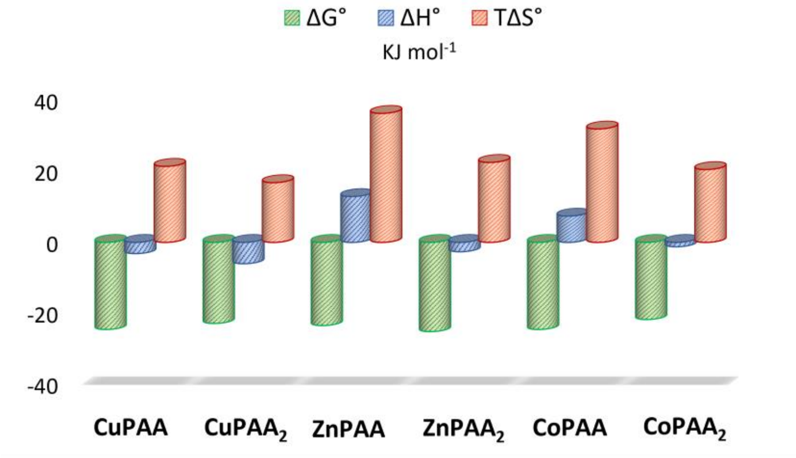

Figure 42. Stepwise thermodynamic parameters for the formation of poly(acrylic acid)-metal(II) complexes at 25 °C and pH 7.4.

1.5 Quercetin-metal(II)-polymer assemblies

As metal(II) can form complexes with both quercetin and poly(acrylic acid) in solution, the expected DDSs based on Que, metal ion and PAA were rationally designed and formed by taking advantage of the interactions occurring among these components as well as the quantitative information on the species and binding affinities experimentally determined at pH 7.4.

For the copper(II)-based assembly, the flavonoid complex species was first prepared in solution by mixing copper(II) and quercetin at 1:1 metal/ligand molar ratio. Solutions prepared at different molar ratios (M:L from 0.5:1 to 1.6:1) resulted in the formation of a precipitate upon the addition of metal ion to the flavonoid solution. The knowledge of the quercetin affinity toward copper(II) ion and a simple species distribution calculation (*Supplementary materials - Chapter II, Figure S6*) indicated that, under the employed conditions, ML_2 is the main species present in the solution. Typical UV-Vis titration is shown in *Figure 43*.

The spectrum of the quercetin–copper(II) complex at 1:1 molar ratio is characterized by two bands at 275 and 436 nm, respectively. The intensity of these two bands decreases upon the stepwise addition of polymer to metal-flavonoid complex solution.

The band at 436 nm also shows a concomitant blue-shift as a consequence of the interaction process; furthermore, a new absorption band at 340 nm along with a shoulder at about 416 nm can be observed. This suggests that the metal(II)-Que complex is surrounded by a more hydrophobic environment, due to a conformational change of the polymer backbone which, upon interaction with the copper ion in solution, rearranges from a more extended, rod-like conformation to a coil one thus enabling the "physical" entrapment the $CuQue_2$ species within this newly formed pocket. The two isosbestic points at 308 and 390 nm provided evidence that a new species is forming during the titration.

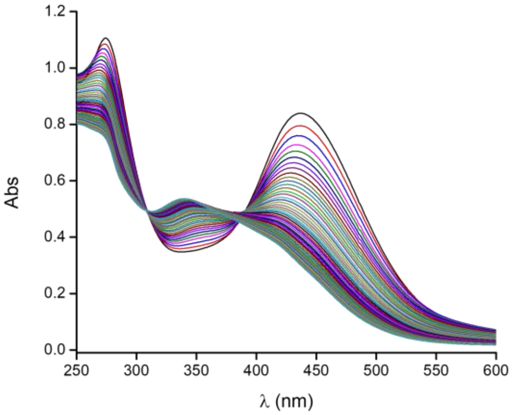

Figure 43. Typical UV-Vis titration of PAA (12.5 mM) into quercetin-copper(II) complex solution (Cu(II):Que 1:1, C_{Que} = 0.06 mM) at 25 °C and pH 7.4; the molar ratio curve is shown in *Supplementary materials - Chapter II, Figure S8*.

The determined metal ions affinities toward quercetin and polyacrylic acid indicated that the formation of the metal-coordinated assemblies containing zinc(II) and cobalt(II) have to be investigated by titrating the flavonoid with the metal(II)-polymer complex solution, unlike in the case of copper(II). Indeed, a first attempt of titrating zinc(II)-quercetin complex with polymer (*Figure 44*) revealed a competitive interaction: the addition of PAA caused the displacement of the metal ion from the ZnQue complex restoring the whole initial spectrum of free ligand. The complex species formed by zinc(II) with poly(acrylic acid) has a higher binding affinity than the complexes formed by zinc(II) with quercetin. Therefore, the metal ion is subtracted from the ZnQue complex upon the addition of the polymer to form the M(PAA)$_2$ species. This was not observed for the copper-based system as quercetin has a much higher binding affinity for copper than for the polymer (*Table 1* and *Table 3*). This highlights the importance of studying the whole set of equilibria occurring in solution between all the components of a drug delivery system in order to optimize its preparation and formation.

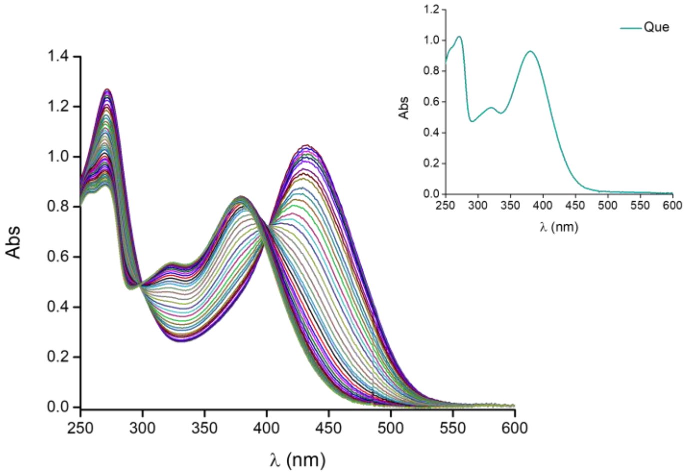

Figure 44. Typical UV-Vis titration of PAA (9.00 mM) into quercetin-zinc(II) complex solution (Zn(II):Que 3.7:1, C_{Que} = 0.06 mM) at 25 °C and pH 7.4. *Inset:* spectrum of free Que (0.06 mM) at 25 °C and pH 7.4.

To overcome this displacement issue, quercetin was titrated by the metal(II)-polymer complex solution. The metal-polymer complex was first prepared in solution by mixing Zn(II) or Co(II) and poly(acrylic acid) in a proper molar ratio. Thus, once the concentration of the polymer was fixed (C_{PAA} = 9.00 mM), solutions at different metal/polymer ratios were prepared trying to increase the number of possible binding sites (i.e., metal ions that could act as anchoring/bridging points) between the polymer and the flavonoid that otherwise could not interact. Metal(II)-polymer solutions prepared at 1:1 or 1:2 molar ratios resulted in the formation of a precipitate upon the addition of the metal ion to the polymer solution. A lower concentration of the metal ion would avoid the precipitation of the metal-polymer complex; therefore, M(II) and PAA were mixed at a 1:3 molar ratio to have the largest possible number of binding sites while preventing precipitation events. The combination of carefully selected PAA concentration and metal/polymer ratio permitted to have the optimal number of potential binding sites for quercetin. The knowledge of the polymer affinity toward Zn(II) and Co(II) ions and a simple species distribution calculation (*Supplementary materials* - *Chapter II, Figure S7*) indicated that, under our conditions, $M(PAA)_2$ is the main species present in the solution. These distribution diagrams indicate that, for both metal ions, about 60% of the polymer is complexed while the remaining 40% is free. To reduce the amount of free polymer, a higher metal–polymer ratio would be needed, with consequent precipitation drawback; however, the non-complexed polymer in solution is not an issue, as it is not able to bind quercetin. Moreover, PAA is reported to be a non-toxic, biocompatible, and biodegradable polymer, and its concentration should not have significant side effects in view of possible biological applications. Typical UV-Vis titrations of quercetin with Zn(II) or Co(II)-polymer complex solutions are shown in *Figure 45*.

The addition of the metal(II)-polymer complex to the ligand solution determines a decrease in the intensity of the quercetin bands. In both cases, a simultaneous red-shift of band I is observed as a consequence of the interaction of the flavonoid with the metal(II)-polymer complex. For the zinc(II)-polymer system, a new absorption band at 425 nm appears indicating an extension of the conjugated system due to the complexation process. For the cobalt(II)-polymer system, the shift is more evident than that for the UV-Vis titration of the free cobalt(II) into the flavonoid. Moreover, two isosbestic points at 282 and 412 nm for the zinc(II)-based and at 285 and 352 nm for the cobalt(II)-based system may be detected, indicating that quercetin can form complex species with the metal(II)-poly(acrylic acid) system. In all cases, band II does not show any change suggesting that the complexation does not affect the benzoyl system.

Since quercetin cannot bind the free polyacrylic acid, the metal ions proved to be essential for the formation of the final assembly, as it acts as a bridging unit between Que and PAA.

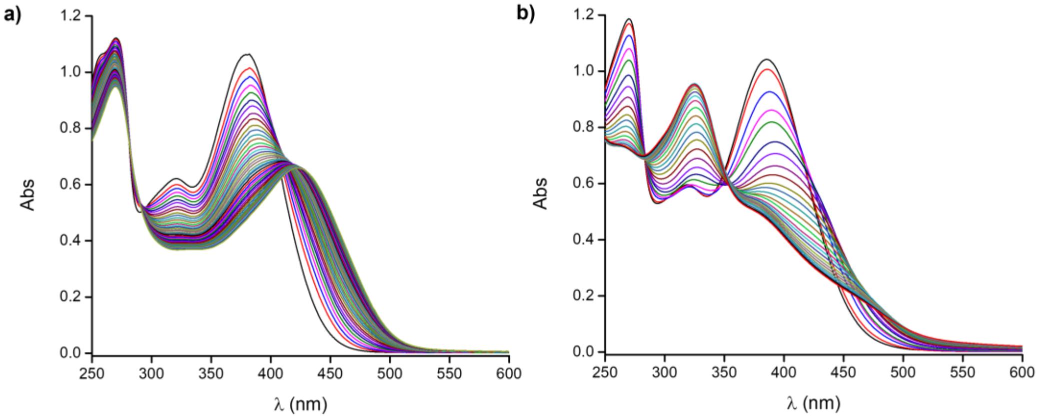

Figure 45. Typical UV-Vis titrations of *a)* zinc(II)- and *b)* cobalt(II)-polymer complex (M(II):PAA 1:3; C_{PAA} = 9.00 mM) into Que (0.06 mM) at 25 °C and pH 7.4; the molar ratio curves are shown in *Supplementary materials - Chapter II, Figure S8*.

The multi-wavelength analysis of the spectroscopic data in the 368-568 nm, 305-465 nm and 250-480 nm range for copper(II)-, zinc(II)- and cobalt(II)-based systems, respectively, allowed for the accurate determination of the complex species and their conditional stability constants at pH 7.4. For data analysis, all the possible equilibria involving the system components and their binding parameters were considered (i.e., the metal-ligand and the metal-polymer complex species described in *Table 1* and *Table 3*) and included in the overall model. The interaction of the polymer with the copper(II)-quercetin complex led to the formation of the $L_2M(PAA)$ species, whilst the interaction of the zinc(II)- and cobalt(II)-polymer complexes with quercetin led to the formation of the $LM(PAA)_2$ species. $L_2M(PAA)$ for copper(II) and $LM(PAA)_2$ for both zinc(II) and cobalt(II) are indeed the species representing the expected metal coordinated assemblies containing quercetin properly designed and prepared as potential drug delivery systems. The determined binding affinities are listed in *Table 4*.

Table 4. Overall conditional stability constant values[a,b] for the formation of metal(II)-coordinated assemblies containing quercetin at 25 °C and pH 7.4 (MOPS 10 mM).

Metal ion	**Species**	**Log β**
Cu(II)	$L_2M(PAA)$	13.83 (2)
Zn(II)	$LM(PAA)_2$	12.03 (1)
Co(II)	$LM(PAA)_2$	11.85 (2)

[a] refers to the equilibrium $qL + pM + rP \rightleftarrows L_qM_pP_r$ where charges are omitted for simplicity; [b] σ in parenthesis.

To highlight the crucial role played by the metal in acting as a linker between the flavonoid and the metal, UV-Vis titrations of quercetin with zinc(II)-polymer complex prepared at different Zn(II):PAA molar ratios from 1:4 to 1:6, (C_{PAA} = 9.00 mM) were carried out (*Supplementary materials - Chapter II, Figure S9*). Based on the binding constant values (*Table 3*), it was possible to determine that $ZnPAA_2$ is the main species present in solution when the concentration of the metal ion is still quite large (Zn(II):PAA 1:4), while the free polymer is the main species at lower zinc concentration (Zn(II):PAA 1:5 or 1:6). The red-shift observed for the band I of flavonoid upon the addition of titrant solution becomes less pronounced in the case of metal-polymer solutions prepared at Zn(II):PAA 1:4 and 1:5 (with respect to that performed with Zn(II):PAA 1:3), whilst it disappears when using a smaller amount of metal ion (Zn(II):PAA 1:6). In the latter case, the changes recorded in the UV-Vis spectra are solely due to the dilution of the ligand thus allowing to assume that no interaction occurs. The analysis of the spectroscopic data allowed the determination of the species and the binding constants that are lower than that determined using a metal/polymer complex species with the largest possible number of binding sites.

Isothermal titration calorimetry was further employed to unveil the energetics of the formation of the metal-coordinated assemblies containing quercetin in solution. ITC titrations are shown in *Figure 46* while the determined thermodynamic parameters are listed in *Table 5*.

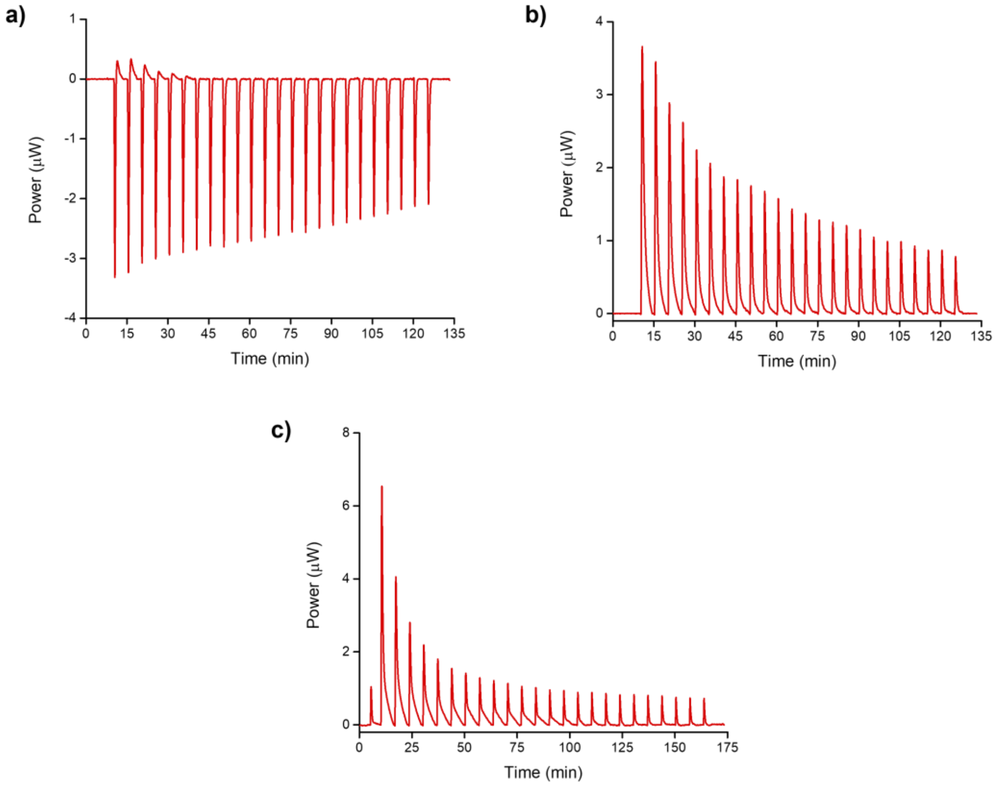

Figure 46. Typical ITC titrations of *a)* PAA (12.5 mM) into quercetin-copper(II) complex solution (Cu(II):Que 1:1, C_{Que} = 0.12 mM), *b)* zinc(II)- and *c)* cobalt(II)-polymer complex (M(II):PAA 1:3; C_{PAA} = 9.00 mM) into Que (0.15 mM) at 25 °C and pH 7.4; the integrated heat data are shown in *Supplementary materials - Chapter II, Figure S10*.

Table 5. Overall thermodynamic parameters[a,b,c] for the formation of metal(II)-coordinated assemblies containing quercetin at 25 °C and pH 7.4 (MOPS 10 mM).

Metal ion	**Species**	**$-\Delta G^0$**	**ΔH^0**	**$T\Delta S^0$**
Cu(II)	$L_2M(PAA)$	78.94	15 (2)	94
Zn(II)	$LM(PAA)_2$	68.67	-10.1 (3)	58.6
Co(II)	$LM(PAA)_2$	71.9	-8.01 (2)	63.9

[a] refers to the equilibrium $qL + pM + rP \rightleftarrows L_qM_pP_r$ where charges are omitted for simplicity; [b] σ in parenthesis; [c] in kJ mol $^{-1}$.

The results show that the formation of all assemblies is a spontaneous process and the main contribution to the Gibbs free energy is of entropic nature. As widely discussed in the literature, the favourable positive entropy change is mainly due to metal and ligand(s) desolvation, i.e. to the release of hydration water molecules upon complexation. However, the heat measured by ITC experiments (and consequently the ΔH^0 and $T\Delta S^0$ values determined) originates from the overall reactions occurring in the calorimeter sample cell and therefore the measured observable is the combination of the heat from several events, including not only the assembly formation but also the quercetin-metal complexes and polymer-metal complexes equilibria. Thus, to obtain the driving forces for the actual quercetin-metal(II)-polymer complexation equilibria, the contribution of the reactions concerning the binary species of Que and/or PAA must be properly considered in the model. Significant insights into the formation mechanisms can be obtained by calculating the stepwise thermodynamic parameters, graphically represented in *Figure 47*, which refer to the following equilibrium (charges are omitted for simplicity):

$$qL + M_pP_r \rightleftarrows L_qM_pP_r \qquad K_{L_qM_pP_r} \qquad \textit{Equation 1}$$

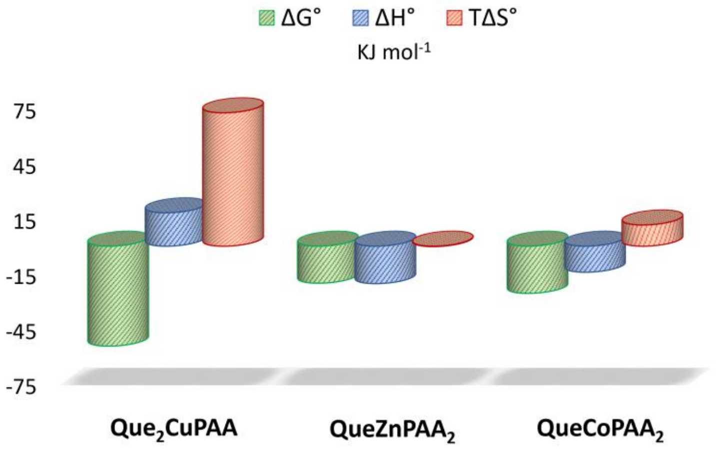

Figure 47. Stepwise thermodynamic parameters for the formation of metal-coordinated assemblies containing quercetin at 25 °C and pH 7.4.

The Que_2CuPAA assembly formation is entropically favoured and driven but enthalpically unfavoured. The strong entropic mark that drives the formation of this system can be attributed to several events which occur simultaneously in solution. The interactions between the carboxyl moieties of the polymer chain and copper(II) ions in solution produce a variation in the number of charged groups of the polymer backbone, causing conformational changes of the polyelectrolyte which may rearrange from an extended rigid state (as it is fully negatively charged)[244] to a coiled conformation.[245,246] The interaction between poly(acrylic acid) functional groups and copper(II) is known to be entropically favoured and driven (*Table 3*, *Figure 42*). Furthermore, the entrapment of the $CuQue_2$ complex into the pocket created by the polymer coil backbone (*Figure 48*) by a hydrophobic effect may give an additional favourable contribution to the entropy value. [220,247,248] However, the energy cost needed for desolvation overlaid any possible favourable enthalpic gain leading to an unfavourable ΔH^0 value.

The formation of the $QueZn(PAA)_2$ is enthalpically favoured and driven. This is likely due to the favourable interactions that occur between Que and the metal centres of the Zn(II)-polymer complex. Similarly, the $QueCo(PAA)_2$ complex formation occurs thanks to an enthalpically and entropically favoured process; enthalpy and entropy changes contribute almost comparably to the Gibbs free energy of the reaction. The favourable entropic term is due to the desolvation of both quercetin and the polymer-metal complex; the enthalpy gain, which prevails on the energy cost for desolvation, is attributable to the favourable attractive forces between Que and the metal ions of the Co(II)-polymer complex. This enthalpic term, which is comparable to that determined for the formation of the CoQue species, supports the idea that the coordination features of the metal ion in the final three-component assembly are satisfied by the quercetin functional groups and two carboxyl groups of the polymer chain (*Figure 48*).

These studies on solution equilibria and speciation are indispensable for optimizing the design of drug delivery systems which may ensure an increase in the bioavailability of quercetin and an enhancement of its physiological activity.

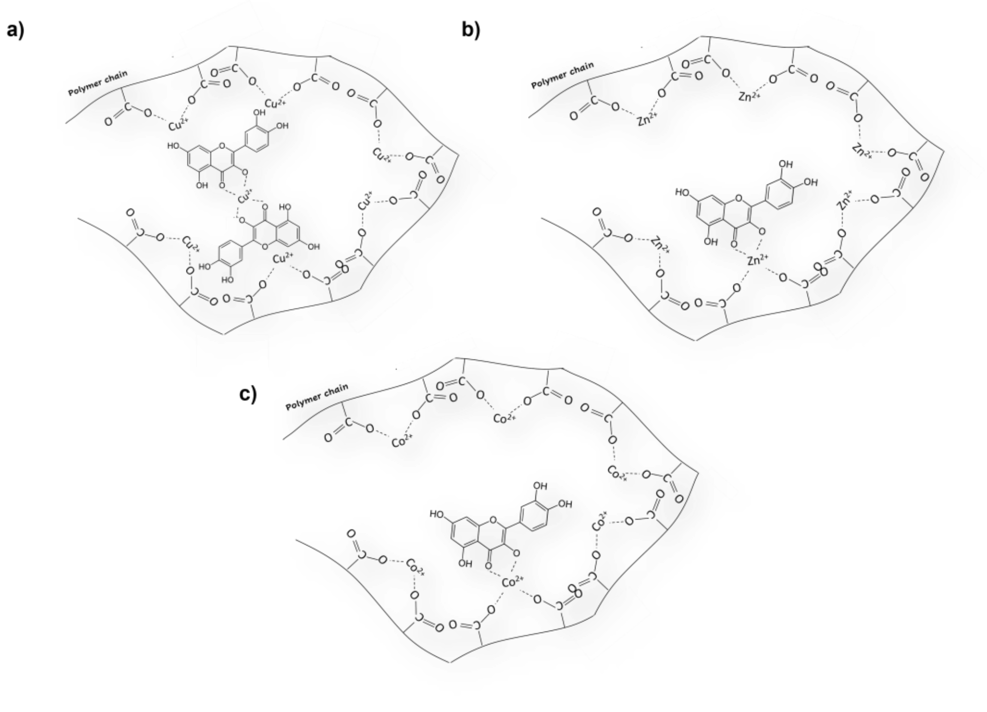

Figure 48. Proposed structure for the *a)* CuQue$_2$PAA *b)* QueZnPAA$_2$ and *c)* QueCoPAA$_2$ assembly.

The formation of the cobalt(II)-coordinated assembly was also investigated at the solid-liquid interface by quartz-crystal microbalance with dissipation monitoring (QCM-D) experiments. QCM-D is a real-time, surface-sensitive technique for analysing film formation, layer properties and surface-interaction processes with high sensitivity. The technique enables monitoring the adsorption and desorption of small molecular systems such as drugs without the use of probes.[249-251] The molecule-surface interactions are detected as changes in mass (mass uptake or loss) as molecules adsorb or desorb on/from the surface. The drug uptake and release are detected in real-time by monitoring the changes in the frequency oscillation and energy dissipation of a gold-coated quartz sensor upon absorption/desorption. Both kinetic and thermodynamic parameters related to complexation processes occurring at the interface may be determined. [252]

The changes in frequency (ΔF) and dissipation (ΔD) in a typical QCM-D experiment with the Co(II)-based system are shown in *Figure 49*; for simplicity, only data relating to the third overtone ($\Delta f_3/3$ and ΔD_3) are reported.

A rapid decrease in frequency is observed after *step 2* (see *Figure 49*) due to the adsorption of the cobalt(II)–polymer system to the sensor surface at pH 7.4; this also determines an increase in energy dissipation, owing to the less-rigid structure of the adsorbed layer of the polymeric complex onto the gold sensor.[253] During the subsequent rinsing step, a significant decrease in the dissipation is observed with time, likely due to the rearrangement of the film, resulting in a more compact, rigid layer. It should be pointed out that, in both cases, the dissipation value is fairly small, with the $|\Delta D_n/(\Delta f_n/n)|$ ratio being much smaller than 4×10^{-7} Hz^{-1}; [254] consequently, the adsorbed film can be considered as basically rigid. Thus, the Sauerbrey relationship may be used to convert the change in frequency to the adsorbed mass. The adsorption of quercetin onto the polymeric layer (*step 4*) causes a decrease in frequency, assuming that the flavonoid could be trapped in the adsorbed metal-polymer layer through hydrophobic interactions and/or by metal-ion coordination. The frequency increase observed after the rinse in *step 5* corresponds to the removal of the non-adsorbed flavonoid.

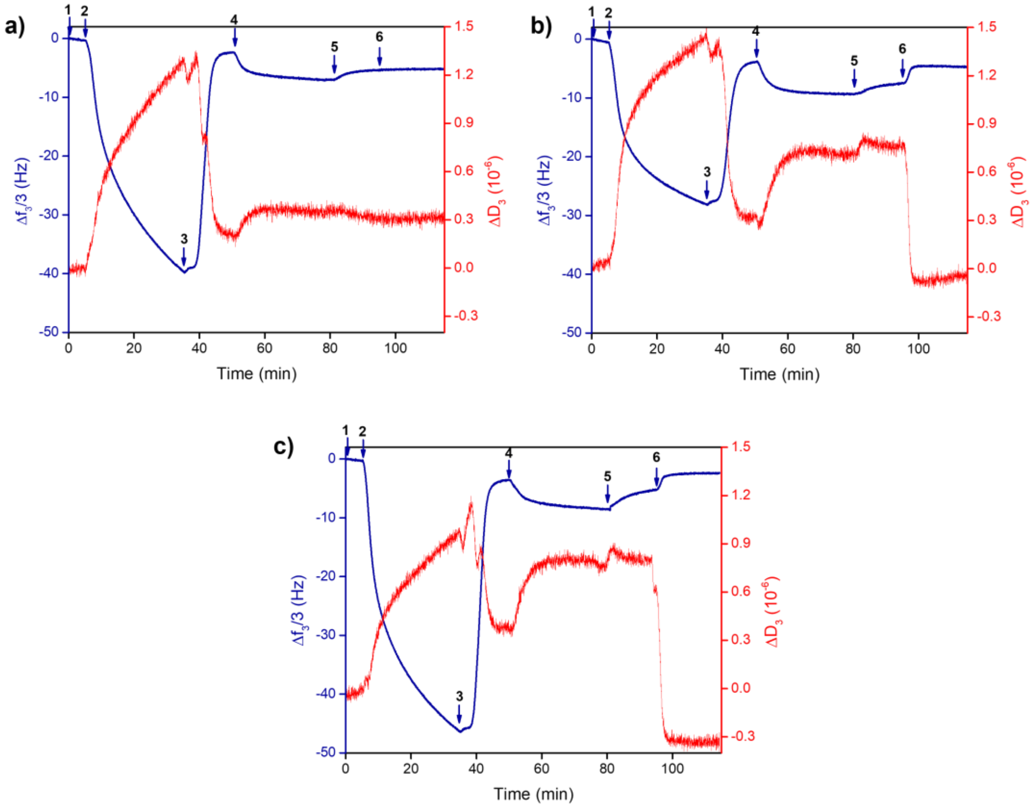

Figure 49. Normalized frequency $\Delta F_n/n$ (blue) and dissipation ΔD_n (red) change (for simplicity, only data referring to the third overtone are shown, n = 3) for the adsorption of the cobalt(II)-polymer layer onto a gold-coated quartz crystal and subsequent loading and release of quercetin at 25 °C. 1) Baseline: 10 mM MOPS at pH 7.4; 2) adsorption of the cobalt(II)-polymer system (M:PAA 1:3, C_{PAA}= 9.00 mM) in 10 mM MOPS at pH 7.4; 3) rinsing with 10 mM MOPS at pH 7.4; 4) uptake of quercetin from its solution (C_{Que} = 0.15 mM) in 10 mM MOPS at pH 7.4; 5) rinsing with 10 mM MOPS at pH 7.4; 6) rising with 10 mM MOPS at *a)* pH 7.4, *b)* pH 5.4 and *c)* pH 4.5.

The plot of the adsorbed mass (ng/cm^2), calculated using the Sauerbrey equation, is shown in *Figure 50*. About 50 ± 12 ng/cm^2 of quercetin was absorbed onto the cobalt(II)-polymer layer.

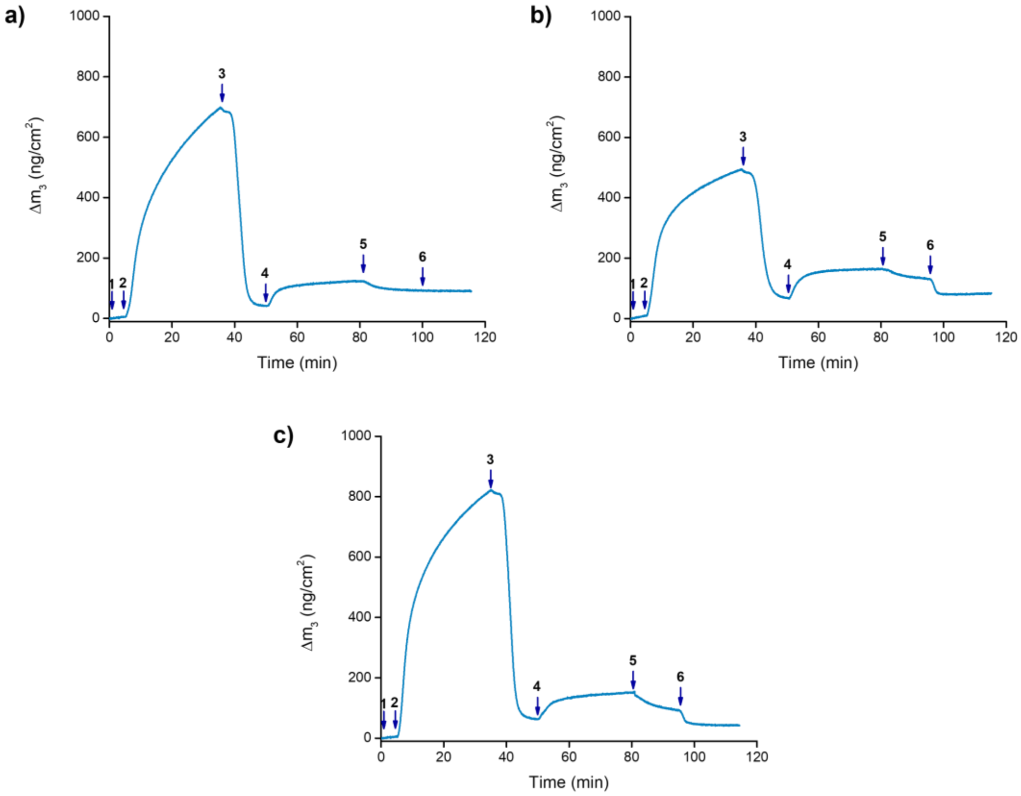

Figure 50. Mass changes (Δm) for cobalt(II)-coordinated assembly adsorption onto a gold-coated quartz crystal and subsequent loading (and release) of quercetin at 25 °C. The conditions for each flowing step are described in the caption of *Figure 49*.

The time dependency of the frequency (and thus of the mass) changes also allowed to determine the kinetic rate constants (k_{on} and k_{off}) as well as the association constant (K_{ass}) at the solid-liquid interface.[255,256]

As widely reported in the literature, to quantitatively determine these parameters, both the adsorption and desorption processes must follow the Langmuir model and fulfil its relevant assumptions.[257] The binding process is described by the following equation:

$$L + M(PAA)_2 \underset{K_{off}}{\overset{K_{on}}{\rightleftarrows}} LM(PAA)_2 \qquad \textit{Equation 2}$$

According to the Langmuir model, the adsorption process of the ligand can be described by the function:

$$\theta(t) = \theta_{eq} \cdot (1 - e^{-(kon \cdot C + koff) \cdot t}) \qquad \textit{Equation 3}$$

in which:

- $\theta(t)$ is the time-dependent surface coverage,
- θ_{eq} is the concentration-dependent equilibrium surface coverage,
- k_{on} and k_{off} are the kinetic rate constants for the binding and unbinding process,
- C is the concentration of the adsorptive ligand;

whilst the desorption process is described by the following equation:

$$\theta(t) = \theta_{eq} \cdot e^{-koff \cdot t} \qquad \textit{Equation 4}$$

The analysis of the kinetics of adsorption and desorption processes (*Figure 51*) through *Equation 3* and *Equation 4* allowed to determine the rate constants k_{on} and k_{off} as well as to calculate the association constant $K_{ass} = k_{on}/k_{off}$.

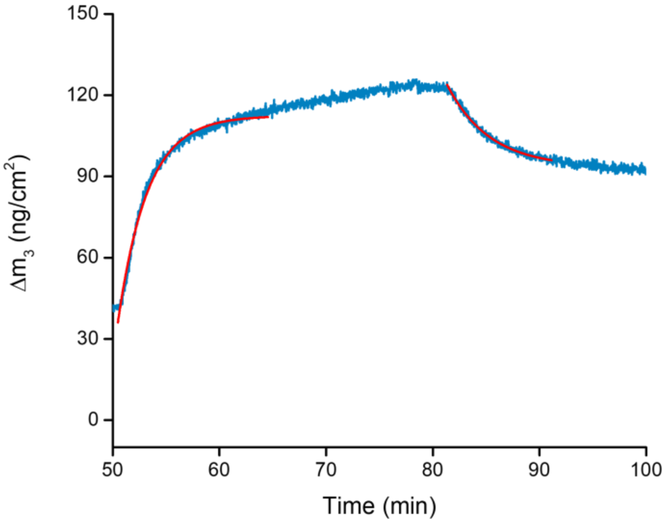

Figure 51. Curve fitting of the adsorption and desorption profiles of quercetin from cobalt(II)-polymer layer. The curve is a magnification of *steps 4* and *5* of the mass change plots in *Figure 50*; the experimental curves are in cyan while the calculated ones are in red.

The kinetic rate constants are k_{on} = 634 ± 87 M^{-1} min^{-1} and k_{off} = 0.21 ± 0.04 min^{-1}. Using these values, a K_{ass} of 3019 ± 87 M^{-1} was calculated at the solid-liquid interface (log K_{ass} = 3.47 (1)), which is in good agreement with that determined in solution by UV-Vis/ITC experiments.

1.6 Stability of the metal(II)-coordinated assemblies

A key feature in the development of drug delivery platforms is their ability to enhance the stability of drugs in the physiological environment. Kinetic stability studies were performed to evaluate if the presence of the metal ion as well as of the polymer to form the metal-coordinated assemblies allows stabilizing the quercetin, which easily degrades in solution when alone. As reported in the literature, quercetin undergoes an autooxidation process in solution resulting in the formation of a quercetin auto-oxidation product.[190] The spectral changes of Que in solution were first recorded over time (*Figure 52a*) as a control to determine the flavonoid half-life.

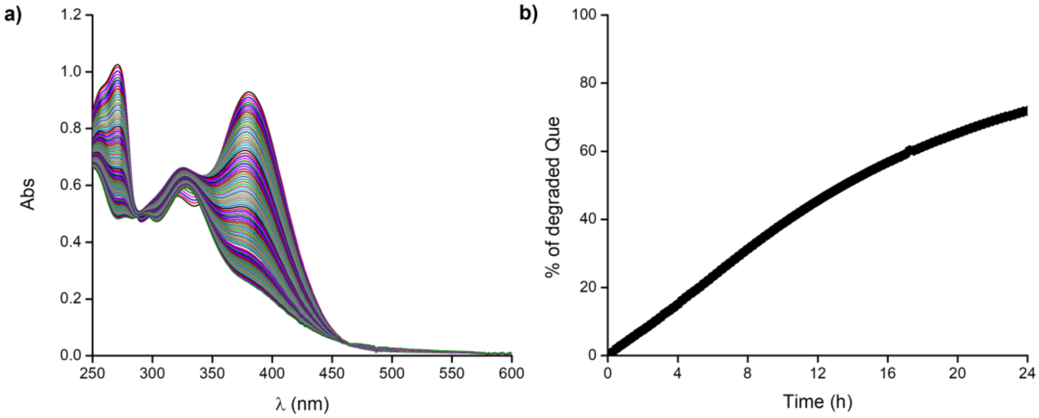

Figure 52. *a)* UV-Vis spectra of Que (0.06 mM) at 25 °C and pH 7.4 recorded for 24 h; *b)* % of degraded Que (Abs 379 nm).

Band I of Que decreases over time and simultaneously a new absorption band at 321 nm appears indicating the formation of the flavonoid autoxidation products. The spectral changes at 379 nm were used to determine the percentage of quercetin degradation in 24 h. As shown in *Figure 52b*, 70 % of quercetin was degraded within 24 hours. The flavonoid degradation behaviour and mechanism were evaluated determining the degradation rate obtained by fitting kinetic data to different mathematical models. The spectroscopic data in *Figure 52* were fitted according to zero, first and second-order kinetics,[258,259] using the linear equations $A_i=f(t)$, $ln(A_0/A_i)=f(t)$ and $1/A_i=f(t)$, respectively, where A_0 and A_i represent the absorbance values at the initial time and at a well-determined time *"t"*. The slopes of the straight lines represent the rate constants (*k*) of the reactions. It should be noted that the zero and second-order kinetic models describe systems where the degradation rate is dependent on the initial concentration of the quercetin. The kinetic models applied for the Que degradation reaction, considering the absorbance of band I, are shown in *Figure 53* and the results obtained are reported in *Table 6*.

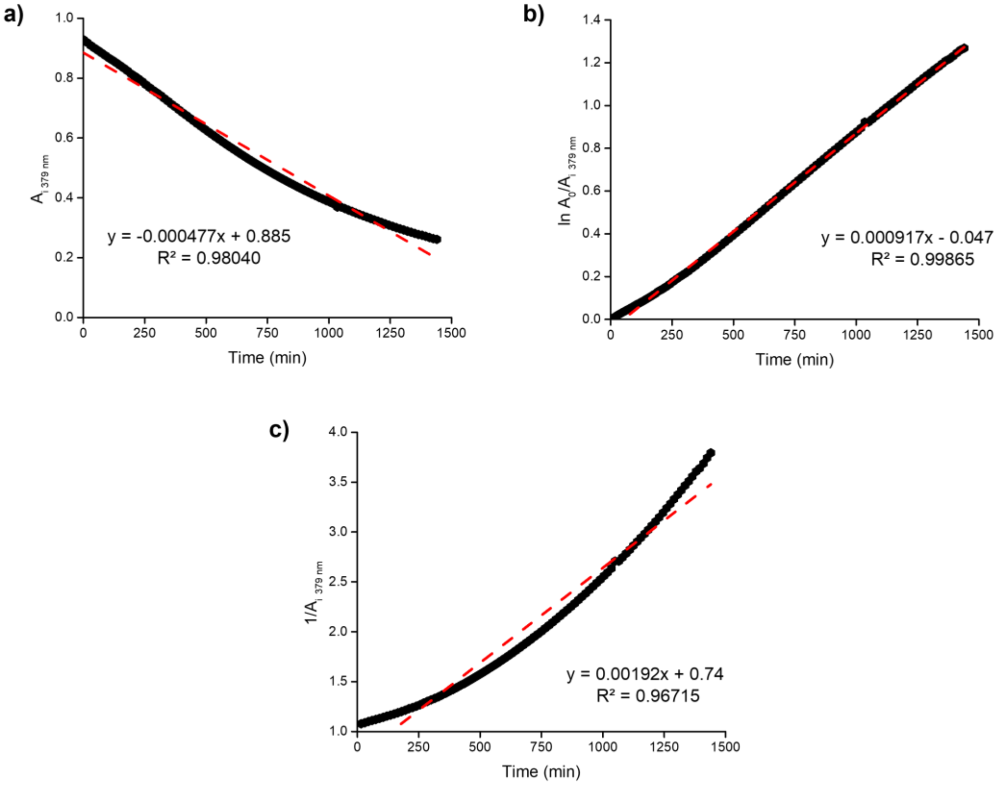

Figure 53. Rate of degradation of Que at 25 °C and pH 7.4: *a)* zero-order; *b)* first-order; *c)* second-order kinetic models.

Table 6. Kinetic models for Que degradation at 25 °C and pH 7.4.

Kinetic model	**Rate constant (*k*)**	**R^2**
Zero-order	$4.77(9)^a \times 10^{-4}$ a.u. min^{-1}	0.98040
First-order	$9.17(4) \times 10^{-4}$ min^{-1}	0.99865
Second-order	$1.92(4) \times 10^{-3}$ a.u.^{-1} min^{-1}	0.96715

[a] σ in parenthesis.

The best fit of the quercetin degradation rate is obtained by applying a first-order kinetic, as demonstrated by the largest regression coefficient (R^2, *Figure 53*), in line with the most encountered models in pharmaceutical stability studies. The half-life of quercetin is roughly 12.6 h in these conditions.

With the same approach, the kinetic stability of the quercetin-metal complexes and metal-coordinated assemblies was investigated. The spectral changes of the complex systems recorded over time are shown in *Figure 54* and *Figure 55* for the copper(II)- and the zinc(II)-based systems, respectively.

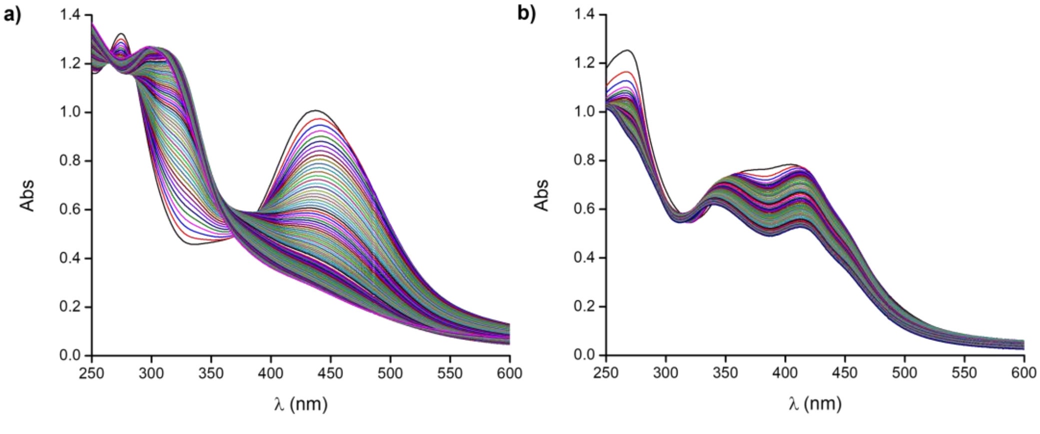

Figure 54. UV-Vis spectra of *a)* $CuQue_2$ and *b)* Que_2CuPAA species at 25 °C and pH 7.4 recorded for 24 h.

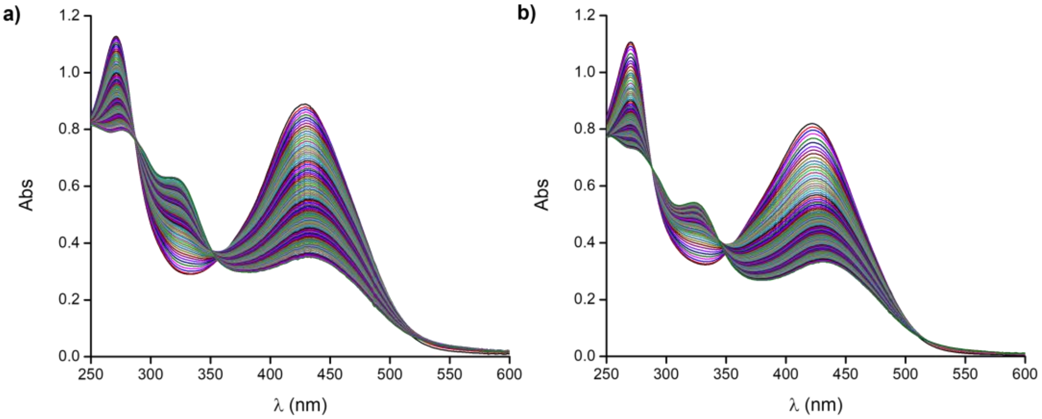

Figure 55. UV-Vis spectra of *a)* ZnQue and *b)* QueZnPAA$_2$ species at 25 °C and pH 7.4 recorded for 24 h.

From the UV-Vis spectra, a decrease in the intensity of the band at 436 nm for CuQue$_2$, 404 nm for Que$_2$CuPAA, 429 nm for ZnQue and 431 nm for QueZnPAA$_2$ can be detected. These spectral changes were used to determine the degradation rate of each system in 24 h as shown in *Figure 56*. For comparison, the degradation rate of quercetin in 24 h is also reported in the same plots.

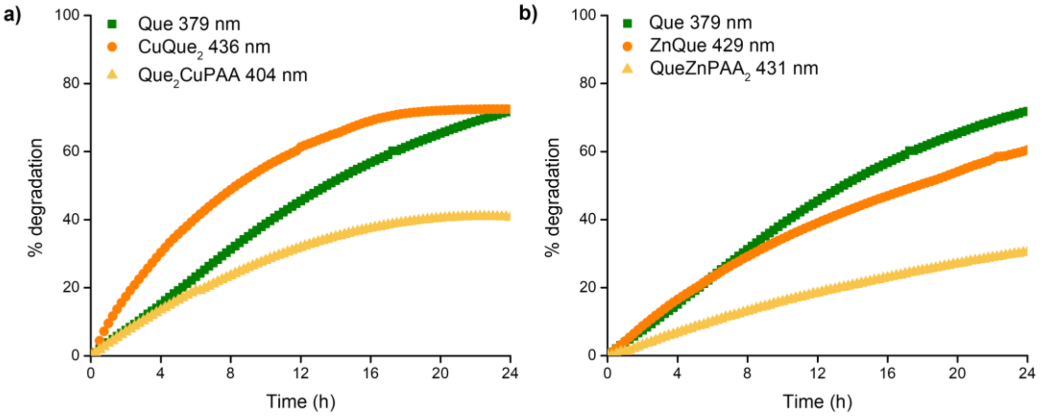

Figure 56. % degradation of *a)* copper(II)- and *b)* zinc(II)-based systems at 25 °C and pH 7.4.

It can be observed that the $CuQue_2$ complex undergoes a larger degradation than quercetin itself as it degrades by about 70% in less than 24 hours. Instead, the ZnQue complex species degrades by about 60%. This different behaviour can be ascribed to the strongly oxidizing ability of the copper(II) ions which promote ligand oxidation.[227] Indeed, a parallel increase in the absorption at 321 nm, typical of the quercetin oxidation products, can be observed in *Figure 54a*.

Interestingly, the flavonoid degradation process is reduced for the systems containing the polymer: both copper(II)- and zinc(II)-based assemblies show a much smaller % degradation (about 40% for Que_2CuPAA and 25% for $QueZnPAA_2$) compared to that of free uncomplexed quercetin or quercetin-metal(II) complexes. This can be attributed to the presence of the polymer which influences the quercetin environment somehow protecting the drug and decreasing the oxidation process in aqueous solution, as highlighted by a much smaller increase of the absorption band at 321 nm for the metal-coordinated assemblies.

The polymer conformations in solution depend on concentration, pH and ionic strength.[260] PAA undergoes a reversible conformational transition that is driven by the state of ionization of the carboxylic groups. At low pH, PAA adopts a compact globular conformation while, when the pH is increased, the polymer expands into a fully solvated extended conformation due to ionization events.[261] However, the presence of metal ions induces the transition from a rigid state to a coiled one of the polymer which can hold quercetin-metal complexes species by limiting the contact of the flavonoid with the surrounding aqueous environment.[246]

The experimental data obtained by the spectrophotometric experiments were analyzed according to zero, first and second-order kinetics. The kinetic models applied for the degradation reaction of the copper(II) and zinc(II)-based systems are shown in *Figure* 57 and *Figure 58*, respectively, and the results obtained are in *Table 7*.

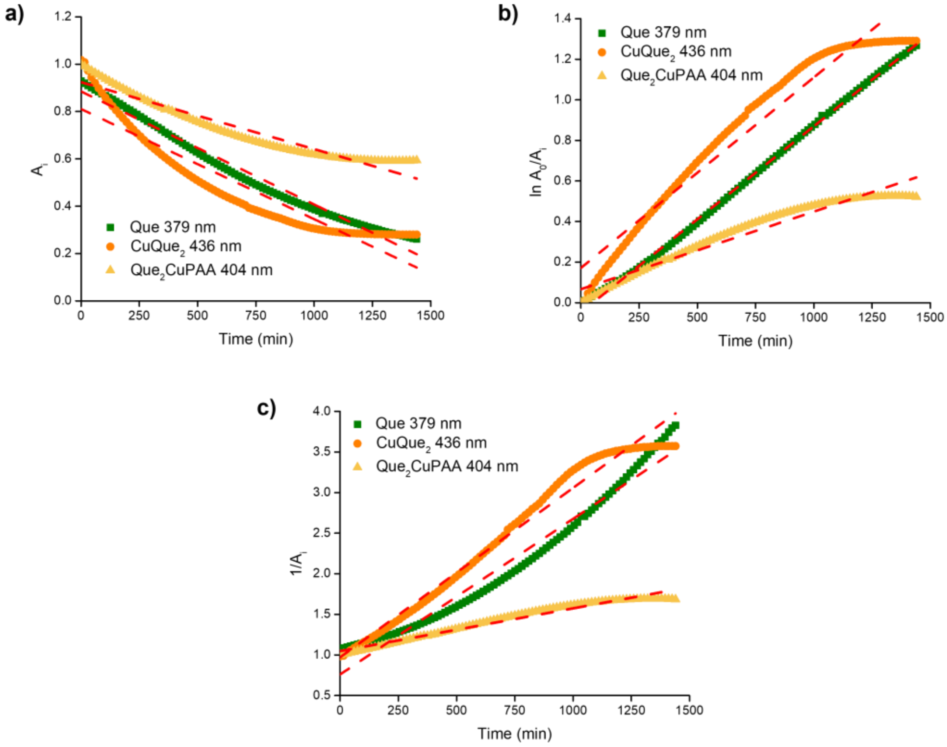

Figure 57. Rate of degradation of copper(II)-based systems at 25 °C and pH 7.4: *a)* zero-order; *b)* first-order; *c)* second-order kinetic models.

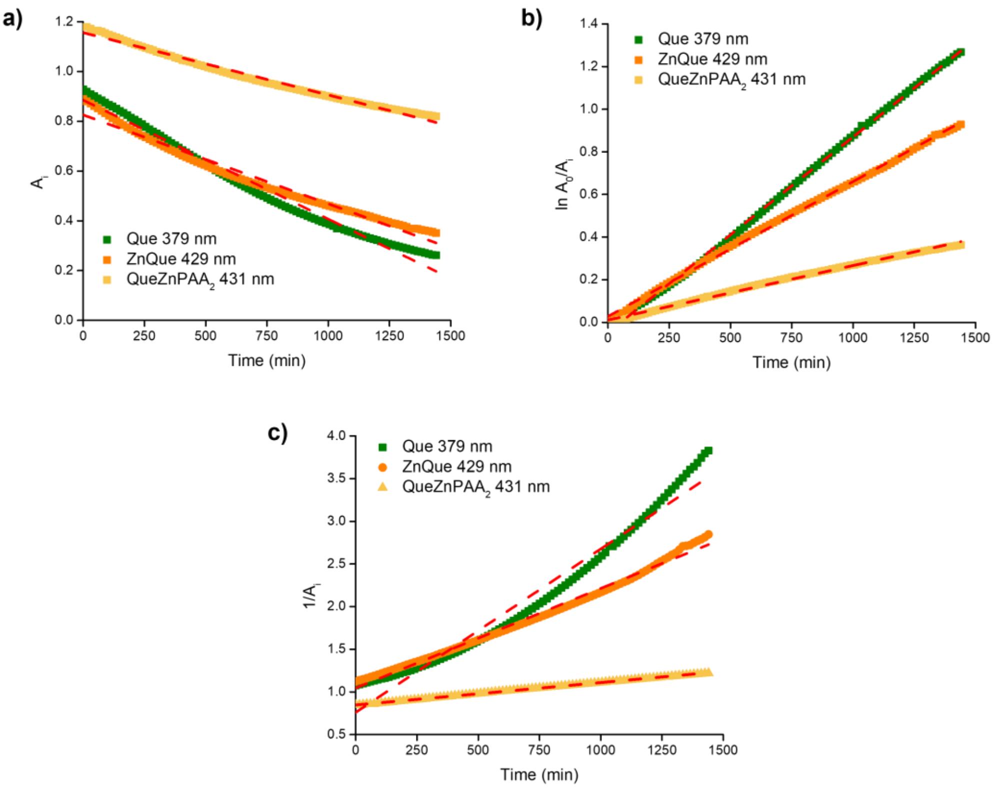

Figure 58. Rate of degradation of zinc(II)-based systems at 25 °C and pH 7.4: *a)* zero-order; *b)* first-order; *c)* second-order kinetic models.

Table 7. Kinetic models for the degradation of copper(II) and zinc(II)-based systems at 25 °C and pH 7.4.

Species	**Kinetic model**	**Rate constant (*k*)**	**R^2**
$CuQue_2$	Zero-order	$4.7\ (2)^{a} \times 10^{-4}$ a.u. min^{-1}	0.86609
	First-order	$9.4\ (5) \times 10^{-4}\ min^{-1}$	0.94564
	Second-order	$2.09\ (3) \times 10^{-3}$ a.u.$^{-1}$ min^{-1}	0.97791
Que_2CuPAA	Zero-order	$2.38\ (8)^{a} \times 10^{-4}$ a.u. min^{-1}	0.92115
	First-order	$3.83\ (9) \times 10^{-4}\ min^{-1}$	0.94845
	Second-order	$5.26\ (9) \times 10^{-4}$ a.u.$^{-1}$ min^{-1}	0.96779
ZnQue	Zero-order	$3.57\ (6) \times 10^{-4}$ a.u. min^{-1}	0.97464
	First-order	$6.32\ (3) \times 10^{-4}\ min^{-1}$	0.99831
	Second-order	$1.17\ (1) \times 10^{-3}$ a.u.$^{-1}$ min^{-1}	0.99094
$QueZnPAA_2$	Zero-order	$2.50\ (3) \times 10^{-4}$ a.u. min^{-1}	0.98629
	First-order	$2.56\ (2) \times 10^{-4}\ min^{-1}$	0.99519
	Second-order	$2.626\ (6) \times 10^{-3}$ a.u.$^{-1}$ min^{-1}	0.99948

[a] σ in parenthesis.

The best fit for the $CuQue_2$ and Que_2CuPAA degradation rate is obtained by applying second-order kinetics, as demonstrated by the regression coefficient (R^2). The half-life of $CuQue_2$ is about 8.2 h while that of Que_2CuPAA is 30.2 h at the experimental conditions employed. In the latter case, however, it is necessary to point out that Que_2CuPAA is not the main reaction product as uncomplexed Que is present in comparable amounts. Consequently, kinetic data emphasize the key stabilizing effect of the polymer if compared to that of either Que alone or $CuQue_2$ complex.

A first-order kinetic model best describes the degradation of the ZnQue complex while a second-order kinetics best describes the $ZnQuePAA_2$ decomposition rate. The half-life of ZnQue and $ZnQuePAA_2$ are 18.3 h and 53.8 h, respectively. Overall, the kinetic studies revealed that the Que-metal(II)-polymer assemblies have a longer half-life of about twice and forth times than that of the quercetin alone, thus strongly emphasizing that the presence of the suitably designed metal-coordinated assemblies valuably improves the kinetic stability of the flavonoid.

1.7 pH triggered release of quercetin from metal-coordinated assemblies

The release of quercetin from copper(II)- and zinc(II)-coordinated assemblies of quercetin was investigated at 37 °C and pH 7.4 and 5.4. These pH values were selected to assess the ability of the metal-coordinated assemblies to promote flavonoid release in an acidic microenvironment rather than a neutral one. Linear regression equations for quercetin calibration curves obtained in the concentration range 0.006-0.02 mM at the proper pH value (*Supplementary materials* - *Chapter II*, *Figure S11*) were used to determine the amount of cumulative quercetin released as a function of time from absorbance values at 379 nm (for pH 7.4) and 367 nm (for pH 5.4). The percentage of the quercetin released under different pH values was calculated using *Equation 5* and is shown in *Figure 59*:

$$\text{Que released \%} = \frac{\text{Que release}}{\text{Total Que}} * 100 \qquad \textit{Equation 5}$$

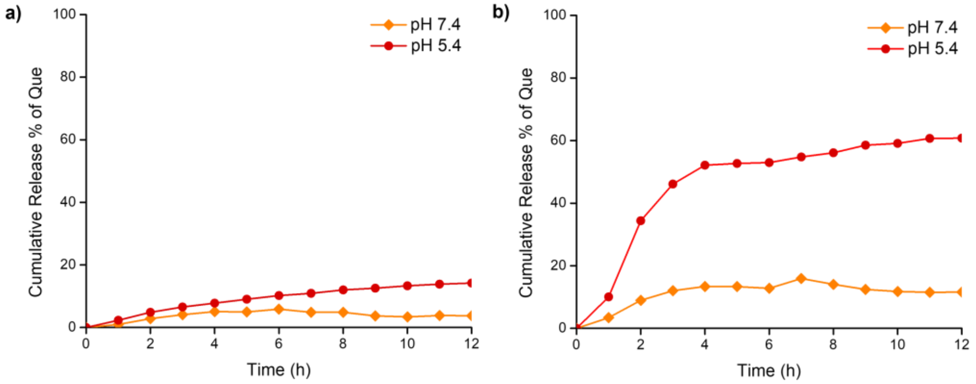

Figure 59. Plots of cumulative release % of quercetin from *a)* copper(II) and *b)* zinc(II)-coordinated assemblies at 37 °C and pH 7.4 or 5.4.

The metal-coordinated assemblies containing quercetin can respond to an acidic microenvironment; indeed, as shown in *Figure 59*, a higher release of flavonoid from both Que_2CuPAA and $QueZnPAA_2$ assemblies occurs under acidic rather than physiological pH. For Que_2CuPAA, the amount of Que released changes from 3.7 ± 0.8 % at pH 7.4 to 15 ± 1% under acidic conditions, whilst for the $QueZnPAA_2$ system the amount of flavonoid released increases from 15.9 ± 0.6 % to 62.8 ± 0.7%. Although the release profiles of the quercetin from the copper(II)- and zinc(II)-based systems are quite similar under physiological conditions (*ca.* 5% and 15% respectively), the amount of the flavonoid released under acidic conditions significantly differs. Indeed, after 12 hours only 15% of quercetin is released from the copper(II)-based assembly while a higher release ratio of Que (*ca.* 60%) is achieved from the zinc(II) system. We may speculate that the different release rates can be associated with the different assembly arrangements which somehow favours the release mechanism in the latter case. As previously described, the $CuQue_2$ complex is entrapped within the pocket of the polymer coil backbone to form the final assembly while the $QueZnPAA_2$ formation is mostly due to the acid-labile linkage between the metal ion and Que.

The cumulative release % of quercetin for each system was fitted to several kinetic models (zero-order, first-order, Higuchi, Hixson-Crowell and Korsmeyer-Peppas) to figure out the release mechanism in both neutral and acidic conditions. The more convincing release mechanism was determined at the investigated pH based on the parameters of the best-fitting regression model. At neutral conditions, the R^2 value determined for each model (*Supplementary materials - Chapter II, Table S1*) is not so satisfying as to discriminate between the different release kinetic mechanisms. Conversely, at acidic conditions, the regression models (*Supplementary materials - Chapter II, Table S2*) allowed us to identify the release mechanisms. Specifically, Que release from Que_2CuPAA fits better the Higuchi model which is used for the release of a drug in which both diffusion and dissolution are involved. The Korsmeyer-Peppas model, specifically developed for the release of a drug molecule from a polymeric matrix and commonly applied when the release mechanism is quite complex, also shows a good fit of the kinetic data. The *n* parameter of the model, which corresponds to a diffusional exponent representing the mechanism of drug release, has a value of 0.6966 suggesting that the release mechanism is anomalous (non-Fickian) and is governed by diffusion and swelling transport. [262-264]

For $QueZnPAA_2$, the R^2 values indicated that the Higuchi model fits the release data better than other models; thus, diffusion and dissolution processes can be considered mainly responsible for the flavonoid release from the zinc(II)-based assembly.

For the cobalt(II)-coordinated assembly, the release of quercetin was instead investigated at the solid-liquid interface through QCM-D experiments (*Figure 49*). After assessing the adsorption of the flavonoid onto the cobalt(II)-polymer layer, either neutral or acidic solutions (*step 6, Figure 49*) were flown through the sensor surface. The neutral solution (pH 7.4, *Figure 49a*) did not determine further frequency variations whereas the acidic solutions (pH 5.4 or 4.5, *Figure 49b* and *Figure 49c*), caused an increase in the frequency up to values similar to those obtained after the removal of the non-adsorbed cobalt(II)-polymer complex layer (*step 3*). This evidence may be explained by assuming a pH-induced breakdown of the coordination bonds between quercetin and cobalt(II) ions (which act as the anchoring sites to the polymer chain) and the consequent release of the flavonoid from the assembly. Moreover, the protonation of the free carboxyl groups of the polymer which led to a complementary pH-dependent swelling mechanism might also be invoked.[155] As pH decreases approaching the pKa value of 4.5, the equilibrium between the $-COO^-$ and -COOH moieties shifts towards COOH and therefore the overall charge of PAA decreases with a consequent rearrangement of the polymer chains which further contributes to the release of the drug likey entrapped into the polymeric layer.

A very small amount of quercetin is released under neutral conditions (ca. 6%); conversely, 62% and 64 % of the adsorbed quercetin is released from the assembly at pH 5.4 and 4.5, respectively. This evidence proves that the cobalt(II)-based assembly can respond to changes in the pH value thus allowing a controlled release of the loaded flavonoid. Overall, the ability of the developed metal(II)-coordinated assemblies is significant to guarantee an adequate concentration of the quercetin at the interested site thus increasing the physiological activities of the flavonoid and avoiding its leaking in undesired places.

2. CONCLUSIONS

The study of the multiple equilibria occurring in aqueous solution at pH 7.4 among quercetin, metal(II) ions, and polyacrylic acid is proposed for the design and development of metal-based assemblies containing the flavonoid as a model drug. Combined UV-Vis and ITC experiments enabled the accurate determination of the binding parameters for the complex species formation in solution. Quercetin forms ML complex species with all metal ions and an additional ML_2 species with copper(II) and cobalt(II). The ML complex formed with copper(II) is both enthalpically and entropically favoured; the formation of ML_2, the main complex species, is driven by entropy mostly due to metal and ligand desolvation. The ML complex formed by zinc(II) with Que is entropy favoured and driven. The formation of cobalt(II)-quercetin complexes occurs by enthalpically favoured processes. The carboxyl groups of the polyacrylic acid chains allow for the complexation of the metal(II) ions forming M(PAA) and $M(PAA)_2$ species; the complexation process is entropically favoured and driven mostly due to desolvation and conformational changes of the polymer chains. The metal(II) ions work as anchoring/bridging sites for the efficient binding of quercetin to the polymer backbone to form the metal-coordinated assemblies. The analysis of the overall equilibria involved permits to prove the formation of a Que_2CuPAA complex in solution through an entropically favoured and driven process and of $QueZn(PAA)_2$ complex in an enthalpically favoured and driven manner. Enthalpy and entropy equally contribute to the formation of the $QueCo(PAA)_2$ complex. The affinity of the flavonoid toward the cobalt(II)–polymer complex was also confirmed at the solid-liquid interface.

The developed assemblies have a longer half-life than the uncomplexed quercetin, pointing out that their formation and action improve the kinetic stability of the bound/entrapped flavonoid. The determination of the amount of quercetin released under different pH conditions proves that the carefully designed delivery system enables a controlled release of the loaded drug. Overall, these studies offer a versatile strategy for the design and construction of a smart system exhibiting a pH-controlled delivery of quercetin with great potential for the treatment of several diseases.

3. EXPERIMENTAL SECTION

3.1 Materials

Quercetin (Que) (purity ≥ 95%, HPLC), copper(II) perchlorate hexahydrate (purity ≥ 98%), zinc(II) perchlorate hexahydrate (purity ≥ 98%), cobalt(II) perchlorate hexahydrate (purity ≥ 98%), 4-morpholinepropanesulfonic acid (MOPS) (purity ≥ 99.5%, titration), dimethylsulfoxide for spectroscopy (DMSO) (purity ≥ 99.8%), and poly(acrylic acid sodium salt) (PAA) (average Mw ~5100, GPC, purity ≥ 99%) were purchased from Sigma-Aldrich and used without purification. Dialysis membranes (MWCO = 3.5KDa) were obtained by Spectrum Laboratories Inc. Stock solutions of Que were prepared in pure DMSO and then properly diluted in a buffered aqueous solution (pH 7.4, MOPS 10 mM) to have a final organic solvent content of only 5% v/v. Buffer solutions were prepared by weighing proper amounts of MOPS and titrating with a sodium hydroxide solution to the desired pH. All Que solutions were always freshly prepared and stored in the dark to avoid possible light-induced alterations. The metal(II) stock solutions were prepared by dissolving the corresponding perchlorate salts in water and titrating the resulting solutions with standard EDTA using the proper indicator depending on the metal ion (murexide, eriochrome black T or orange xylenol).[265] Poly(acrylic acid) stock solutions were prepared at pH 7.4 in MOPS 10 mM; the concentration of the polymer was expressed per monomer unit of acrylic acid. High-purity water (Millipore, Milli-Q Element A 10 ultrapure water) and A-grade glassware were employed throughout.

3.2 UV-Vis titrations

UV-Vis titrations were carried out at 25 °C in aqueous solution (pH 7.4, MOPS 10 mM) with an Agilent 8453 diode-array (Agilent Technologies, USA) or a V-770 UV-Vis/NIR spectrophotometer (Jasco, Europe) spectrophotometer in a 1 cm path length quartz cells. The temperature of the cell holder was maintained constant by a circulating water bath. Increasing amounts of the proper titrant solutions were added with a precision pipette (Gilson or Hamilton) into the cell containing 2 mL of the sample solution. All solutions were prepared to have the same % (v/v) amount of DMSO. The reaction mixture in the cell was stirred during the titrations. Injection time intervals were chosen to ensure equilibrium conditions before each subsequent addition.

Quercetin-metal(II) complexes: UV-Vis titrations for the study of metal-ligand complex formation were conducted by adding a solution of Cu(II) (0.20-0.30 mM), Zn(II) (0.80-0.90 mM) or Co(II) (0.40-1.00 mM) into Que solution (0.05-0.06 mM).

Quercetin-poly(acrylic acid) interactions: The interactions occurring between quercetin and poly(acrylic acid) were investigated spectrophotometrically by titrating the flavonoid (0.05-0.06 mM) with a PAA solution (0.05-9.00 mM).

Quercetin-metal(II)-polymer assemblies: For the copper(II)-based assembly, the quercetin-copper complex was first prepared at 1:1 molar ratio (C_{Que} = 0.05-0.06 mM) and titrated with a PAA solution (12.0-12.5 mM). The copper/quercetin molar ratio was chosen to optimize the complex species formation.

For the Zn(II)-based assembly, two different strategies were adopted. Firstly, aqueous solutions of the zinc(II)-quercetin complex were titrated with poly(acrylic acid) solutions. Increasing amounts of poly(acrylic acid) solutions (8.00-9.00 mM) were added into the cell containing a solution of Zn(II)-quercetin complex (Zn(II):Que 3.6:1, C_{Que} = 0.06-0.07 mM). The zinc/quercetin molar ratio was chosen to optimize the complex species formation. Alternatively, increasing amounts of zinc(II)-poly(acrylic acid) complex solutions were added into the cell containing the quercetin solution (0.05-0.06 mM). Zinc(II)-poly(acrylic acid) solutions were prepared by combining Zn(II) and PAA in different molar ratios (Zn(II):PAA ranging from 1:3 to 1:6, C_{PAA} = 8.50-9.00 mM).

For the cobalt(II)-based assembly, Que solution (0.05-0.06 mM) in the cell was titrated with the metal(II)-polymer solution prepared by properly mixing Co(II) and PAA at 1:3 molar ratio (C_{PAA} = 9.00 mM).

About 30-40 scans were recorded for each titration and at least three independent runs were collected for each system. The analysis of the spectral data was performed using Hyperquad software,[266] which is specifically designed to determine equilibrium constant and molar absorptivity values. The program allows for a multi-wavelength treatment of the spectral data through a non-linear least-squares minimization procedure and the simultaneous refinement of data obtained from different titrations.

3.3 Isothermal titration calorimetry (ITC) measurements

Calorimetric titrations were performed at 25 °C in buffered aqueous solution (pH 7.4, MOPS 10 mM) with a nano-isothermal titration calorimeter Nano-ITC (TA Instruments, USA). Titrant solutions contained in a 250 µL syringe were injected into sample solutions placed in the cell with an active volume of 0.988 mL. Injection time intervals were chosen to guarantee equilibrium conditions before each subsequent addition. The reaction mixture in the sample cell was stirred at 250 rpm during the titration. The reference cell was always filled with ultrapure water. All solutions were stirred and degassed under vacuum for about 15 min before each run. Measurements were run in the overfilled mode.[267] At least three titrations were carried out per system.

Quercetin-metal(II) complexes: ITC titrations for the study of the interaction of Que with metal ions were carried out by titrating a solution of the flavonoid (0.08-0.15 mM) with Cu(II) (0.50-0.60 mM), Zn(II) (1.30-1.50 mM) or Co(II) (0.50–0.60 mM) solutions.

Quercetin-poly(acrylic acid) interactions: The interactions occurring between poly (acrylic acid) and the flavonoid were investigated by titrating a polymer solution (3.50-9.00 mM) into Que solutions (0.12-0.15 mM) and different polymer/quercetin ratios were explored.

Poly(acrylic acid)-metal(II) complexes: Metal(II)–polymer complex formation was investigated by titrating a solution of metal(II) (2.50–3.50 mM) into PAA solutions (0.25–0.50 mM).

Quercetin-metal(II)-polymer assemblies: For the copper-based assembly, calorimetric titrations were conducted by titrating a solution of PAA (11.5-12.0 mM) into the copper-quercetin complex (Cu(II):Que 1:1, C_{Que} = 0.10 mM); for the other two assemblies, a solution of Zn(II)- or Co(II)-polymer complex (M(II):PAA 1:3, C_{PAA} = 9.00 mM) was titrated into the flavonoid solution (0.12-0.15 mM).

Heats of dilution were determined in separate "blank" experiments by titrating the proper titrant solution into the buffer solution (pH 7.4, MOPS 10 mM). In all experiments, the % (*v*/*v*) of DMSO in the syringe and the cell was the same to avoid heat effects caused by solvent dilution. The power curve was integrated by NanoAnalyze (TA Instruments) to obtain the gross heat of the reaction. The calorimeter was calibrated chemically by a test HCl/TRIS reaction according to the procedure described.[268] The instrument was also checked by electrical calibration. The net heats of the reaction, obtained by subtracting the heat evolved/absorbed in the blank experiments, were analyzed using HypCal software, which enables the determination of both equilibrium constants and enthalpies of complex formation through a non-linear least-squares minimization of the calorimetric data obtained from different titrations.[269]

3.4 Quartz-crystal microbalance with dissipation monitoring (QCM-D) experiments

Quartz crystal microbalance with dissipation monitoring (QCM-D) is an interface-specific technique based on changes in frequency and energy dissipation of a gold-coated quartz crystal upon material adsorption, which is recorded at multiple overtones of the crystal fundamental resonance frequency. This parameter is sensitive to the mass of the adsorbed film and its viscoelastic properties.[270,271] At certain conditions, the use of the microbalance is based on the linear relationship between changes in the resonator mass and the resonance frequency according to the Sauerbrey equation:

$$\Delta m = -C * \frac{\Delta f}{n} \qquad \textit{Equation 6}$$

where Δm is the mass area change (in ng/cm^2), C is the mass sensitivity of the gold-coated sensor (17.7 ng cm^{-2} Hz^{-1} at the oscillation frequency of 5 MHz), and *n* is the overtone number.[254] This relationship could be used only in the case of a rigid layer for which changes in the normalized frequency $\Delta f/n$ do not exhibit a significant dependence on the harmonic number. [251,270,272,273]

QCM-D measurements were performed using a QSense E1 instrument (Biolin Scientific, Sweden) in a flow-through cell equipped with a precise temperature controller, which contained a sensor crystal, and was connected to a peristaltic pump that forced the solution through the chamber. The sensor crystals were gold-coated AT-cut quartz with gold-plated polished electrodes (QSX 301, Biolin Scientific, Sweden). All the instrument modules were connected to a computer that monitored the different signals (resonance, oscillation frequency, and temperature). All measurements were carried out at 25 °C and a flow rate of 50 µL/min. Before each experiment, the crystals were thoroughly cleaned according to the QSense cleaning protocol (sequential treatment with ozone for 10 min, a mixture of Milli-Q water/NH_4OH/H_2O_2 = 5:1:1 at 75 °C for 5 min, rinsing with Milli-Q water, drying with a nitrogen flux, and final ozone treatment for 10 min).

Quercetin-cobalt(II)-polymer assembly formation and release studies at controlled pH: Each measurement started recording the baseline while flowing a MOPS 10 mM, pH 7.4 solution. The polymer-metal complex, prepared by properly mixing cobalt(II) and PAA at 1:3 molar ratio (C_{PAA} = 9.00 mM), was then adsorbed on the sensor crystal surface; a washing step using the same buffer solution was later performed to remove any loosely attached material. Afterwards, a 0.15 mM quercetin solution (in MOPS 10 mM, pH 7.4) flowed through the adsorbed film until the frequency change reached equilibrium. A washing step was then required to remove the non-adsorbed drug. Finally, a solution of MOPS 10 mM at pH 7.4, 5.4, or 4.5 flowed until constant frequency changes were recorded to assess the pH-responsiveness of the adsorbed systems. The obtained QCMD data were analyzed using the integrated Qtools software (Biolin Scientific, Sweden).

3.5 Preparation of metal(II)-based assemblies containing quercetin and poly(acrylic acid) for stability and release studies

Solutions of both quercetin-metal(II) complexes and the corresponding metal(II)-coordinated assemblies were prepared in aqueous solution (MOPS 10 mM, pH 7.4) by properly mixing the components of each system so to optimize the formation of the desired complex species ($CuQue_2$, Que_2CuPAA, ZnQue or $QueZnPAA_2$ as shown in *Supplementary materials - Chapter II, Figure S12* and *Figure S13*) according to the previously determined binding constants listed in *Table 1, Table 3* and *Table 4*. The crucial point in the preparation of the solutions was the choice of the molar ratio among quercetin, metal ions and polymer as well as the order of addition of each component to ensure the optimal formation of the desired complex.

For the preparation of the solution of quercetin-metal(II) complexes, the metal ions were added to the quercetin solution: quercetin-copper(II) complex (Cu(II):Que 1:1, $C_{Cu(II)}$= 0.15 mM); quercetin-zinc(II) complex (Zn(II):Que 2:1, $C_{Zn(II)}$ = 0.30 mM).

For the preparation of the metal(II)-coordinated assemblies, the copper(II) systems were prepared by adding PAA to the quercetin-copper(II) complex (Cu(II):Que 1:1, $C_{Cu(II)}$ = 0.15 mM) such that Cu(II):PAA is 1:33; for the zinc(II) system, quercetin was added to the zinc-polymer complex (Zn(II):PAA 1:3, $C_{Zn(II)}$ =1.40 mM) such that Zn(II):Que is 9:1.

3.6 Stability experiments on the metal(II) complexes and assemblies

UV-Vis spectra of the suitable solutions of quercetin-metal(II) complexes and metal(II)-coordinated assemblies containing quercetin were recorded every 15 minutes for 24 h at 25.0 ± 0.2 °C with an Agilent 8453 diode-array (Agilent Technologies, USA) in 1 cm path length quartz cells.

3.7 Quercetin release experiments from the metal(II)-based assemblies at controlled pH

The release of quercetin from both copper(II)- and zinc(II)-based assemblies was investigated at suitable pH values (7.4 and 5.4) by combining the dialysis method and UV-Vis spectrophotometry. The assemblies containing Que were prepared and transferred into dialysis bags (MWCO = 3.5KDa) and then immersed in 25 mL of release medium (pH 7.4 or 5.4, MOPS 10 mM) at 37.0 ± 0.2 °C and stirred at 100 rpm.

To quantify the amounts of the Que released, at selected time intervals (1 hour), 400 μL of the release medium was picked up from the solution and replaced with the same amount of fresh medium to maintain the sink conditions. The absorbance measurements of the withdrawn aliquots were performed on a Jasco V-770 UV-Vis/NIR spectrophotometer (Jasco Europe, Italy).

Chapter III:

Metal-coordinated assemblies containing methotrexate

Methotrexate efficacy is strongly affected by its poor solubility, short half-life in the bloodstream and drug resistance by targeted cells. Furthermore, the ability of the drug to inhibit key cellular functions causes a lack of selectivity toward neoplastic cells, resulting in severe side effects. To overcome these issues, the development of smart DDSs is still required. In this chapter, DDSs based on pH-responsive coordinated assembly containing methotrexate and poly(acrylic acid) are proposed to ensure the effective pH-triggered release of the chemotherapy drug in the acid tumour microenvironment rather than healthy tissues thus ameliorating its therapeutic activity. The delivery systems were rationally designed by accurately examining the species and the energetics of the multiple equilibria occurring in solution among the assembly components. The formation of the methotrexate-metal(II) complexes in the absence or presence of the pH-responsive polyacrylic acid was investigated in buffered aqueous solution at pH 7.4 using spectrophotometric (UV-Vis) and calorimetric (ITC) techniques. Both MTX and PAA are negatively charged at physiological pH and may efficiently interact through the coordination of suitable metal ions. The binding ability of MTX toward the polymer-metal complexes was also examined at the solid-liquid interface by quartz-crystal microbalance with dissipation monitoring (QCM-D). These studies provided evidence for the adsorption of MTX onto both metal(II)-polymer layers confirming their ability to interact as well as to release the drug under different pH values.

Size and surface charge and morphology of the developed MTX-based assemblies were assessed with dynamic light scattering (DLS), ζ-potential and scanning electron microscopy (SEM) experiments.

The *in vitro* cytotoxicity of the assemblies, evaluated in the U87 glioblastoma cell line, highlighted the more efficient anticancer activity of the three-component assemblies compared to the free chemotherapy drug. The role of reactive oxygen species (ROS) generation in the mechanism of cell death was investigated through flow cytometry analysis of cells treated with metal-based assemblies. The internalization of the assemblies in glioblastoma cancer cells was observed by confocal microscopy. The size, surface charge and morphology experiments as well as the *in vitro* assays on the

MTX-based assemblies were carried out during the six-month internship at the University of Basque Country (UPV/EHU) under the supervision of Dr. Aitor Larrañaga and Prof. Marcelo Calderón.

A detailed investigation of the ability of the MTX assemblies to interact with human serum albumin (HSA) in solution and at the interface was also carried out by calorimetric titrations and QCM-D experiments.

Finally, a poly-lysine-based system containing MTX was developed by examining the affinity of the drug towards the positively charged polymer and the related thermodynamic parameters at 25 °C and pH 7.4 through UV-Vis spectrophotometry, and QCM-D experiments. The pH-sensitive release of the drug from a poly-lysine-based system was also investigated.

1. RESULTS AND DISCUSSION

Similarly to what was already described for the assemblies containing quercetin, the ability of metal ions (copper(II) and zinc(II)) and poly(acrylic acid) to establish multiple non-covalent interactions was exploited to develop methotrexate-based polymeric assemblies in aqueous solution at neutral pH. To investigate the multiple equilibria occurring in solution among the constituents of the system, the binding affinities and the energetics for the complexation of M(II) with MTX and polyacrylic acid as well as for the formation of the MTX-M(II)-PAA assemblies were determined. The binding properties of the polymer towards metal(II) ions were already discussed in the previous chapter.

1.1 Methotrexate-metal(II) ions complexes

The complex formation between methotrexate and the metal ions, namely Cu(II) and Zn(II), was studied in a buffered aqueous solution (pH 7.4, MOPS 10 mM). As shown in *Figure 29*, the MTX molecule is characterized by a 2,4-diaminopteridine ring and N,N-dimethyl-p-aminobenzoic acid residue linked to glutamic acid by a peptide bond. Methotrexate has three sites that could undergo deprotonation: the carboxylic groups from the glutamic acid, α-COOH and γ-COOH (pKa values are 2.89 and 4.56, respectively) and the heterocyclic nitrogen (N1)H^+ from the pteridine ring (pKa = 5.65).[204,274-276] Consequently, at the experimental conditions employed in this study, MTX will be completely deprotonated. Typical UV-Vis titrations for the methotrexate-Cu(II) system and methotrexate-Zn(II) system are shown in *Figure 60*.

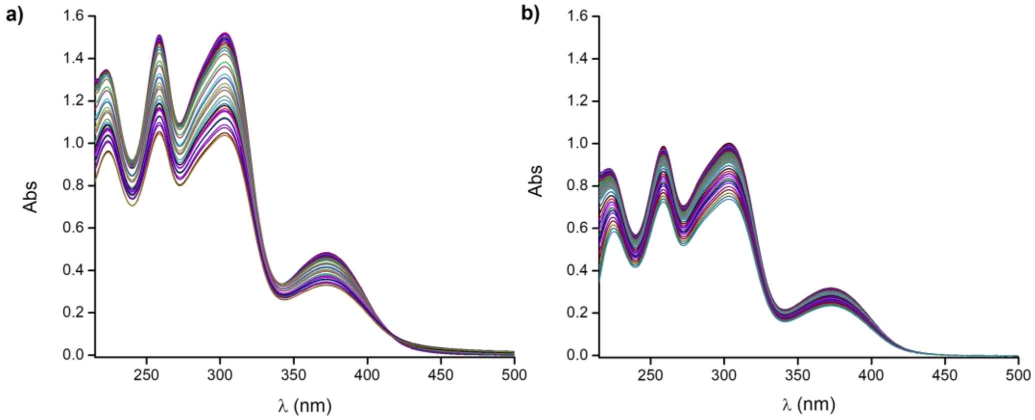

Figure 60. UV-Vis titration of *a)* Cu(II) (1.00 mM) into MTX (0.07 mM) and *b)* Zn(II) (1.00 mM) into MTX (0.04 mM) at 25 °C and pH 7.4.

The UV-Vis spectrum of MTX at pH 7.4 (MOPS, 10 mM) displays characteristic absorption bands in different regions. Based on the literature for the analogous folic acid, the bands at 258 nm, 302 nm and 372 nm can be attributed to π-π* transition due to the pterin ring and *p*-aminobenzoic acid moieties;[277] moreover, an additional band at 221 nm can be detected.

The stepwise addition of the metal ions into the MTX solution in the cell determines a decrease in the intensity of the MTX bands. However, no curvature could be observed in the molar ratio plots (regardless of the wavelength explored). This suggests that the changes recorded in the UV-Vis titrations are solely due to the dilution of the ligand upon titrant addition. However, potentiometric measurements for MTX-Cu(II) as well as the synthesis of the MTX-Zn(II) complex[216] were both reported in the literature thus demonstrating the formation/existence of the MTX-M(II) complexes. Consequently, a calorimetric investigation was performed to assess the binding properties of MTX toward the above metal ions. The net heat curves obtained when titrating the metal ion solutions into the drug showed no appreciable curvature although the heats of the reaction and those of the dilution (blank) experiments were very different to each other.

Conversely, ITC titration of an MTX solution into metal ions solutions permitted to obtain satisfactory binding isotherms despite the very low heat values recorded.

Typical ITC titrations of methotrexate into metal ion solutions and the corresponding molar ratio plots are shown in *Figure 61* and *Figure 62* for copper(II) and zinc(II), respectively. The species, binding constants and thermodynamic parameters determined for each metal ion are listed in *Table 8* and graphically represented in *Figure 63*.

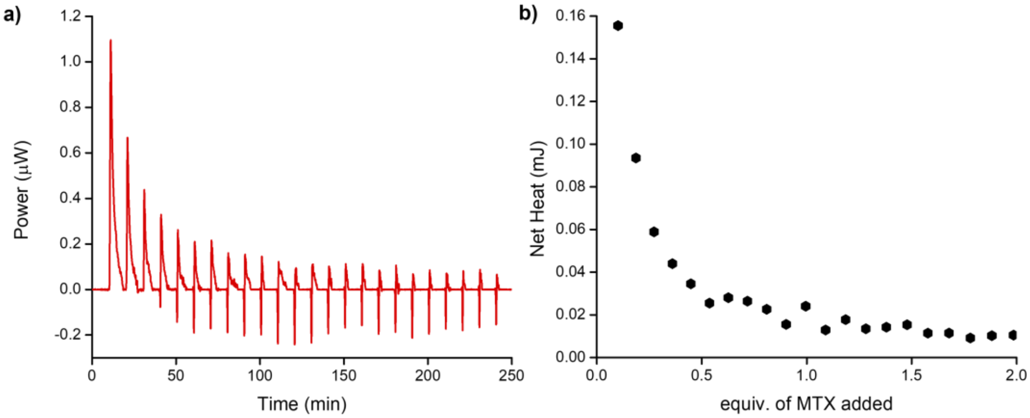

Figure 61. *a)* ITC titration of MTX (2.00 mM) into Cu(II) (0.24 mM) solution at 25 °C and pH 7.4; *b)* integrated heat data for the MTX-Cu(II) system.

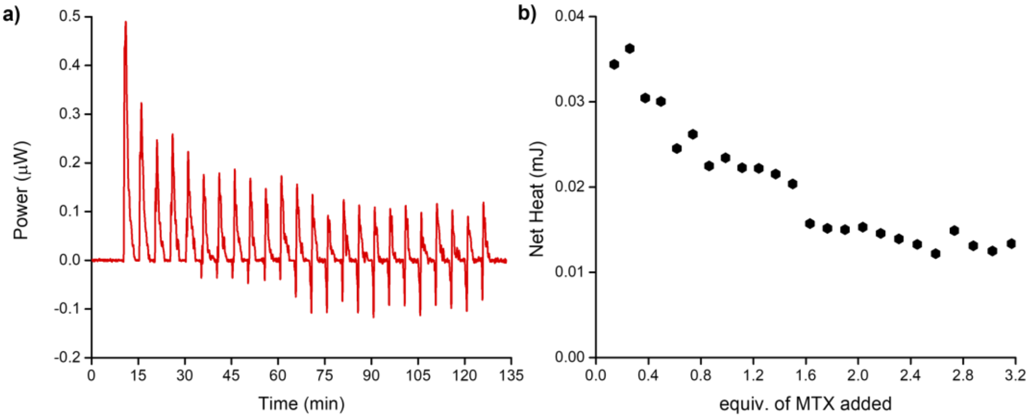

Figure 62. *a)* ITC titration of MTX (2.00 mM) into Zn(II) (0.17 mM) solution at 25 °C and pH 7.4; *b)* integrated heat data for the MTX-Zn(II) system.

Table 8. Conditional stability constant values[a,b] and thermodynamic parameters[a,b,c] for the formation of methotrexate (L) - metal (M) complexes at 25 °C and pH 7.4 (MOPS 10 mM).

Metal ion	**Species**	**Log K**	**-ΔG⁰** [c]	**ΔH⁰** [c]	**TΔS⁰** [c]
Cu(II)	ML	4.0 (2)	22.8	-3.15 (6)	19.7
Zn(II)	ML	3.01 (8)	17.18	-9.82 (5)	7.36

[a] refer to the equilibrium pM + qL ⇄ M_pL_q where charged are omitted for simplicity;
[b] σ in parenthesis; [c] in kJ mol $^{-1}$.

Methotrexate forms ML complex species with both metal ions. The stability constant of the Zn(II)-methotrexate complex is one log unit lower than that of Cu(II), in line with the classical Irving-Williams order of stability. The determined binding constant for copper-complex species is in good agreement with that calculated at pH 7.4 using the value found in the literature[204] while, to the best of our knowledge, this is the first time that the binding properties of methotrexate toward zinc(II) ion are reported. The association constant for the formation of the MTX-Cu(II) complex is quite similar to that reported for the analogous complex formed by the folic acid at the same pH (*log k = 4.78*).[278] Also, the binding constant for the MTX-Zn(II) complex is comparable to that calculated at pH 7.4 for the analogous complex formed by folic acid (*log k = 2.90*). However, it should be noted that the latter was determined by potentiometric titration in a mixed solvent (60% (w/w) DMSO/water) due to solubility issues of the ligand at the concentration used.[279]

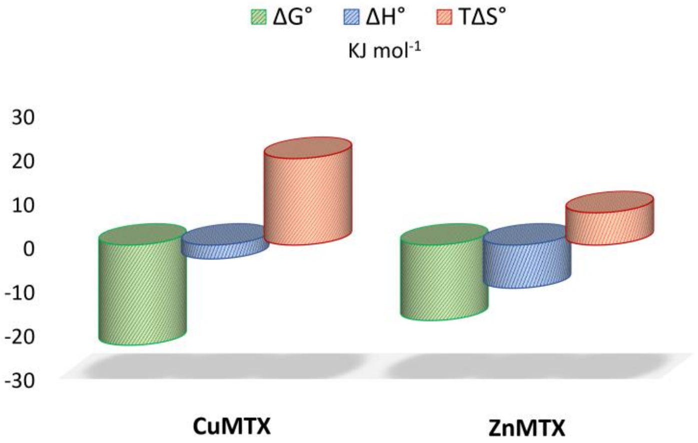

Figure 63. Thermodynamic parameters for the formation of methotrexate-metal(II) complexes at 25 °C and pH 7.4.

Although both enthalpy and entropy favour the formation of metal complexes, the main contribution to the Gibbs free energy is entropic for the copper-complex species (due to ligand and metal desolvation upon complexation) and enthalpic for the zinc one, though in the latter case the two terms are almost comparable. As these interactions do not determine changes in the position of the UV-Vis bands of the ligand upon titration, we can hypothesize that non-absorbing moieties of MTX, such as carboxyl groups, may be the functional groups involved in the complexation process. This behaviour differs from that observed for pteridines and pteridine-derivates which are able to coordinate copper through the O(4) and N(5) atoms.[280]

1.2 Methotrexate-poly(acrylic acid) interactions

To assess whether poly(acrylic acid) can interact with free MTX, both UV-Vis and ITC measurements were carried out. Typical UV-Vis titration and the corresponding molar ratio plots at 302 nm are shown in *Figure 64*. Although the addition of PAA into the MTX solution determines a decrease in the intensity of MTX bands, the molar ratio plot (regardless of the wavelength explored) indicates that these changes are due to the dilution of the ligand upon titrant addition. To confirm that the associative process does not affect the bands of the ligand and, therefore, no binding events occur, ITC titrations were performed by titrating the polymer solution into the methotrexate solution and viceversa. In both cases, the shape of the calorimetric curve and the negligible heat values recorded indicated that no detectable reaction occurred. An example of ITC titration and the related net heat *vs.* molar ratio plot is shown in *Figure 65*.

Overall, these studies proved that PAA and methotrexate are not able to interact. As already observed for quercetin, the electrostatic repulsion between the anionic moieties of the two molecules at neutral pH 7.4 prevents any form of interaction.

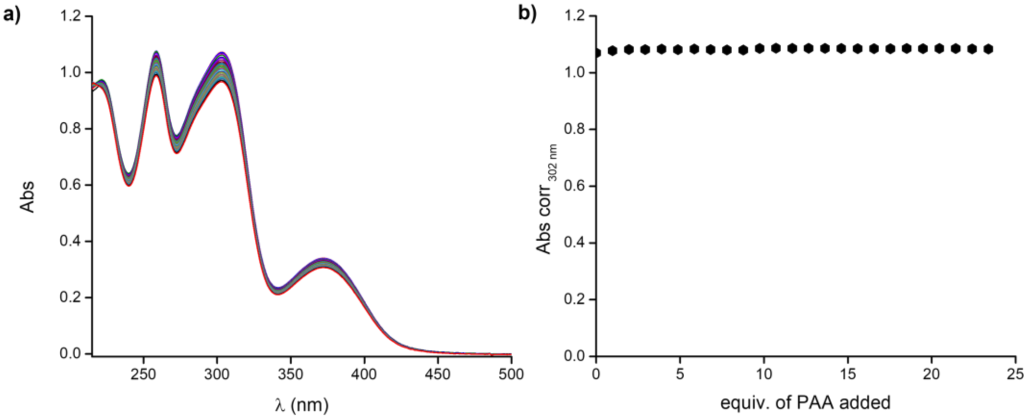

Figure 64. *a)* UV-Vis titration of PAA (9.00 mM) into MTX (0.04 mM) solution at 25 °C and pH 7.4; *b)* molar ratio plot.

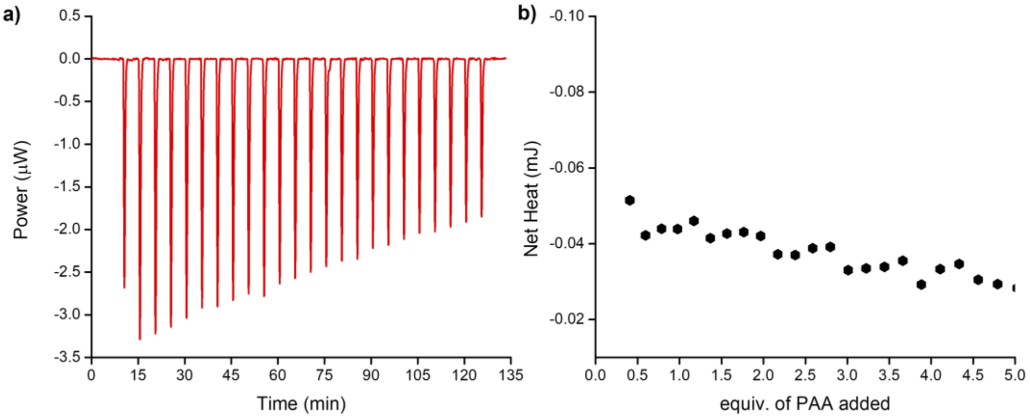

Figure 65. *a)* ITC titration of PAA (9.00 mM) into MTX (0.50 mM) solution at 25 °C and pH 7.4; *b)* integrated heat data for the PAA/MTX system.

1.3 Methotrexate-metal(II)-polymer assemblies

Taking advantage of the interactions occurring among MTX, M(II) and PAA as well as of the quantitative information on the species and binding affinities experimentally determined, metal(II)-coordinated assemblies containing methotrexate were rationally designed. Based on the metal ions affinities toward methotrexate and polyacrylic acid, the formation of the metal-coordinated assemblies containing MTX was investigated by titrating the chemotherapy drug with a metal(II)-polymer complex. These complexes were prepared in solution by mixing metal(II) ions and poly(acrylic acid) in a suitable molar ratio. Once fixed the concentration of the polymer (C_{PAA} = 9.00 mM), metal(II) ions and PAA were mixed at a 1:3, 1:10, 1:30, 1:50 metal/polymer molar ratios. As already observed for zinc(II) (*Supplementary materials - Chapter II, Figure S7a*), the use of 1:3 metal/polymer ratio ensures that $M(PAA)_2$ is the main species present in solution. Also in the case of copper(II), about 60% of the polymer is complexed with the metal ion while the remaining 40% is free (species diagram in *Supplementary materials - Chapter III, Figure S14*). Smaller metal/polymer ratios will cause the formation of a lower % of M(II)-PAA complexes and increased amounts of free polymer, which will become the main species in solution.

Typical UV-Vis titrations for the copper-based system, performed using metal/polymer solutions prepared at different molar ratios as the titrant, are shown in *Figure 66*. For the zinc-based one, the UV-Vis titration using a 1:3 M:PAA titrant solution is shown in *Figure 67*.

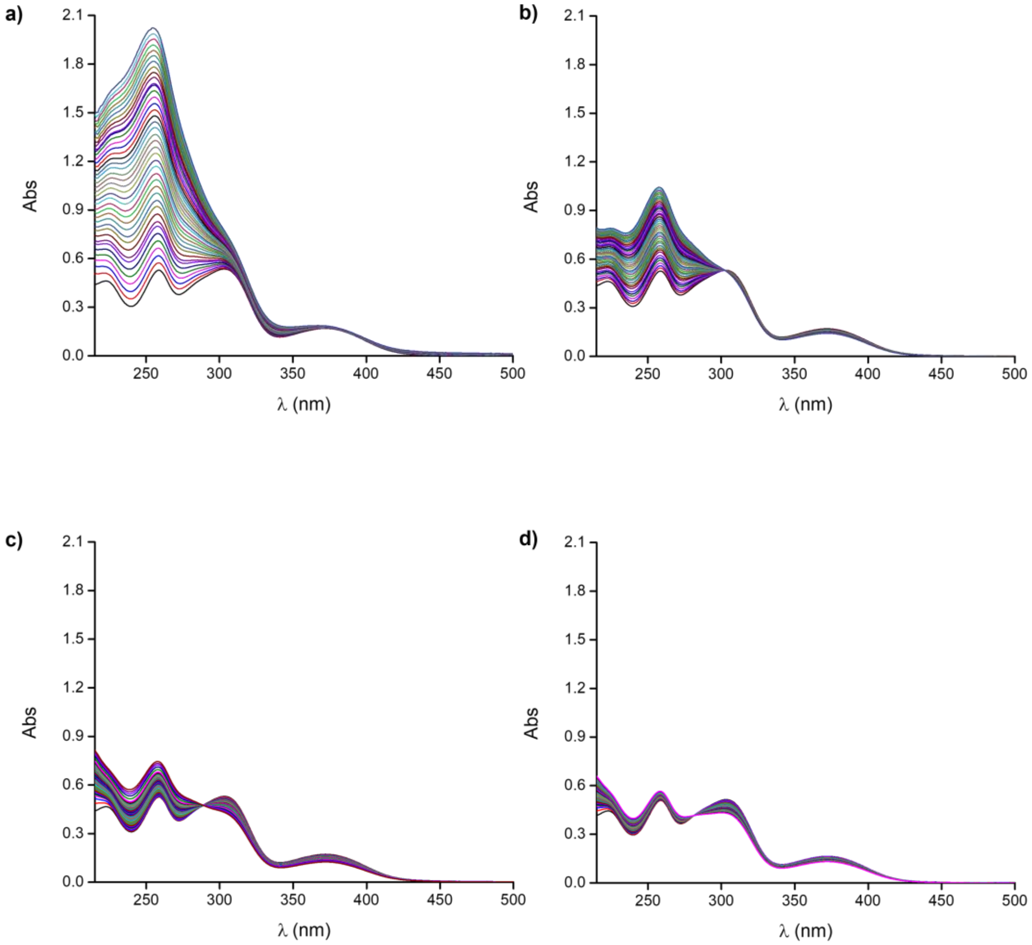

Figure 66. UV-Vis titrations of the copper-polymer complex prepared at *a)* M:PAA 1:3, *b)* M:PAA 1:10, *c)* M:PAA 1:30, and *d)* M:PAA 1:50 (C_{PAA} = 9.00 mM) into MTX (0.05 mM) solution at 25 °C and pH 7.4.

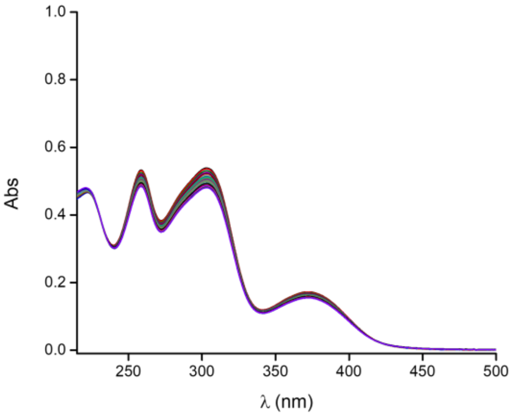

Figure 67. UV-Vis titration of the zinc-polymer complex prepared at M:PAA 1:3 (C_{PAA} = 9.00 mM) into MTX solution (0.05 mM) at 25 °C and pH 7.4.

For the copper-based system, the MTX band at 372 nm shows a gradual decrease in intensity upon the stepwise addition of the metal-polymer complex, regardless of the different metal/polymer molar ratios employed. Instead, bands at 221 nm, 258 nm and 302 nm show a hyperchromic shift. The intensity of these bands increases significantly, especially in the case of the titrant prepared at M:P 1:3 which displays a coalescence of the three bands. Despite these variations should be indicative of interaction events occurring between the polymer-metal complex species and MTX, the treatment of the spectrophotometric data did not allow to obtain a satisfactory fit.

It may be supposed that, in both the final assemblies, the coordination features of the metal ion are satisfied by the carboxyl group of the MTX molecules and the carboxyl groups of the polymer chain. Indeed, the hyperchromic shift in the MTX spectra can be attributed to the establishment of π-π interactions between neighbouring MTX molecules coordinated to the metal ions already bound to the carboxyl groups of the polymer backbone; an example of the possible coordination mode is shown in *Figure 68*. As already reported in the literature, heterocyclic aromatic molecules structurally related to MTX (e.g. purines and pyrimidines) undergo a self-association process and, in the case of folates, these compounds usually form dimers.[281-283] Moreover, MTX could aggregate depending on the concentration and pH[276] and both pteridine and paminobenzoate rings may participate in stacking interactions in a head-to-tail arrangement.[204]

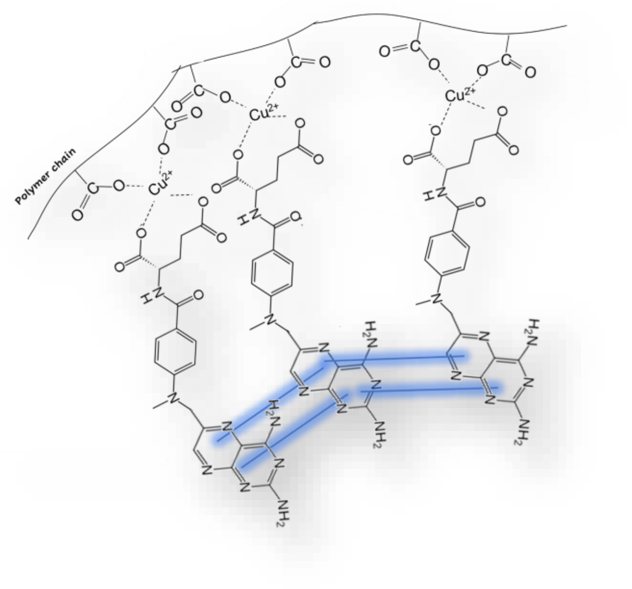

Figure 68. Sketch of a possible arrangement of the copper-coordinated assembly enhancing the π-π interactions between neighbouring MTX molecules bound to the polymer chain.

A smaller hyperchromic shift is observed when the titrant solutions are prepared with different metal/polymer ratios. In these cases, the number of linking sites of the polymer-metal complex to MTX will be smaller, MTX molecules will be much farther from each other and π-π interactions will be reduced/less effective. This evidence highlights the importance of the metal ion in the preparation of these systems as it is responsible for the number of MTX units that could be incorporated into the delivery system.

The same evidence is not observed for the zinc-containing system. In this case, the addition of the metal-polymer complex solution does not cause any variation in the MTX absorption spectrum (*Figure 67*), regardless of the metal/polymer molar ratio employed. Thus, the decrease in the intensity of the MTX bands could be due to the dilution of the ligand upon titrant addition or to the non-absorbing functional groups of MTX yet involved in the interaction events.

Calorimetric titrations were then performed to quantitatively examine the equilibria between MTX and copper(II)-polymer complex and to prove if the drug molecule can bind the zinc(II)-polymer complex. Typical ITC titrations are shown in *Figure 69*. For the analysis of the data, all possible equilibria involving the system components (e.g., metal-MTX and metal-polymer complex formation) were considered in the model. The interaction of the metal(II)-polymer complex with methotrexate led to the formation of the $LM(PAA)_2$ species (L = MTX, M = Cu(II) or Zn(II)). The determined binding affinity and thermodynamic parameters which refer to *Equation 7* (charges are omitted for simplicity) are shown in *Table 9* and graphically represented in *Figure 70* (the parameters for the ML species are also reported for comparison):

$$qL + M_pPAA_r \rightleftarrows L_qM_pPAA_r \qquad \textit{Equation 7}$$

.

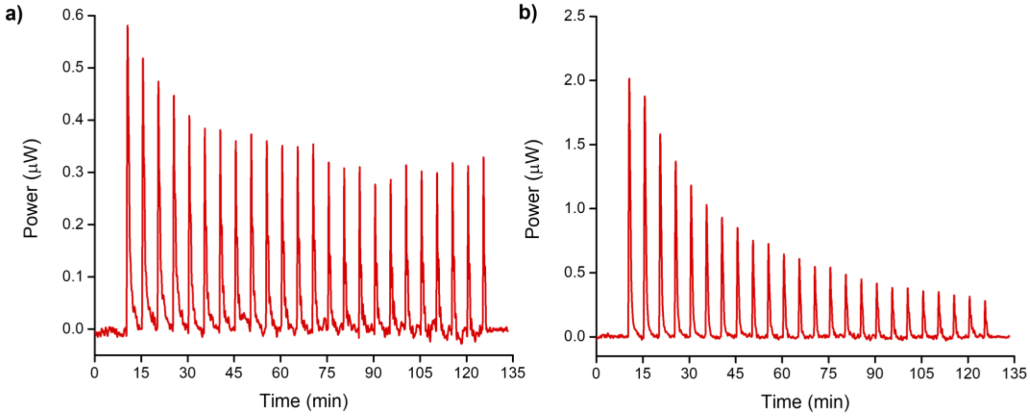

Figure 69. ITC titration of *a)* $CuPAA_2$ (M:PAA 1:3, C_{PAA} = 9.00 mM) and *b)* $ZnPAA_2$ (M:PAA 1:3, C_{PAA} = 9.00 mM) into MTX (0.50 mM) solution at 25 °C and pH 7.4.

Table 9. Conditional stability constant values[a] and thermodynamic parameters[a,b] for the formation of metal(II)-coordinated assemblies containing methotrexate at 25 °C and pH 7.4 (MOPS 10 mM).

Metal ion	**Species**	**Log K**	**$-\Delta G^0$**	**ΔH^0**	**$T\Delta S^0$**
Cu(II)	$ML(PAA)_2$	3.19 (1)	-18.21	3.84 (3)	22.05
Zn(II)	$ML(PAA)_2$	3.0 (1)	-17.1	-3.82 (6)	13.3

[a] σ in parenthesis; [b] in kJ mol $^{-1}$.

Both copper and zinc polymer-metal complexes form with MTX a complex species with similar binding affinity. Although it can be hypothesized that the MTX molecules are coordinated by the metal ions already bound to the polymer chain, in the case of Cu(II) the binding event occurs with a lower affinity than that previously determined for the formation of the binary ML species.

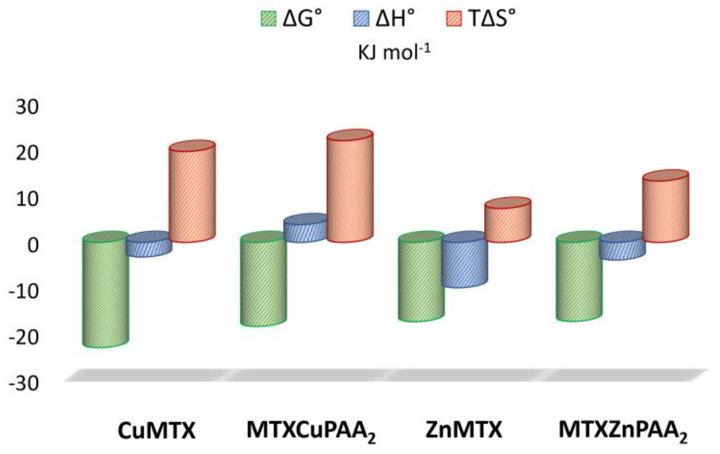

Figure 70. Thermodynamic parameters for the formation of metal(II)-methotrexate complexes and metal-coordinated assemblies at 25 °C and pH 7.4.

For both systems, the assembly formation is entropically favoured and driven due to the desolvation of the drug and the metal-polymer complexes. The zinc-based system also shows a slightly favourable enthalpic contribution. The binding of MTX to the metal-polymer backbone causes a drop in the enthalpy contribution with respect to that of the ML complex, which becomes even unfavourable in the case of the system containing copper. This could be due to the higher enthalpy cost of desolvation for the assembly formation than in the case of ML complex species.

1.4 Metal-coordinated assemblies formation at the interface and drug release at controlled pH

The formation of the metal-coordinated assemblies was also studied at the solid-liquid interface by quartz-crystal microbalance with dissipation monitoring (QCM-D). Specifically, the changes in frequency and dissipation recorded over time provide evidence for the adsorption of MTX onto polymer-metal layers confirming their ability to interact (as already observed in solution) and allowed to determine the mass (ng/cm^2) of the drug absorbed into the polymeric layer. *Figure 71* and *Figure 72* show the changes of frequency (ΔF) and dissipation (ΔD) in a typical QCM-D experiment for the copper(II) and zinc(II)-based systems, respectively; for simplicity, only data relating to the third overtone ($\Delta f_3/3$ and ΔD_3) are reported.

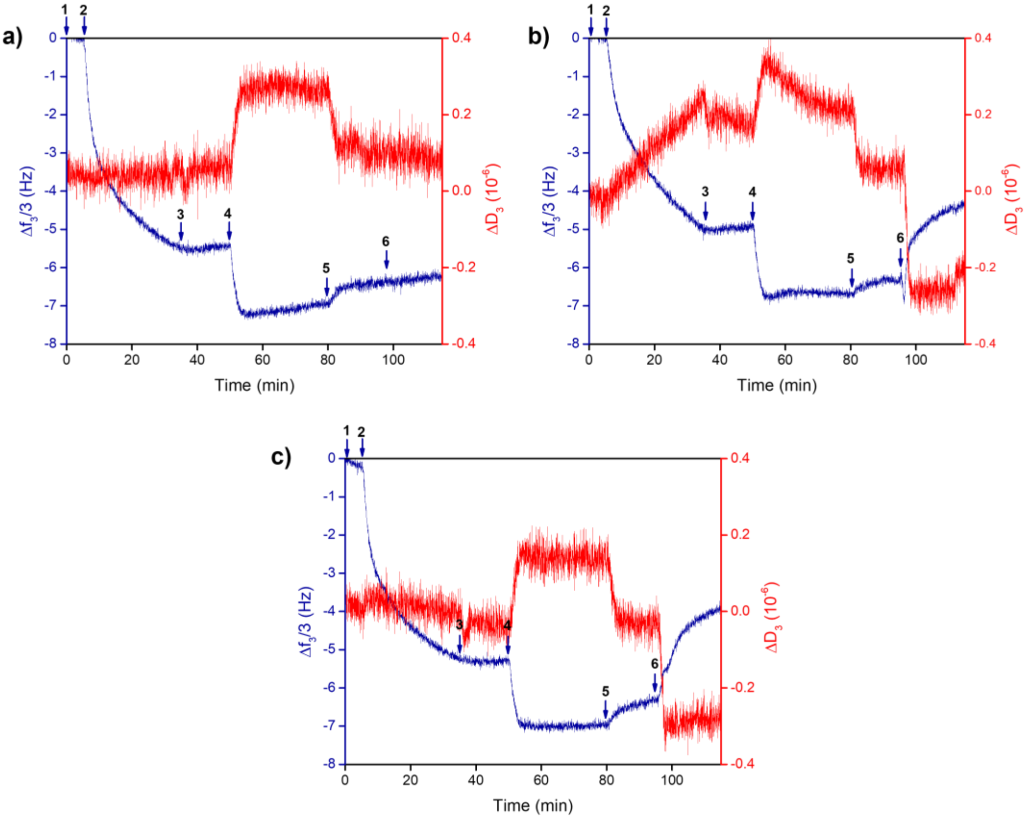

Figure 71. Normalized frequency $\Delta F_n/n$ (blue) and dissipation ΔD_n (red) change (for simplicity, only data referring to the third overtone are shown, n = 3) for the adsorption of the copper(II)-polymer layer onto a gold-coated quartz crystal and subsequent loading and release of methotrexate at 25 °C. 1) Baseline: 10 mM MOPS at pH 7.4; 2) adsorption of the copper(II)-polymer system (M:PAA 1:3, C_{PAA}= 9.00 mM in 10 mM MOPS at pH 7.4; 3) rinsing with 10 mM MOPS at pH 7.4; 4) uptake of methotrexate from its solution (C_{MTX} = 2.20 mM) in 10 mM MOPS at pH 7.4; 5) rinsing with 10 mM MOPS at pH 7.4; 6) rising with 10 mM MOPS at *a)* pH 7.4, *b)* pH 5.4 and *c)* pH 4.5.

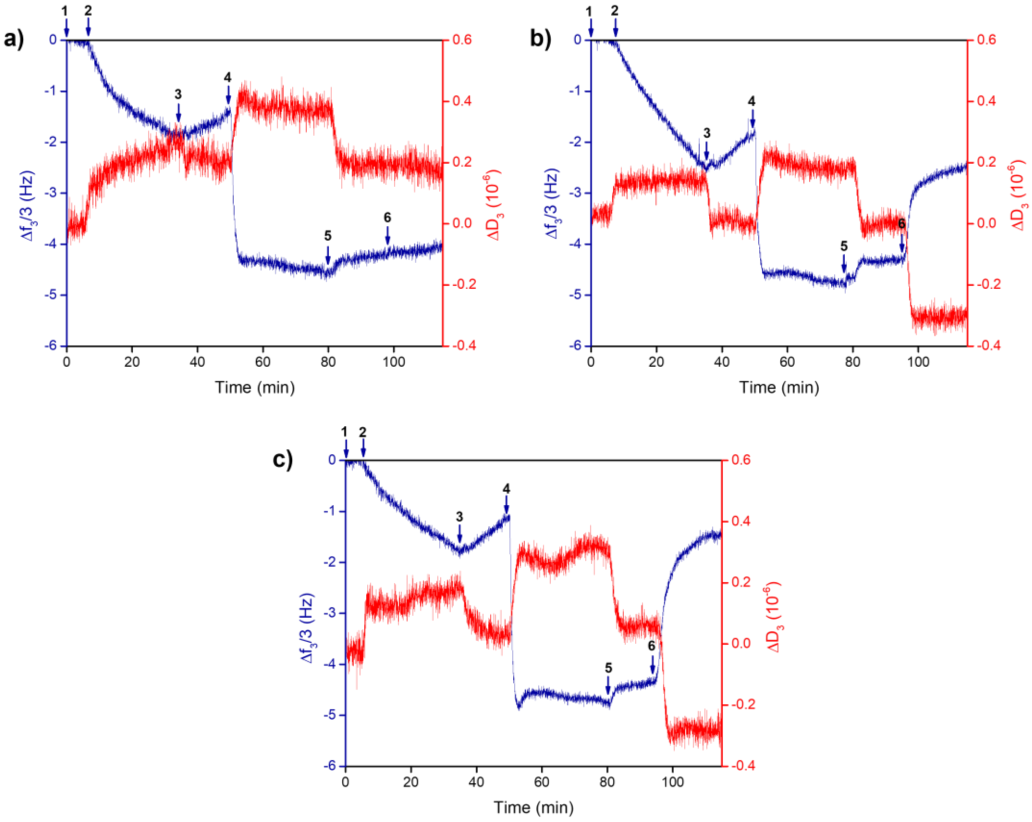

Figure 72. Normalized frequency $\Delta F_n/n$ (blue) and dissipation ΔD_n (red) change (for simplicity, only data referring to the third overtone are shown, n = 3) for the adsorption of the zinc(II)-polymer layer onto a gold-coated quartz crystal and subsequent loading and release of methotrexate at 25 °C. 1) Baseline: 10 mM MOPS at pH 7.4; 2) adsorption of the zinc(II)-polymer system (M:PAA 1:3, C_{PAA}= 9.00 mM in 10 mM MOPS at pH 7.4; 3) rinsing with 10 mM MOPS at pH 7.4; 4) uptake of methotrexate from its solution (C_{MTX} = 2.20 mM) in 10 mM MOPS at pH 7.4; 5) rinsing with 10 mM MOPS at pH 7.4; 6) rising with 10 mM MOPS at *a)* pH 7.4, *b)* pH 5.4 and *c)* pH 4.5.

Similarly to what observed for $Co(PAA)_2$, the adsorption of both $Cu(PAA)_2$ or $Zn(PAA)_2$ to the gold-sensor surface at pH 7.4 determine a decrease in frequency and negligible dissipation energy changes which account for the rigidity of the adsorbed polymeric layers (*step 2*). The entrapment of the MTX onto the adsorbed metal-polymer layer thanks to hydrophobic interactions and/or through the binding of metal ions, induces a further decrease in frequency (*step 4*). The subsequent rinsing step to remove the non-absorbed drug (*step 5*) determines only a small increase in the frequency shifts indicating that most of the drug is retained by the polymer layer. The flowing of either neutral or acidic solutions upon the assembly thus formed onto the sensor surface allows to investigate the release of the therapeutic agent upon pH change. When a neutral solution is flown, no further significant frequency variations are observed (*step 6a*). Conversely, the flowing of an acidic solution at pH 5.4 or 4.5 (*step 6b or 6c*), which are conditions chosen to simulate the tumour microenvironment, produces a large increase in frequency up to values similar to those observed after the removal of the non-adsorbed polymer-metal layer (*step 3*). The pH decrease is expected to disrupt the coordination bonds established between methotrexate and metal ions in the assembly.

The plots of the adsorbed mass, calculated according to the Sauerbrey equation, are shown in *Figure 73*. The drug loading into the $M(PAA)_2$ layer as well as its subsequent release are summarized in *Table 10*. Noticeably, a greater amount of MTX binds to the zinc(II)-polymer layer if compared to the copper-based one. The amount of MTX released by both assemblies in neutral conditions is quite small (from 6 to 12% of the adsorbed MTX for the zinc and copper systems, respectively). Instead, under acidic conditions, the adsorbed MTX is released quantitatively in the case of the Cu(II)-based assembly, while only about 12-22% of the adsorbed MTX remains bound to the zinc(II)-polymer layer. Overall, these results prove that the developed systems can successfully respond to changes in pH thus allowing a controlled and almost complete release of the loaded drug.

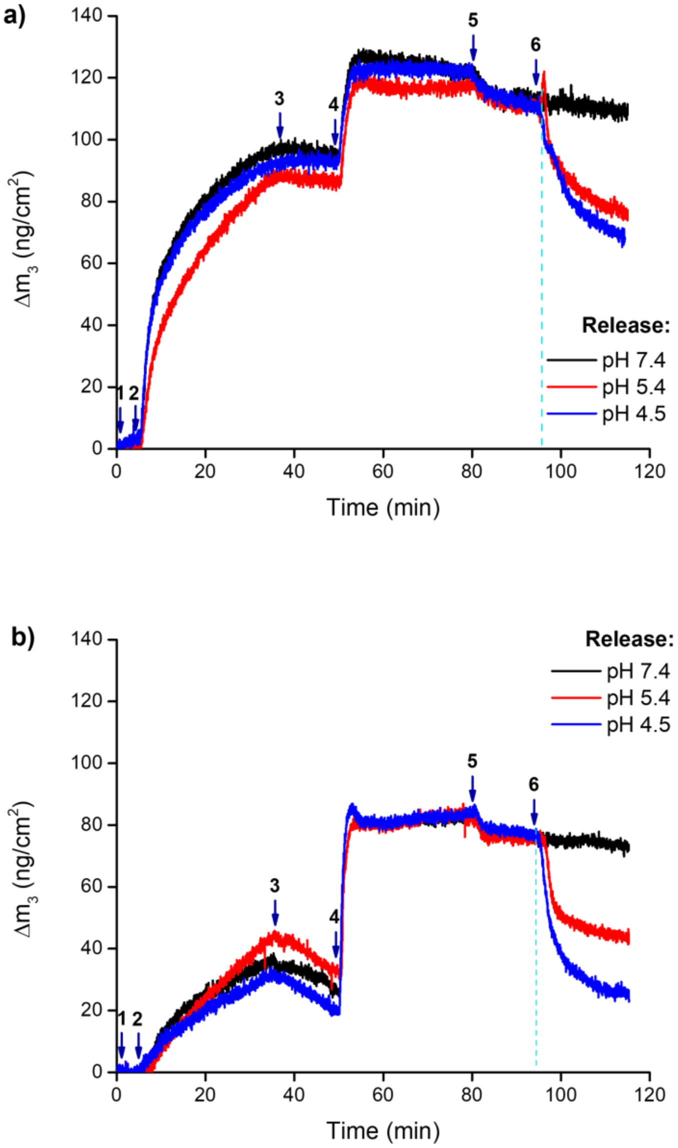

Figure 73. Mass changes (Δm) for the adsorption of *a)* copper(II)- and *b)* zinc(II)-coordinated assembly onto a gold-coated quartz crystal and subsequent loading and release of methotrexate at 25 °C. The conditions for each flowing step are described in the caption of *Figure 71* and *Figure 72*, respectively.

Table 10. Adsorbed mass of methotrexate onto the metal(II)-polymer layer and % of methotrexate released at different pH values at 25 °C.

	CuPAA$_2$ layer			
	MTX loaded	**% MTX released**		
		pH 7.4	**pH 5.4**	**pH 4.5**
Adsorbed mass (ng/cm^2)	20 ± 3	12 %	100 %	100 %

	ZnPAA$_2$ layer			
	MTX loaded	**% MTX released**		
		pH 7.4	**pH 5.4**	**pH 4.5**
Adsorbed mass (ng/cm^2)	50 ± 12	6 %	78 %	88 %

The time dependency of the mass changes for the binding and unbinding processes was analyzed by using *Equation 3* and *Equation 4* of *Chapter II* to obtain the binding and the dissociation rate constants (k_{on} and k_{off}) as well as the association constant (K_{ass}) at the solid-liquid interface.

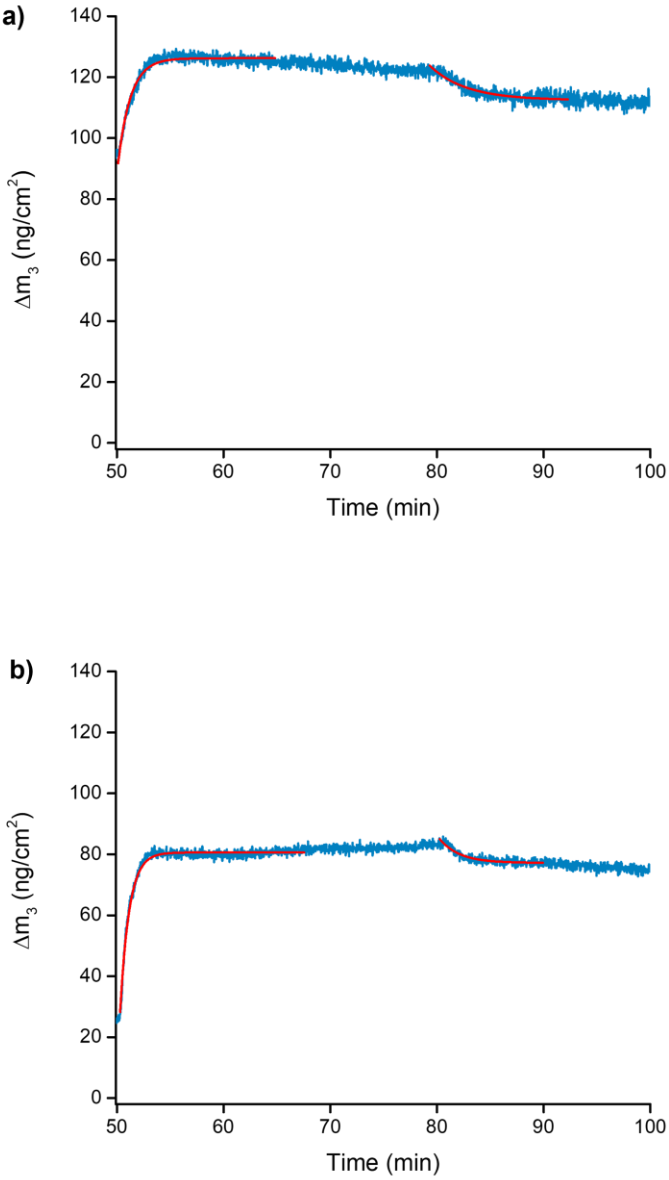

Figure 74. Curve fitting of the adsorption and desorption profiles of MTX from *a)* copper(II)- and *b)* zinc(II)-polymer layer. The curves are a magnification of *step 4* and *step 5* of the mass changes plot in *Figure 73*; the experimental curves are in cyan while the calculated ones are in red.

Typical kinetic fits for the adsorption and desorption process using the above-mentioned equation are shown in *Figure 74.* For the copper-based assembly, the kinetic constants are k_{on} = 278 ± 3 M^{-1} min^{-1} and k_{off} = 0.24 ± 0.04 min^{-1}. Using these rate constants, a K_{ass} value of 1158 ± 3 M^{-1} was calculated which corresponds to a *log* K_{ass} value of 3.064 (1). For the zinc-based assembly, k_{on} = 358 ± 8 M^{-1} min^{-1}, k_{off} = 0.6 ± 0.1 min^{-1} and K_{ass} = 587 ± 8 M^{-1} (*log* K_{ass} = 2.769 (6)). The association constant values obtained from the kinetic analysis of the experiments performed at the solid-liquid interface are in satisfactory agreement with those determined for the analogous processes in solution.

1.5 Physico-chemical and morphological characterization of the metal-coordinated assemblies

The size distribution and the surface charge of the developed metal-coordinated assemblies were investigated through dynamic light scattering (DLS) and ζ-potential measurements. The systems were suitably prepared by suitably mixing PAA, metal ion and MTX to optimize the formation of the assemblies as described in the *Experimental section, Preparation of the metal coordinated assemblies*. Two concentrations of MTX (0.40 mM and 1.00 mM) were chosen to understand if the different amounts of loaded drug could somehow affect the physico-chemical properties of the assemblies. The hydrodynamic diameters and the ζ-potential values determined for each system are listed in *Table 11*.

In particular, DLS results indicated that the hydrodynamic diameters of copper(II)-based metal-coordinated assemblies range between 100 nm and 123 nm with a relatively narrow size distribution as shown in *Figure 75.* The polydispersity index (PDI) values indicate that the assemblies can be considered as monodisperse systems. The same features are observed for the zinc(II)-based systems which show hydrodynamic diameters ranging between 100 nm and 135 nm. The intensity-based distribution is in *Figure 76.*

Table 11. Intensity-based DLS and ζ-potential data of metal-coordinated assemblies at 25 °C and pH 7.4.

Assembly	Size (nm)	Polydispersity index	ζ-potential (mV)
$MTXCuPAA_2$ MTX 0.40 mM	123 ± 3	0.17 ± 0.03	-21.7 ± 0.5
$MTXCuPAA_2$ MTX 1.00 mM	100 ± 2	0.18 ± 0.01	-16.4 ± 0.2
$CuPAA_2$	116 ± 1	0.148 ± 0.007	-23 ± 1
$MTXZnPAA_2$ MTX 0.40 mM	135 ± 5	0.16 ± 0.01	-18.2 ± 0.4
$MTXZnPAA_2$ MTX 1.00 mM	98.4 ± 0.7	0.24 ± 0.01	-17.2 ± 0.4
$ZnPAA_2$	115 ± 4	0.205 ± 0.009	-17.6 ± 0.4

The results obtained from the DLS measurements provide further confirmation of the formation of these polymeric assemblies. Indeed, the presence of the presence of metal ions and the drug determines a decrease in the diameter of the uncomplexed polymer (260.9 ± 0.99 nm) which shows a greater polydispersity (PDI = 0.363 ± 0.001). This evidence could be associated do the “partial” neutralization of negative charges of the carboxyl groups of the polymer chain which enables the polymer to rearrange its structure from an extended shape (due to the electrostatic repulsion between the negative charges of its functionalities) to a coiled conformation. For both copper(II)- and zinc(II)-based systems, the addition of MTX induces an interesting change in the dimensions of the metal-polymer scaffold: in the assemblies with a lower MTX concentration, the hydrodynamic diameter of the $M(PAA)_2$ system increases of about 15 nm whilst the addition of a higher concentration of MTX determines a decrease (about 15 nm) of the $M(PAA)_2$ size. Apparently, the presence of a larger amount of drug favours a more "shrunk" conformation which is certainly desirable to "protect" the drug from the surrounding environment.

The ζ-potential indicated the nature of the surface charge. All the assemblies are negatively charged with ζ values ranging between -16 mV and -23 mV.

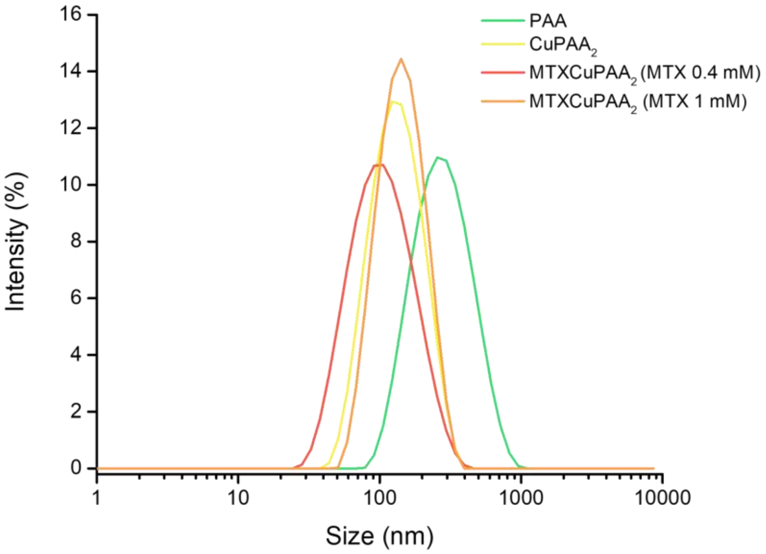

Figure 75. Intensity-based hydrodynamic diameter distribution of the copper(II)-based metal-coordinated assemblies at 25 °C and pH 7.4 (MOPS, 10 mM).

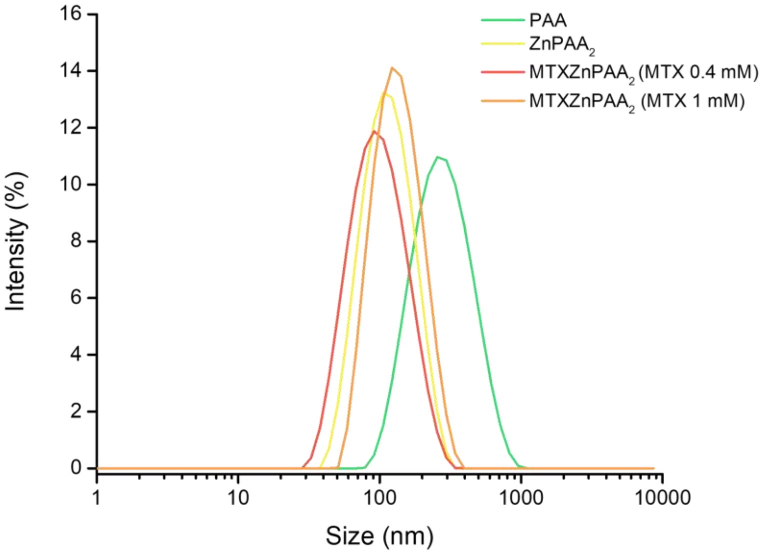

Figure 76. Intensity-based hydrodynamic diameter distribution of the zinc(II)-based metal-coordinated assemblies at 25 °C and pH 7.4 (MOPS, 10 mM).

The morphology of nanoparticles is important in biodistribution, targeting drugs to various organs and circulation time. Moreover, it is widely reported that particles with diameters less than 200 nm have a high potential for drug delivery purposes since they have enhanced permeability and retention effect (EPR) necessary for effective drug release. The morphology was investigated through SEM experiments: the obtained micrographs (*Figure 77-Figure 79*) show that metal-coordinated assemblies are spherical particles with smooth surfaces and suitable nanometer sizes. The mean diameters of the metal-coordinated assemblies were determined by analyzing SEM micrographs using the ImageJ software; the size graphs are shown in *Supplementary materials* - *Chapter III*. Copper(II)-based metal coordinated assemblies have a mean diameter of 111 ± 19 nm (in the case of MTX 0.4 mM) and 73 ± 25 nm (in the case of MTX 1 mM). For the zinc(II)-based systems, mean diameters of 120 ± 25 nm and 125 ± 18 were determined. The presence of a different metal does not seem to influence the morphology and size of these systems.

It was widely reported that variations in the size of nanoparticles between SEM and DLS analysis may occur. Indeed, the diameter of particles in the aqueous dispersion state in the DLS analysis might be larger than that of the dried state in the SEM analysis or, in the latter case, the surface of particles may collapse during the imaging process in the dry state, resulting in a decreased size. However, in both metal-based assemblies containing MTX, no significative differences can be detected.

For the Cu(II)PAA$_2$ and Zn(II)PAA$_2$ some interesting differences can be noticed. The copper (II)-polymer system shows a mean diameter of 14 ± 2 nm and zinc(II)-polymer has a diameter of 12 ± 2 nm. These values significantly differ from those determined in solution and the differences found can be related to the desolvation effect. Since the binding of MTX to metal(II)-polymer complexes is driven by the desolvation of both reacting systems, the metal(II)-polymer systems need to "remove" some water molecules to accommodate the drug. The presence of the drug or water molecules will strongly affect the hydrodynamic dimensions of the systems: as the assemblies containing MTX will not have a huge amount of water molecules in the hydration sphere, they will not "change" their dimension due to the drying phenomenon. Instead, the metal(II)-polymer systems in the dry state will lose their hydration sphere thus reducing their dimensions.

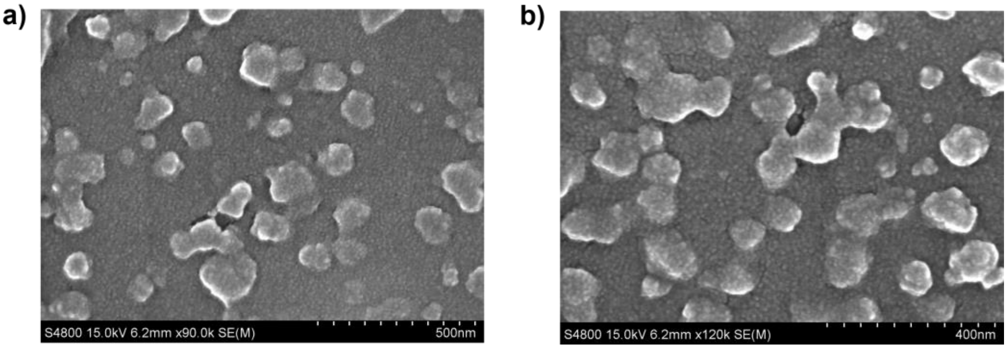

Figure 77. SEM micrographs of *a)* MTXCu(II)PAA$_2$ with MTX 0.40 mM system, scale bar 500 nm and *b)* MTXCu(II)PAA$_2$ with MTX 1.00 mM system, scale bar 400 nm.

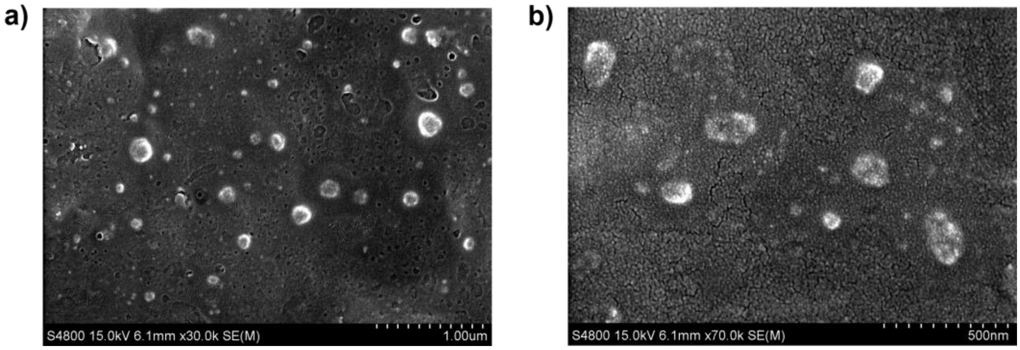

Figure 78. SEM micrographs of *a)* MTXZn(II)PAA$_2$ with MTX 0.40 mM system, scale bar 1.00 μm and *b)* MTXZn(II)PAA$_2$ with MTX 1.00 mM system, scale bar 500 nm.

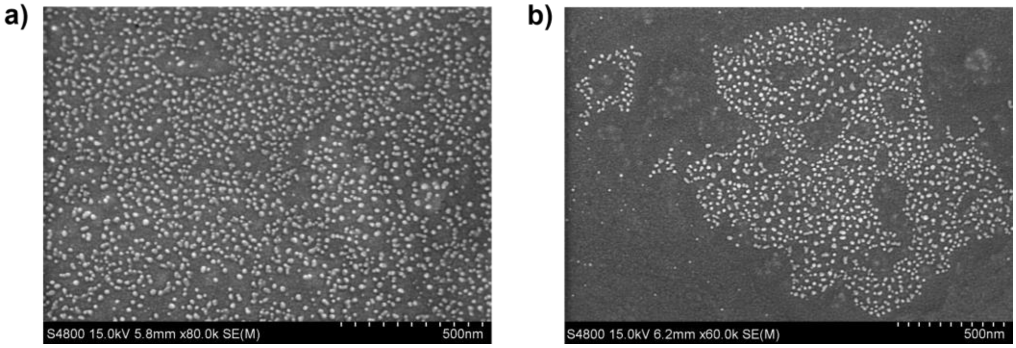

Figure 79. SEM micrographs of *a)* Cu(II)PAA$_2$ and *b)* Zn(II)PAA$_2$ system, scale bar 500 nm.

1.6 In vitro cellular studies

The therapeutic efficacy of the developed metal-coordinated assemblies was assessed in the U87 glioblastoma cell line after 48 h of treatment using the AlamarBlue assay. Cells were treated with varying concentrations of metal-coordinated assemblies (MTX concentration present in the assemblies was 1.1 – 44.0 μM, the concentration of PAA ranged from 9.9 to 396.0 μM, the concentration of Cu(II) and Zn(II) ranged from 12.24 to 489.72 μM and from 11.7 to 467.3 μM, respectively). Cells without metal-coordinated assemblies were used as a control. For reference, the cytotoxic activity of free uncomplexed MTX, M(II)PAA_2 systems as well as polymer and metal(II) ions alone were tested separately.

In the case of the copper(II)-coordinated assemblies, a decrease in the cell viability can be observed at a very low concentration of MTX after two days of incubation (*Figure 80*).

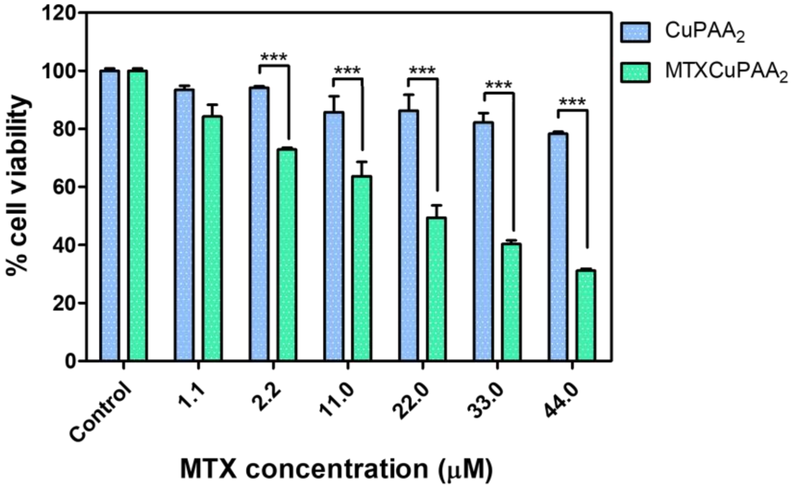

Figure 80. Viability of U87 cells treated for 48 hours with the copper(II)-coordinated assembly in the presence or absence of MTX. *** indicate significant differences ($p < 0.001$) with respect to the copper(II)-polymer scaffold.

If compared to the results obtained for the Cu(II)PAA$_2$ alone, the decrease of the cell viability is significative ($p < 0.001$) at 2.2 μM of MTX; indeed, at the highest concentration of metal-polymer system employed, about 80 % of U87 cells remained viable. Similarly, cells treated with free PAA and free Cu(II) ions at the highest concentration of 396.0 and 489.72 μM have a viability of about 85% and 82%, respectively (*Supplementary materials - Chapter III, Figure S18* and *Figure S19*).

The cell viability for the zinc(II)-based assemblies is shown in *Figure 81*. Again, the assembly containing methotrexate shows a decrease in cell viability at low MTX concentrations. This effect is significative ($p < 0.001$) already at a concentration of MTX 2.2 μM with respect to the simple metal-polymer scaffold. Cells treated with free Zn(II) ions show a viability of 65% at the highest concentration of metal used (467.3 μM) (*Supplementary materials - Chapter III, Figure S20*).

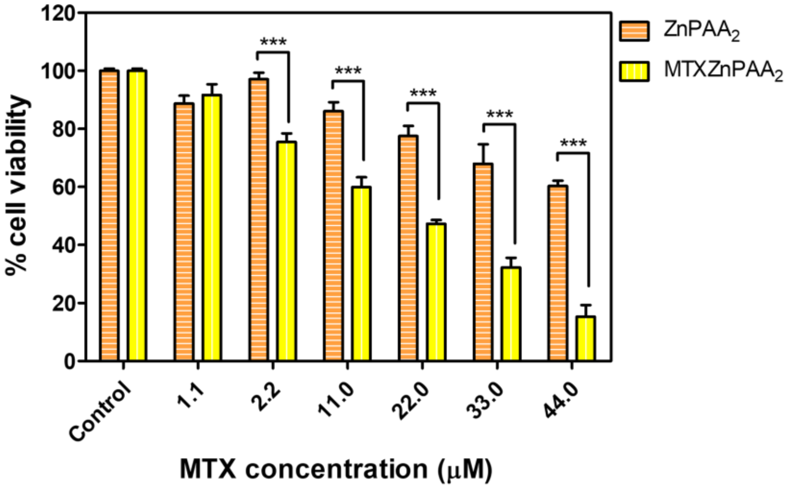

Figure 81. Viability of U87 cells treated for 48 hours with the zinc(II)-coordinated assemblies in the presence or the absence of MTX. *** indicate significant differences ($p < 0.001$) with respect to the zinc(II)-polymer scaffold.

IC_{50} values of 25.03 ± 1.21 μM and 21.16 ± 0.55 μM were determined for MTX when incorporated into copper(II)- and zinc(II)-coordinated assemblies. These results are quite interesting if compared to the effect of the free drug. Cells treated with MTX alone at the very high concentration of 1100 μM (the largest that can be achieved in aqueous solution) have a viability of 77.66% (*Figure 82*). Metal-coordinated assemblies exhibit an increased activity for U87 cells thus enhancing the drug efficacy.

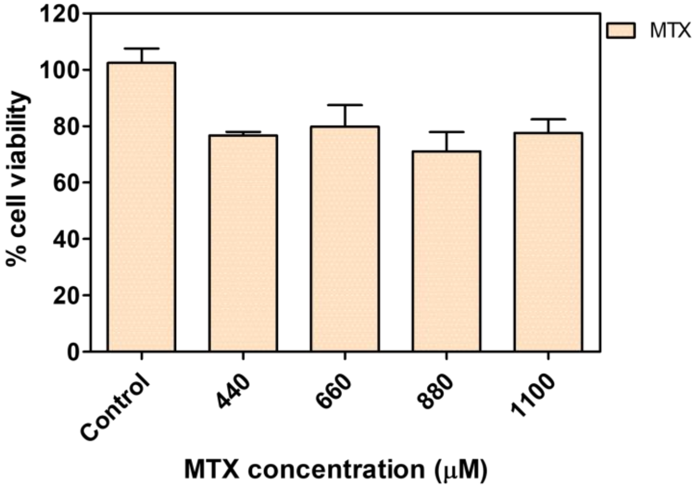

Figure 82. Viability of U87 cells treated with MTX for 48 hours.

FACS-based analysis of the metal-coordinated assemblies (with and without MTX) treated samples was carried out to understand possible mechanisms causing cell death. Cells treated with only MTX and untreated were used as controls. The production of the reactive oxygen species (ROS) was measured using cell-permeable 2',7-dichlorodihydrofluorescin diacetate (DCFH-DA) chemiluminescent probes to measure the redox state of the cell. The nonfluorescent DCFH-DA is de-esterified intracellularly and oxidized to the highly fluorescent (green) 2',7'-dichlorofluorescein (DCF) in the presence of ROS. In the cells treated with metal-coordinated assemblies containing MTX, the fluorescence intensity was found to be shifted (with respect to the cell treated with only the drug or the metal(II)-polymers) thus emphasizing intracellular ROS production upon treatment as shown in *Figure 83*.

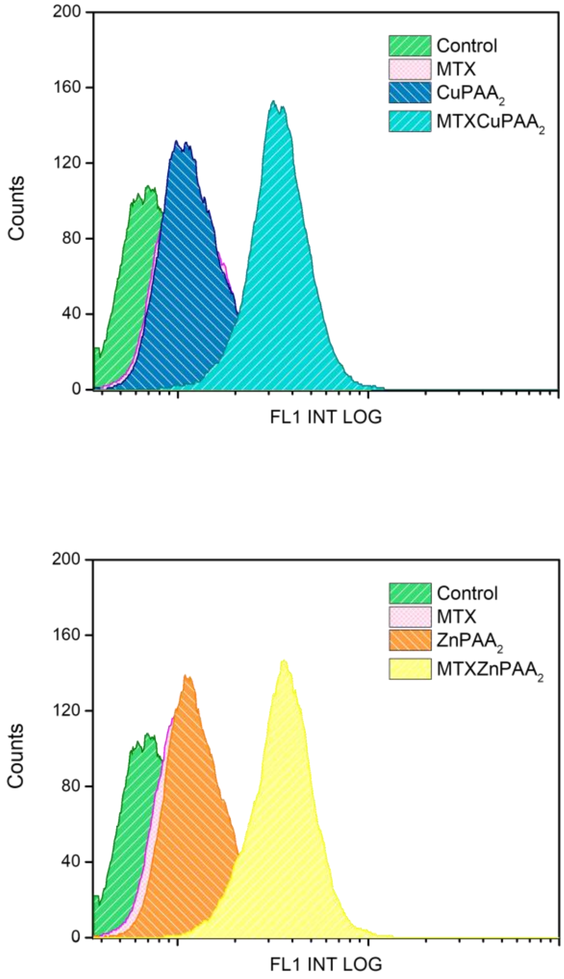

Figure 83. ROS generation of treated cells with copper(II)- *(top)* and zinc(II)-based *(bottom)* assemblies; ROS generation of cells treated with only MTX and untreated cells is also reported in both graphs.

To determine the uptake and distribution of the metal-coordinated assemblies containing MTX in the cellular microenvironment, the developed systems were observed under the confocal microscope after 3 and 12 hours of incubation by exploiting the emission of MTX-based systems (due to the presence of MTX) in the blue region *(Supplementary materials - Chapter III, Figure S21)*. Although the metal-coordinated assemblies are negatively charged (as much as the cellular membrane), they are internalized and mainly localized around the nuclei (*Figure 84* and *Figure 85*).

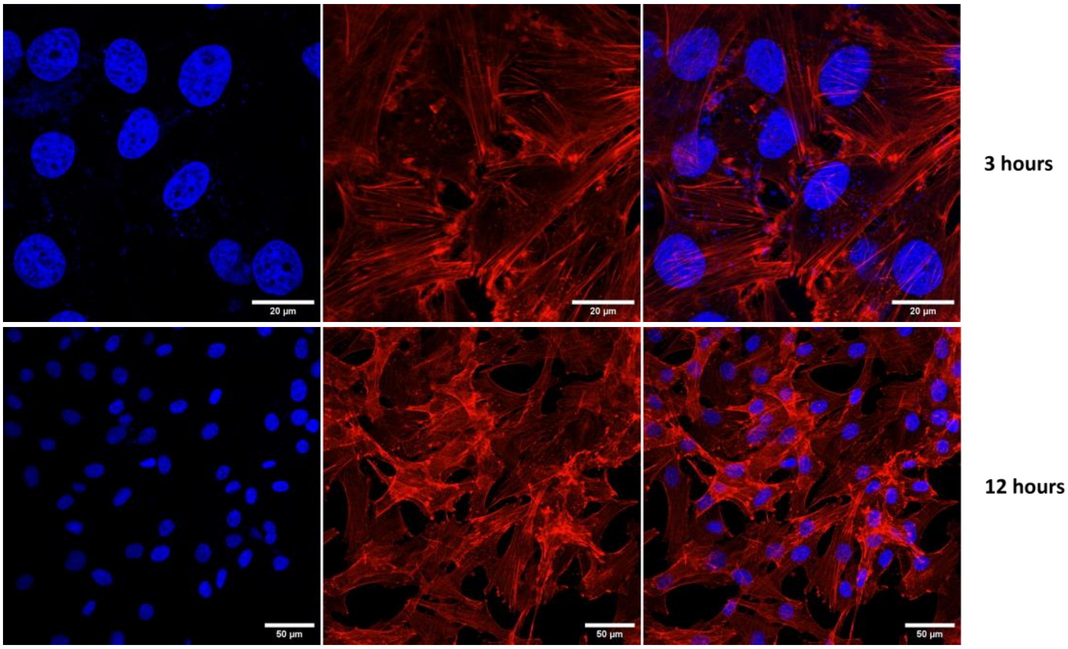

Figure 84. Confocal images of U87 cells incubated with copper(II)-based assembly containing MTX for 3 hours (MTX 44.0 µM, scale bare 20 µm) and 12 hours (MTX 22.0 µM, scale bare 50 µm); Nuclei-DAPI: blue; Cytoplasm-Rhodamine/Phalloidin: red; metal(II)-coordinated assembly: blue.

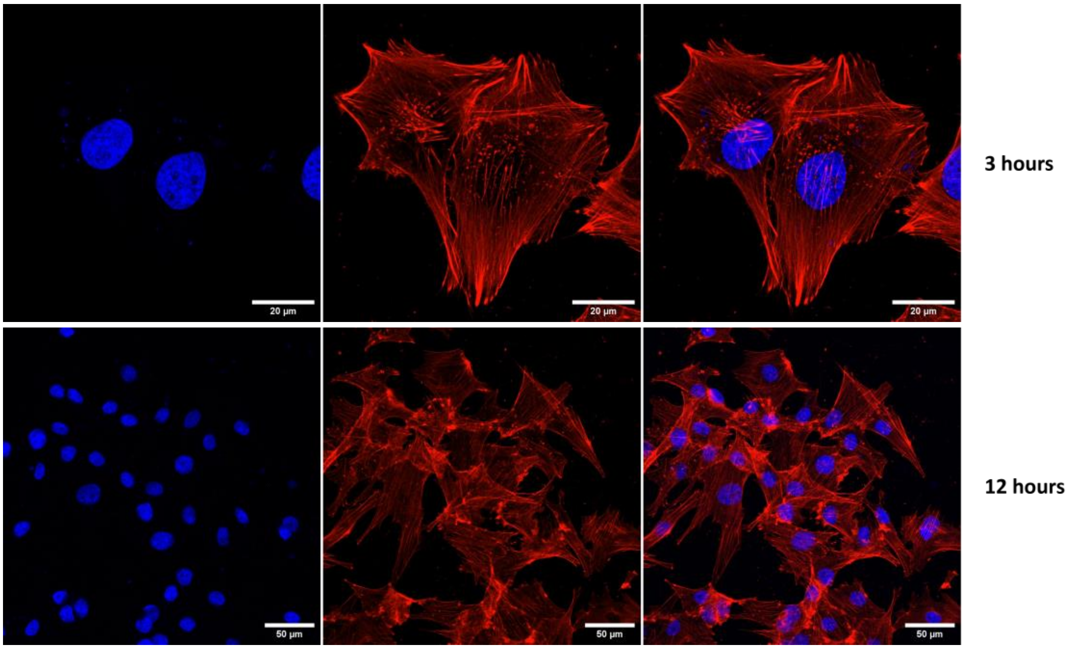

Figure 85. Confocal images of U87 cells incubated with zinc(II)-based assembly containing MTX for 3 hours (MTX 22.0 µM, scale bare 20 µm) and 12 hours (MTX 11.0 µM, scale bare 50 µm); Nuclei-DAPI: blue; Cytoplasm-Rhodamine/Phalloidin: red; metal(II)-coordinated assembly: blue.

As the emission of both DAPI and metal(II)-based assemblies occurs in the same wavelength range, further investigations (using a mounting media without DAPI to stain the nuclei of the cells) are needed to confirm cellular uptake and localization.

1.7 Interactions of methotrexate and metal-coordinated assemblies with human serum albumin (HSA)

It is well-known that the bioavailability, biodistribution and metabolism of drug molecules can be strongly affected by protein-ligand (small molecule) interactions in the bloodstream, which can also affect the stability and toxicity of the drugs. Indeed, ligands can bind serum albumin with a high affinity determining the formation of a stable protein-drug complex which may influence the bioavailability and efficacy of the drug *in vivo*. [284,285]

Also, the employment of nanocarriers can be a great challenge in clinical applications due to the difficulty in regulating/tuning the interactions of the transport systems with biological molecules. Upon entrance into the biological environment (e.g. plasma), the surface of the carriers will be rapidly covered by sets of blood plasma proteins forming the so-called "protein corona".[286,287] A typical protein corona in human plasma consists of proteins such as serum albumin (SA), immunoglobulins (Ig), fibrinogen (FIB) and apolipoproteins (Apo).[288] Serum albumin and fibrinogen may interact with the carrier surface at short times but they will be subsequently displaced by less abundant proteins having higher affinity and slower kinetics (Vroman effect).[289] The formation of the protein corona could greatly influence the in vivo biodistribution and cellular uptake of the systems of interest and it may also cover the targets thus hindering their specific reaction with ligands. Consequently, the knowledge of the affinities and the thermodynamic fingerprint of the interactions of the nanocarriers with plasma proteins is of paramount importance.[290] To this aim, the binding of the metal-coordinated assemblies (using methotrexate as control) with human serum albumin (HSA) was investigated in solution through calorimetric measurements.

The ability of HSA to bind MTX was studied through many analytical techniques in the past years[291-296] and the binding mechanisms were examined in terms of conformational aspects and affinity parameters. Few literature reports reported a thermodynamic analysis of the binding processes through the application of the Van't Hoff equation to fluorescence data, which may have limitations in the detection of the binding sites as well as of the interaction events which involve protein regions far away from tryptophan residue (used for the fluorescence measurements).[284] There is still indeed a lack of knowledge about the energetics of the MTX-protein interactions in solution.

Typical ITC titrations are shown in *Figure 86*; the determined binding affinities and thermodynamic parameters are listed in *Table 12*.

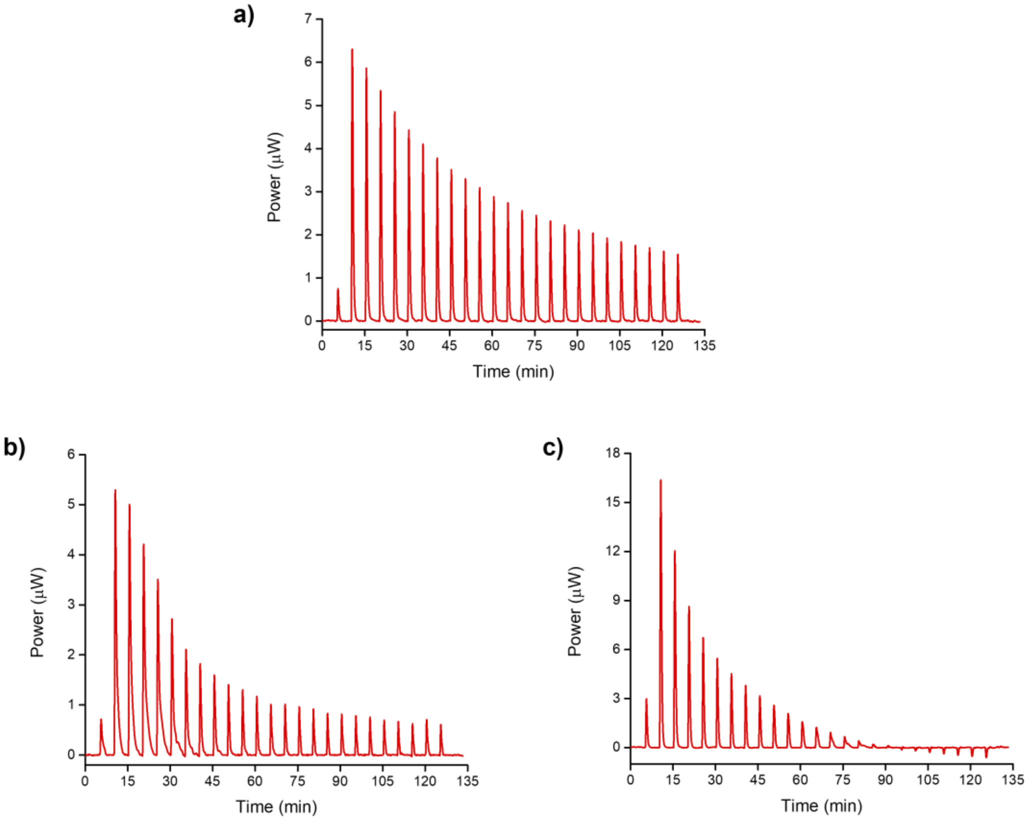

Figure 86. ITC titration of *a)* MTX (2.25 mM) into HSA (0.07 mM), *b)* MTXCuPAA$_2$ (0.38 mM) into HSA (0.015 mM) and *c)* MTXZnPAA$_2$ (0.33 mM) into HSA (0.06 mM) solutions at 25 °C and pH 7.4; integrated heat data are shown in *Supplementary materials - Chapter III, Figure S22*.

The binding process occurring in solution between small molecules, drugs or nanocarriers and biomolecules, such as proteins, may occur thanks to different interactions (hydrogen bonds, van der Waals forces, and hydrophobic and electrostatic interactions). The establishment of the different types of interactive forces is strictly related to the structural properties of the two interacting systems.[296,297]

Table 12. Conditional stability constant values[a] and thermodynamic parameters[a,b] for the interaction of either free methotrexate or the metal-coordinated assemblies with human serum albumin at 25 °C and pH 7.4 (MOPS 10 mM).

Complex	**Log K**	**-ΔG^0**	**ΔH^0**	**$T\Delta S^0$**
MTX-HSA	3.16 (5)	-18.04	-96.56 (3)	-78.52
MTXCuPAA$_2$-HSA	4.79 (1)	-27.34	-100.55 (1)	-73.21
MTXZnPAA$_2$-HSA	5.4 (1)	-30.8	-72.2 (2)	-41.4

[a] σ in parenthesis; [b] in kJ mol $^{-1}$.

Although it has been reported that the main regions for MTX binding to HSA are located in the hydrophobic site I (subdomain IIA) and site II (subdomain IIIA) respectively,[291] ITC data indicate only one possible binding site. The determined binding constant is in line with those previously reported which range from 10^3 to 10^5 M^{-1}. Analogously, ITC data on the metal-coordinated assemblies confirmed the formation of a simple 1:1 binding adduct. It is worth noting that the affinity of HSA towards the metal(II)-based assembly increases by 1.6 log units in the case of copper(II) and 2.2 log units in the case of zinc(II) if compared to the uncomplexed drug. A thorough analysis of the thermodynamic parameters, graphically represented in *Figure 87*, enables to unveil the forces contributing to the higher stability of the assembly-protein complexes.

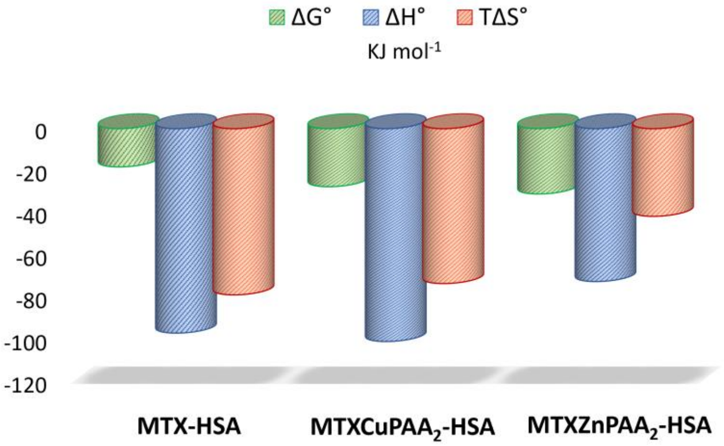

Figure 87. Thermodynamic parameters for the interaction of methotrexate or metal-coordinated assemblies containing methotrexate with human serum albumin at 25 °C and pH 7.4.

The interactions of HSA with MTX and its metal-based assemblies is a spontaneous process as indicated by the negative ΔG^0 values. In all cases, the binding reaction occurs through an enthalpically favoured and driven process while the entropy term is always unfavoured indicating a loss of degree of freedom of the protein structure (it becomes more rigid) upon the interaction events.

A detailed inspection of methotrexate and HSA structural features could help in the understanding of the binding events.[284] MTX contains both hydrophilic hydroxyl- and amino-groups and hydrophobic side chains that can interact with the amino- and the hydroxyl group of the serum protein. The formation of strong hydrogen bonding results in the rearrangement of the polypeptide carbonyl hydrogen bonding network. Moreover, at pH 7.4, MTX has both positively charged amine groups and negatively charged carboxyl groups and is expected to bind at a site enclosing both positive and negatively charged residues of the protein. Lastly, hydrophobic interactions between the aromatic moieties of the methotrexate and the hydrophobic pockets (subdomains) of the protein could occur, as reported for the analogous folic acid.[298]

The strong exothermicity observed for the binding reactions suggests that the formation of hydrogen bonds between the aminoacid residues of HSA and MTX along with electrostatic interactions are the predominant forces that contribute to the stability of the complexes. The formation of hydrogen bonds involving both sites (pocket I and II) of the protein was previously reported by molecular docking studies which revealed the presence of a larger number of hydrogen bonds in site I; this suggests the stronger binding activity of pocket I towards methotrexate.[296]

In the case of the metal-coordinated assemblies, the great enthalpic mark could be ascribable to the electrostatic interactions occurring between the negatively charged systems and positively charged amine groups of the protein as well as hydrogen bond formation and van der Waals forces.[299-301] The increase in the affinity of HSA towards the Zn(II)-coordinated assemblies is accompanied by a less favourable enthalpy and a less unfavourable entropy contribution. This suggests that the interaction with the zinc(II)-based system determines a lower rigidity of the protein structure (compared to the copper(II)-based system) or greater conformational variations (which generally contribute to the entropy changes) of the protein or the assembly. The second hypothesis seems to be more acceptable and can be supported by a careful comparison of the titrations of the zinc(II)-based assembly with HSA (*Figure 86*c) and with a buffer solution only (*Figure 88*). The last part of the titration curve of $MTXZnPAA_2$ into HSA solution cannot be attributed *tout-court* to the simple dilution process; the endothermic heat recorded in the last part of the thermogram in *Figure 86*c indicates a further event occurring in the calorimetric cell that could be likely ascribed to the conformational changes of the protein/assembly.

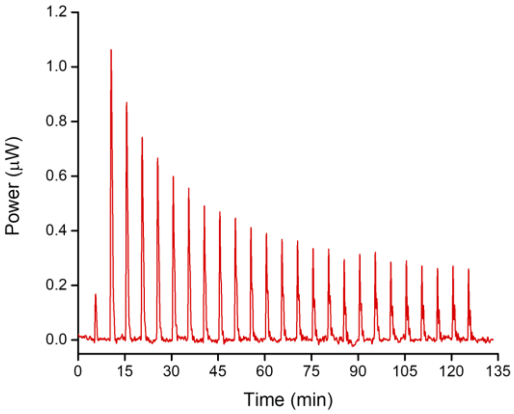

Figure 88. ITC titration of $MTXZnPAA_2$ (0.33 mM) into MOPS 10 mM pH 7.4 at 25 °C.

The interactions of MTX and the metal(II)-based systems were also investigated at the interface through the QCM-D technique.[302] Small molecule-protein, as well as nanoparticle-protein binding processes, were broadly explored in real-time by QCM-D studies.[303-305] Representative time-resolved QCM-D measurement parameters shifts are presented in *Figure 89*, revealing the characteristic frequency (ΔF) and dissipation (ΔD) profiles as a result of the interactions between the protein and MTX or copper(II) and zinc(II)-based system. After a stable baseline was acquired, the flowing of the HSA solution (*step 2*) determined a rapid decrease in frequency and a modest increase in energy dissipation, followed by much more gradual changes of ΔF and ΔD until steady states were reached. The changes in frequency and dissipation indicate the adsorption of HSA onto the gold-sensor surface.[306]

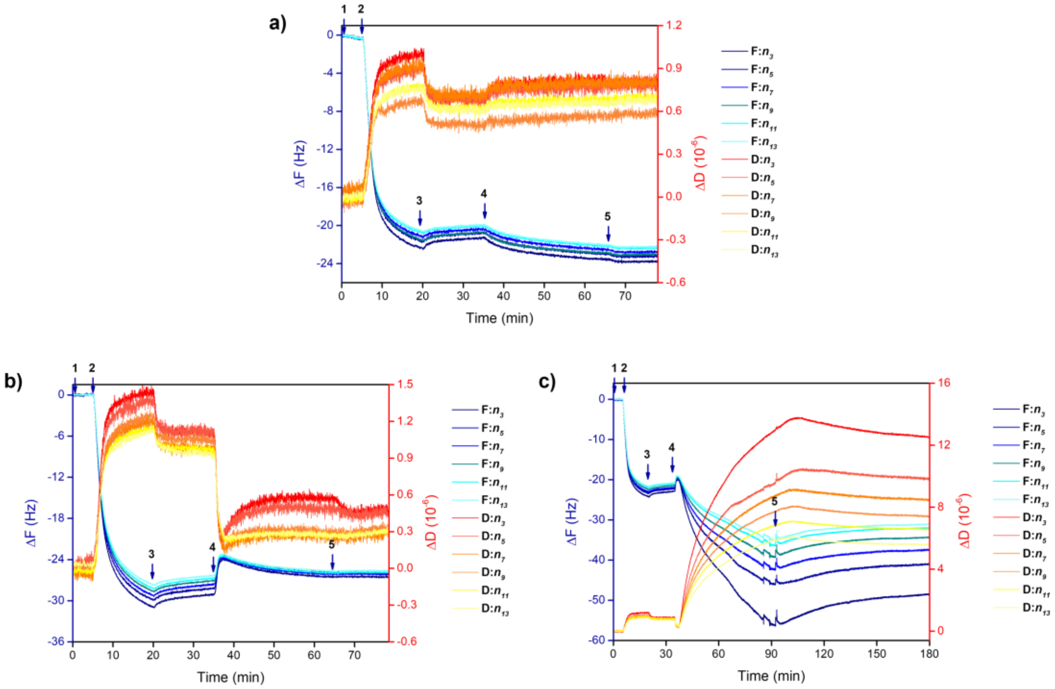

Figure 89. Frequency ΔF (blue scale) and dissipation ΔD (red scale) changes for the adsorption HSA onto a gold-coated quartz crystal and subsequent interaction with *a)* MTX, *b)* copper(II)-based assembly containing MTX or *c)* zinc(II)-based assembly containing MTX at 25 °C. 1) Baseline: 10 mM MOPS at pH 7.4; 2) adsorption of HSA (1 mg/mL in 10 mM MOPS at pH 7.4; 3) rinsing with 10 mM MOPS at pH 7.4; 4) uptake of *a)* MTX (C_{MTX} = 2.20 mM) *b)* $MTXCuPAA_2$ (Cu(II):PAA 1:3, C_{PAA} = 9.00 mM, C_{MTX} = 1.00 mM) or *c)* $MTXZnPAA_2$ (Zn(II):PAA 1:3, C_{PAA} = 9.00 mM, C_{MTX} = 1.00 mM) in 10 mM MOPS at pH 7.4; 5) rinsing with 10 mM MOPS at pH 7.4; curves for the overtones, *n*, *3*-*13* are shown.

Serum albumin can adsorb onto a surface with different orientations, “side-on” and “end-on”, that can be distinguished by analysing the dissipation shift and thickness values. Generally, low dissipation values ($< 10^{-6}$) correspond to a “side-on” orientation that creates a more rigid film, while a single “end-on” layer implies significantly high dissipation.[307] Hence, considering the changes recorded in the energy dissipation for the investigated systems, we can assume that the protein adsorbs in a “side-on” orientation. During the subsequent rinsing (*step 3*), a smaller increase in the frequency shifts as well as a decrease in the energy dissipation was recorded indicating the removal of unbound or loosely bound protein from the sensor surface. The interaction of MTX or its metal-coordinated assemblies with the adsorbed protein layer induces a further decrease in frequency and a simultaneous increase in dissipation changes (*step 4*). It is worth to note the different behaviour of the various systems during the interaction process. In the case of the free drug or the copper(II)-based assembly, the frequency and dissipation changes due to the binding are comparable for all the overtones. This, along with the small ratio between dissipation and the frequency change values, indicates a more “rigid” structure of the interacting systems. Instead, for the zinc(II)-based assembly, a significant difference in the signal is observed at different overtones. Specifically, the frequency and dissipation variations decrease as the number of the overtones increases. This evidence accounts for the viscoelastic properties acquired by one or both the interacting systems as a result of the binding process. Moreover, for the free MTX and the copper(II)-based system, the rinsing (*step 5*) does not induce further frequency and dissipation changes indicating that the systems are stably bound to the protein layer. Instead, for the zinc(II)-based assembly, the same final rinsing step causes an increase in the frequency variations and a decrease in dissipation energy. These changes indicate the removal of the loosely bound system and can be further attributed to conformational changes of the adsorbed protein or the assembly when it is rinsed away.[302] Control experiments were performed for both metal-coordinated assemblies (*Figure 90*) to exclude that the viscoelastic properties observed for the assembly-HSA adduct could be attributable only to the adsorption of the metal-coordinated assembly onto the sensor rather than to the binding process at the interface. In *Figure 90,* the changes in frequency are comparable among the different overtones and very small energy dissipation was recorded suggesting the rigid behaviour of the adsorbing systems. Hence, the detected viscoelastic properties of the system could be ascribed to conformational changes of the protein (which tilts from a "side-on" to an "end-on" orientation) and of the zinc-coordinated assembly upon binding.

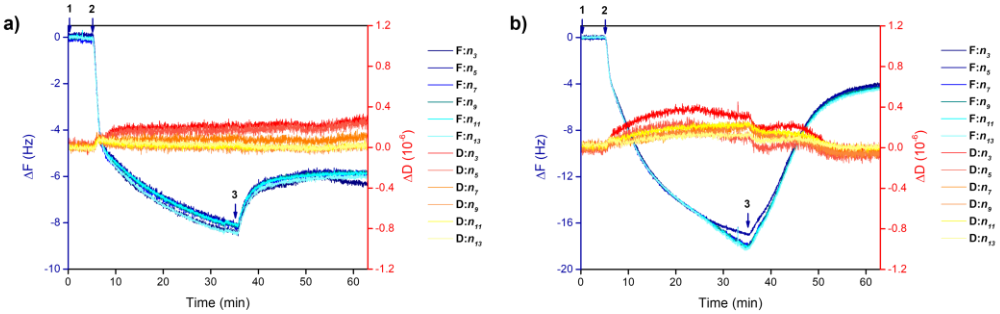

Figure 90. Frequency ΔF (blue scale) and dissipation ΔD (red scale) changes for the adsorption of metal-coordinated assemblies onto a gold-coated quartz crystal at 25 °C. 1) Baseline: 10 mM MOPS at pH 7.4; 2) adsorption of *a)* MTXCuPAA$_2$ (Cu(II):PAA 1:3, C_{PAA} = 9.00 mM, C_{MTX} = 1.00 mM) or *b)* MTXZnPAA$_2$ (Zn(II):PAA 1:3, C_{PAA} = 9.00 mM, C_{MTX} = 1.00 mM) in 10 mM MOPS at pH 7.4; 5) rinsing with 10 mM MOPS at pH 7.4; values for the overtones, *n*, *3-13* are reported.

To gain further insights into the nature and properties of the MTX-containing systems adsorbed on the protein layer, both the ΔF and ΔD data were carefully analyzed. The dissipation to frequency shift ratio offered information regarding both the kinetics and the viscoelastic properties of the adsorbed layer.[302,308,309] The time-dependent ΔD/ΔF plot for the MTXCuPAA$_2$ and MTXZnPAA$_2$ adsorption onto the protein layer is shown in *Supplementary materials - Chapter III, Figure S23*. The slope of the ΔD/ΔF curves indicates the formation of a viscoelastic, hydrated layer for the MTXZnPAA$_2$ system and a more rigid, less elastic layer in the case of MTXCuPAA$_2$ assembly. The two systems also show different adsorption profiles, namely a single-phase for the copper(II)-based assembly and a two-phase for the zinc(II)-based one.

The amount of the adsorbed MTX and copper(II)-based assembly onto the HSA layer (both having a rigid structure) were determined by applying the Saurbrey equation. The viscoelastic features observed in the case of the zinc(II) assembly preclude the use of the simple Sauerbrey-based analysis and the amount of adsorbed material was determined using the Voigt-Kelvin viscoelastic model to the overtone 3-13. [254,270] About 44 ± 2 ng/cm^2 of MTX or MTXCuPAA$_2$ assembly was adsorbed onto the protein layer, whereas about 794 ± 6 ng/cm^2 of MTXZnPAA$_2$ assembly was adsorbed. Plots of the adsorbed mass are shown in *Figure 91*.

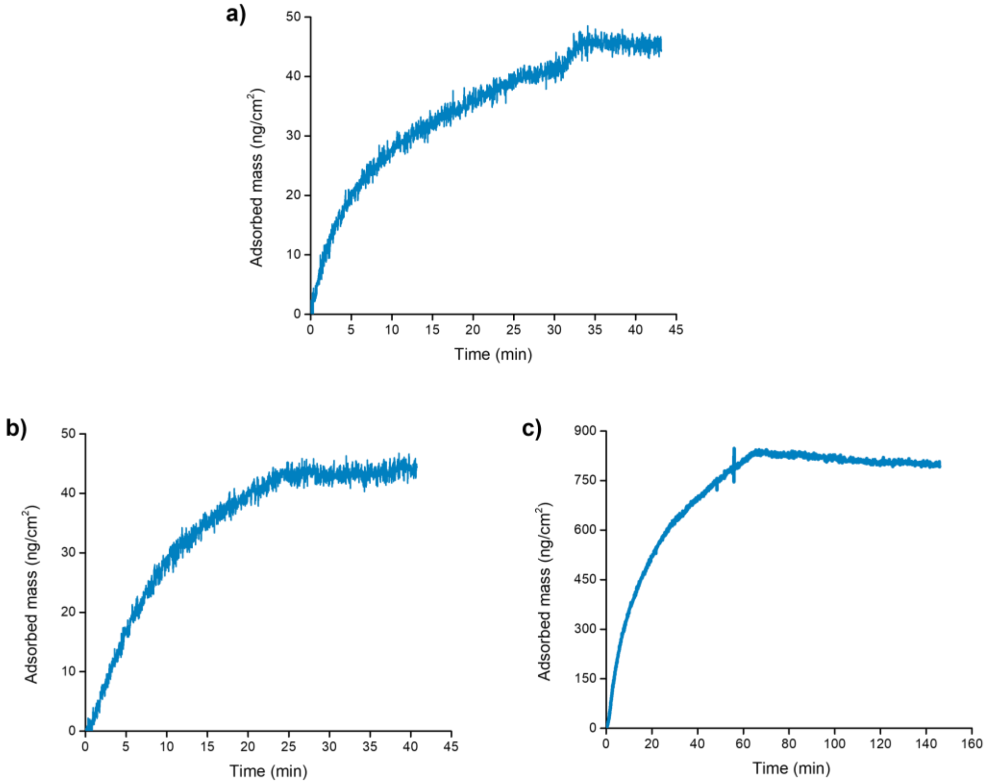

Figure 91. Mass changes for *a)* MTX, *b)* MTXCuPAA$_2$ or *c)* MTXZnPAA$_2$ interactions with human serum albumin at 25 °C. The curves represent the adsorption and desorption processes described in *step 4* and *step 5* of the QCM-D measurements in *Figure 89*.

1.8 Methotrexate-poly-lysine interactions and drug release at controlled pH

Since at physiological pH the methotrexate is negatively charged, the electrostatic interactions between the ionic groups of the ligand and the positively charged groups of a pH-responsive molecule could be used to develop a pH-responsive construct for carrying the chemotherapy drug. Very recently MTX/poly-lysine nanoparticles with high loading capacity and anti-tumour activity were proposed.[310]

The binding properties of the drug towards the pH-responsive poly-lysine (PLys) polymer, which is positively charged at neutral pH, were investigated in aqueous solution at pH 7.4 (MOPS 10 mM) to determine the species and the energetics of the interaction. UV-Vis and calorimetric titrations are shown in *Figure 92*; the corresponding molar ratio plots are shown in *Supplementary materials - Chapter III, Figure S24.* The species, binding constant and thermodynamic parameters are listed in *Table 13.*

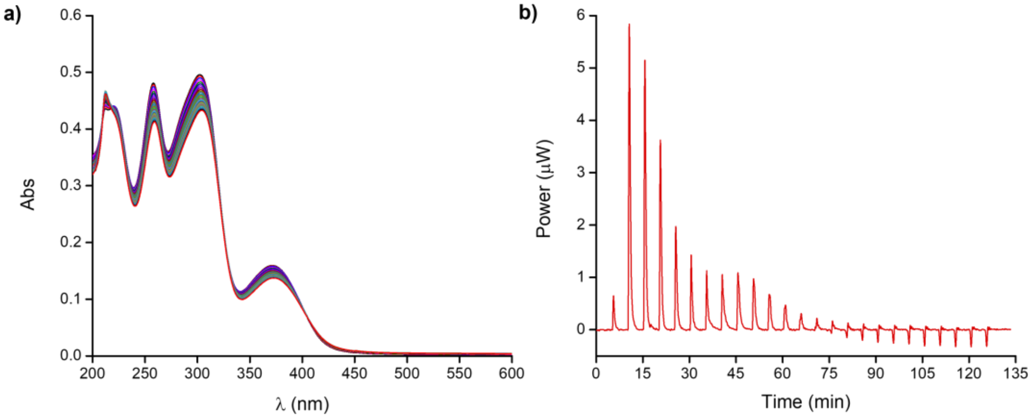

Figure 92. *a)* UV-Vis titration of PLys (1.00 mM) into MTX (0.023 mM) solution and *b)* ITC titration of MTX (2.20 mM) into PLys (0.015 mM) solution at 25 °C and pH 7.4.

Table 13. Conditional stability constant values[a] and thermodynamic parameters[a,b] for the methotrexate (L) - poly-lysine (P) complex formation at 25 °C and pH 7.4 (MOPS 10 mM).

Species	**Log K**	**-ΔG⁰**	**ΔH⁰**	**TΔS⁰**
LP	4.26 (1)	-26.3	-8.22 (7)	18.0

[a] σ in parenthesis; [b] in kJ mol $^{-1}$.

As shown in *Figure 92a*, the addition of PLys to the methotrexate solution determines a decrease in the absorption of the MTX bands and a slight red-shift of the band at 372 nm. The multi-wavelength analysis of the spectroscopic data in the 240-450 nm range allowed for the accurate determination of the complex species and conditional stability constant at pH 7.4.

PLys forms with MTX a stable 1:1 complex species with an enthalpically and entropically favoured process. The enthalpic gain is due to the favourable electrostatic interactions between the oppositely charged moieties, i.e. the carboxyl groups of the MTX and the nitrogen units of the polymer. The entropy contribution, which drives the formation of the adduct, is due to the desolvation of both MTX and polymer as well as conformational changes of the polymer chains which rearrange upon drug complexation. The determined binding constant is 0.7 log units higher than that reported at 37 °C and pH 7.4 (acetate buffer 150 mM).[311] The difference can be attributed to both the technique employed (dynamic dialysis *vs.* UV-Vis spectroscopy/isothermal titration calorimetry) and the experimental conditions (temperature and concentration of the buffering agent). For example, the authors report a decrease in the binding constant due to the increase in temperature. Furthermore, as the interaction between MTX and PLys is expected to depend on the electrostatic forces between the charged species, the concentration of the solvent plays a significant role in any interaction. The use of high buffer concentration may reduce the strength of the electrostatic interaction due to a “shielding” effect induced by the increased concentration of ions in solution. Both these explanations are in line with the higher binding constant shown in *Table 13*.

The binding process between MTX and PLys was also investigated at the solid-liquid interface; typical QCM-D experiments are shown in *Figure 93*.

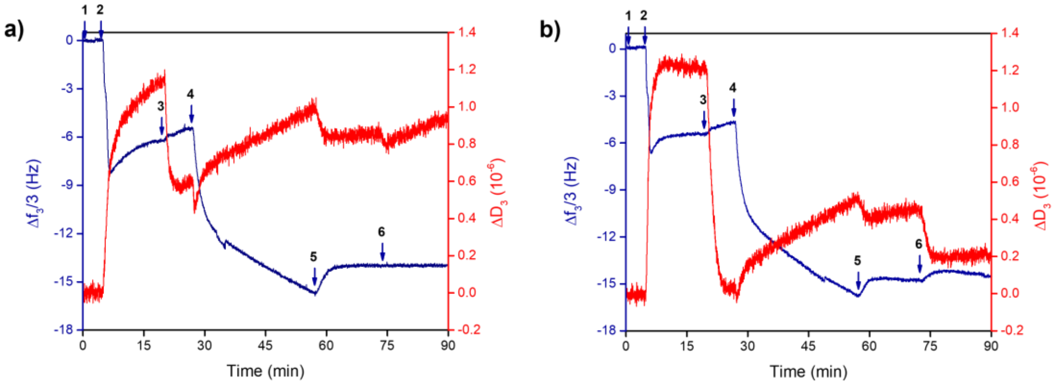

Figure 93. Normalized frequency $\Delta F_n/n$ (blue) and dissipation ΔD_n (red) change (for simplicity, only data referring to the third overtone are shown, n = 3) for the adsorption of the poly-lysine onto a gold-coated quartz crystal and subsequent loading of methotrexate at 25 °C. 1) Baseline: 10 mM MOPS at pH 7.4; 2) adsorption of the PLys (0.5 mg/mL) in 10 mM MOPS at pH 7.4; 3) rinsing with 10 mM MOPS at pH 7.4; 4) uptake of methotrexate from its solution (C_{MTX} = 1.00 mM) in 10 mM MOPS at pH 7.4; 5) rinsing with 10 mM MOPS at pH 7.4; 6) rinsing with 10 mM MOPS at *a)* pH 7.4 and *b)* pH 4.5.

The observed decrease in frequency (*step 2*) is due to the adsorption of poly-lysine to the sensor surface at pH 7.4; the subsequent rinsing step does not cause significant changes in the frequency over time. The further decrease in frequency (*step 4*) accounts for the adsorption of methotrexate onto the polymeric layer confirming the binding interaction between the drug and the macromolecules already observed in solution. The frequency increase observed after the rinse in *step 5* corresponds to the removal of the non-adsorbed drug. Changes in dissipation are very small for all the described steps thus indicating the rigidity of the absorbing layers.

QCM-D measurements enabled also to investigate the release of the drug from the polymeric layer upon pH change at the solid-liquid interface (*step 6*). The flowing of a neutral solution as well as of an acidic one does not cause further/significant frequency variations.

The plots of the adsorbed methotrexate, calculated according to the Sauerbrey equation, and the % of drug release at different pH values are shown in *Figure 94*.

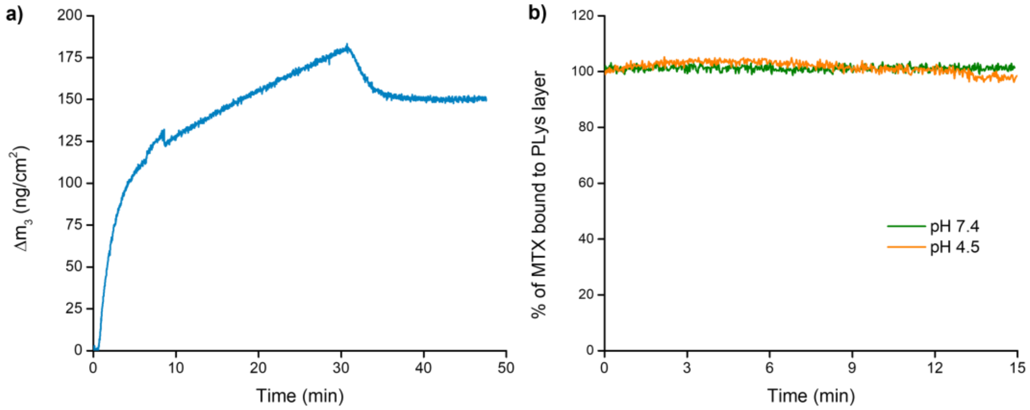

Figure 94. *a)* Total amount (ng/cm^2) of methotrexate adsorbed onto the PLys layer; the curves refer to *step 4* and *step 5* of *Figure 93*; *b)* % of methotrexate bound to PLys layer after the flowing of solution at different pH.

About 150 ± 1 ng/cm^2 of methotrexate was absorbed onto the polymeric layer. As expected from the higher binding constant value, the amount of MTX bound to PLys is larger than that adsorbed onto the copper(II)- and zinc(II)-polymer layer. However, unlike the metal-coordinated assemblies, the PLys/MTX system does not allow a controlled release of the loaded drug. As shown in *Figure 94b*, both at neutral and acidic pH, the MTX remains completely bound to the polymeric layer.

Release studies were also performed in solution at 37 °C and pH 7.4 and 4.5 by combining dialysis and UV-Vis spectroscopy. The linear regression equations from methotrexate calibration curves obtained in the concentration range 0.0002-0.0018 mM at the proper pH value (*Supplementary materials - Chapter II, Figure S25*) were used to determine the amount of cumulative MTX released as a function of time. The percentage of the methotrexate released under different pH values calculated using *Equation 5* (*Chapter II*) is shown in *Figure 95*.

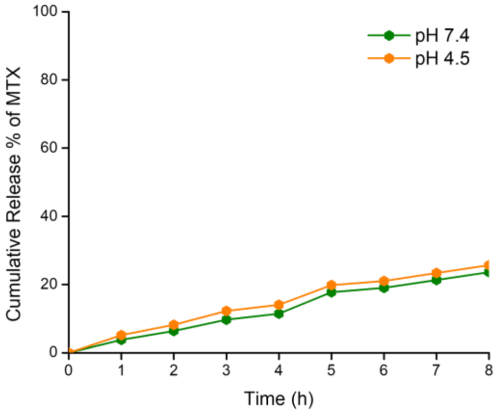

Figure 95. Plot of cumulative release % of methotrexate at 37 °C and pH 7.4 or 5.4.

Again, there are no differences between the amount of MTX released in solution under physiological or acidic pH, confirming what was already observed at the interface. Approximately 20% of the drug is released from the PLys/MTX system at both pH values. This result can be rationalized considering the ionization state of the polymer carrier and its affinity for the drug. Unlike the negatively charged PAA, the decrease in pH will not influence the ionization state of the responsive PLys and will promote exclusively the protonation of the carboxyl groups of the methotrexate. This is not sufficient to ensure a controlled release of the drug which remains bound to the polymeric carrier. Furthermore, the higher binding constant between the methotrexate and the positively charged polymer determines the formation of a much more stable complex than those formed by the same drug with the metal-PAA systems.

Once again, these observations allow to highlight how the knowledge of the affinity of a drug for a carrier is of paramount importance for developing not only stable systems with high loading capacity but also with smart release capability able to simultaneously meet the needs to protect/stabilize the drugs and respond to the desired stimuli.

2. CONCLUSIONS

The study of multiple equilibria occurring in aqueous solution at pH 7.4 among methotrexate, metal(II) ions, and polyacrylic acid was crucial for the development of *smart* pH-responsive metal-based assemblies containing the chemotherapy drug. ITC experiments allowed the determination of the binding parameters for the complex species formation in solution. Methotrexate forms ML complex species with both metal ions. The complex formed with copper(II) is entropically driven with a favourable enthalpic contribution whereas enthalpy and entropy equally contribute to the ML species formed by zinc(II). Methotrexate and poly(acrylic acid) could interact thanks to the metal(II) ions which act as a bridge between the two molecules. The $MTXM(PAA)_2$ complexes are formed with both metal ions through entropically favoured and driven processes mainly due to desolvation and conformational changes of the metal(II)-polymer scaffold upon the complexation. The combination of ITC and UV-Vis measurements suggested a possible arrangement/conformation of the developed metal-coordinated assemblies.

The affinity of the drug toward the metal(II)–polymer complexes was also confirmed at the solid-liquid interface by QCM-D experiments. These studies also provided evidence of the ability of the metal-coordinated assemblies to release the drug under pH control: the methotrexate is almost quantitatively released from the metal(II)-based systems at acidic pH while remaining bound to the polymeric layer under physiological conditions. The developed assemblies (with or without the drug) are negatively charged and have a spherical shape and sizes in the nanoscale range. As demonstrated by the *in vitro* studies, the metal(II)-based systems can be internalized by glioblastoma cells; moreover, they have a more efficient cytotoxicity than the free uncomplexed drug which can be explained by assuming their ability to generate a higher level of ROS. The polymeric systems can interact with human serum albumin both in solution and at the interface. The strength of these interactions resides in the electrostatic forces occurring between the two interacting systems as suggested by the energetics of the binding process.

The negatively charged methotrexate can interact with the pH-responsive poly-lysine forming a stable complex thanks to an enthalpically favoured and driven process. However, this system does not allow a controlled release of the drug upon pH control due to the ionization state of the carrier and its high affinity towards MTX.

These studies provide a rational strategy for the design and development of a versatile polymeric system exhibiting a pH-controlled release of methotrexate and advanced cytotoxic activity towards cancer cells.

3. EXPERIMENTAL SECTION

3.1 Materials

Methotrexate (MTX), copper(II) perchlorate hexahydrate (purity ≥ 99.8 %), zinc(II) perchlorate hexahydrate (purity ≥ 99.8 %), 4-morpholinepropanesulfonic acid (MOPS) (purity ≥ 99.5 %, titration), poly(acrylic acid sodium salt) (average Mw ~5100, GPC) (PAANa), poly-lysine (PLys, 15.000-30.000 by viscosity, purity ≥ 99.8 %)), fluoroshield with 4’,6-diamidino-2-phenylindole dihydrochloride (DAPI), Triton X-100, Tween 20, and human serum albumin (HSA, lyophilized powder, ≥ 96% by agarose gel electrophoresis) were purchased from Sigma-Aldrich and used without purification. Dulbecco’s modified Eagle’s medium, fetal bovine serum (FBS), penicillin−streptomycin (P/S), Hanks' Balanced Salt Solution (HBSS) without calcium and magnesium and HBSS/phenol-free media, phosphate-buffered saline (PBS), AlamarBlue cell viability reagent, 16% formaldehyde solution (w/v), 2'-7'-dichlorodihydrofluorescein diacetate (DCFH-DA), menadione sodium bisulfide, N-acetyl cystein and rhodamine-phalloidin were purchased from Thermo Fisher Scientific. Buffer solution (pH 7.4, MOPS 10 mM) was prepared by weighing proper amounts of MOPS and titrating it with a sodium hydroxide solution to the desired pH. Cu(II) and Zn(II) stock solutions were prepared by dissolving the corresponding perchlorate salts in water. Their concentration was determined by titrating the resulting solution with standard EDTA using murexide and eriochrome black T as the indicator, respectively.[265] MTX, PAA and PLys stock solutions were prepared at pH 7.4 in MOPS 10 mM; the concentration of the polymers was expressed per monomer unit of acrylic acid or lysine, respectively. HSA solutions were prepared at pH 7.4 in MOPS 10 mM and kept in the dark at 4 °C; the concentration was checked by UV-Vis spectroscopy before each experiment.[312]

High-purity water (Millipore, Milli-Q Element A 10 ultrapure water) and A-grade glassware were employed throughout.

3.2 UV-Vis titrations

UV-Vis titrations were carried out at 25 °C in aqueous solution (pH 7.4, MOPS 10 mM) with an Agilent 8453 diode-array spectrophotometer in a 1 cm path length quartz cells following the procedure described in *Chapter II - Experimental section, UV-Vis titrations.*

Methotrexate-metal(II) complexes: UV-Vis titrations for the study of metal-ligand complex formation were conducted by adding a solution of Cu(II) (0.8-1.0 mM) or Zn(II) (0.8-1.0 mM) into a MTX solution (0.04-0.07 mM).

Methotrexate-poly(acrylic acid) interactions: The interactions occurring between poly(acrylic acid) and MTX were investigated spectrophotometrically by titrating the drug (0.04-0.7 mM) with a polymer solution (9.00-12.0 mM).

Methotrexate-metal(II)-polymer assemblies: UV-Vis titrations were conducted by titrating a metal-polymer solution prepared at different M(II):PAA molar ratio (C_{PAA} = 9.00 mM) into a MTX solution (0.12-0.15 mM).

Methotrexate-poly-lysine interactions: Drug-poly-lysine complex formation was investigated by titrating a polymer solution (1.00-1.20 mM) into a MTX solution (0.02-0.023 mM).

3.3 Isothermal titration calorimetry (ITC) measurements

Calorimetric titrations were performed at 25 °C with a nano-isothermal titration calorimeter Nano-ITC (TA Instruments, USA) following the procedure described in *Chapter II - Experimental section, Isothermal titration calorimetry (ITC) measurements.*

Methotrexate-metal(II) complexes: ITC titrations for the complexation of MTX with metal ions were carried out by titrating a solution of the drug (2.00-2.20 mM) into Cu(II) (0.20-0.25 mM) or Zn(II) (0.15-0.20 mM) solutions.

Methotrexate-poly(acrylic acid) interactions: The interactions between poly (acrylic acid) and MTX were investigated by titrating a polymer solution (12.0 9.00 mM) into a drug solution (0.40-0.50 mM).

Methotrexate-metal(II)-polymer assemblies: ITC titrations were performed by titrating a metal-polymer solution prepared at M(II):PAA 1:3 molar ratio (C_{PAA} = 9.00 mM) into a MTX solution (0.40-0.50 mM).

Interactions of methotrexate and metal-coordinated assemblies with human serum albumin: Calorimetric titrations were carried out by titrating an HSA solution (0.015 mM-0.15 mM) with MTX (2.00-2.20 mM) or copper-based (0.365-0.385 mM) or zinc-based (0.330-0.350 mM) assembly.

Methotrexate-poly-lysine interactions: Drug-poly-lysine complex formation was investigated by titrating a drug solution (2.00-2.20 mM) into polymer solutions (0.10-0.30 mM).

Heats of dilution were determined in separate "blank" experiments by adding the proper titrant solution into the buffer solution (pH 7.4, MOPS 10 mM) only. Net heat values were analyzed using the HypCal software.

3.4 Quartz-crystal microbalance with dissipation monitoring (QCM-D) experiments

Quartz crystal microbalance with dissipation monitoring (QCM-D) measurements were performed using a Q-Sense E1 instrument (Biolin Scientific, Gothenburg, Sweden) following the procedure described in *Chapter II - Experimental section, Quartz-crystal microbalance with dissipation monitoring (QCM-D) experiments*.

Methotrexate-metal(II)-polymer assemblies formation, methotrexate-poly-lysine interactions and drug release at controlled pH: The poly(acrylic) acid-metal complex (prepared by properly mixing copper(II) or zinc(II) and PAA at 1:3 molar ratio (C_{PAA}= 9.00 mM)) or poly-lysine solution (0.5 mg/mL) were initially adsorbed on the sensor crystal surface; a washing step using the same buffer solution was later performed to remove any loosely attached material. Afterwards, 2.20 mM (in the case of the metal-polymer layer) or 1.00 mM (for the poly-lysine layer) methotrexate solution (MOPS 10 mM, pH 7.4) was flowed through the adsorbed film until the frequency change reached equilibrium. A washing step was then required to remove the non-adsorbed drug. Finally, a solution of MOPS 10 mM at pH 7.4, 5.4 or 4.5 was flowed until constant frequency changes were recorded to assess the pH-responsiveness of the adsorbed systems.

Interaction of methotrexate and metal-coordinated assemblies with human serum albumin (HSA): The HSA solution (1 mg/mL) (MOPS 10 mM, pH 7.4) was initially adsorbed on the sensor crystal surface. A washing step using the same buffer solution was then performed to remove any loosely attached protein. Afterwards, methotrexate (2.20 mM) or metal-coordinated assemblies (M(II):PAA 1:3, C_{PAA}= 9.00 mM, MTX 1.00 mM) (MOPS 10 mM, pH 7.4) was flowed through the adsorbed film until the frequency change reached equilibrium. Finally, a rinsing step was performed to remove the non-adsorbed drug/assembly.

3.5 Preparation of the metal-coordinated assemblies and methotrexate-poly-lysine system

Both metal(II)-polymer complexes and the corresponding metal(II)-coordinated assemblies were prepared in aqueous solution (MOPS 10 mM, pH 7.4) by properly mixing the components of each system to optimize the formation of the desired complex species according to the determined binding constants listed in *Table 3* (*Chapter II*), *Table 8* and *Table 9* (*Chapter III*). The molar ratio at which system components were mixed was chosen to ensure the optimal formation of the desired complex or assembly. More specifically, $CuPAA_2$ and $ZnPAA_2$ were prepared by mixing the metal(II) ions and polymer at 1:3 metal/polymer ratio (C_{PAA} = 9.00 mM). As previously described (*Chapter II*), these conditions are intended to guarantee the proper formation of the complex species of our interest maximizing the binding sites for the loading of the drug yet avoiding precipitation phenomena. For preparing $MTXCuPAA_2$ and $MTXZnPAA_2$ assemblies, methotrexate (0.40 mM or 1.00 mM) was added to the metal(II)-polymer complex (M(II):PAA 1:3, M(II):MTX 7.5 or 3:1, $C_{M(II)}$ = 3.00 mM). For both metal ions, these conditions ensured the formation of the desired assembly (*Supplementary materials* - *Chapter III, Figure S26* and *Figure S27*).

Methotrexate/poly-lysine adduct was prepared in aqueous solution (MOPS 10 mM, pH 7.4) by mixing drug and polymer at MTX:PLys 1:0.67 molar ratio (C_{PLys} = 1.50 mM) which, according to the determined binding constant, ensured the formation of the polymeric complex species (*Supplementary materials - Chapter III, Figure S28*).

3.6 Size, surface charge and morphology of metal-coordinated assemblies

Hydrodynamic size and the ζ-potential of the metal-coordinated assemblies were performed at 25 °C and pH 7.4 (MOPS 10 mM) on a Malvern Instrument Zetasizer (ZEN 3690) equipped with a 633 nm laser at a scattering angle of 90°. Metal-coordinated assemblies solution were freshly prepared and all measurements were done using a low-volume rectangular quartz cuvette. The shape of the metal-coordinated assemblies as well as their morphological aspect in the dry state was analyzed with a scanning electron microscope (Hitachi S-4800). The microscope was operated at a working voltage of 15 kV and a working current of 20 nA.

3.7 In vitro cellular studies

U87 cell seeding: U87 glioblastoma cells (ATCC) were grown in T-75 flasks with complete medium (DMEM + 10% FBS + 1% P/S) and incubated at 37 °C in a 5% CO_2 atmosphere. A density of 10.000 cells/well on a 96-well plate was used for metabolic activity measurements. A density of 10.000 cells/well on a 24-well plate was used for internalization studies. A density of 50.000 cells/well on a 6-well plate was used for ROS production studies.

Cytotoxicity measurements: To evaluate the cytotoxicity of the metal-coordinated assemblies, the metabolic activity of U87 cells in the presence of polymeric systems was measured using the AlamarBlue® assay. Cells were seeded in 96-well plates and treated with metal-coordinated assemblies at different concentrations. Cells cultured in the presence of only polymer-metal complexes, polymer and metal ions at the same concentrations and free drugs as well as in the absence of the above-mentioned systems were used as a control. At the selected time (48 h), the culture media was removed and replaced by fresh media containing AlamarBlue® (10% v/v). Cells were then incubated for 75 min at 37 °C in 5% CO_2 atmosphere sheltered from light. Finally, 200 µL of the assay media was transferred to a 96-well plate and the fluorescence intensity (λ_{ex} = 545 nm/λ_{em} = 590 nm) was read on a microplate reader (BioTek Synergy H1M). The results are presented as mean ± SD, with n = 3. For standard statistical analysis, Graph Pad Prism 5 software was used. Two-way analysis of variance (ANOVA) was used to test the statistical differences between groups, with the Bonferroni post hoc test and a confidence level of 95% ($p < 0.001$).

FACS analysis for reactive oxygen species (ROS) generation: The reactive oxygen species (ROS) generated by U87 cells were determined by cell-permeable fluorescent and chemiluminescent 2′-7′-dichlorodihydrofluorescein diacetate (DCFH-DA) probes. Cells were incubated for 4 hours with the metal-coordinated assemblies (33 μM in terms of MTX) in the presence and the absence of metal ions as well as with the free drug (1100 μM). Afterwards, the DCFH-DA (10 μM) dye, prepared in HBSS/phenol red-free media, was added to each well and kept for 30 min at 37 °C. Simultaneously, a batch of untreated cells was also maintained as a control. For positive control, cells were incubated with freshly prepared menadione sodium bisulfide solution (1 mM), while for negative control cells were incubated with N-acetyl cysteine (5 mM) for 1 hour at 37 °C. The cells were then washed thrice with HBSS, treated with trypsin to dissociate the adherent cells from the plate, redispersed in prewarmed HBSS (500 μL) and analyzed in the FITC channel (535 nm, green emission) of a flow cytometer (Beckman Coulter Gallios Flow Cytometer) using a 488 nm laser for excitation.

Cellular uptake: The uptake of the metal-coordinated assemblies by U87 cells was investigated by exploiting the emission properties of the methotrexate and the related metal-coordinated assembly. Cells were allowed to grow on the sterile coverslips with complete DMEM medium (and incubated at 37 °C in a 5% CO_2 atmosphere). After 24 hours, cells were treated with the metal-coordinated assemblies for 3 and 12 hours. For copper-based assembly, concentrations in terms of MTX of 44.0 μM and 22.0 μM were employed, respectively, while the zinc-based assembly concentrations in terms of MTX of 22.0 μM and 11.0 μM were used.

Afterwards, the culture media was removed, and the cells were washed twice with PBS. Subsequently, they were incubated for 10 min with 4% paraformaldehyde to fix them.

Cells were then washed with PBS and permeabilized with 300 uL of 0.5% Triton X-100 prepared in PBS for 10 min under slight agitation. After that, Triton X-100 was removed and the cells were washed twice. Cells were then incubated with a 1% BSA solution in PBS in the presence of rhodamine-phalloidin (300 uL: 10 µl of dye per 1 mL of 1% BSA in PBS) for 15 min. Finally, the dye was removed and cells were washed twice with PBS-T (0.1% Tween 20). The coverslips were gently lifted with the aid of tweezers and placed upside down on a glass slide. Nuclei staining with DAPI was carried out directly on the samples by adding a drop of mounting media before being observed under the confocal microscope (Zeiss LSM800).

3.8 Methotrexate release studies from poly-lysine-based system at controlled pH

The release of methotrexate was investigated at suitable pH values (7.4 and 4.5) by combining the dialysis method and UV-Vis spectrophotometry. The MTX/PLys system properly prepared was transferred into dialysis bags (MWCO = 3.5 KDa) and then immersed in 25 mL of release medium (pH 7.4 or 4.5, MOPS 10 mM) at 37± 0.2 °C and stirred at 100 rpm. To quantify the amounts of the MTX released, at selected time intervals (1 hour), 400 µL of the release medium was picked up from the solution and replaced with the same amount of fresh medium to maintain the sink conditions. The absorbance measurements of the withdrawn aliquots were performed on a Jasco V-770 UV-Vis/NIR spectrophotometer (Jasco Europe, Italy).

Chapter IV:

Development of LbL-based nanoparticles using metal-coordinated assemblies

The employment of the *layer-by-layer* (LbL) strategy with several charged components (such as polyelectrolytes, polypeptides, and nanoparticles) offers the opportunity for designing multi-component carriers with desired morphological characteristics and tunable functionalities in the nano/micrometre range. The features of the charged layers can be exploited to obtain a smart system for the efficient triggered delivery of the included therapeutic agent. Either internal or external stimuli can facilitate the breakage of the system by different mechanisms. For example, a decrease in pH induces a repulsion between the charged layer, leading to the release of the encapsulated drug. Furthermore, the use of magnetic-, ultrasound- or near-infrared-responsive nanoparticles for decorating the membrane could promote the disassembly of the polymeric shell and the subsequent release of the loaded cargo.

In this chapter, the developed metal-coordinated assemblies are integrated with the LbL approach to create multilayer polymeric systems capable of loading/releasing a model drug in response to the biologically relevant pH change stimulus.

Novel LbL-based systems were fabricated by depositing alternate layers of MTX-Cu(II)-PAA assembly or Cu(II)-PAA system or poly(acrylic acid) and poly-lysine (PLys) on mesoporous silica nanoparticles (MSNPs) as a template. The physicochemical and morphological properties of the developed systems were thoroughly determined through ζ-potential, scanning electron microscopy (SEM) and transmission electron microscopy (TEM) measurements.

1. RESULTS AND DISCUSSION

1.1 Fabrication of LbL-based polymeric nanoparticles

Mesoporous silica nanoparticles (MSNPs) were chosen as the template for the development of the LbL-based nanoparticles as the self-assembly on the surface of mesoporous materials has proven to be a practical approach for the development of nanoscale hybrid materials for controlled drug release.[313] The broad use of MSNPs in the field of drug delivery can be attributed to their satisfactory biocompatibility, chemical stability, high surface areas, uniform and tunable pore sizes, and controllable surface functionalization. However, the application of only porous silica nanoparticles as carriers is limited by uncontrolled drug release. Herein, the surface of MSNPs was coated with polypeptide and metal-coordinated assemblies or polyelectrolytes to obtain pH-sensitive nanocarriers. Given the possible future applications, the employment of mesoporous nanoparticles could also be exploited to retain a further therapeutic agent (such as an enzyme or a second drug) thus obtaining multifunctional *layer-by-layer* based nanoparticles.

Nanoparticles containing five layers were fabricated using PLys as the positive layer and the Cu(II)PAA$_2$ assemblies, with and without MTX, as the negative layer. For nanoparticles containing six layers, Cu(II)PAA$_2$ was used as a layer in the final polymeric architecture to ensure that the amount of drug in the differently charged nanoparticles is the same for systems containing either five or six layers. With this precaution, any differences that might be observed in future biological applications of these systems can be attributed solely to their different charge (which might influence specific properties or the internalization mechanisms of the nanoparticles).

Systems containing five or six layers were developed using PLys and PAA (negative layer) as control. PLys was chosen due to its extensive use in the fabrication of LbL nanoparticles or nanocapsules for its desirable properties, including biocompatibility, resistance to hydrolysis and easy functionalization.[145,314,315] The MTX-copper(II)-PAA coordinated assemblies were chosen as model pH-responsive nanoparticles.

A schematic representation of the fabrication of LbL-based nanoparticles is shown in *Figure 96*.

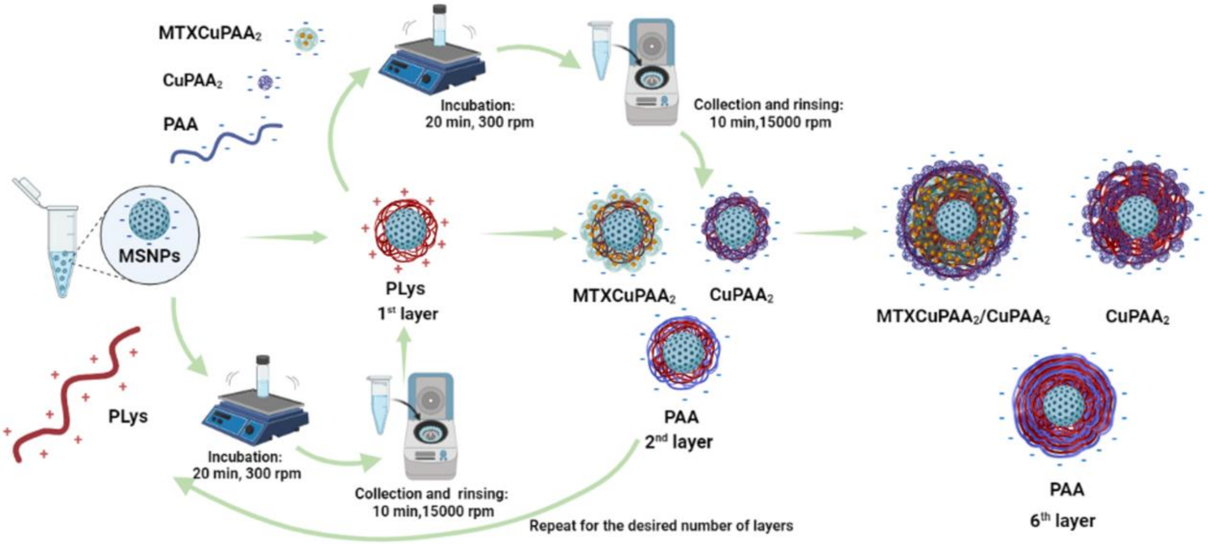

Figure 96. Schematic representation of the fabrication of polymeric nanoparticles.

As the mesoporous silica template is negatively charged, it was first incubated with PLys. This resulted in a shift in its surface charge from −27.5 ± 0.3 to +29.3 ± 2.6 mV. The ζ-potential changes indicate the successful coating of a PLys layer onto the surface of MSNPs. Afterwards, PAA-based and polypeptide layers were assembled alternatively and a change in the ζ-potential value was observed after each deposition step, confirming the successful layer assembly (*Figure 97*).

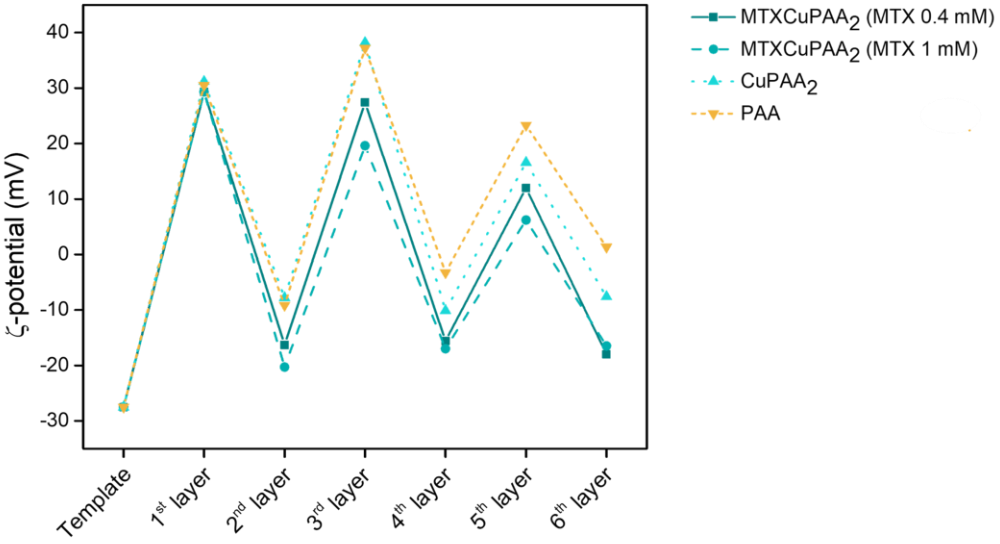

Figure 97. ζ-potential plot of polymeric nanoparticles.

1.2 Physico-chemical and morphological characterization of LbL-based nanoparticles

The morphology of the fabricated nanoparticles was investigated using scanning electron microscopy (SEM) and transmission electron microscopy (TEM). The SEM and TEM micrographs for each fabricated (positively and negatively charged) system are shown in *Figure 98* and *Figure 99* for PLys/MTXCu(II)PAA$_2$ with MTX 0.4 mM, *Figure 100* and *Figure 101* for PLys/MTXCu(II)PAA$_2$ with MTX 1 mM, *Figure 102* and *Figure 103* for PLys/Cu(II)PAA$_2$, *Figure 104* and *Figure 105* for PLys/PAA.

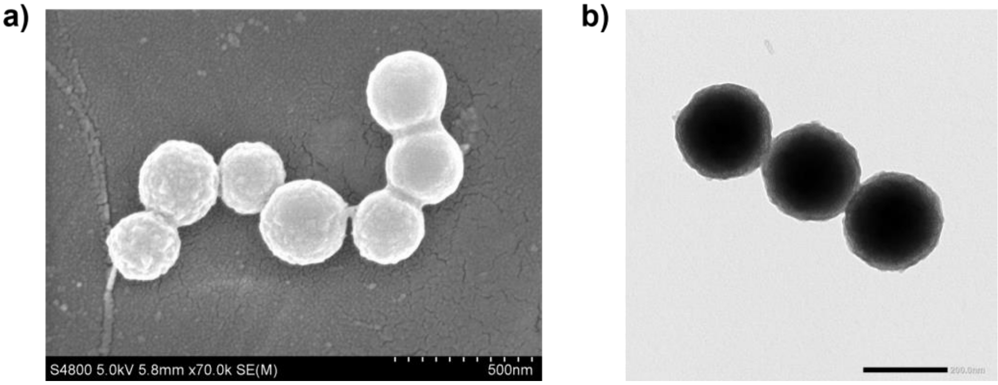

Figure 98. Positively charged PLys/MTXCu(II)PAA$_2$ (with MTX 0.40 mM) system: *a)* SEM micrograph, scale bar 500 nm; *b)* TEM micrograph, scale bar 200 nm.

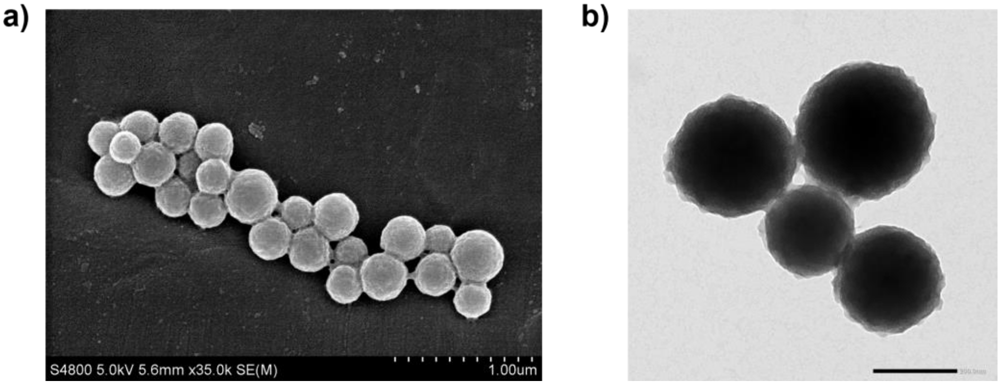

Figure 99. Negatively charged PLys/MTXCu(II)PAA$_2$/Cu(II)PAA$_2$ (with MTX 0.40 mM) system: *a)* SEM micrograph, scale bar 1μm; *b)* TEM micrograph, scale bar 200 nm.

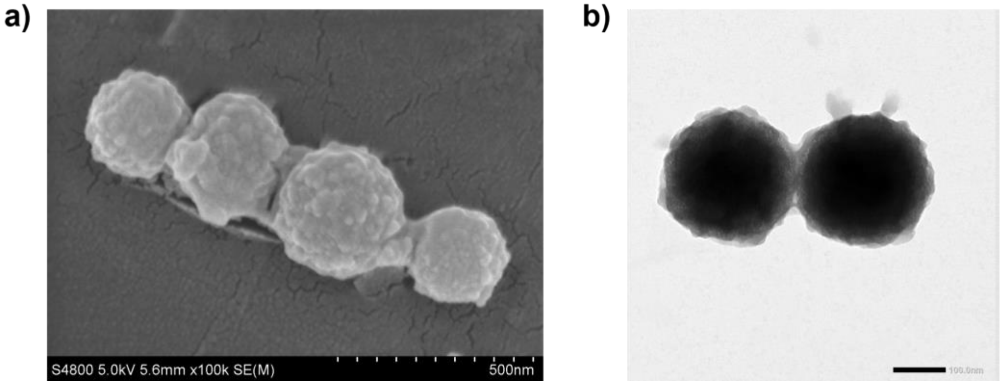

Figure 100. Positively charged PLys/MTXCu(II)PAA$_2$ (with MTX 1.00 mM) system: *a)* SEM micrograph, scale bar 500 nm; *b)* TEM micrograph, scale bar 100 nm.

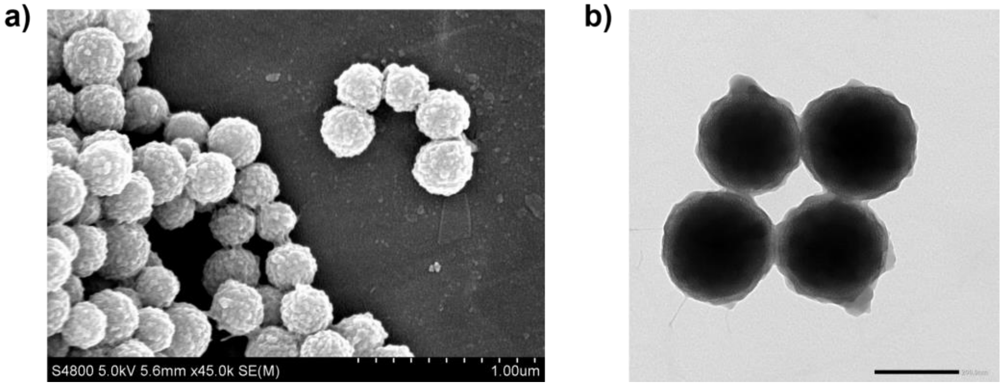

Figure 101. Negatively charged PLys/MTXCu(II)PAA$_2$/Cu(II)PAA$_2$ (with MTX 1.00 mM) system: *a)* SEM micrograph, scale bar 1μm; *b)* TEM micrograph, scale bar 200 nm.

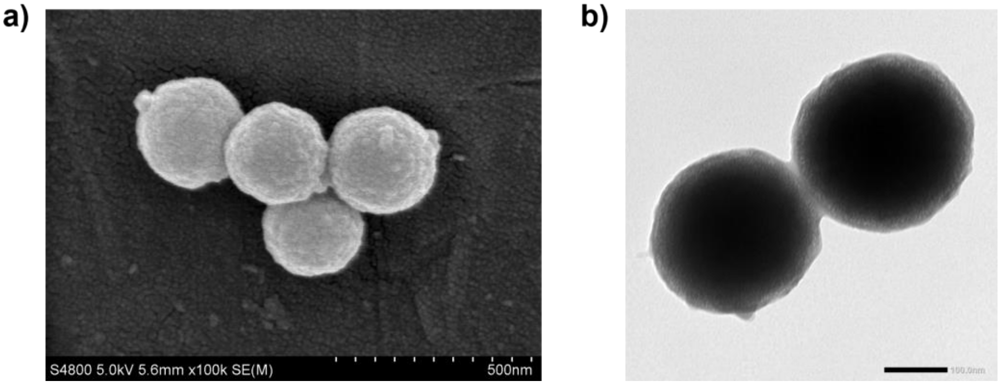

Figure 102. Positively charged PLys/Cu(II)PAA$_2$ system: *a)* SEM micrograph, scale bar 500 nm; *b)* TEM micrograph, scale bar 100 nm.

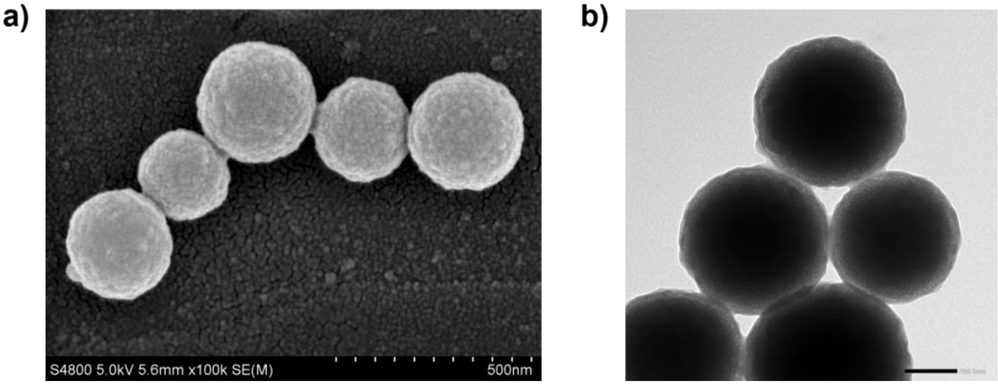

Figure 103. Negatively charged PLys/Cu(II)PAA$_2$ system: *a)* SEM micrograph, scale bar 500 nm; *b)* TEM micrograph, scale bar 200 nm.

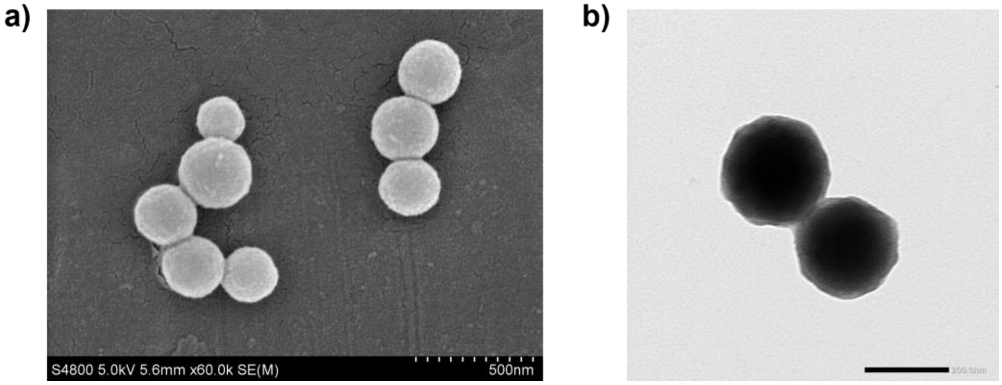

Figure 104. Positively charged PLys/PAA system: *a)* SEM micrograph, scale bar 500 nm; *b)* TEM micrograph, scale bar 200 nm.

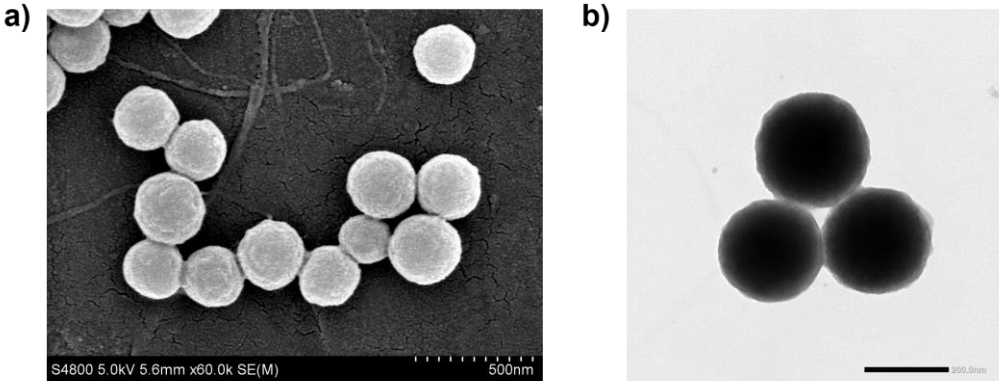

Figure 105. Negatively charged PLys/PAA system: *a)* SEM micrograph, scale bar 500 nm; *b)* TEM micrograph, scale bar 200 nm.

The *layer-by-layer*-based nanoparticles showed a well-defined spherical shape. The mean diameter size of each system in the dried state was determined from SEM and TEM micrographs analysis using ImageJ software and is reported in *Table 14*; nanoparticle size graphs are shown in *Supplementary materials - Chapter IV, Figure S29-Figure S32*.

Table 14. Mean diameter size of LbL-based nanoparticles.

LbL-based nanoparticles	Charge	Mean diameter size (nm)
PLys/MTXCu(II)PAA$_2$ (MTX 0.40 mM)	Positive	264 ± 36
PLys/MTXCu(II)PAA$_2$/Cu(II)PAA$_2$ (MTX 0.40 mM)	Negative	290 ± 31
PLys/MTXCu(II)PAA$_2$ (MTX 1.00 mM)	Positive	285 ± 32
PLys/MTXCu(II)PAA$_2$/Cu(II)PAA$_2$ (MTX 1.00 mM)	Negative	300 ± 32
PLys/Cu(II)PAA$_2$	Positive	262 ± 23
PLys/Cu(II)PAA$_2$	Negative	279 ± 35
PLys/PAA	Positive	258 ± 20
PLys/PAA	Negative	260 ± 31

Nanoparticles have a diameter ranging from ~ 260 nm to ~ 300 nm. The very small differences between the differently charged nanoparticles are due to the presence of an additional layer in the negatively charged ones. Instead, a comparison between nanoparticles made with different negatively charged layers (MTXCu(II)PAA$_2$, Cu(II)PAA$_2$ or PAA) highlights higher differences among the systems that may be ascribed to the different sizes of the negative particle layers added.

Both SEM and TEM analyses highlight differences in nanoparticle morphology. PLys/PAA nanoparticles surface (*Figure 104* and *Figure 105*) appears having a flat and continuous morphology, while the PLys/Cu(II)PAA$_2$ and PLys/MTXCu(II)PAA$_2$ architectures show a rougher surface. More specifically, spherical bumps can be detected in the outer shell of both positively and negatively charged nanoparticles. These bumps are poorly defined for the PLys/Cu(II) systems (*Figure 102* and *Figure 103*), whereas are well marked up in the case of the MTXCu(II)PAA$_2$-containing systems (*Figure 98-Figure 101).* These bumps are more prominent for the system containing a larger quantity of MTX; this evidence suggests that, although a different concentration of drug in the assembly does not influence much the size of the LbL-based nanoparticles, it affects the surface morphology of the nanostructures (*Figure 100* and *Figure 101*). This peculiar "nanoraspberries" surface could be advantageous since, according to literature reports, nanoparticles with an irregular surface could improve cellular uptake and enhance tumour penetration. [212,316]

The amount of MTX present in the LbL-based nanoparticles was evaluated regarding the initial drug concentration present in the MTX metal-coordinated assemblies. Calibration curves obtained for both assemblies containing 0.4 mM or 1 mM of MTX (*Figure 106* and *Figure 107*) allowed to determine the amount of MTX present in MTXCu(II)PAA$_2$ system that is not tied to the growing multilayer system; this quantity was obtained by the UV-Vis spectra of the supernatant solutions (properly diluted) after deposition, centrifugation and washing steps (*Supplementary materials - Chapter IV, Figure S33* and *Figure S34*).

In the fabrication process of nanoparticles containing MTXCu(II)PAA$_2$ assembly prepared with MTX 0.40 mM, a concentration of 90.88 μg of MTX will be added for each of the two negatively charged layers corresponding to a total amount of 181.78 µg of MTX. Instead, for the nanoparticles containing MTXCu(II)PAA$_2$ assembly prepared with MTX 1.00 mM, 227.22 µg of MTX are added for each layer corresponding to a total MTX amount of 454.44 µg.

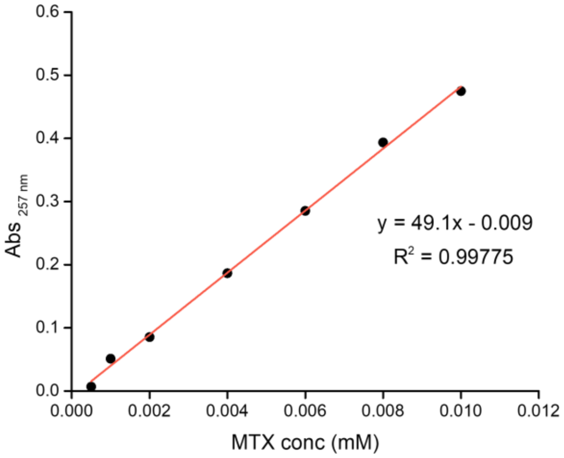

Figure 106. Calibration plot for the MTXCu(II)PAA$_2$ assembly with MTX 0.40 mM.

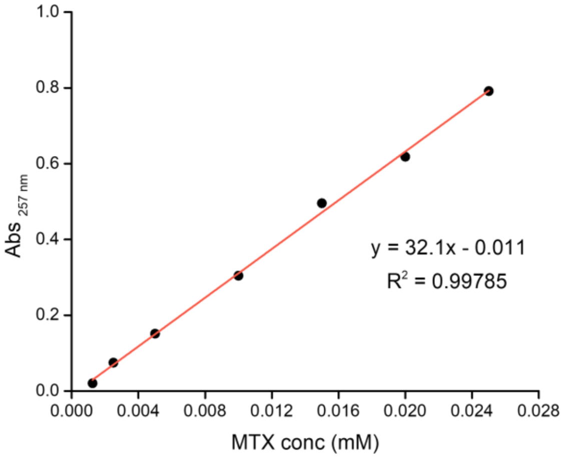

Figure 107. Calibration plot for the MTXCu(II)PAA$_2$ assembly with MTX 1.00 mM.

At the end of the fabrication process, a total amount of 19 ± 4 µg of drug was loaded in the system prepared using the assembly with 0.4 mM MTX, while a total amount of 172 ± 7 µg of drug was loaded in the nanoparticles when using the assembly containing 1 mM MTX.

The entrapment efficiency (EE %) of the system can be calculated from the following equation:

$$EE\ \% = \frac{loaded\ drug}{total\ drug\ added} * 100 \qquad \textit{Equation 8}$$

LbL-nanoparticles prepared with MTXCu(II)PAA$_2$ assembly at lower drug concentration have an entrapment efficiency of 10.45 %; this value increases up to 37.85 % when loading the assembly with higher drug concentration (1 mM).

The amount of PLys present in the various nanoparticles that can be considered indicative of the nanoparticles concentration, essential for potential biological application, was determined spectrophotometrically according to the reported standard microplate protocol for the Bradford assay. The quantity of PLys determined for each system is 1290 ± 15 µg/mL. No differences were found among the systems, meaning that the use of different negatively charged layers does not affect the fabrication process. This value can be also used as an indication of the "unit weight of NPs" to determine the loading capacity (LC %) from the equation below:

$$LC\ \% = \frac{loaded\ drug}{unit\ weight\ of\ NPs} * 100 \qquad \textit{Equation 9}$$

LbL-nanoparticles fabricated with MTXCu(II)PAA$_2$ assembly at lower drug concentration gave a loading capacity of 1.47 %, while a value of 13.33 % was calculated for the nanoparticles made the assembly at higher drug concentration.

By comparing the two multilayer systems containing different concentrations of MTX, it is evident that the use of a larger quantity of drug in the polymeric layer accounts for a greater loading capacity as well as for a greater encapsulation efficiency of the system.

To assess their stability, nanoparticles were incubated in PBS (pH 7.4) at 37 °C and SEM micrographs were acquired after one week. As can be observed in *Figure 108*-

Figure 111, nanoparticles maintained their spherical shape and surface morphology, confirming their stability over time.

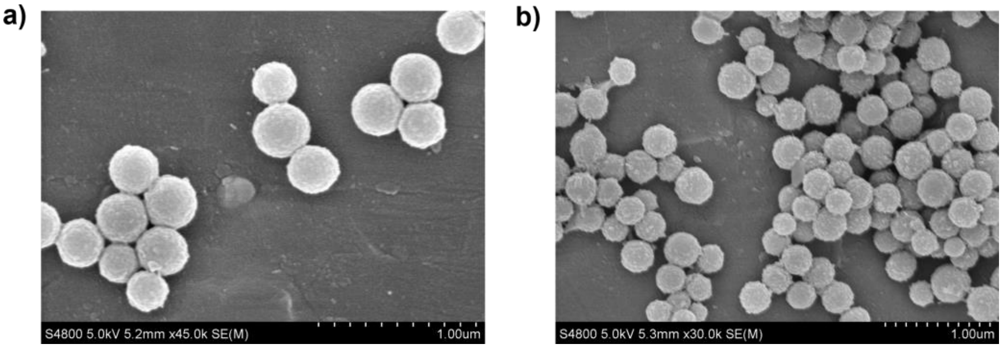

Figure 108. SEM micrographs of PLys/MTXCu(II)PAA$_2$ (MTX 0.40 mM) *a)* positively and *b)* negatively charged after one week in PBS (pH 7.4) at 37 °C.

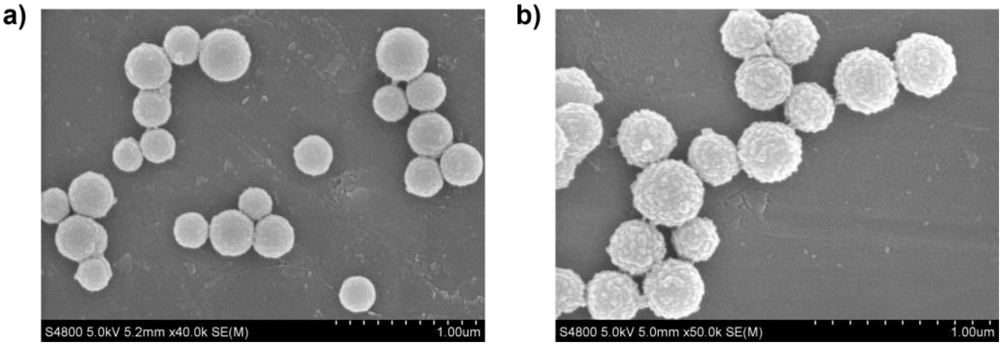

Figure 109. SEM micrographs of PLys/MTXCu(II)PAA$_2$ (MTX 1.00 mM) *a)* positively and *b)* negatively charged after one week in PBS (pH 7.4) at 37 °C.

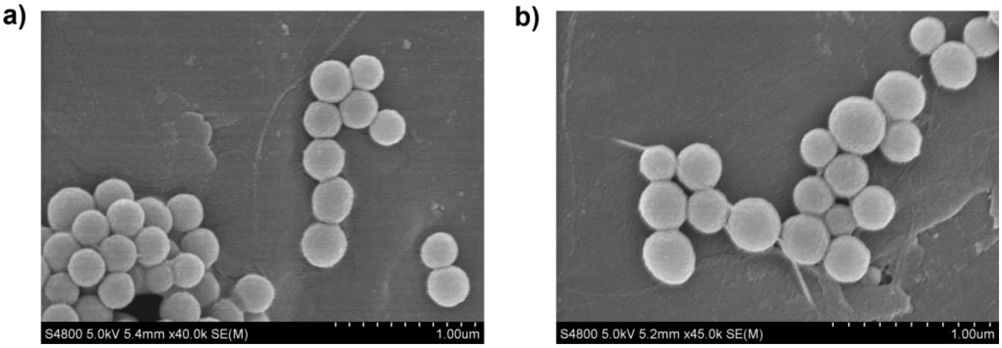

Figure 110. SEM micrographs of PLys/Cu(II)PAA$_2$ *a)* positively and *b)* negatively charged after one week in PBS (pH 7.4) at 37 °C.

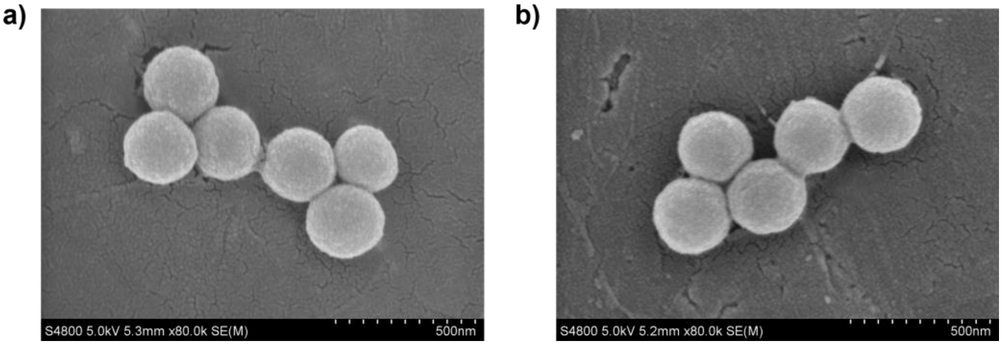

Figure 111. SEM micrographs of PLys/PAA *a)* positively and *b)* negatively charged after one week in PBS (pH 7.4) at 37 °C.

2. CONCLUSIONS

The *layer-by-layer* approach was successfully integrated with the copper(II)-coordinated assembly for developing novel multilayer polymeric nanoparticles for the delivery and controlled release of methotrexate. The nanoparticles fabricated have a well-defined spherical shape with a mean diameter size ranging from 260 nm to 300 nm. The use of the metal-coordinated assemblies as the layer constituent affects the surface morphology of the polymeric nanocarriers which exhibit characteristic bumps in the outer shell.

Future investigations will focus on the methotrexate release from the developed positively and negatively charged nanoparticles under different pH values to evaluate the pH-responsiveness of the systems. Moreover, *in vitro* studies will be carried out to assess the therapeutic efficacy and the cellular uptake of the polymeric nanoparticles. Finally, the ability of these systems to interact with plasma proteins, such as human serum albumin will be explored.

3. EXPERIMENTAL SECTION

3.1 Materials

Mesoporous silica nanoparticles (MSNPs) (200 nm particle size, pore size 4 nm), copper(II) perchlorate hexahydrate, methotrexate (MTX), 4-morpholinepropanesulfonic acid (MOPS), poly(acrylic acid sodium salt) (average Mw ~5100 Da, GPC) (PAANa), were purchased from Sigma-Aldrich. *n*-butyl-poly(α-L-lysine) hydrobromide (n-Bu-PLys$_{200}$ HBr, Mw ~42000 Da) was obtained from Polypeptide Therapeutic Solutions. Bradford reagent was purchased from Thermo Scientific. The Cu(II) stock solution was prepared by dissolving the corresponding perchlorate salt in water; its concentration was determined by titrating the resulting solution with standard EDTA using murexide as the indicator. Polyelectrolyte and polypeptide solutions were prepared at pH 7.4 in MOPS 10 mM; high-purity water (Millipore, Milli-Q Element A 10 ultrapure water) was employed throughout.

3.2 Fabrication of LbL-based polymeric nanoparticles

Polymeric nanoparticles were fabricated via the *LbL* approach. Cu(II)PAA$_2$ and MTXCu(II)PAA$_2$ systems were prepared in solution (MOPS 10 mM, pH 7.4) as described in *Chapter III - Experimental section, Preparation of the metal-coordinated assemblies.* The concentration of PAA (9.00 mM) employed to prepare the assembly corresponds to 0.65 mg/mL of PAA in the system, while two different concentrations of MTX were used (0.40 mM and 1.00 mM), which correspond to 0.18 mg/mL and 0.45 mg/mL, respectively.

MSNPs were dispersed in MOPS 10 mM, pH 7.4 to have a final concentration of 3.2 mg/mL. As MSNPs have a negative surface charge, PLys (0.65 mg/mL in MOPS 10 mM pH 7.4) was used as the first polymeric layer. 0.5 mL of MSNPs suspension was added to PLys solution to have a final concentration of 1.6 mg/mL of MSNPs and 0.33 mg/mL of PLys (5:1 weighed ratio). After an incubation time of 20 min at 300 rpm, the nanoparticles were collected by centrifugation (15000 rpm, 10 min) and washed twice with 1 mM NaCl solution. The obtained nanoparticles were then resuspended in

0.5 mL of buffer solution and sonicated to avoid aggregation phenomena. Following the same procedure, the second layer (of MTXCu(II)PAA$_2$ or Cu(II)PAA$_2$ or PAA) was deposited. The cyclic procedure was performed to grow up the third and fourth layers (positively and negatively charged, respectively). Nanoparticles containing five or six layers were fabricated with a final shell architecture of PLys/PAA or PLys/Cu(II)PAA$_2$.

3.3 Surface charge, morphology, size and characterization of LbL-based nanoparticles

The ζ-potential was monitored after each polyelectrolyte/polypeptide deposition step with a Malvern Instrument Zetasizer (ZEN 3690). A scanning electron microscope (Hitachi S-4800) operating at a working voltage of 5 kV and a working current of 10 nA as well as a transmission electron microscope (JEM-1400 Plus Electron microscope) operating with an acceleration voltage of 100 kV were used to investigate the morphological aspects of the polymer particles. The total amount of loaded MTX in the polymeric systems was determined spectrophotometrically using a Lambda 265 UV-Vis spectrophotometer (Perkin Elmer) or Jasco V-770 UV-Vis/NIR spectrophotometer. The concentration of MTX in the supernatant (unloaded) after the deposition of each MTXCu(II)PAA$_2$ layer and the rinsing steps was calculated using the linear regression equation obtained from the assembly calibration curve. The actual encapsulated drug concentration was therefore determined by difference from the initial MTX concentration present in the assembly.

The total amount of PLys present in the polymeric systems was spectrophotometrically determined using the Bradford protein assay. The procedure is based on the formation of a complex between the dye, Brilliant Blue G, and protein in solution. The complex causes a shift in the absorption maximum of the dye from 465 to 595 nm which is proportional to the protein present. Hence, 10 μL of each sample were placed in a 96-well plate and properly added of Bradford reagent (300 μL). After an incubation of 10 minutes at room temperature, the absorbance at 595 nm was measured with a microplate reader (BioTek Synergy H1M). Following the same procedure, a calibration plot of PLys in the presence of Bradford reagent was constructed in the PLys concentration range of 0-160 μg/mL (*Supplementary materials - Chapter IV, Figure S35*).

The morphological stability of the developed nanoparticles was determined by SEM measurements after the incubated nanoparticles were in PBS (pH 7.4) at 37 °C for one week.

Chapter V:

Molecular recognition properties of charged species by macrocyclic hosts

Carboxylate prism[n]arenes could provide ideal platforms for the development of supramolecular carriers. Indeed, the inclusion of a drug into the host cavity achieves a molecular-level control of the interacting components and quantitative drug loading by the host-guest complexation. Moreover, the dynamic nature of non-covalent interactions makes “supramolecular therapy” sensitive to internal/external stimuli, facilitating efficient targeted release.[317,318]

Within the framework of a collaboration with the research group of Prof. P. Neri and C. Gaeta (University of Salerno), the ability of carboxylate prism[n]arenes receptors to recognise positively charged model species (*Figure 112*) in aqueous solution was investigated through isothermal titration calorimetry (ITC) measurements to assess how the different guest charge, size, shape and/or receptor size/conformation can affect the inclusion process.

Tetramethylammonium iodide (**Me_4N^+**)

Tetraethylammonium iodide (**Et_4N^+**)

Dabcodihexyl diiodide (**$DABCOHe_2^{2+}$**)

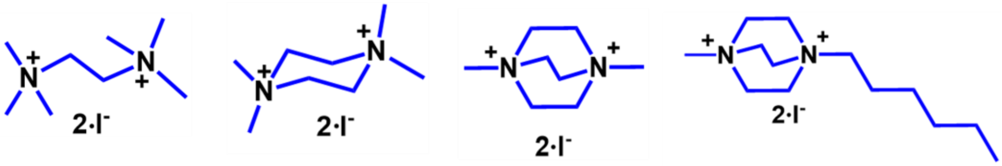

Hexamethyl ethylenediammonium diiodide (**$Et(Me_3N)_2^{2+}$**)

Tetramethyl piperazonium diiodide (**Me_4Pip^{2+}**)

Dabcodimethyl diiodide (**$DABCOMe_2^{2+}$**)

Dabcohexylmethyl iodide (**$DABCOHeMe^{2+}$**)

Figure 112. Mono and double charged cationic guests.

1. RESULTS AND DISCUSSION

Calorimetric measurements provided key information on the binding affinities and the energetics of the recognition processes occurring in solution between prims[n]carboxy and guests of different sizes, shapes and charge.[47] The determination of the enthalpic and entropic contribution to the Gibbs free energy revealed striking features on the forces driving the complexation equilibria in solution and their dependence on the host and/or guest structural features.

Typical ITC titrations for the $Et(Me_3N)_2^{2+}$-PrS[5]^{carboxy} and Me_4Pip^{2+}-PrS[6]^{carboxy} complex formation at 25 °C in buffered aqueous solution (pH 7.6) are shown in *Figure 113* and *Figure 114*, respectively. Further ITC titration curves are shown in *Supplementary materials - Chapter V, Figure S36 - Figure S47*. The binding constant and thermodynamic parameter values are listed in *Table 15* and displayed in *Figure 115*.

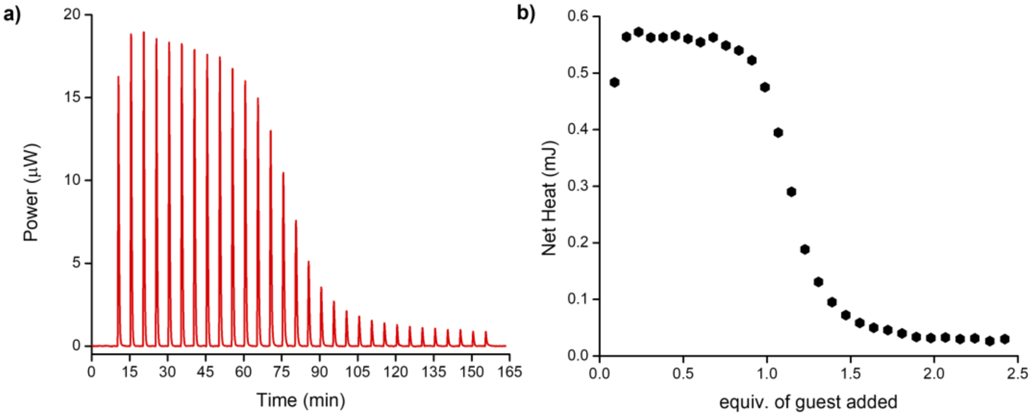

Figure 113. *a)* ITC titration of $Et(Me_3N)_2^{2+}$ (3.04 mM) into a PrS[5]^{carboxy} (0.35 mM) solution at 25 °C and pH 7.6 and *b)* integrated heat data for the $Et(Me_3N)_2^{2+}$/ PrS[5]^{carboxy} system.

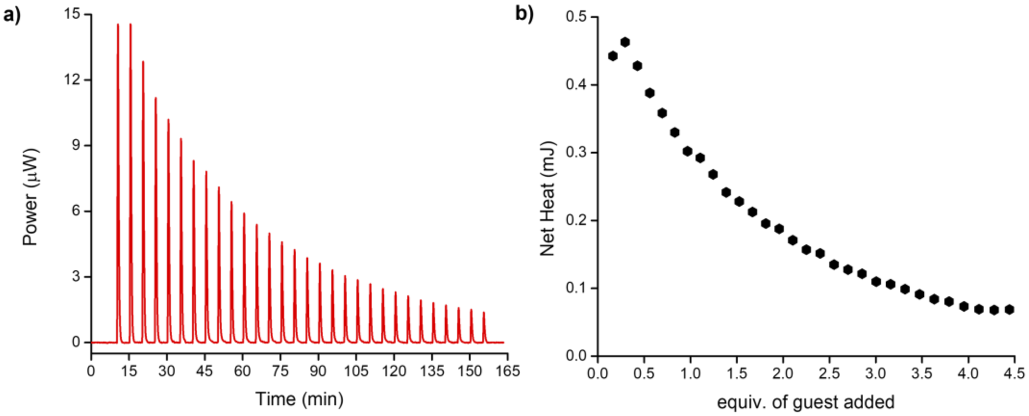

Figure 114. *a)* ITC titration of Me_4Pip^{2+} (10.0 mM) into a $PrS[6]^{carboxy}$ (0.63 mM) solution at 25 °C and pH 7.6 and *b)* integrated heat data for the $Me_4Pip^{2+}/PrS[6]^{carboxy}$ system.

Table 15. Log K values[a] and thermodynamic parameters[a] for host-guest complex formation at 25 °C at pH 7.6.

	$PrS[5]^{carboxy}$			**$PrS[6]^{carboxy}$**		
Guest	**Log K**	**ΔH^0 [b]**	**ΔS^0 [c]**	**Log K**	**ΔH^0 [b]**	**ΔS^0 [c]**
Me_4N^+	4.51 (9)	-15.21 (2)	36 (2)	3.5 (2)	-1.33 (6)	63 (4)
Et_4N^+	3.50 (3)	-24.66 (1)	-15.8 (6)	3.3 (2)	-1.54 (6)	58 (4)
$Et(Me_3N)_2^{2+}$	5.1 (2)	-26.45 (2)	9 (3)	3.10 (5)	-7.95 (2)	32.7 (9)
$DABCOHe_2^{2+}$	4.5 (1)	-30.02 (2)	-14 (3)	3.41 (6)	-12.21 (2)	25 (2)
$DABCOHeMe^{2+}$	4.5 (1)	-33.65 (3)	-27 (3)	3.29 (1)	-12.63 (1)	20.5 (4)
$DABCOMe_2^{2+}$	3.87 (6)	-18.53 (2)	13 (2)	2.91 (3)	-14.92 (1)	5.7 (6)
Me_4Pip^{2+}	5.3 (2)	-33.91 (3)	-12 (4)	3.05 (3)	-16.71 (1)	2.3 (6)

[a] σ in parentheses; [b] in $kJ\cdot mol^{-1}$; [c] in $J\cdot K^{-1}\cdot mol^{-1}$.

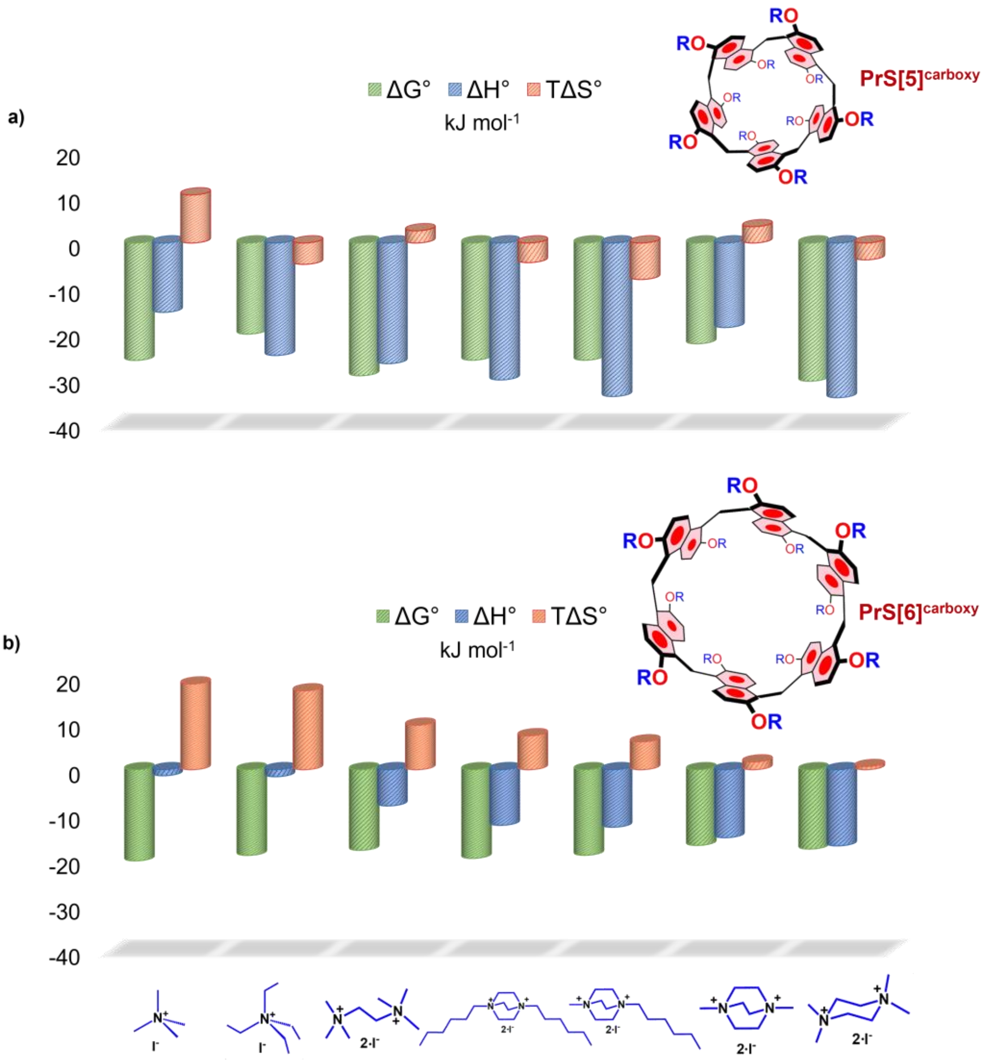

Figure 115. Thermodynamic parameters for host-guest complex formation of *a)* prism[5]^{carboxy} and *b)* prism[6]^{carboxy} with positively charged guests at 25 °C in buffered aqueous solution (pH 7.6).

Prism[5]^{carboxy} host forms 1:1 complexes with all the mono- and bis-N-alkyl-ammonium guests confirming what has been observed by NMR titrations carried out in the group of Prof. Neri and Gaeta. Different species and their combinations were tested in the model but they were always rejected by the program which always converged to the 1:1 species. This result further proves that the macrocycle cavity is unable to encapsulate more than one guest while the negatively charged rims prevent the possible assembling of a 2:1 capsular structure due to the strong electrostatic repulsion between the two facing prism[5]^{carboxy} receptors. The inclusion complexes exhibit affinity constant values ranging from 10^3 to 10^5 M^{-1}, which are reasonably smaller than those previously determined for the inclusion of some of these guests into the homologous prism[5]arene cavity in organic solvent.[319] The drop in the guest affinity is expected due to the different complexation environments as water competes strongly for hydrogen bonds and efficiently solvates charged species.[320,321]

Results in *Table 1* suggest that the stability of the host-guest complexes is significantly affected by the structural features of the differently charged guests. The largest binding affinities were achieved for prism[5]^{carboxy}- Me_4Pip^{2+} and - $Et(Me_3N)_2^{2+}$, with log K values of 5.3 (2) and 5.1 (2) respectively, as these guests successfully meet the requirements to fill the host cavity volume and establish a larger number of favourable interactions. As for monocations, prism[5]^{carboxy} displays a greater affinity for Me_4N^+ than Et_4N^+ with a selectivity ratio $Me_4N^+/Et_4N^+$of 9.5, thus pointing out a correlation between affinity and selectivity which may be relevant for host-guest systems in which electrostatic interactions perform important roles.[322]

The larger binding affinity for dicationic than for monocationic analogues suggests that Coulombic favourable interactions between the carboxylate groups of the host rims and the ammonium ions, along with cation-π interactions with the prismarene cavity, are fundamental for an efficient complexation as they contribute enhancing the free energy of binding by *ca.* 4 $kJ \cdot mol^{-1}$. Noteworthy, the binding of the triethylenediamine derivatives is affected by the guest size. $DABCOMe_2^{2+}$ has the smallest affinity for prims[5]^{carboxy} while the presence of longer alkyl chains in $DABCOHeMe^{2+}$ and $DABCOHe_2^{2+}$ increases their stability of about 0.6 log unit, resulting in a selectivity ratio of the latter two guests *vs.* $DABCOMe_2^{2+}$ of 4.3. Significantly, the second alkyl chain in $DABCOHe_2^{2+}$ does not provide any relevant contribution to the free energy of binding of this guest.

The inclusion of all ammonium cations into the hydrophobic cavity of prism[5]^{carboxy} is due to enthalpically favorable attractive forces (including electrostatic, cation-π, and

CH-π interactions) which drive the molecular recognition process. The sizable enthalpy gain (ΔH^0 ranges from -15.21 to -33.91 kJ·mol^{-1}) overrides the cost in energy needed for the desolvation of the interacting components. The complexation of bulkier guests is driven by larger enthalpy values as the result of a more favoured interaction with the host interior walls mostly due to enhanced CH-π binding sites.

The complexation of Me_4Pip^{2+} and $DABCOHeMe^{2+}$ is a more exothermic event than in the case of other guests but with an entropic penalty which accounts for the loss of degrees of freedom due to host-guest complex formation and/or to a lower desolvation upon inclusion in the aromatic cavity of the host. Desolvation is still a relevant process for the binding of methyl-terminated guests (such as $DABCOMe_2{}^{2+}$ and $Et(Me_3N)_2{}^{2+}$) and Me_4N^+, which benefits from a favourable entropic contribution.

Calorimetry measurements indicated that prism[6]^{carboxy} also forms only 1:1 inclusion complexes with all the charged guests despite its larger cavity size. The association constants are all in the order of 10^3 M^{-1} and the smaller binding affinities than prism[5]^{carboxy} could be attributed to the greater conformational flexibility of this large macrocycle which causes an unsuitable fit between the guest size and the host cavity. A similar trend was already observed in organic solvent for the guest binding involving the homologous non-water-soluble prism[5] and [6]arenes. [44,319]

Unlike prism[5]^{carboxy}, the stability constant values determined for prism[6]^{carboxy} are quite comparable regardless of shape, size, charge and length of the aliphatic chains of the different guests. The free energy gain that one would expect when complexing double-charged molecules is not observed in this case[325] thus indicating, at first glance, that the structural features of the guests do not affect the stability of the complex species likely due to the levelling effect of the conformational mobility of the macrocyclic cavity. Slightly larger affinities were found for the complexation of Me_4N^+ and $DABCOHe_2{}^{2+}$. Overall, the host-guest complexes formed by both prism[5] and [6]^{carboxy} with monocationic guests have greater stability than those formed by other neutral macrocyclic receptors such as 18-crown-6, β-cyclodextrins and resorcin[4]arenes in aqueous and/or organic solvent, with affinities for the latter systems being in the order of 10^2 M^{-1}. This evidence emphasizes the role of the anionic moieties of the prism[n]^{carboxy} macrocycles which favour electrostatic interactions and thus provide supplementary anchoring points for guest complexation. However, curcubit[7]uril are reported to form more stable inclusion complexes with Me_4N^+ and Et_4N^+.[323]

Although binding free energy for all the complexes formed by prism[6]^{carboxy} is comparable (*ca.* -19 kJ·mol^{-1}), intriguing differences can be revealed when the enthalpic and entropic contributions are determined. The ammonium guests may be arranged in two main classes depending on their charge. The encapsulation of monocations into the prism[6]^{carboxy} cavity is an entropically favored and driven process ($T\Delta S^0$ is *ca.* 18 kJ·mol^{-1} on average). Desolvation of the cations as well as the release of water molecules from the solvent-filled cavity of the host to the bulk of the solvent account for the large entropic gain. The encapsulation process also presents a slightly favorable enthalpic contribution as the result of attractive/favorable host-guest interactions and the release of "high energy" water molecules from the prism[6]^{carboxy} cavity interior towards the hydrogen-bond network of the aqueous solvent upon complexation.[324,325]

Conversely, the electrostatic interactions occurring with the carboxylate residues of prismarene rims along with multiple cation-π and CH-π interactions with the host cavity drive the molecular recognition of the double-charged guests, as indicated by the enthalpy guide of the process. However, the structural features of the guests seem to heavily influence the enthalpic gain values for the complexation of the bis-N-alkyl-ammonium guests (ΔH^0 gain follows the order $DABCOMe_2^{2+}$ > $DABCOHeMe^{2+}$ > $DABCOHe_2^{2+}$). Longer side alkyl chains (which, in turn, increase the size of the guest) confer larger hydrophobicity and a smaller charge-to-radius ratio resulting in a lower overall charge density. Accordingly, electrostatic and/or cation-π interactions are less efficient while the role of desolvation and CH-π interactions with the host cavity walls are enhanced.[326] The positive entropic term indicates a favourable contribution to the ΔG^0 value due to host and guest desolvation although to a smaller extent than in the case of monocations likely due to the reduced conformational flexibility of the host cavity walls upon encapsulation of the bulkier dicationic guests.[327] An intermediate feature is shown by the complex formed with $Et(Me_3N)_2^{2+}$, whose enthalpy and entropy changes contribute comparably to the ΔG^0 of the reaction, with a slight prevalence of the latter term. Indeed, the peculiar structure of this double-charged guest, which can be thought of as the combination of two monocations held together by an alkyl linker, places it between the two classes of guests.

Overall, the formation of the host-guest complexes displays a larger entropic contribution in the case of the prism[6]^{carboxy} cavity as a consequence of its greater conformational freedom and more significant desolvation upon guest inclusion than in the case of the smaller and more rigid prism[5]^{carboxy} host. However, the preorganization of the latter macrocycle results in a more efficient binding affinity for the charged guests. These findings are confirmed by the enthalpy–entropy compensation effect which is commonly observed in supramolecular recognition systems. [236,328-330]

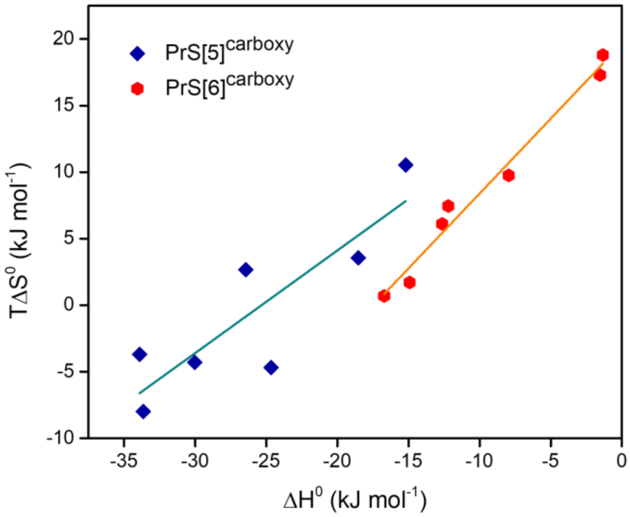

Figure 116. Enthalpy-entropy compensation plot for prism[n]^{carboxy} - guest complex formation at 25 °C at pH 7.6.

Although this topic has been much debated, a linear correlation between $T\Delta S^0$ and ΔH^0 values occurs for the host-guest complexes formed by both prism[n]^{carboxy} with all the charged guests, clearly indicating that the enthalpy changes are offset by the corresponding changes in the entropic contribution (*Figure 116*). The slope and the intercept ($T\Delta S_0^0$) of the $T\Delta S^0$ *vs.* ΔH^0 plot might provide quantitative insights for changes in conformation and desolvation of both host and guest.[236] Generally, slope values lower than unity might be expected for macrocycles characterized by a rigid structure whilst a slope closer to unity could be indicative of a rearrangement of the hydrogen-bond network and a conformational change of the macrocycle structure.[329] The complexation thermodynamic fingerprint for prism[5]^{carboxy} affords a slope of 0.7 (1) and an intercept of 19 (4) kJ·mol^{-1} which can be attributed to a low flexibility of the macrocycle host. Conversely, prims[6]^{carboxy} exhibits a larger slope of 1.12 (7) and a $T\Delta S_0^0$ value of 19.6 (8) kJ·mol^{-1} which both account for a greater host flexibility and a larger number of water molecules in the interior and exterior of the macrocycle cavity than in the case of prism[5]^{carboxy}. Despite results obtained for different host-guest systems may not be directly compared as the complexation process involves different interactions, the $T\Delta S_0^0$ term obtained for both systems is fairly higher than that reported for supramolecular systems involving cyclodextrins (13 kJ·mol^{-1}) or crown ethers (12 kJ·mol^{-1}) and nicely comparable with receptors bearing hydrophilic flexible moieties. [236] On the whole, these values reveal that the larger entropic gain observed for the complexes formed by prismarenes mostly arises from desolvation upon guest inclusion.

2. CONCLUSIONS

The calorimetric study provided a critical comprehension of the efficiency of the prismarene host to include molecules of different sizes/shapes and gave essential information about the role played by the guest charge in the complexation process. Prism[5]^{carboxy} forms 1:1 complexes with all the investigated guests. Complexes exhibit affinity constant values ranging from 10^3 to 10^5 M^{-1} and the inclusion processes are overall driven by enthalpically favorable attractive forces.

PrS[6]^{carboxy} host also forms 1:1 species with both mono- and bis-N-alkyl ammonium guests in neutral aqueous solution. The properties of the different guests do not affect the stability of the host-guest complexes which have a similar binding affinity. However, different contributions to the ΔG^0 values emerge when the entropic and enthalpic terms are determined. Host and guest desolvation along with the release of high-energy water from the host cavity to the bulk of the solvent drive the formation of the complexes with the monocation guests. Enthalpically favorable attractive forces drive the formation of the complexes with dication molecules, whose energetic profile is clearly influenced by their size.

The thermodynamic fingerprint of the guest complexation phenomena could pave the way for the construction of new prismarene-based supramolecular systems with intriguing properties that could be employed both for molecular recognition and drug loading/release applications in aqueous medium.

3. EXPERIMENTAL SECTION

3.1 Materials

Prism[6]carboxy and prism[5]carboxy (PrS[n]^{carboxy,} n = 5, 6) as well as monocationic (tetramethylammonium iodide (Me_4N^+), tetraethylammonium iodide (Et_4N^+)) and dicationic (hexamethyl ethylenediammonium diiodide ($Et(Me_3N)_2^{2+}$), dabcodihexyl diiodide ($DABCOHe_2^{2+}$), dabcohexylmethyl iodide ($DABCOHeMe^{2+}$), dabcodimethyl diiodide ($DABCOMe_2^{2+}$), tetramethyl piperazonium diiodide (Me_4Pip^{2+})) guests were provided by the research group of Prof. P. Neri and C. Gaeta (University of Salerno) and used as received. Phosphate buffer (PB, 70 mM, pH 7.6) was prepared by weighting proper amounts of sodium phosphate dibasic dihydrate and sodium phosphate monobasic purchased from Sigma-Aldrich Sigma-Aldrich. High-purity water (Millipore, Milli-Q Element A 10 ultrapure water) and A grade glassware were employed throughout.

3.2 Isothermal titration calorimetry (ITC) measurements

Calorimetric titrations were carried out following the procedure described in *Chapter II - Experimental section, Isothermal titration calorimetry (ITC) measurements*.
Aqueous buffered solutions of each guest (2.5÷20.0 mM) were titrated into an aqueous buffered solution of PrS[n]^{carboxy} (0.25÷1.2 mM) host. All solutions were prepared in 70 mM phosphate buffer (pH 7.6). Typically, three independent experiments were run for each host-guest system. Heats of dilution were determined in separate "blank" experiments by titrating the solutions of each guest into phosphate buffer (pH 7.6, 70 mM) only. Net heat values were analyzed using the HypCal software.

Chapter VI:

Conclusions and Future Perspectives

The doctoral thesis proposes a detailed thermodynamic analysis of the equilibria occurring in solution as the key strategy for designing and developing stimuli-responsive drug delivery systems. Specifically, the multiple non-covalent interactions occurring among selected model drugs (quercetin, Que and methotrexate, MTX), the pH-sensitive poly(acrylic acid) (PAA) and metal ions of biological interest (Cu(II), Zn(II) and Co(II)) were exploited to develop pH-responsive assemblies. The accurate examination of all the equilibria involving the three system components was crucial to determine the species, the binding features and the energetics for the interaction of the drugs (Que or MTX) with the metal ions and PAA as well as of the metal ions with PAA in aqueous solution at 25 °C and pH 7.4. Striking aspects on the forces driving the interaction processes and the possible mechanisms involved in the complex formation were revealed and ensured the accurate control and optimization of the stability, drug loading and release capabilities of the resulting Que and MTX-based assemblies.

The stability over time of the systems containing quercetin and the release of both model drugs from the assemblies under pH stimuli proved that the rational design of the delivery platforms permitted reducing/overcoming the degradation issues of the drugs and achieving their site- and time-controlled release. Particularly, these studies highlighted the longer half-life of the metal-coordinated assemblies containing quercetin than the free flavonoid, pointing out the ability of the polymeric systems to enhance the stability of the quercetin over time. The non-covalent nature of the interactions involving the system components was found to be responsible for the reversible binding that enabled the release of the drug in a pH-dependent manner thus increasing its efficacy. These features make the assemblies desirable tools for antimicrobial and/or anticancer applications since they should reduce the drug side effects on the healthy physiological environment.

Physico-chemical and morphological studies allowed a structural characterization (morphology, size and charge) of the assemblies containing MTX. The therapeutic efficacy of the developed systems was assessed in the U87 glioblastoma cell line. Proper *in vitro* assays demonstrated the higher cytotoxic activity of the metal-coordinated assemblies compared to that of free uncomplexed MTX in glioblastoma cancer cells. FACS-based analysis suggested the ability of the metal-coordinated assemblies to generate a higher amount of ROS that can be considered a possible mechanism of cell death.

Since the biodistribution and cellular uptake of a delivery system can be affected by the interaction with plasma proteins that may cover the targets and hinder their specific reaction with ligands, the ability of the MTX-based assemblies to interact with human serum albumin (HSA) was explored.

A potential delivery system for MTX based on the electrostatic interactions occurring between the drug and a positively charged polymer was also prepared. The higher affinity between methotrexate and polymer allowed the formation of a much more stable complex than those formed with the metal-PAA systems but no controlled release of the drug was unfortunately observed. This evidence pointed out the importance of the presence of metal ions to develop pH-responsive systems for MTX and emphasised that the accurate knowledge of the affinity of a drug for a carrier is crucial to develop not only stable systems with high loading capacity but also platforms with smart release properties.

Moreover, the MTX-copper based assembly was suitably employed for developing polymeric nanoparticles using the *layer-by-layer* technique and their characterization unveiled the optimal morphology structural properties for an efficient internalization.

Finally, the investigation of the inclusion processes of positively charged guests into synthetic macrocyclic cavities having different sizes and conformational mobility provided the complete thermodynamic fingerprint needed for the development of successful supramolecular carriers.

Overall, this doctoral work highlighted the fundamental impact of examining multiple solution equilibria for the design and development of a versatile delivery platform exhibiting stability over time, pH-controlled release of the loaded drug and enhanced cytotoxic activity towards cancer cells.

The results could pave the way for developing new metal-coordinated assemblies containing different antimicrobial or anticancer drugs and molecules able to respond to physiological and/or external stimuli. The development of new delivery systems for quercetin/methotrexate and their metal complexes using additional polymeric or micellar systems that could improve the stability of the drugs and/or their controlled release is the natural follow-up of the present work. Further studies will be conducted to evaluate whether the antioxidant and/or oxidant properties of these drugs are somehow influenced by the formation of the assemblies. The stabilization and biological/cytotoxic properties of the new delivery platforms will be investigated along with the characterization of the interactions with specific molecules of biological interest and membrane models. The development of multi-functional multi-layer nanoparticles based on the metal-coordinated assemblies will be a further area of investigation.

.

Supplementary materials

Chapter II:
Metal-coordinated assemblies containing quercetin

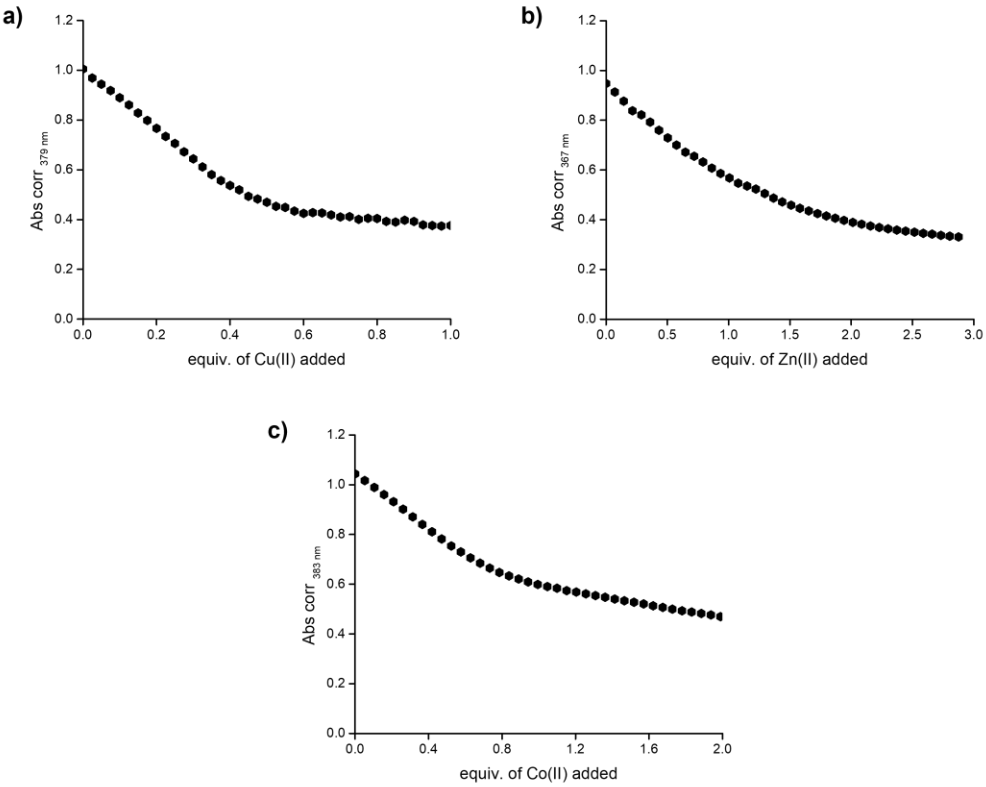

Figure S1. Molar ratio plot for the UV-Vis titration of Que (0.06 mM) with *a)* Cu(II) (0.30 mM), *b)* Zn(II) (0.87 mM) and *c)* Co(II) (0.60 mM) at 25 °C and pH 7.4 in *Figure 35*.

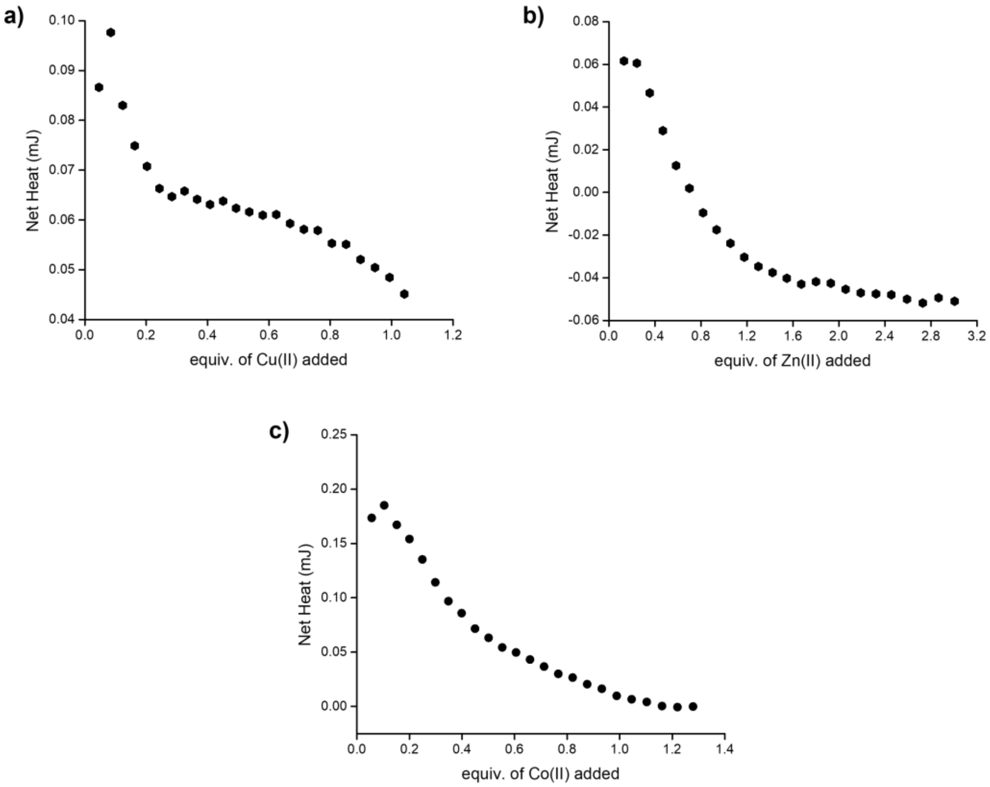

Figure S2. Integrated heat data for the ITC titration of *a)* Cu(II) (0.56 mM) into Que (0.15 mM), *b)* Zn(II) (1.40 mM) into Que (0.13 mM) and *c)* Co(II) (0.55 mM) into Que (0.12 mM) solution at 25 °C and pH 7.4 in *Figure 36*.

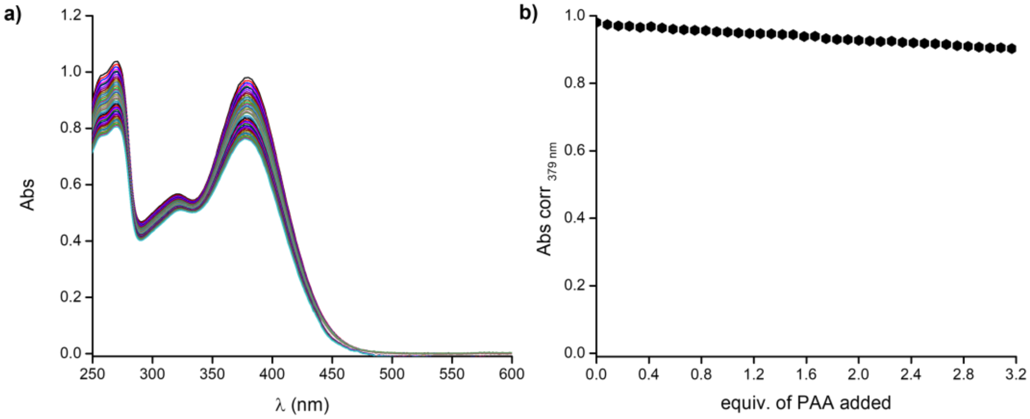

Figure S3. *a)* Typical UV-Vis titration of PAA (1.00 mM) into Que (0.06 mM) solution at 25 °C and pH 7.4; *b)* Molar ratio curve at 379 nm.

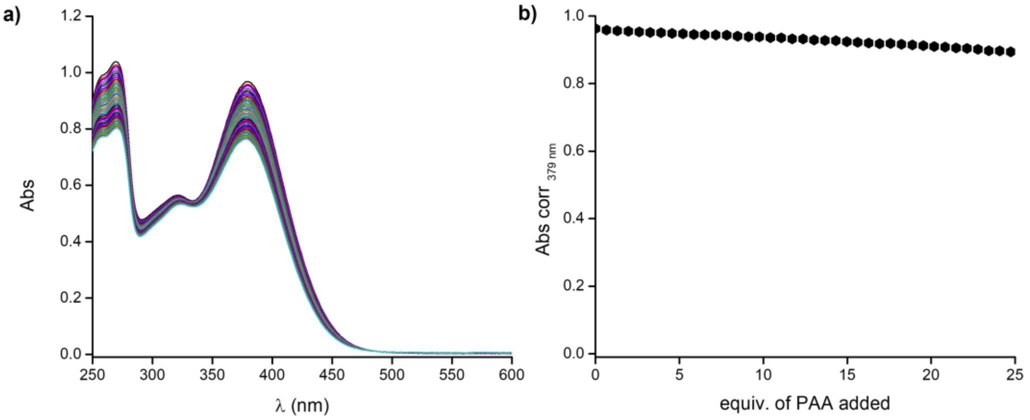

Figure S4. *a)* Typical UV-Vis titration of PAA (7.80 mM) into Que (0.06 mM) solution at 25 °C and pH 7.4; *b)* Molar ratio curve at 379 nm.

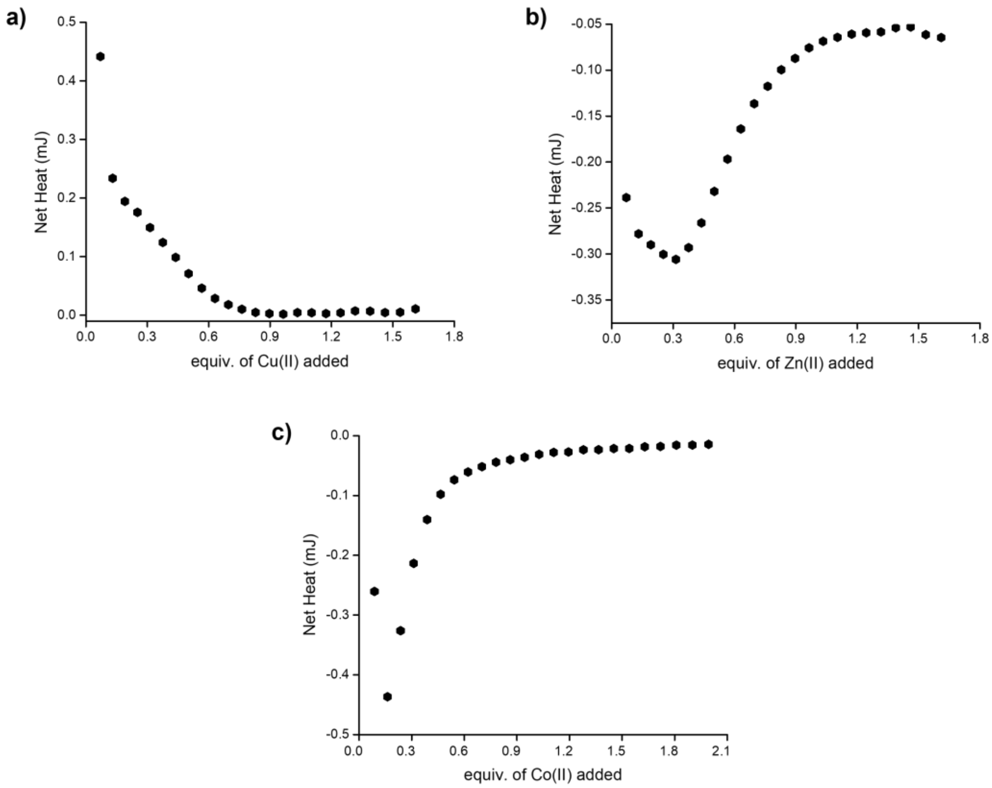

Figure S5. Integrated heat data for the ITC titration of *a)* Cu(II) (3.00 mM) into PAA (0.50 mM), *b)* Zn(II) (3.00 mM) into PAA (0.60 mM) and *c)* Co(II) (3.50 mM) into PAA (0.50 mM) solution at 25 °C and pH 7.4 in *Figure 40*.

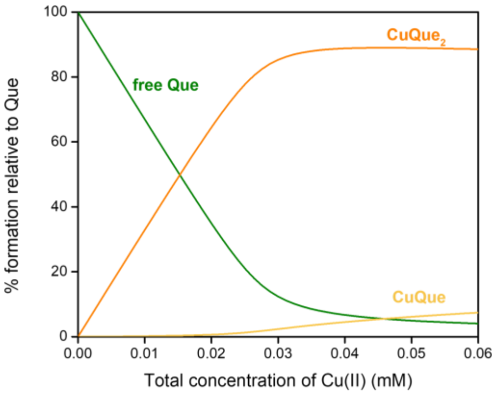

Figure S6. Distribution diagram for the copper(II)-quercetin complex species (Cu(II):Que 1:1, C_{Que} = 0.06 mM) computed by using the data in *Table 1*.

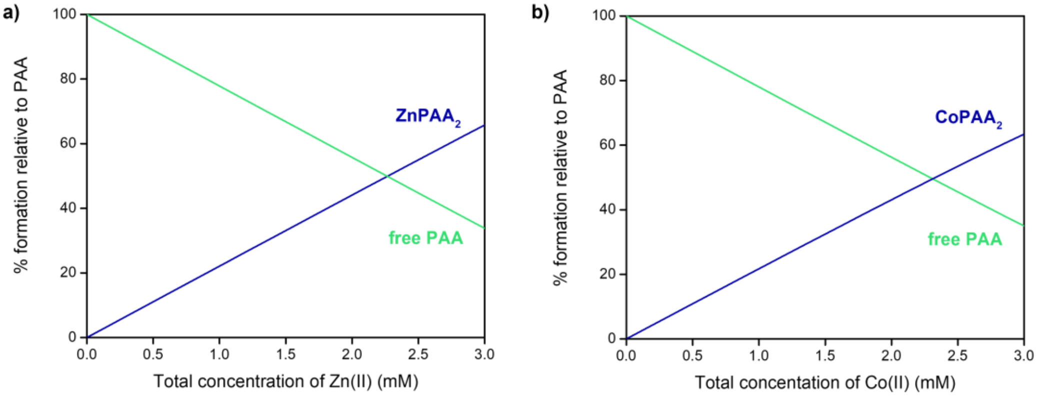

Figure S7. Distribution diagram for the metal(II)-polymer complex species (M(II):PAA 1:3, C_{PAA} = 9.00 mM) computed by using the data in *Table 3*.

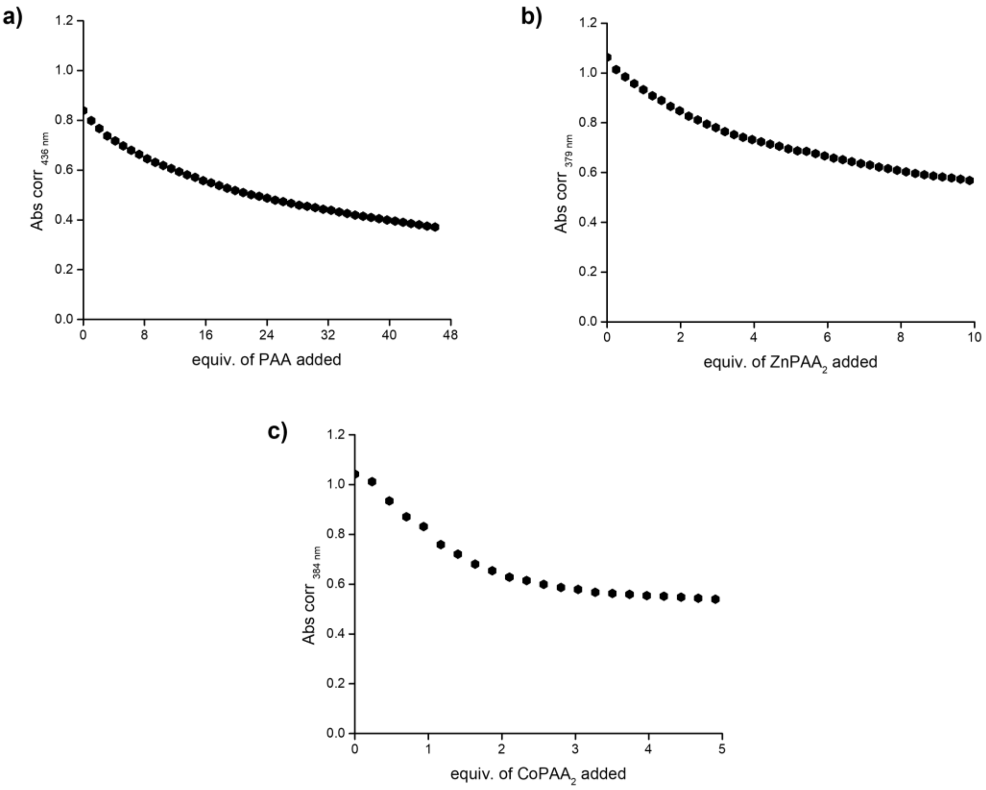

Figure S8. Molar ratio plot for the UV-Vis titration of *a)* CuQue (Cu(II):Que 1:1, C_{Que} = 0.06 mM) with PAA (12.5 mM) in *Figure 43*, *b)* Que (0.06 mM) with $ZnPAA_2$ (Zn(II):PAA 1:3; C_{PAA} = 9.00 mM) in *Figure 45a* and *c)* Que (0.06 mM) with $CoPAA_2$ (Co(II):PAA 1:3; C_{PAA} = 9.00 mM) in *Figure 45b* at 25 °C and pH 7.4.

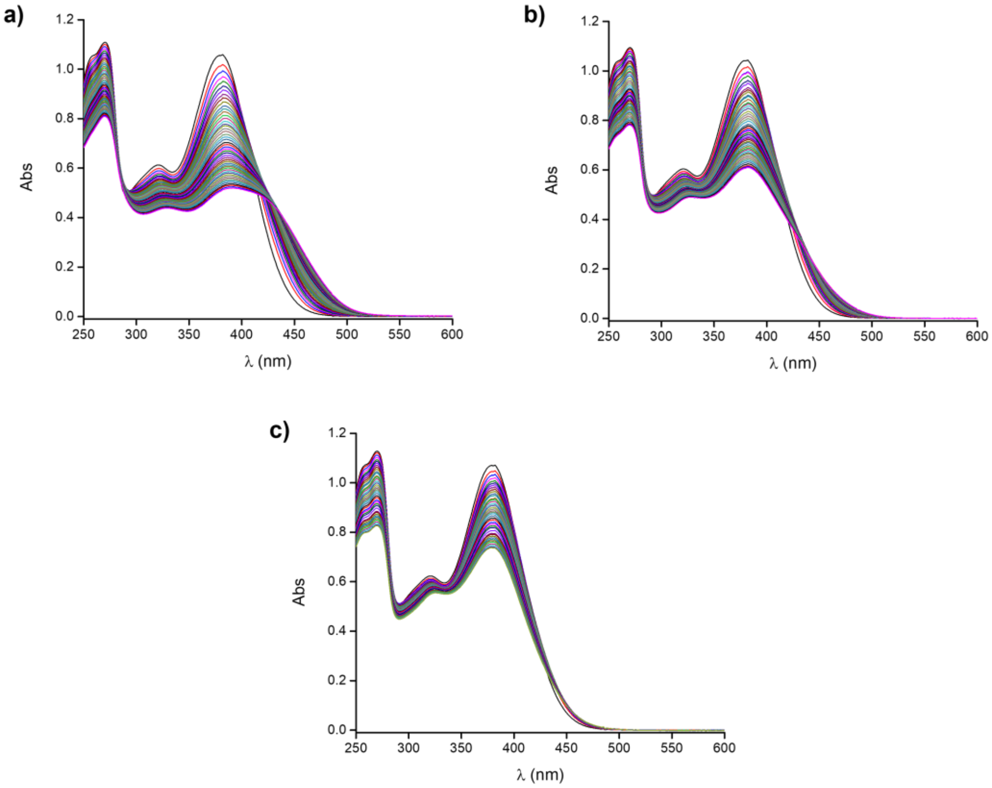

Figure S9. Typical UV-Vis titrations of Que (0.06 mM) with zinc(II)-polymer complex prepared at *a)* (M(II):PAA 1:4; C_{PAA} = 9.00 mM), *b)* (M(II):PAA 1:5; C_{PAA} = 9.00 mM) and *c)* (M(II):PAA 1:6; C_{PAA} = 9.00 mM) at 25 °C and pH 7.4

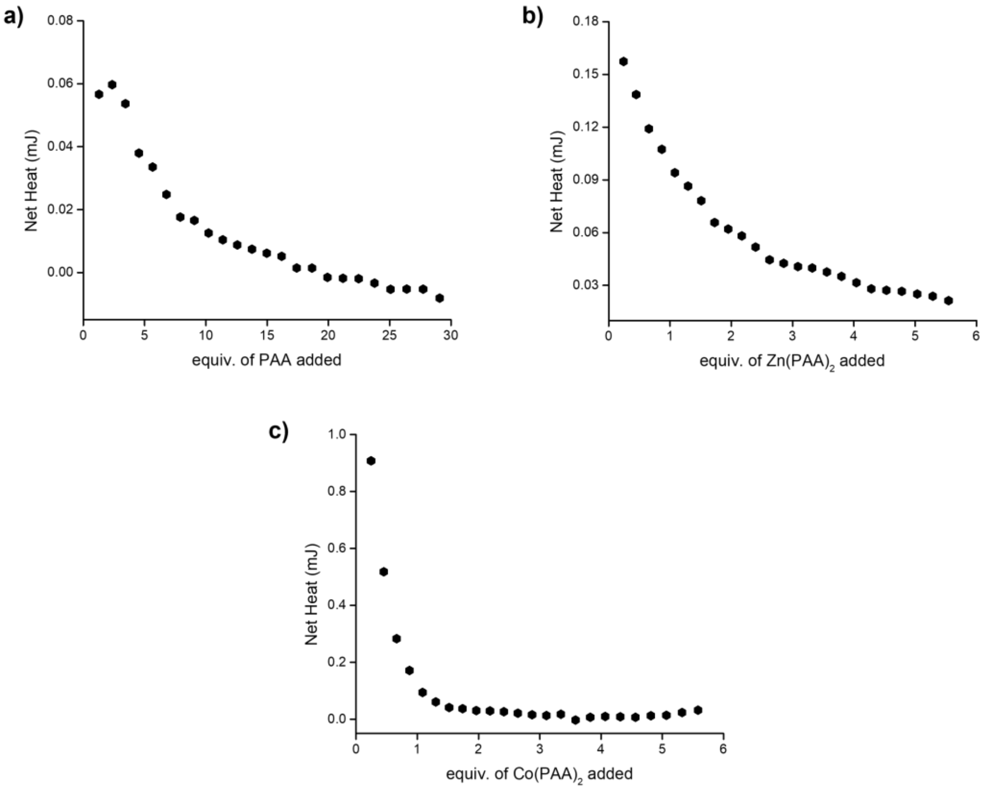

Figure S10. Integrated heat data for the titration of *a)* PAA (12.5 mM) into quercetin-copper(II) complex solution (Cu(II):Que 1:1, C_{Que} = 0.12 mM), *b)* zinc(II)- and *c)* cobalt(II)-polymer complex (M(II):PAA 1:3; C_{PAA} = 9.00 mM) into Que (0.15 mM) at 25 °C and pH 7.4 in *Figure 46*.

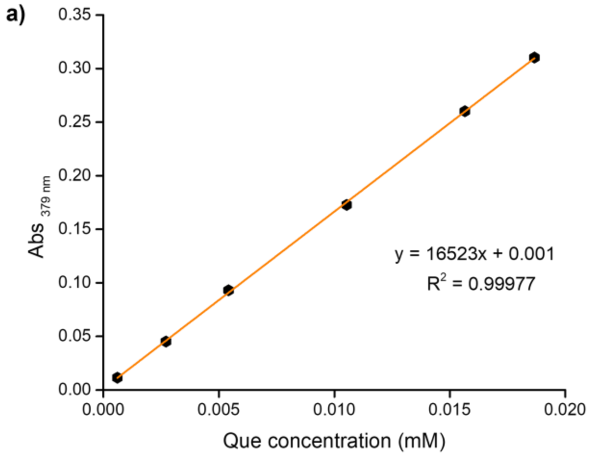

Que $\varepsilon_{379\ nm}$: 16523 M^{-1} cm^{-1}

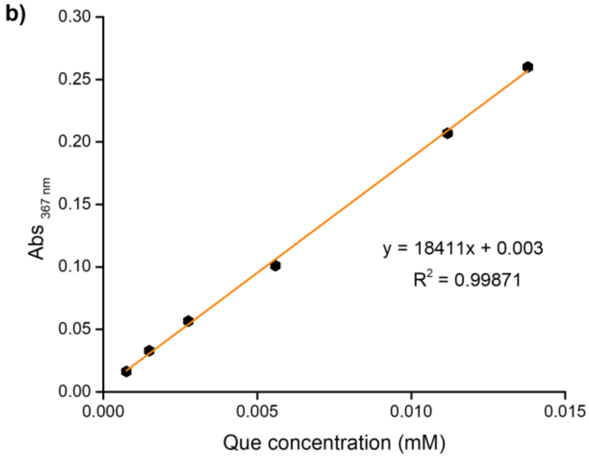

Que $\varepsilon_{367\ nm}$: 18411 M^{-1} cm^{-1}

Figure S11. Que calibration plot in aqueous solution (MOPS 10 mM) at pH *a)* 7.4 and *b)* 5.4.

Table S1. Kinetic release models of quercetin from metal(II)-coordinated assemblies at 37 °C and pH 7.4.

		pH 7.4	
Assembly	**Kinetic model**	**Equation**	**R^2**
Que_2CuPAA	Zero-order	y = 0.2053 x + 2.481	0.232
	First-order	y = -0.0021 x + 4.5798	0.228
	Higuchi	y = 1.0985 x + .2414	0.4449
	Hixson-Crowell	y = -0.0684 x + 32.506	0.232
	Korsmeyer-Peppas	y = -0.4048 x + 0.6422	0.4279
$QueZnPAA_2$	Zero-order	y = 0.6949 x + 6.6906	0.3747
	First-order	y = -0.0075 x + 4.534	0.3692
	Higuchi	y = 3.4362 x + 3.1286	0.6138
	Hixson-Crowell	y = -0.2316 x + 31.103	0.3747
	Korsmeyer-Peppas	y = 0.3877 x + 1.7652	0.5466

Table S2. Kinetic release models of quercetin from metal(II)-coordinated assemblies at 37 °C and pH 5.4.

		pH 5.4	
Assembly	**Kinetic model**	**Equation**	**R^2**
Que$_2$CuPAA	Zero-order	y = 1.1261 x + 2.2935	0.9377
	First-order	y = -0.0123 x + 4.5828	0.9475
	Higuchi	y = 4.4662 x - 0.9986	0.9881
	Hixson-Crowell	y = -0.3754 x + 32.569	0.9377
	Korsmeyer-Peppas	y = 0.6966 x + 1.0199	0.9765
QueZnPAA$_2$	Zero-order	y = 4.5108 x + 0.188	0.7322
	First-order	y = -0.0776 x + 4.3744	0.8249
	Higuchi	y = 19.312 x + 3.8028	0.899
	Hixson-Crowell	y = -1.5036 x + 26.604	0.7322
	Korsmeyer-Peppas	y = -0.7518 x + 2.7095	0.8088

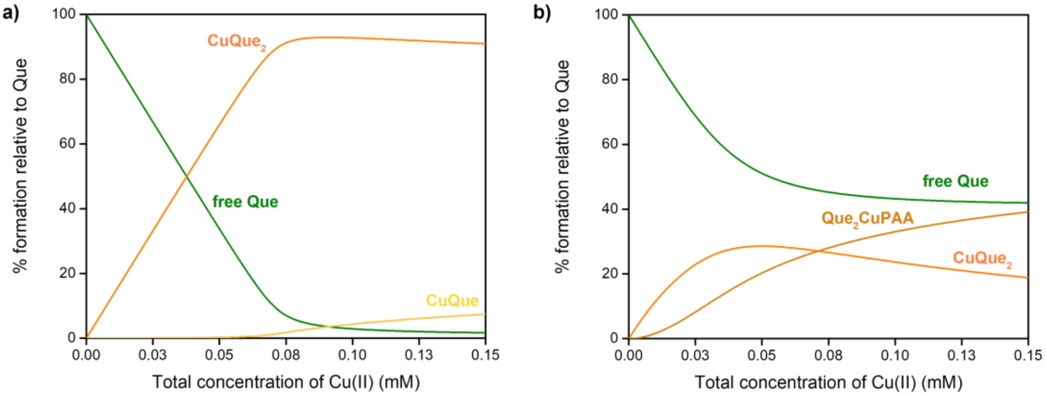

Figure S12. Distribution diagram for *a)* copper(II)-quercetin complex species (Cu(II):Que 1:1, $C_{Cu(II)}$ = 0.15 mM) and *b)* copper(II)-coordinated assembly containing quercetin (Cu(II):Que 1:1, Cu(II):PAA 1:33, $C_{Cu(II)}$ = 0.15 mM) computed by using the data in *Table 1*, *Table 3* and *Table 4*.

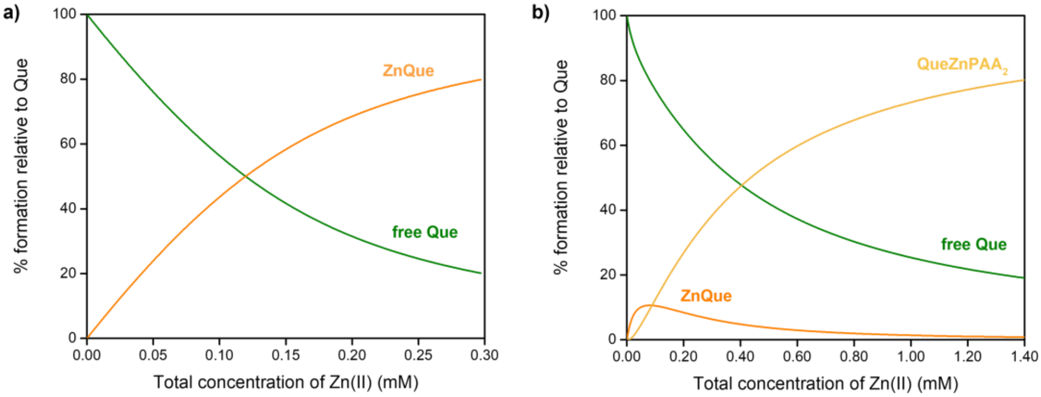

Figure S13. Distribution diagram for *a)* zinc(II)-quercetin complex species (Zn(II):Que 1:1, $C_{Zn(II)}$ = 0.15 mM) and *b)* zinc(II)-coordinated assembly containing quercetin (ZnII):Que 9:1, Zn(II):PAA 1:3, $C_{Zn(II)}$ = 1.40 mM) computed by using the data in *Table 1*, *Table 3* and *Table 4*.

Chapter III:

Metal-coordinated assemblies containing methotrexate

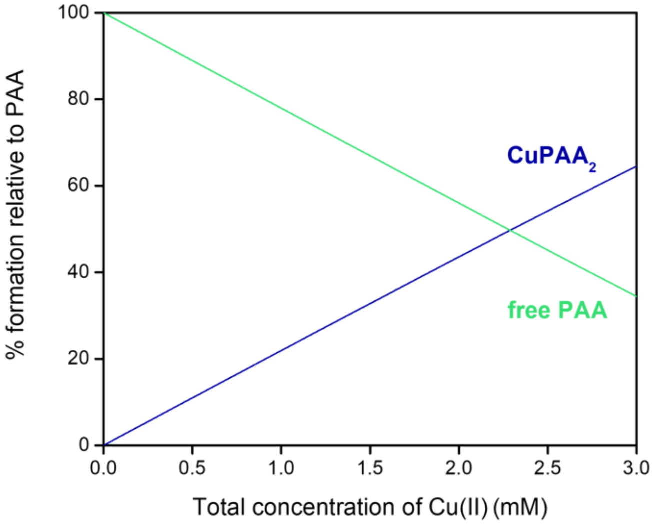

Figure S14. Distribution diagram for the copper(II)-polymer complex species (Cu(II):PAA 1:3, C_{PAA} = 9.00 mM) computed by using the data in *Table 3*.

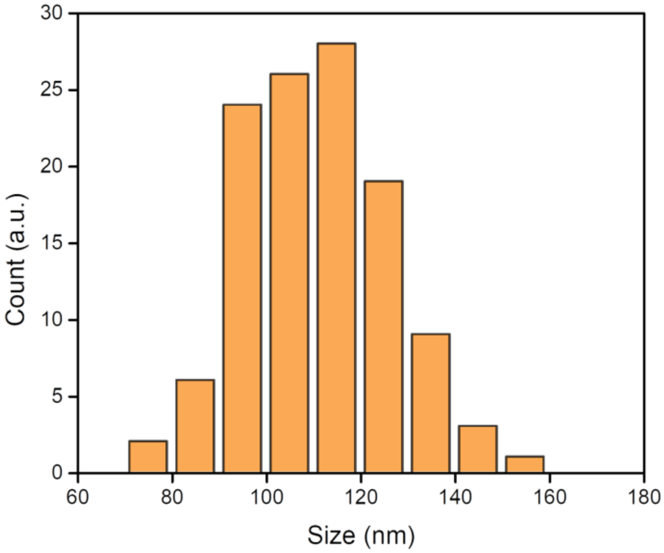

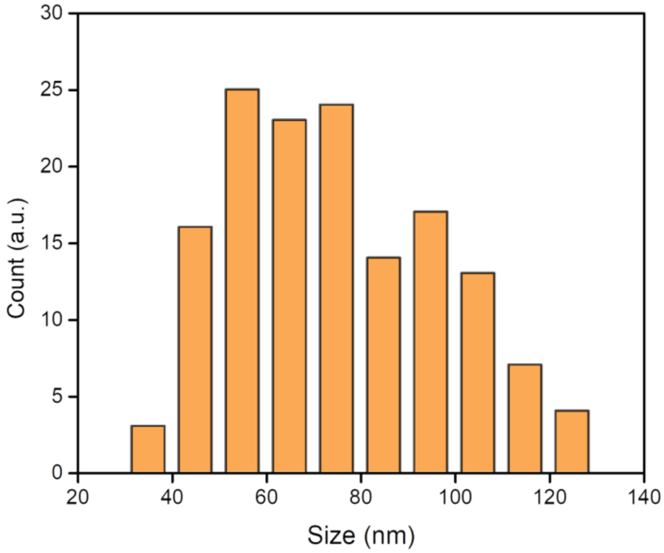

Figure S15. Copper(II)-based assemblies size graphs: $MTXCuPAA_2$ with MTX 0.40 mM (*top*) and $MTXCuPAA_2$ with MTX 1.00 mM (*bottom*).

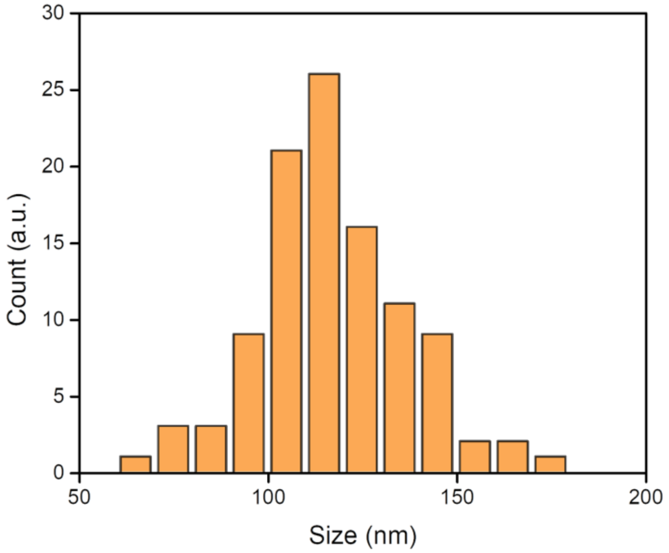

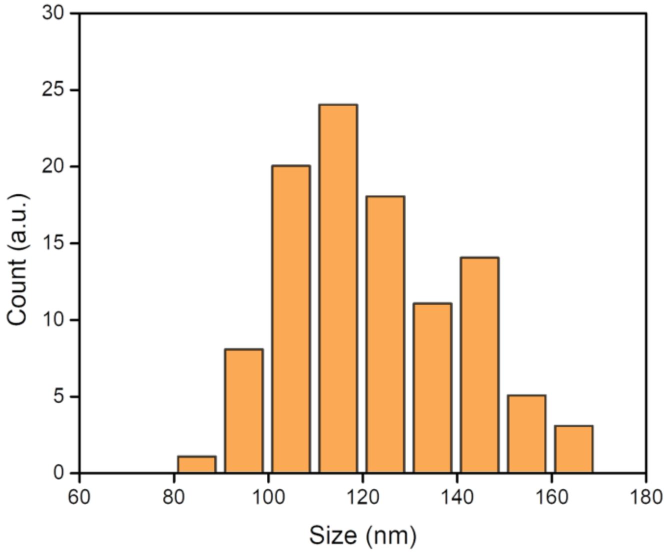

Figure S16. Zinc(II)-based assemblies size graphs: $MTXZnPAA_2$ with MTX 0.40 mM (*top*) and $MTXZnPAA_2$ with MTX 1.00 mM (*bottom*).

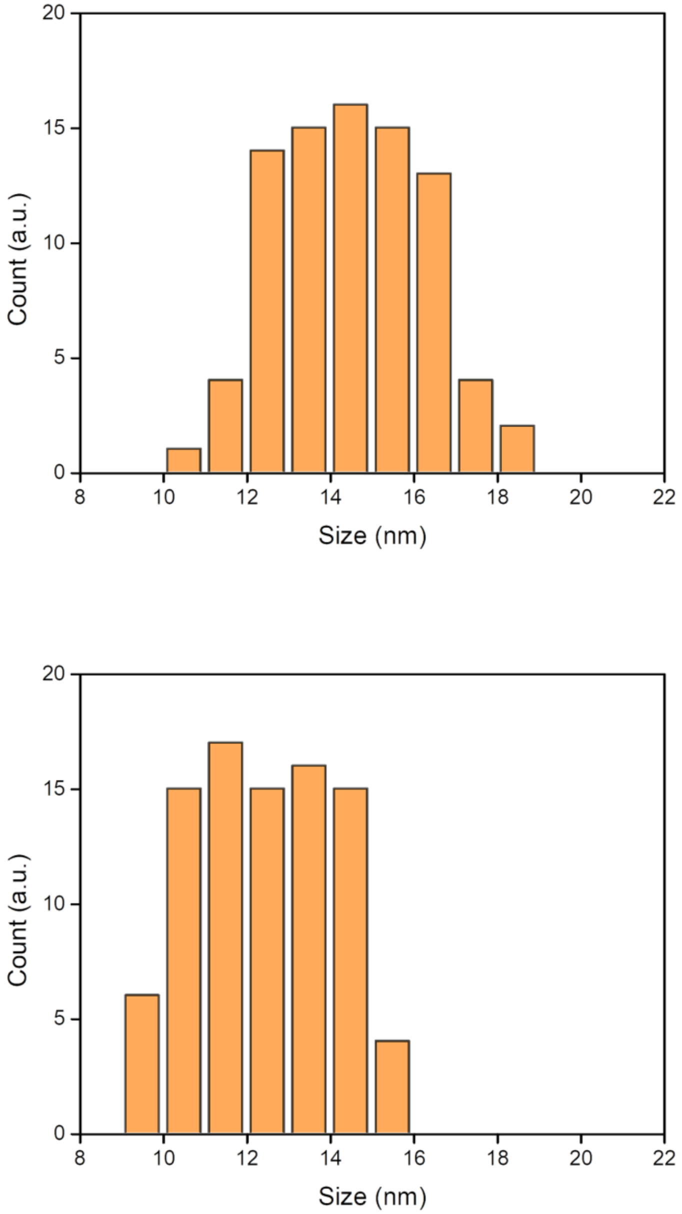

Figure S17. CuPAA$_2$ (*top*) and ZnPAA$_2$ (*bottom*) assemblies size graphs.

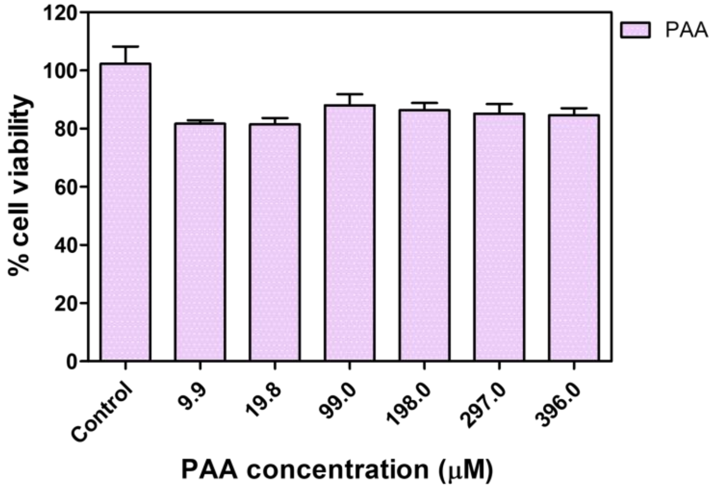

Figure S18. Viability of U87 cells treated for 48 hours with PAA.

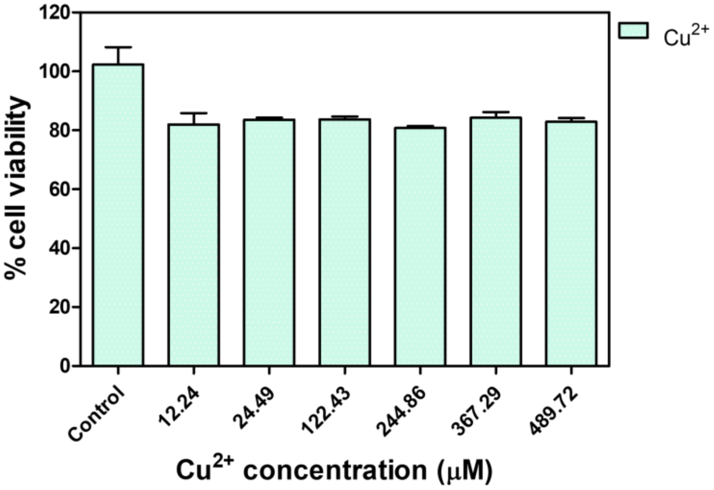

Figure S19. Viability of U87 cells treated for 48 hours with Cu(II) ions.

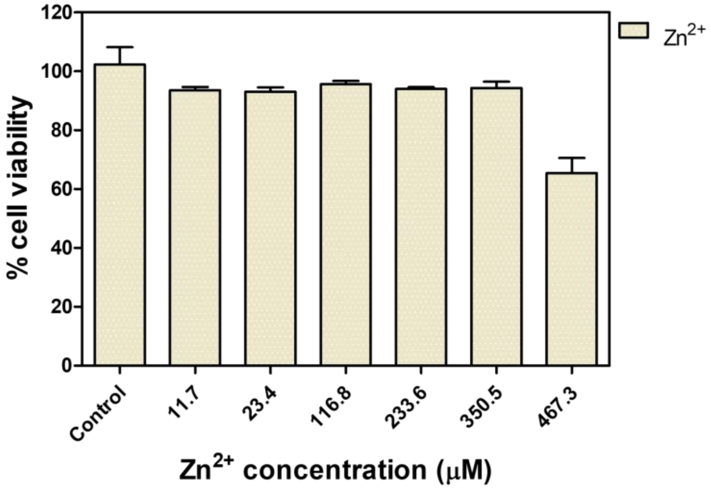

Figure S20. Viability of U87 cells treated for 48 hours with Zn(II) ions.

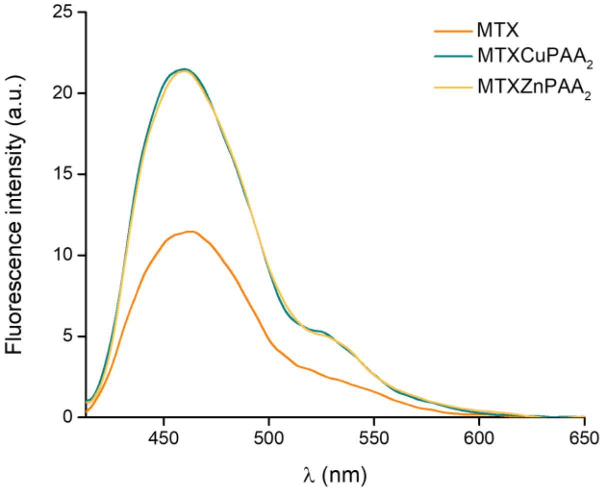

Figure S21. Fluorescence emission spectra of MTX and MTX-containing assemblies (C_{MTX} = 0.025 mM) at pH 7.4 (λ_{ex} = 340 nm).

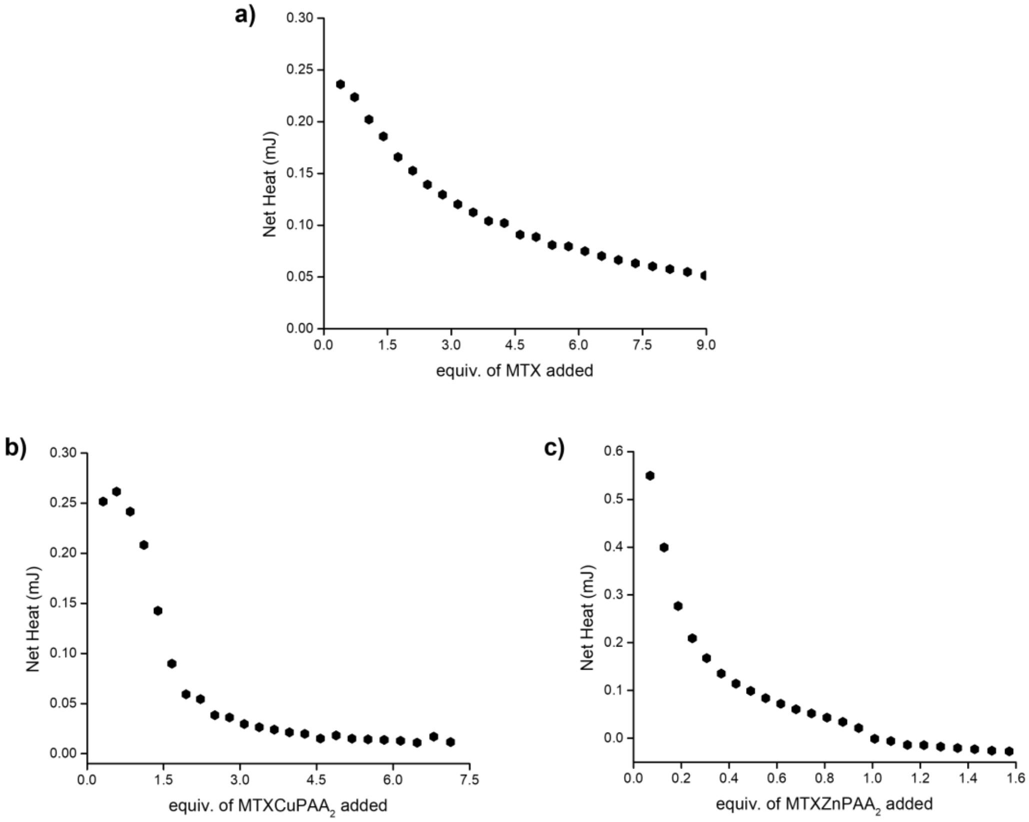

Figure S22. Integrated heat data for the titration of *a)* MTX (2.25 mM) into HSA (0.07 mM), *b)* MTXCuPAA$_2$ (0.38 mM) into HSA (0.015 mM) and *c)* MTXZnPAA$_2$ (0.33 mM) into HSA (0.06 mM) solution at 25 °C and pH 7.4 in *Figure 86*.

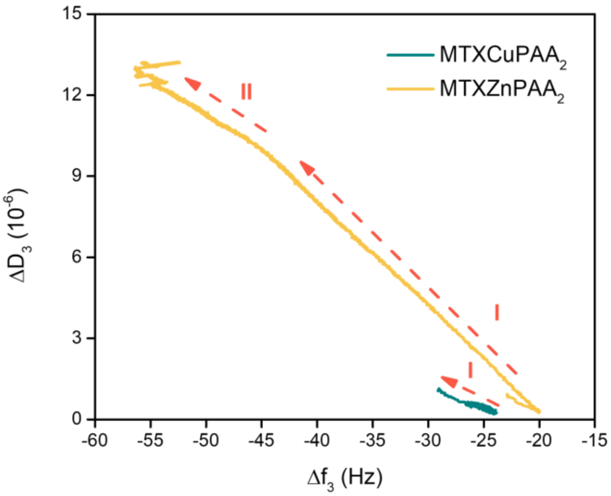

Figure S23. Representative time-dependent ΔD/ΔF data plot for MTXCuPAA$_2$ and MTXZnPAA$_2$ adsorption onto HSA layer; frequency and dissipation data are from the third overtone.

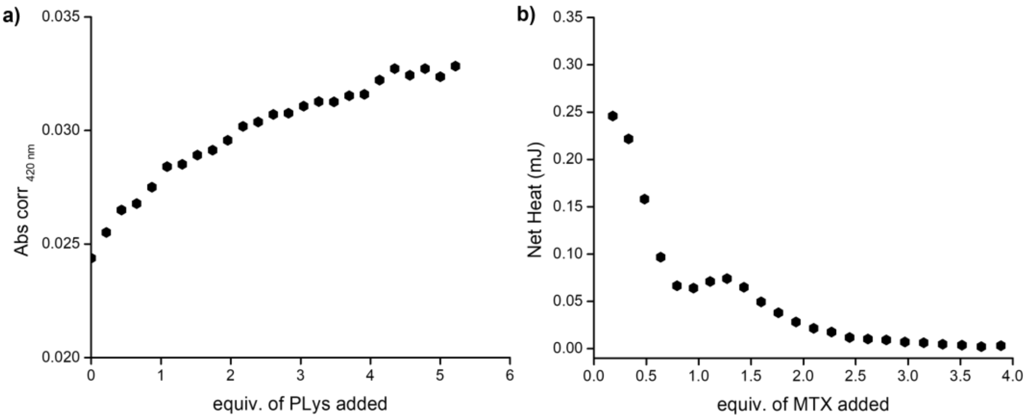

Figure S24. *a)* Molar ratio plot for the UV-Vis titration of PLys (1.00 mM) into MTX (0.023 mM) solution and *b)* integrated heat data for the titration of MTX (2.20 mM) into PLys (0.015 mM) solution at 25 °C and pH 7.4 in *Figure 92*.

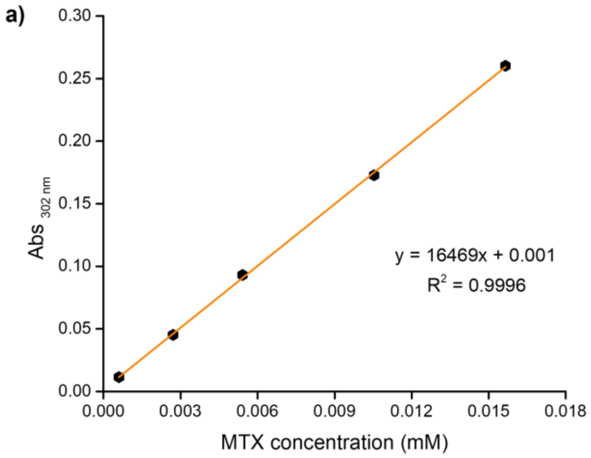

MTX $\varepsilon_{302\ nm}$: 16469 M^{-1} cm^{-1}

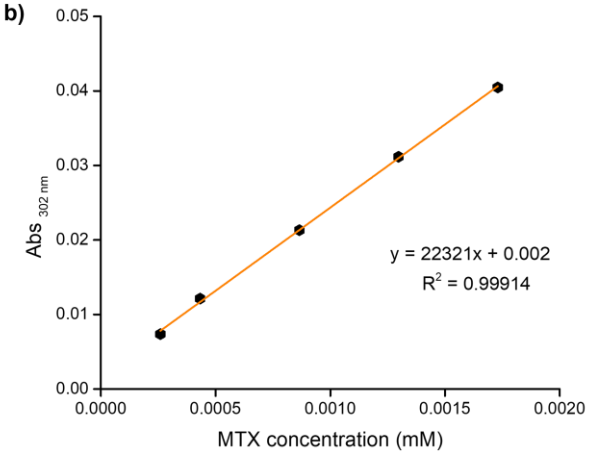

MTX $\varepsilon_{302\ nm}$: 22321 M^{-1} cm^{-1}

Figure S25. MTX calibration plot in aqueous solution (MOPS 10 mM) at pH *a)* 7.4 and *b)* 4.5.

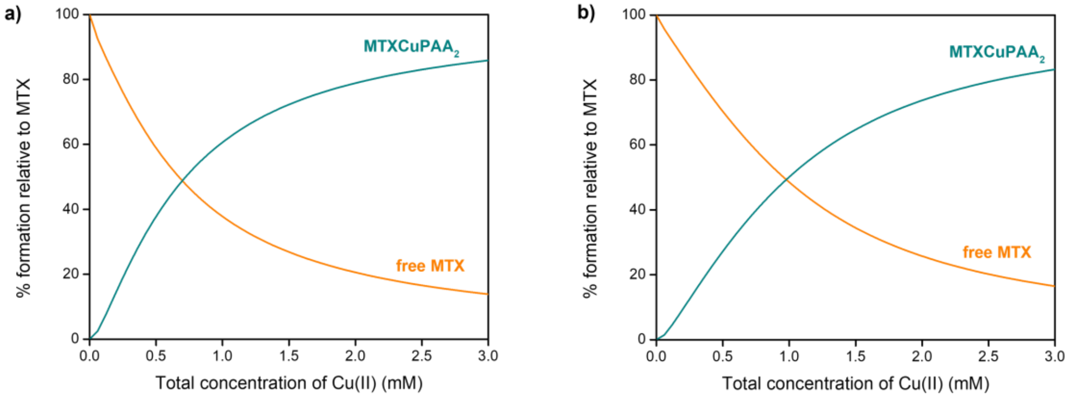

Figure S26. Distribution diagram for copper(II)-based assembly (Cu(II):PAA 1:3, $C_{Cu(II)}$ = 3.00 mM) with MTX *a)* 0.40 mM and *b)* 1.00 mM computed by using the data in *Table 3*, *Table 8* and *Table 9*.

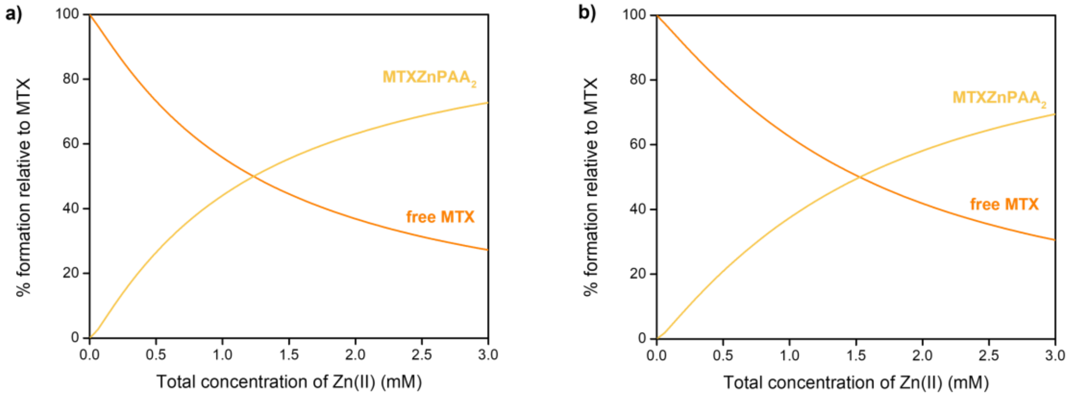

Figure S27. Distribution diagram for zinc(II)-based assembly (Zn(II):PAA 1:3, $C_{Zn(II)}$ = 3.00 mM) with MTX *a)* 0.40 mM and *b)* 1.00 mM computed by using the data in *Table 3*, *Table 8* and *Table 9*.

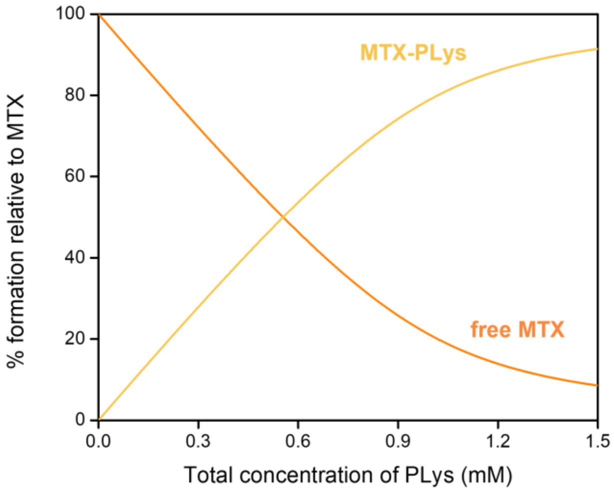

Figure S28. Distribution diagram for the methotrexate-poly-lysine system (MTX:PLys 1:0.67, C_{MTX} = 1.00 mM).

Chapter IV:

Integration of metal-coordinated assemblies with the LbL approach

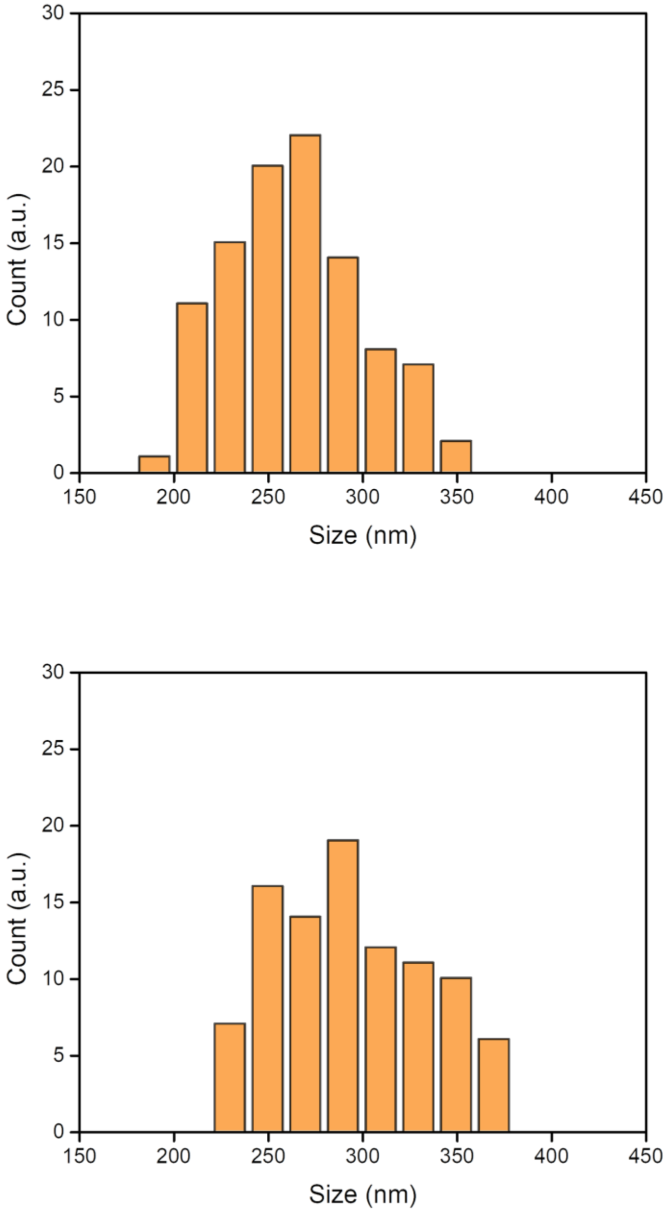

Figure S29. LbL-based nanoparticles size graphs: PLys/MTXCu(II)PAA$_2$ (MTX 0.40 mM) - positively (*top*) and negatively (*bottom*) charged systems.

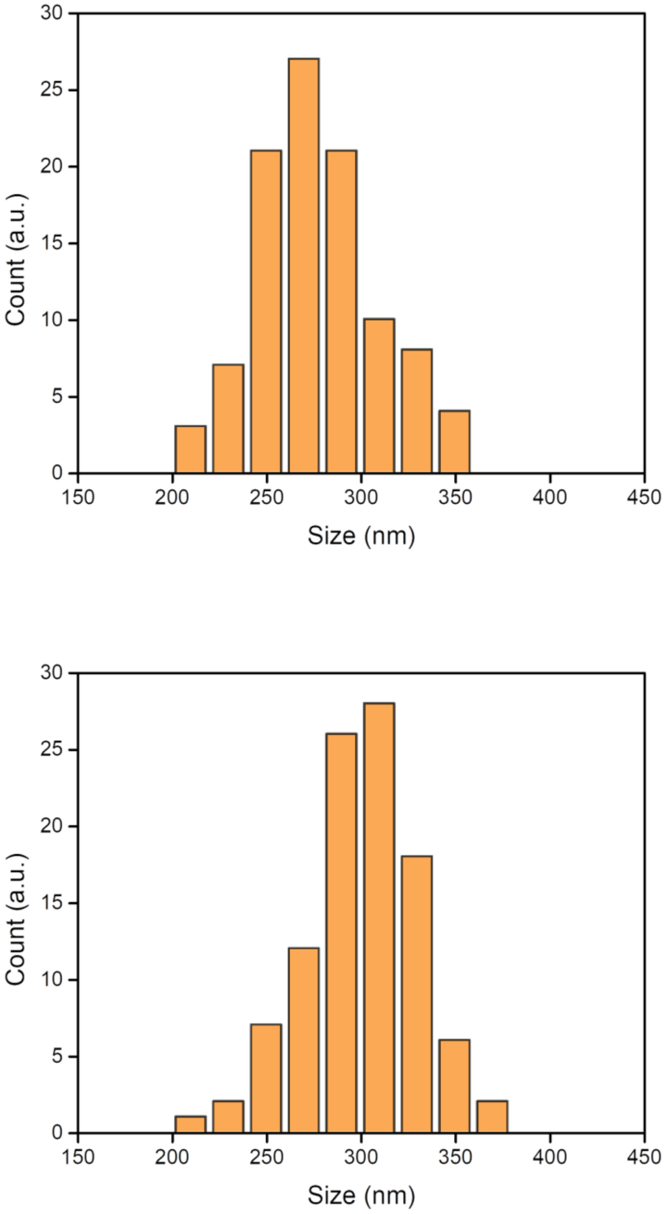

Figure S30. LbL-based nanoparticles size graphs: PLys/MTXCu(II)PAA$_2$ (MTX 1.00 mM) - positively (*top*) and negatively (*bottom*) charged systems.

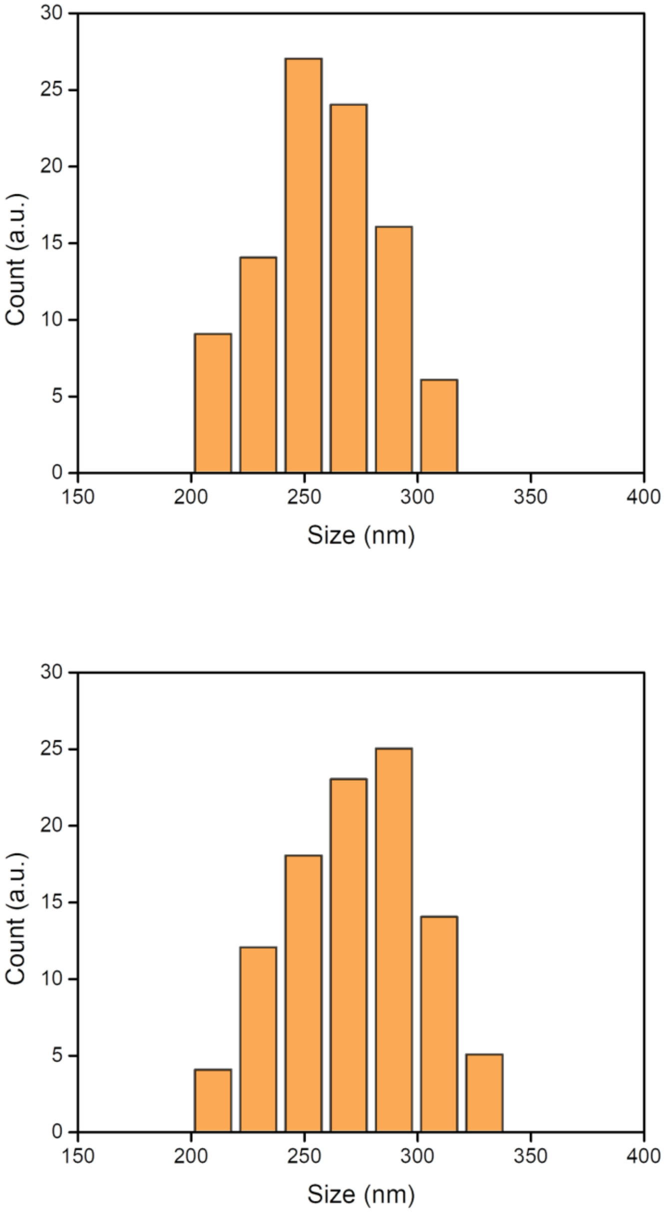

Figure S31. LbL-based nanoparticles size graphs: PLys/Cu(II)PAA$_2$ - positively (*top*) and negatively (*bottom*) charged systems.

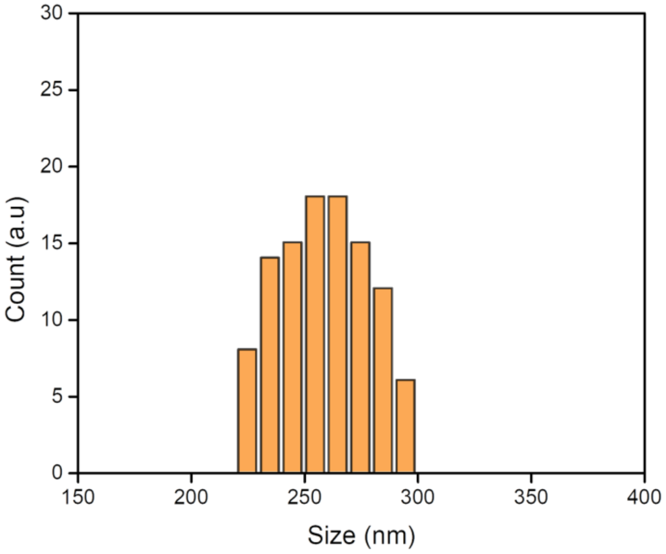

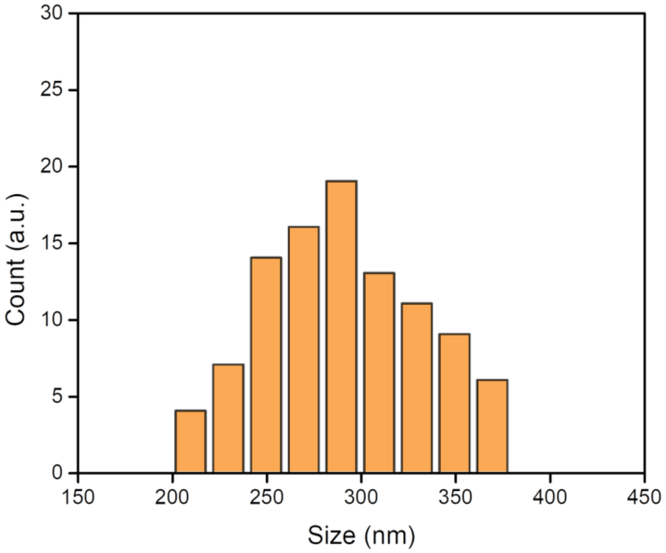

Figure S32. LbL-based nanoparticles size graphs: PLys/PAA - positively (*top*) and negatively (*bottom*) charged systems.

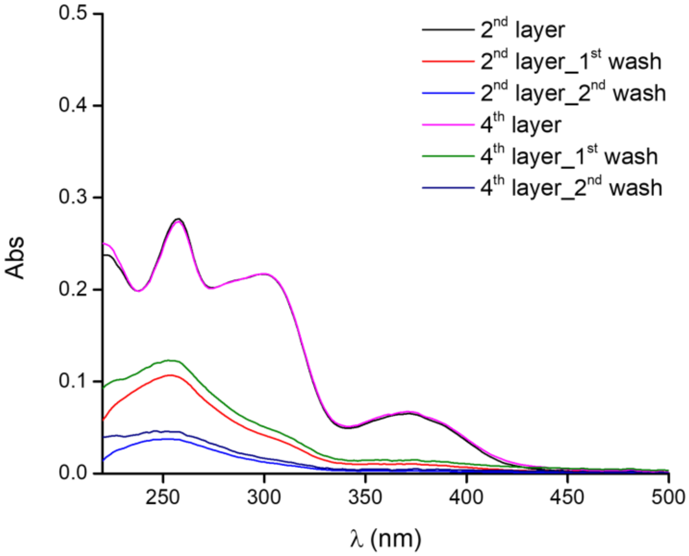

Figure S33. Example of UV-Vis spectra of the supernatant after $MTXCuPAA_2$ (with MTX 0.40 mM) layer incubation and subsequent rinsing steps.

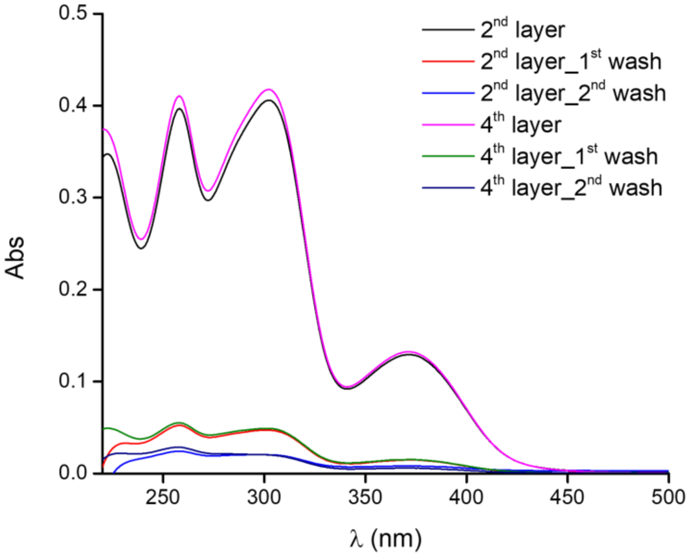

Figure S34. Example of UV-Vis spectra of the supernatant after $MTXCuPAA_2$ (with MTX 1.00 mM) layer incubation and subsequent rinsing steps.

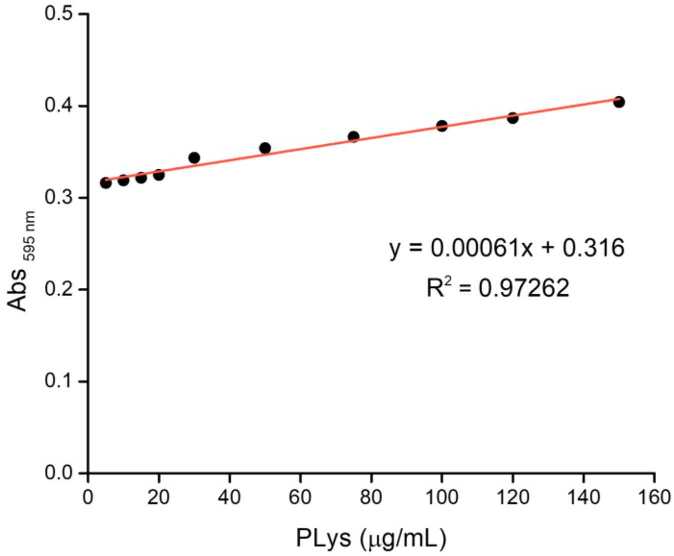

Figure S35. Calibration plot for PLys according to Bradford assay protocol.

Chapter V:

Molecular recognition properties of charged species by macrocyclic hosts

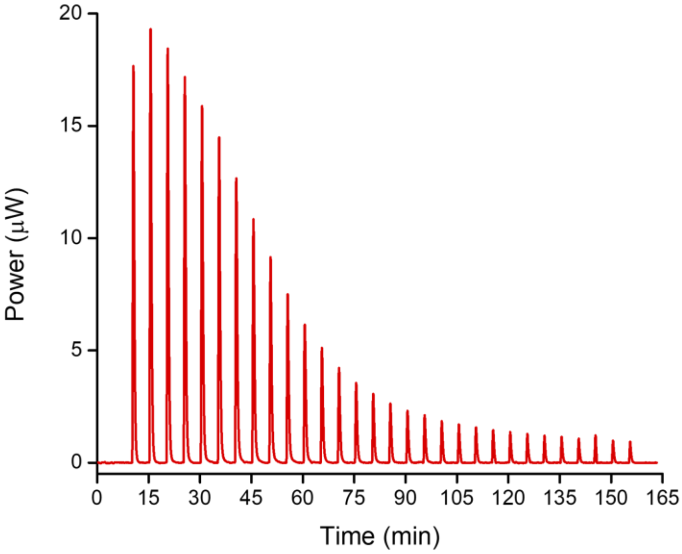

Figure S36. ITC titration of Me_4N^+ (5.03 mM) into a PrS[5]^{carboxy} (0.47 mM) solution at 25 °C and pH 7.6.

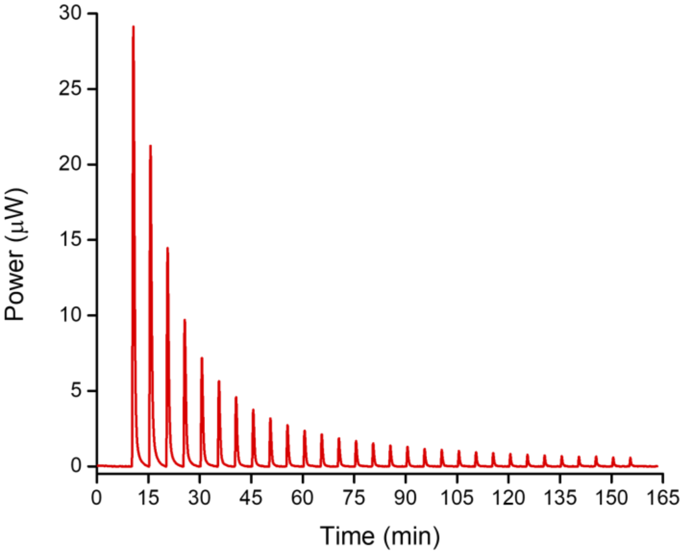

Figure S37. ITC titration of Et_4N^+ (19.68 mM) into a PrS[5]^{carboxy} (0.26 mM) solution at 25 °C and pH 7.6.

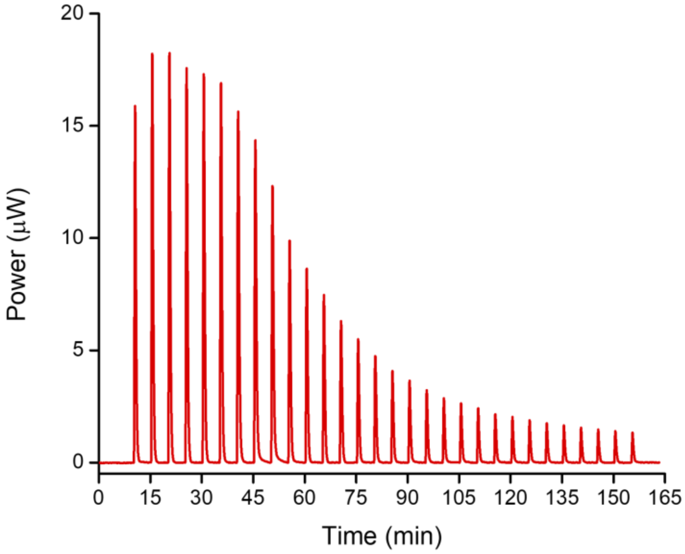

Figure S38. ITC titration of DABCOHe$_2^{2+}$ (2.99 mM) into a PrS[5]$^{\text{carboxy}}$ (0.33 mM) solution at 25 °C and pH 7.6.

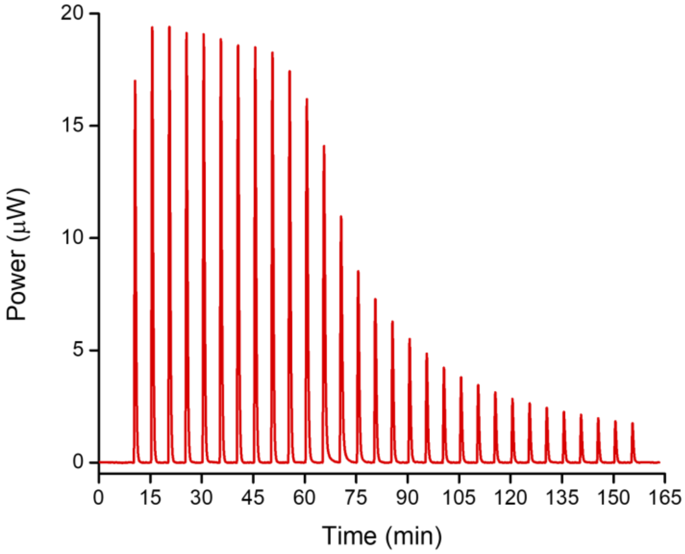

Figure S39. ITC titration of DABCOHeMe^{2+} (2.99 mM) into a PrS[5]$^{\text{carboxy}}$ (0.34 mM) solution at 25 °C and pH 7.6.

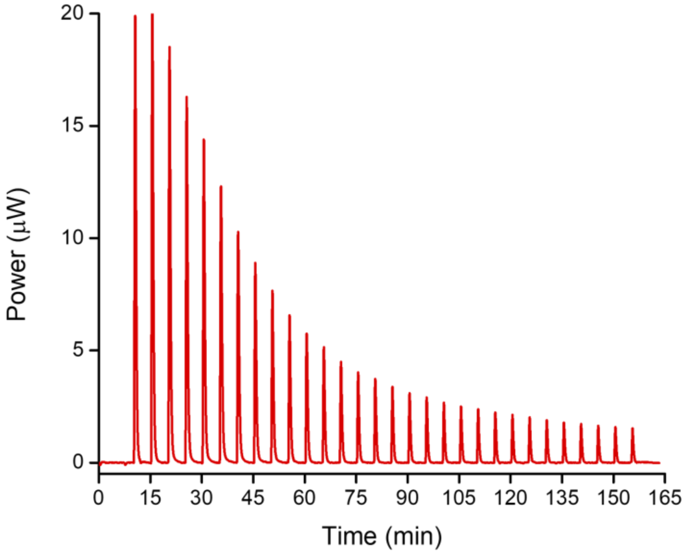

Figure S40. ITC titration of DABCOMe$_2^{2+}$ (6.45 mM) into a PrS[5]^{carboxy} (0.42 mM) solution at 25 °C and pH 7.6.

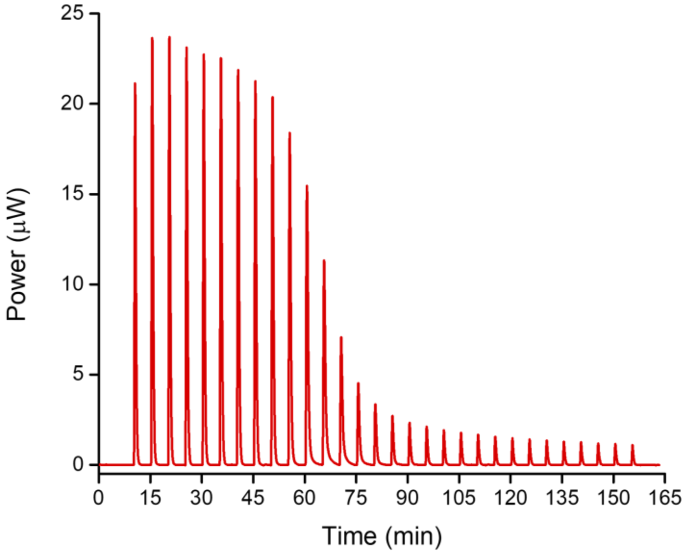

Figure S41. ITC titration of Me$_4$Pip^{2+} (2.51 mM) into a PrS[5]^{carboxy} (0.32 mM) solution at 25 °C and pH 7.6.

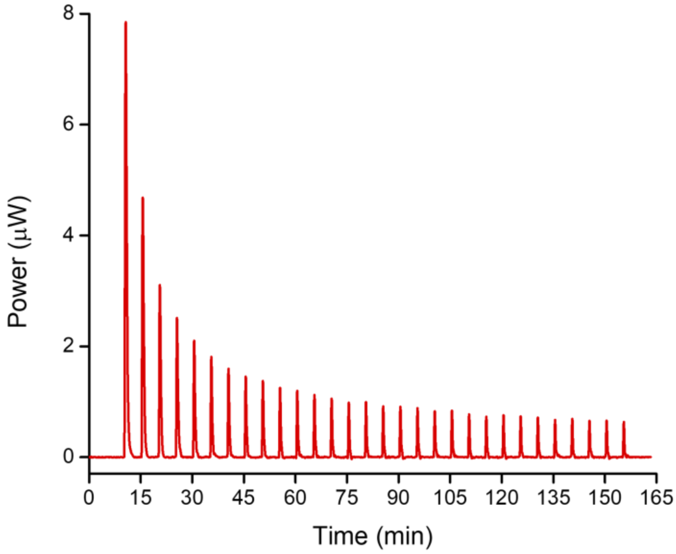

Figure S42. ITC titration of Me_4N^+ (11.0 mM) into a PrS[6]^{carboxy} (0.75 mM) solution at 25 °C and pH 7.6.

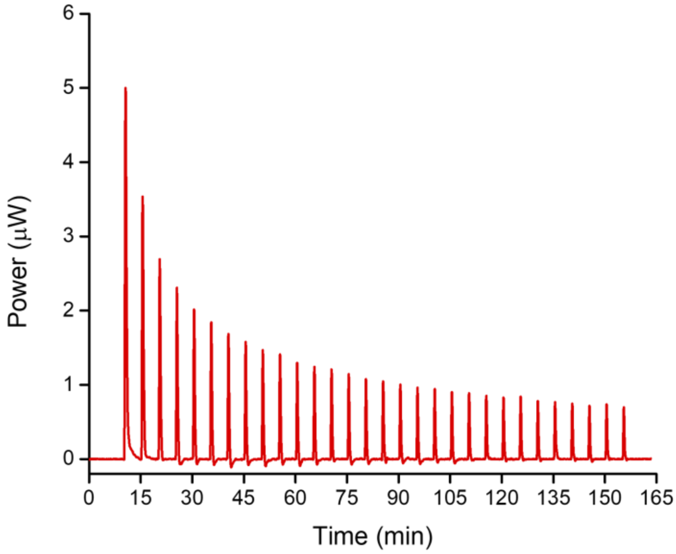

Figure S43. ITC titration of Et_4N^+ (9.57 mM) into a PrS[6]^{carboxy} (0.75 mM) solution at 25 °C and pH 7.6.

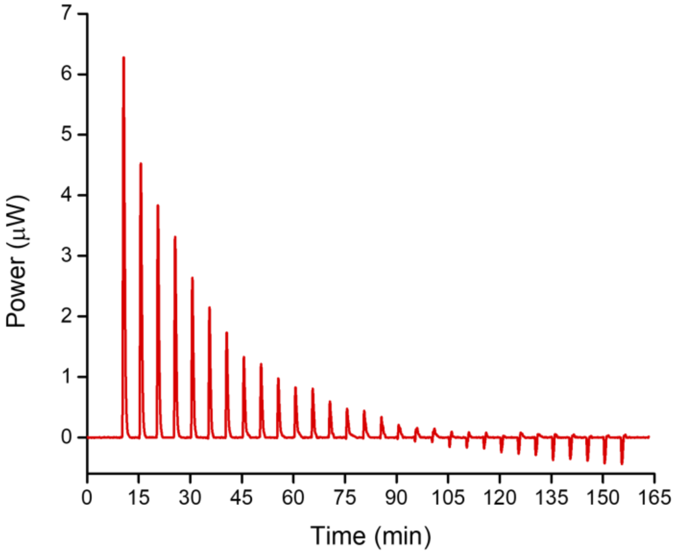

Figure S44. ITC titration of $Et(Me_3N)_2^{2+}$ (10.50 mM) into a PrS[6]^{carboxy} (0.51 mM) solution at 25 °C and pH 7.6.

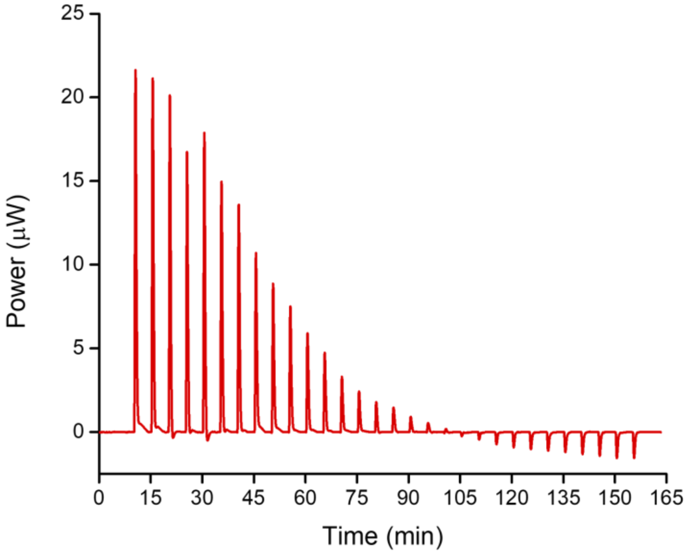

Figure S45. ITC titration of $DABCOHe_2^{2+}$ (14.34 mM) into a PrS[6]^{carboxy} (0.98 mM) solution at 25 °C and pH 7.6.

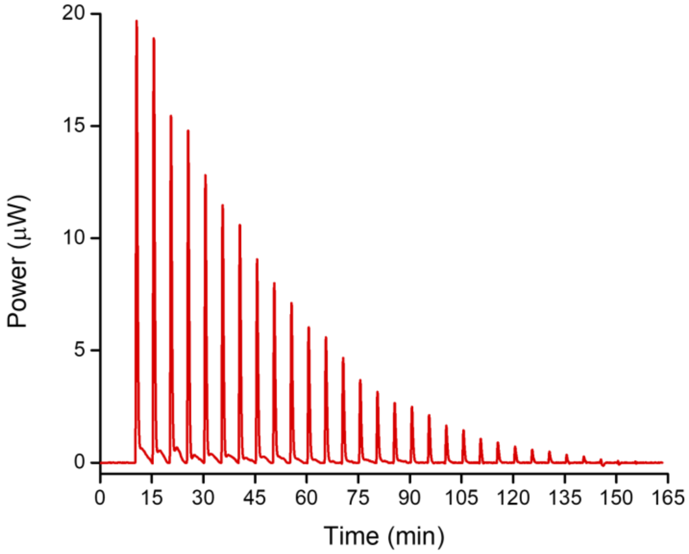

Figure S46. ITC titration of DABCOHeMe^{2+} (12.92 mM) into a PrS[6]^{carboxy} (0.82 mM) solution at 25 °C and pH 7.6.

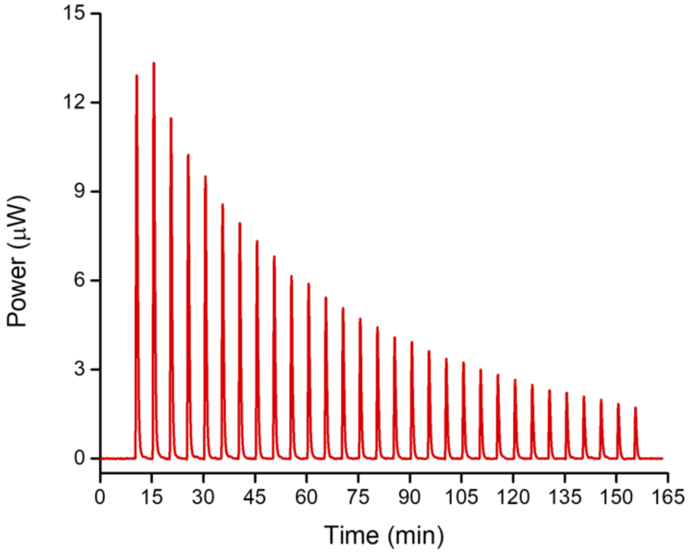

Figure S47. ITC titration of DABCOMe$_2^{2+}$ (9.65 mM) into a PrS[6]^{carboxy} (0.75 mM) solution at 25 °C and pH 7.6.

Outreach and other activities

Internships

Ph.D. visiting student

- Group of Science and Engineering of Polymeric Biomaterials, Department of Mining-Metallurgy Engineering and Materials Science, University of the Basque Country (Bilbao, Spain) and Responsive Polymer Therapeutics Group, Polymat, (Donostia-San Sebastián, Spain)
  From 29th August 2022 to 28th February 2023 (6 months)
  Supervisors: Dr. Aitor Larrañaga and Prof. Marcelo Calderón.
- Center for Nuclear Sciences and Technologies of Instituto Superior Técnico, University of Lisbon (Portugal)
  Short-Term Scientific Mission in the framework of the COST Action NECTAR (CA18202) grant recipient.
  From 1st to 15th October 2023 (two weeks)
  Supervisors: Dr. Sofia Gama and Prof. João D. G. Correia.

Publications

Papers

- Rocco Del Regno,§ **Giuseppina D. G. Santonoceta**,§ Paolo Della Sala, Margherita De Rosa, Annunziata Soriente, Carmen Talotta, Aldo Spinella, Placido Neri, Carmelo Sgarlata, and Carmine Gaeta. Molecular Recognition in an Aqueous Medium Using Water-Soluble Prismarene Hosts. *Organic Letters*, 2022, 24, 14, 2711-2715. § These authors contributed equally to this work.
- **Giuseppina D. G. Santonoceta**, and Carmelo Sgarlata. pH-Responsive Cobalt(II)-Coordinated Assembly Containing Quercetin for Antimicrobial Applications. *Molecules*, 2023, 28(14), 5581.
- **Giuseppina D. G. Santonoceta**, and Carmelo Sgarlata. Metal-coordinated

assemblies containing quercetin: solution equilibria are the key for the development of pH-responsive drug delivery systems. *Manuscript in preparation.*

- **Giuseppina D. G. Santonoceta**, Upashi Goswami, Tarita Biver, Giampaolo Barone, Marcelo Calderón, Aitor Larrañaga, and Carmelo Sgarlata. pH-responsive metal-coordinated assemblies containing methotrexate: from multiple solution equilibria to in vitro anticancer applications. *Manuscript in preparation.*

Oral communications

- **Giuseppina D. G. Santonoceta**, Carmelo Sgarlata. Metal-coordinated assemblies containing quercetin: a solution equilibria study for the development of pH-responsive drug delivery systems. International Symposium on Thermodynamics of Metal Complexes, ISMEC 2022, 5-8 June 2022, València, Spain. ISSN: 2239-2459.
- **Giuseppina D. G. Santonoceta**, Carmelo Sgarlata. Stimuli-responsive metal-coordinated assemblies of quercetin as effective drug delivery systems in aqueous solution. XV Italian Conference on Supramolecular Chemistry, Supramol 2022, 28 June-1 July 2022, Salerno, Italy.
- Rocco Del Regno, **Giuseppina D. G. Santonoceta**, Paolo Della Sala, Margherita De Rosa, Annunziata Soriente, Carmen Talotta, Aldo Spinella, Placido Neri, Carmelo Sgarlata, Carmine Gaeta. Water-soluble prismarene hosts: molecular recognition of ammonium cations in aqueous solution. 3rd European NECTAR Conference, 24-26 August 2022, Ljubljana, Slovenia. ISBN: 978-961-7078-29-9 (Invitation by the COST-NECTAR Committee).
- **Giuseppina D. G. Santonoceta**, Carmelo Sgarlata. Binding properties of methotrexate-metal-poly(acrylic acid) complexes in solution and at the solid-liquid interface for the development of pH-responsive delivery systems. Supramolecular Chemistry Days for Young Researchers 2023, 30 May-1 June 2023, Cagliari, Italy.

- **Giuseppina D. G. Santonoceta**, Upashi Goswami, Marcelo Calderón, Aitor Larrañaga, Carmelo Sgarlata. pH-responsive metal-coordinated assemblies containing methotrexate: from multiple solution equilibria to in vitro anticancer applications. International Symposium on Thermodynamics of Metal Complexes, ISMEC 2023, 11-14 June 2023, Urbino, Italy. ISSN: 2239-2459.
- **Giuseppina D. G. Santonoceta**, Carmelo Sgarlata. Methotrexate-based metal-coordinated assemblies responding to pH stimuli: a multiple equilibria study in solution and at the interface. XXX Congresso della Divisione di Chimica Analitica della Società Chimica Italiana, 17-21 September 2023, Vasto, Italy; *grant recipient*.

Poster communications

- **Giuseppina D. G. Santonoceta**, Carmelo Sgarlata. Metal-coordinated assemblies as promising drug delivery platforms. International Symposium on Thermodynamics of Metal Complexes, ISMEC 2021, 16-18 June 2021, Byalistok, Poland (online) ISSN: 2239-2459.
- **Giuseppina D. G. Santonoceta**, Carmelo Sgarlata. Metal-coordinated assemblies of quercetin with a stimuli-responsive polymer: a solution equilibria study. XXVII National Congress of SCI, 14-23 September 2021, Milan, Italy (online) ISBN: 978-88-94952-24-7.
- **Giuseppina D. G. Santonoceta**, Carmelo Sgarlata. Metal-coordinated assemblies of quercetin with a pH-responsive polymer as potential DDSs in neutral aqueous solution. Supramolecular Chemistry Days for Young Researchers, 13-15 October 2021, virtual edition (online).
- Rocco Del Regno, **Giuseppina D. G. Santonoceta**, Paolo Della Sala, Margherita De Rosa, Annunziata Soriente, Carmen Talotta, Aldo Spinella, Placido Neri, Carmelo Sgarlata, Carmine Gaeta. Molecular recognition of ammonium cations by novel water-soluble prismarene hosts. International

Symposium on Thermodynamics of Metal Complexes, ISMEC 2022, 5-8 June 2022, València, Spain. ISSN: 2239-2459.

- Rocco Del Regno, **Giuseppina D. G. Santonoceta**, Paolo Della Sala, Margherita De Rosa, Annunziata Soriente, Carmen Talotta, Aldo Spinella, Placido Neri, Carmelo Sgarlata, Carmine Gaeta. Water-Soluble Prismarene Hosts: Molecular Recognition of Ammonium Cations in Aqueous Solution. XV Italian Conference on Supramolecular Chemistry, Supramol 2022, 28 June-1 July 2022, Salerno, Italy.

Co-authored communications

- Carmelo Sgarlata, **Giuseppina D. G. Santonoceta**. Metal coordinated assemblies based on quercetin: solution equilibria are crucial for developing pH-responsive drug delivery systems. XXIX Congresso della Divisione di Chimica Analitica della Società Chimica Italiana, 11-15 September 2022, Milazzo, Italy (Oral Communication) ISBN: 978-88-94952-30-8.
- Rocco Del Regno, **Giuseppina D. G. Santonoceta**, Paolo Della Sala, Margherita De Rosa, Annunziata Soriente, Carmen Talotta, Aldo Spinella, Placido Neri, Carmelo Sgarlata, Carmine Gaeta. Molecular recognition of ammonium cations by novel water-soluble prismarene hosts. 13th European Symposium on Thermal Analysis and Calorimetry - ESTAC-13, 19-22 September 2022, Palermo, Italy (Oral Communication).

Training schools and other meetings

- 1st ISMEC – NECTAR Training School on the Determination, Analysis and Use of Thermodynamic Data, SOLvE – Advances in SOLution Equilibria (26-28 July 2021); *grant recipient*.
- CHESS School 2022 - Conventional and High-Energy Spectroscopies for Inorganic, Organic and Biomolecular Surfaces and Interfaces (21-25 February 2022).
- WG2, WG4 NECTAR Workshop, 9-10 June 2022, Valencia, Spain.
- 2nd ISMEC – NECTAR Training School on the Determination, Analysis and Use of Thermodynamic Data, SOLvE – Advances in SOLution Equilibria (25-27 July 2022); *grant recipient*.
- NECTAR Training School on Calorimetry, Ljubljana, Slovenia (27 August 2022); grant recipient.
- NECTAR Training School on Communication in Science (NECTAR-SciComm), Cagliari, Italy (29 May 2023); *member of the organizing committee*.
- WG5 NECTAR Workshop, 30 May 2023, Cagliari, Italy.
- WG2, WG4 NECTAR Workshop, 12-14 June 2023, Urbino, Italy.
- 3rd ISMEC – NECTAR Training School on the Determination, Analysis and Use of Thermodynamic Data, SOLvE – Advances in SOLution Equilibria (24-26 July 2023); *grant recipient*.

Acknowledgements

Finding the words to express my sincere gratitude to all the people who were beside me (both personally and professionally) during these years is perhaps the most difficult part of completing this PhD experience.

Firstly, I am extremely grateful to my supervisor, Prof. Carmelo Sgarlata, for giving me the possibility of working under his valuable guidance and for the stimulating scientific discussions. He instilled in me an unwavering desire to learn and improve my capacities and gave me the opportunity to be “creative” encouraging and supporting my ideas.

I am also grateful to Dr. Aitor Larrañaga (University of the Basque Country (UPV/EHU), Bilbao, Spain) and Prof. Marcelo Calderón (Polymat, Donostia-San Sebastián, Spain) for hosting me in their laboratories and allowing me to use their facilities and acquire new skills.
I also thank all the amazing people of the ZIBIO group for making me feel part of the group, for their support during the research work at the University of the Basque Country (Bilbao), and all the fun during the internship in the Basque Country.

I am very grateful to Dr. Sofia Gama (Centro de Ciências e Tecnologias Nucleares, Instituto Superior Técnico, University of Lisbon, Portugal) for allowing me to join her lab for a short stay and acquire some expertise on NMR experiments.

A huge thanks goes to all the people I met over these years, with whom I shared many moments and emotions, and who became my friends.
I would like to thank Rossella, Giusy and Valentina for the consistent encouragement and personal and scholarly advice I received throughout this experience (and before).
A special thanks goes to Noemi, friend and colleague, with whom I shared every day of this doctoral experience. Thank you for the continuous support, the time spent laughing and for always trying to make me feel positive about any situation.

Furthermore, I would like to thank Ania, whom I met by chance but became a great friend. Thank you for the advice, the support, the good moments spent together and for always being present despite the distance.

Also, I would like to thank the people of the University of Catania, Noemi Bellassai, Gaetano Rizzo, Lidia Zuccarello, and Mrs. Sabrina Tosto for their support during the PhD experience.

A “thank you!” to the *"equilibria people"* certainly cannot be missed: I gained a lot from their personal and scientific interactions.

Last but not least, my biggest thanks goes to my Family who supported (and endured) me along the way. An infinite thanks for your love, constant presence, support, the advice that made me grow and without whom I certainly wouldn’t be the person I am, and I would never have reached this goal.

Each of you contributed to make my PhD a great and unforgettable experience!

References

[1] Chen, H., Liu, D., Guo, Z. (2016). Endogenous stimuli-responsive nanocarriers for drug delivery. Chemistry Letters, 45(3), 242-249.

[2] Washington, N., Washington, C., Wilson, C. (2000). Physiological pharmaceutics: barriers to drug absorption. CRC Press.

[3] Savjani, K. T., Gajjar, A. K., Savjani, J. K. (2012). Drug solubility: importance and enhancement techniques. International Scholarly Research Notices, 2012.

[4] Kumar, S., Ahmad, M. K., Waseem, M., Pandey, A. K. (2015). Drug targets for cancer treatment: an overview. Med chem, 5(3), 115-123.

[5] Glassman, P. M., Muzykantov, V. R. (2019). Pharmacokinetic and pharmacodynamic properties of drug delivery systems. Journal of Pharmacology and Experimental Therapeutics, 370(3), 570-580.

[6] Jaimes-Aguirre, L., Gibbens-Bandala, B. V., Morales-Avila, E., Ocampo-García, B. E., Seyedeh-Fatemeh, M., Amirhosein, A. (2016). Polymer-based drug delivery systems, development and pre-clinical status. Current Pharmaceutical Design, 22(19), 2886-2903.

[7] Das, S. S., Bharadwaj, P., Bilal, M., Barani, M., Rahdar, A., Taboada, P., ... Kyzas, G. Z. (2020). Stimuli-responsive polymeric nanocarriers for drug delivery, imaging, and theragnosis. Polymers, 12(6), 1397.

[8] Migliore, R., D'Antona, N., Sgarlata, C., Consoli, G. M. (2021). Co-loading of temozolomide and curcumin into a calix[4]arene-based nanocontainer for potential combined chemotherapy: binding features, enhanced drug solubility and stability in aqueous medium. Nanomaterials, 11(11), 2930.

[9] Migliore, R., Granata, G., Rivoli, A., Consoli, G. M. L., Sgarlata, C. (2021). Binding affinity and driving forces for the interaction of calixarene-based micellar aggregates with model antibiotics in neutral aqueous solution. Frontiers in Chemistry, 8, 626467.

[10] Migliore, R., Ferreri, L., Aleo, D., Leotta, C. G., Pitari, G. M., D'Antona, N., ... Consoli, G. M. L. (2023). p-Sulfonato-Calix[4]arene Micelles Stabilize a Povidone

---

Iodine Solution: Supramolecular Interactions, Iodine Retention, and Bactericidal Activity. Nanomaterials, 13(2), 286.

[11] Liu, P., Chen, G., Zhang, J. (2022). A review of liposomes as a drug delivery system: current status of approved products, regulatory environments, and future perspectives. Molecules, 27(4), 1372.

[12] Ghosn, Y., Kamareddine, M. H., Tawk, A., Elia, C., El Mahmoud, A., Terro, K., ... Farhat, S. (2019). Inorganic nanoparticles as drug delivery systems and their potential role in the treatment of chronic myelogenous leukaemia. Technology in cancer research & treatment, 18, 1533033819853241.

[13] Wang, J., Li, B., Qiu, L., Qiao, X., Yang, H. (2022). Dendrimer-based drug delivery systems: history, challenges, and latest developments. Journal of Biological Engineering, 16(1), 1-12.

[14] Bai, H., Wang, J., Li, Z., Tang, G. (2019). Macrocyclic compounds for drug and gene delivery in immune-modulating therapy. International journal of molecular sciences, 20(9), 2097.

[15] Duro-Castano, A., Movellan, J., Vicent, M. J. (2015). Smart branched polymer drug conjugates as nano-sized drug delivery systems. Biomaterials science, 3(10), 1321-1334.

[16] Abdelhamid, M. A., Ki, M. R., El-Hafeez, A. A. A., Son, R. G., Pack, S. P. (2023). Tailored Functionalized Protein Nanocarriers for Cancer Therapy: Recent Developments and Prospects. Pharmaceutics, 15(1), 168.

[17] Mallakpour, S., Nikkhoo, E., Hussain, C. M. (2022). Application of MOF materials as drug delivery systems for cancer therapy and dermal treatment. Coordination Chemistry Reviews, 451, 214262.

[18] Parveen, S., Sahoo, S. K. (2008). Polymeric nanoparticles for cancer therapy. Journal of drug targeting, 16(2), 108-123.

[19] Jain, Kewal K. (2008). Drug Delivery Systems - An OverviewDrug Delivery Systems. Methods in Molecular Biology™, Volume 437. Humana Press.

---

[20] Yusuf, A., Almotairy, A. R. Z., Henidi, H., Alshehri, O. Y., Aldughaim, M. S. (2023). Nanoparticles as Drug Delivery Systems: A Review of the implication of nanoparticles' physicochemical properties on responses in biological systems. Polymers, 15(7), 1596.

[21] Shen, S., Wu, Y., Liu, Y., Wu, D. (2017). High drug-loading nanomedicines: progress, current status, and prospects. International journal of nanomedicine, 12, 4085.

[22] Hassanin, I. A., Elzoghby, A. O. (2020). Self-assembled non-covalent protein-drug nanoparticles: an emerging delivery platform for anti-cancer drugs. Expert Opinion on Drug Delivery, 17(10), 1437-1458.

[23] Núñez-Lozano, R., Cano, M., Pimentel, B., de la Cueva-Méndez, G. (2015). 'Smartening'anticancer therapeutic nanosystems using biomolecules. Current opinion in biotechnology, 35, 135-140.

[24] Davis, M. E., Shin, D. M. (2008). Nanoparticle therapeutics: an emerging treatment modality for cancer. Nature reviews. Drug discovery, 7(9), 771-782.

[25] Kobayashi, H., Watanabe, R., Choyke, P. L. (2014). Improving conventional enhanced permeability and retention (EPR) effects; what is the appropriate target?. Theranostics, 4(1), 81-89.

[26] Maeda, H. (2013). The link between infection and cancer: tumour vasculature, free radicals, and drug delivery to tumours via the EPR effect. Cancer science, 104(7), 779-789.

[27] Zhao, M., Hu, B., Gu, Z., Joo, K. I., Wang, P., Tang, Y. (2013). Degradable polymeric nanocapsule for efficient intracellular delivery of a high molecular weight tumour-selective protein complex. Nano Today, 8(1), 11-20.

[28] Samal, S. K., Dash, M., Van Vlierberghe, S., Kaplan, D. L., Chiellini, E., Van Blitterswijk, C., Moroni, L., Dubruel, P. (2012). Cationic polymers and their therapeutic potential. Chemical Society Reviews, 41(21), 7147-7194.

[29] Santos, A. C., Costa, D., Ferreira, L., Guerra, C., Pereira-Silva, M., Pereira, I., Veiga, F. (2021). Cyclodextrin-based delivery systems for in vivo-tested anticancer therapies. Drug Delivery and Translational Research, 11, 49-71.

---

[30] Das, D., Assaf, K. I., Nau, W. M. (2019). Applications of cucurbiturils in medicinal chemistry and chemical biology. Frontiers in chemistry, 7, 619.

[31] Basilotta, R., Mannino, D., Filippone, A., Casili, G., Prestifilippo, A., Colarossi, L., Campolo, M. (2021). Role of Calixarene in Chemotherapy Delivery Strategies. Molecules, 26(13), 3963.

[32] Wu, X., Gao, L., Hu, X. Y., Wang, L. (2016). Supramolecular Drug Delivery Systems Based on Water-Soluble Pillar [n] arenes. The Chemical Record, 16(3), 1216-1227.

[33] Ma, X., Zhao, Y. (2015). Biomedical applications of supramolecular systems based on host–guest interactions. Chemical reviews, 115(15), 7794-7839.

[34] Yu, G., Chen, X. (2019). Host-guest chemistry in supramolecular theranostics. Theranostics, 9(11), 3041.

[35] Brewster, M. E., Loftsson, T. (2007). Cyclodextrins as pharmaceutical solubilizers. Advanced drug delivery reviews, 59(7), 645-666.

[36] Brewster, M. E., Loftsson, T., Estes, K. S., Lin, J. L., Fridriksdóttir, H., Bodor, N. (1992). Effect of various cyclodextrins on solution stability and dissolution rate of doxorubicin hydrochloride. International journal of pharmaceutics, 79(1-3), 289-299.

[37] Zheng, Y., Haworth, I. S., Zuo, Z., Chow, M. S., Chow, A. H. (2005). Physicochemical and structural characterization of quercetin-β-cyclodextrin complexes. Journal of pharmaceutical sciences, 94(5), 1079-1089.

[38] Geng, W. C., Sessler, J. L., Guo, D. S. (2020). Supramolecular prodrugs based on host–guest interactions. Chemical Society Reviews, 49(8), 2303-2315.

[39] Li, S., Gao, Y., Ding, Y., Xu, A., Tan, H. (2021). Supramolecular nano drug delivery systems mediated via host-guest chemistry of cucurbit [n] uril (n= 6 and 7). Chinese Chemical Letters, 32(1), 313-318.

[40] Wu, X., Zhang, Y. M., Liu, Y. (2016). Nanosupramolecular assembly of amphiphilic guest mediated by cucurbituril for doxorubicin delivery. RSC advances, 6(102), 99729-99734.

[41] Noruzi, E. B., Molaparast, M., Zarei, M., Shaabani, B., Kariminezhad, Z., Ebadi, B., Pietrasik, J. (2020). Para-sulfonatocalix [n] arene-based biomaterials: Recent progress

---

in pharmaceutical and biological applications. European journal of medicinal chemistry, 190, 112121.

[42] Renziehausen, A., Tsiailanis, A. D., Perryman, R., Stylos, E. K., Chatzigiannis, C., O'Neill, K., ..., Syed, N. (2019). Encapsulation of temozolomide in a calixarene nanocapsule improves its stability and enhances its therapeutic efficacy against glioblastoma. Molecular cancer therapeutics, 18(9), 1497-1505.

[43] Li, B., Meng, Z., Li, Q., Huang, X., Kang, Z., Dong, H., Li, C. (2017). A pH responsive complexation-based drug delivery system for oxaliplatin. Chemical science, 8(6), 4458-4464.

[44] Della Sala, P., Del Regno, R., Talotta, C., Capobianco, A., Hickey, N., Geremia, S., Gaeta, C. (2020). Prismarenes: a new class of macrocyclic hosts obtained by templation in a thermodynamically controlled synthesis. Journal of the American Chemical Society, 142(4), 1752-1756.

[45] Della Sala, P., Del Regno, R., Di Marino, L., Calabrese, C., Palo, C., Talotta, C., Gaeta, C. (2021). An Intramolecularly Self-Templated Synthesis of Macrocycles: The Self-Filling Effects on the Formation of Prismarenes. Chemical Science.

[46] Yang, L. P., Jiang, W. (2020). Prismarene: An Emerging Naphthol-Based Macrocyclic Arene. Angewandte Chemie International Edition, 59(37), 15794-15796.

[47] Del Regno, R., Santonoceta, G. D., Della Sala, P., De Rosa, M., Soriente, A., Talotta, C., ..., Gaeta, C. (2022). Molecular Recognition in an Aqueous Medium Using Water-Soluble Prismarene Hosts. Organic Letters, 24(14), 2711-2715.

[48] Salari, N., Faraji, F., Torghabeh, F. M., Faraji, F., Mansouri, K., Abam, F., ..., Mohammadi, M. (2022). Polymer-based drug delivery systems for anticancer drugs: A systematic review. Cancer Treatment and Research Communications, 100605.

[49] Gagliardi, A., Giuliano, E., Venkateswararao, E., Fresta, M., Bulotta, S., Awasthi, V., Cosco, D. (2021). Biodegradable polymeric nanoparticles for drug delivery to solid tumours. Frontiers in pharmacology, 12, 601626.

[50] Rajput, R., Narkhede, J., Naik, J. (2020). Nanogels as nanocarriers for drug delivery: A review. Admet and DMPK, 8(1), 1-15.

---

[51] Baskar, R., Lee, K. A., Yeo, R., Yeoh, K. W. (2012). Cancer and radiation therapy: current advances and future directions. International journal of medical sciences, 9(3), 193.

[52] Dzhardimalieva, G. I., Rabinskiy, L. N., Kydralieva, K. A., Uflyand, I. E. (2019). Recent advances in metallopolymer-based drug delivery systems. RSC Advances, 9(63), 37009-37051.

[53] Shende, P., Patil, A., Prabhakar, B. (2020). Layer-by-layer technique for enhancing physicochemical properties of actives. Journal of Drug Delivery Science and Technology, 56, 101519.

[54] Poptoshev, E., Schoeler, B., Caruso, F. (2004). Influence of solvent quality on the growth of polyelectrolyte multilayers. Langmuir, 20(3), 829-834.

[55] Xiao, F. X., Pagliaro, M., Xu, Y. J., Liu, B. (2016). Layer-by-layer assembly of versatile nanoarchitectures with diverse dimensionality: a new perspective for rational construction of multilayer assemblies. Chemical Society Reviews, 45(11), 3088-3121.

[56] Picart, C., Caruso, F., Voegel, J. C. (2014). Layer-by-layer films for biomedical applications. John Wiley & Sons.

[57] Srivastava, S., Kotov, N. A. (2008). Composite layer-by-layer (LBL) assembly with inorganic nanoparticles and nanowires. Accounts of chemical research, 41(12), 1831-1841.

[58] Marin, E., Tapeinos, C., Sarasua, J. R., Larrañaga, A. (2022). Exploiting the layer-by-layer nanoarchitectonics for the fabrication of polymer capsules: A toolbox to provide multifunctional properties to target complex pathologies. Advances in Colloid and Interface Science, 304, 102680.

[59] Pargaonkar, N., Lvov, Y. M., Li, N., Steenekamp, J. H., de Villiers, M. M. (2005). Controlled release of dexamethasone from microcapsules produced by polyelectrolyte layer-by-layer nanoassembly. Pharmaceutical research, 22, 826-835.

[60] Chen, J., Ratnayaka, S., Alford, A., Kozlovskaya, V., Liu, F., Xue, B., ..., Kharlampieva, E. (2017). Theranostic multilayer capsules for ultrasound imaging and guided drug delivery. ACS nano, 11(3), 3135-3146.

---

[61] Kurapati, R., Groth, T. W., Raichur, A. M. (2019). Recent developments in layer-by-layer technique for drug delivery applications. ACS Applied Bio Materials, 2(12), 5512-5527.

[62] Lammers, T., Kiessling, F., Hennink, W. E., Storm, G. (2012). Drug targeting to tumours: principles, pitfalls and (pre-) clinical progress. Journal of controlled release, 161(2), 175-187.

[63] Mura, S., Nicolas, J., Couvreur, P. (2013). Stimuli-responsive nanocarriers for drug delivery. Nature materials, 12(11), 991-1003.

[64] Yatvin, M. B., Weinstein, J. N., Dennis, W. H., Blumenthal, R. (1978). Design of liposomes for enhanced local release of drugs by hyperthermia. Science, 202(4374), 1290-1293.

[65] Mi, P. (2020). Stimuli-responsive nanocarriers for drug delivery, tumour imaging, therapy and theranostics. Theranostics, 10(10), 4557.

[66] Hossen, S., Hossain, M. K., Basher, M. K., Mia, M. N. H., Rahman, M. T., Uddin, M. J. (2019). Smart nanocarrier-based drug delivery systems for cancer therapy and toxicity studies: A review. Journal of advanced research, 15, 1-18.

[67] An, X., Zhu, A., Luo, H., Ke, H., Chen, H., Zhao, Y. (2016). Rational design of multi-stimuli-responsive nanoparticles for precise cancer therapy. Acs Nano, 10(6), 5947-5958.

[68] Chountoulesi, M., Naziris, N., Pippa, N., Pispas, S., Demetzos, C. (2020). Stimuli-responsive nanocarriers for drug delivery. In Nanomaterials for Clinical Applications (pp. 99-121). Elsevier.

[69] Liu, M., Du, H., Zhang, W., Zhai, G. (2017). Internal stimuli-responsive nanocarriers for drug delivery: Design strategies and applications. Materials Science and Engineering: C, 71, 1267-1280.

[70] Zhang, H., Jiang, W., Liu, R., Zhang, J., Zhang, D., Li, Z., Luan, Y. (2017). Rational design of metal organic framework nanocarrier-based codelivery system of doxorubicin hydrochloride/verapamil hydrochloride for overcoming multidrug resistance with efficient targeted cancer therapy. ACS Applied Materials & Interfaces, 9(23), 19687-19697.

---

[71] Granata, G., Paterniti, I., Geraci, C., Cunsolo, F., Esposito, E., Cordaro, M., Blanco, A. R., Cuzzocrea, S., Consoli, G. M. (2017). Potential Eye Drop Based on a Calix [4] arene Nanoassembly for Curcumin Delivery: Enhanced Drug Solubility, Stability, and Anti-Inflammatory Effect. Molecular Pharmaceutics, 14(5), 1610-1622.

[72] van Elk, M., Murphy, B. P., Eufrásio-da-Silva, T., O'Reilly, D. P., Vermonden, T., Hennink, Duffy, G. P., Ruiz-Hernández, E. (2016). Nanomedicines for advanced cancer treatments: Transitioning towards responsive systems. International journal of pharmaceutics, 515(1), 132-164.

[73] Li, C., Xing, L., Che, S. (2012). Coordination bonding based pH-responsive albumin nanoparticles for anticancer drug delivery. Dalton Transactions, 41(13), 3714-3719.

[74] Bai, L., Song, F., Wang, X. H., Han, X., Wang, X. L., Wang, Y. Z. (2015). Ligand–metal-drug coordination-based micelles for efficient intracellular doxorubicin delivery. RSC Advances, 5(59), 47629-47639.

[75] Majumder, J., Minko, T. (2021). Multifunctional and stimuli-responsive nanocarriers for targeted therapeutic delivery. Expert opinion on drug delivery, 18(2), 205-227.

[76] Luo, Z., Cai, K., Hu, Y., Zhao, L., Liu, P., Duan, L., Yang, W. (2011). Mesoporous silica nanoparticles end-capped with collagen: redox-responsive nanoreservoirs for targeted drug delivery. Angewandte Chemie, 123(3), 666-669.

[77] Liu, J., Ai, X., Zhang, H., Zhuo, W., Mi, P. (2019). Polymeric micelles with endosome escape and redox-responsive functions for enhanced intracellular drug delivery. Journal of Biomedical Nanotechnology, 15(2), 373-381.

[78] Chang, Y., Yang, K., Wei, P., Huang, S., Pei, Y., Zhao, W., Pei, Z. (2014). Cationic vesicles based on amphiphilic pillar[5]arene capped with ferrocenium: a redox-responsive system for drug/siRNA co-delivery. Angewandte chemie international edition, 53(48), 13126-13130.

[79] Hu, X., Hu, J., Tian, J., Ge, Z., Zhang, G., Luo, K., Liu, S. (2013). Polyprodrug amphiphiles: hierarchical assemblies for shape-regulated cellular internalization, trafficking, and drug delivery. Journal of the American Chemical Society, 135(46), 17617-17629.

---

[80] Shahriari, M., Zahiri, M., Abnous, K., Taghdisi, S. M., Ramezani, M., Alibolandi, M. (2019). Enzyme responsive drug delivery systems in cancer treatment. Journal of Controlled Release, 308, 172-189.

[81] Zhang, J., Yuan, Z. F., Wang, Y., Chen, W. H., Luo, G. F., Cheng, S. X., ..., Zhang, X. Z. (2013). Multifunctional envelope-type mesoporous silica nanoparticles for tumour-triggered targeting drug delivery. Journal of the American Chemical Society, 135(13), 5068-5073.

[82] Ryu, J. H., Na, J. H., Ko, H. K., You, D. G., Park, S., Jun, E., ... , Kim, K. (2014). Non-invasive optical imaging of cathepsin B with activatable fluorogenic nanoprobes in various metastatic models. Biomaterials, 35(7), 2302-2311.

[83] Tian, J., Ding, L., Wang, Q., Hu, Y., Jia, L., Yu, J. S., Ju, H. (2015). Folate receptor-targeted and cathepsin B-activatable nanoprobe for in situ therapeutic monitoring of photosensitive cell death. Analytical chemistry, 87(7), 3841-3848.

[84] Xiong, M. H., Bao, Y., Yang, X. Z., Wang, Y. C., Sun, B., Wang, J. (2012). Lipase-sensitive polymeric triple-layered nanogel for “on-demand” drug delivery. Journal of the American Chemical Society, 134(9), 4355-4362.

[85] Rodbard, D. (1981). The role of regional body temperature in the pathogenesis of disease. New England Journal of Medicine, 305(14), 808-814.

[86] Bae, Y. H., Okano, T., Kim, S. W. (1991). “On–Off” thermocontrol of solute transport. I. Temperature dependence of swelling of N-isopropylacrylamide networks modified with hydrophobic components in water. Pharmaceutical research, 8, 531-537.

[87] Barhoumi, A., Wang, W., Zurakowski, D., Langer, R. S., Kohane, D. S. (2014). Photothermally targeted thermosensitive polymer-masked nanoparticles. Nano letters, 14(7), 3697-3701.

[88] Zhang, X. Z., Zhuo, R. X., Cui, J. Z., Zhang, J. T. (2002). A novel thermo-responsive drug delivery system with positive controlled release. International journal of pharmaceutics, 235(1-2), 43-50.

[89] Chen, K. J., Liang, H. F., Chen, H. L., Wang, Y., Cheng, P. Y., Liu, H. L., ..., Sung, H. W. (2013). A thermoresponsive bubble-generating liposomal system for triggering localized extracellular drug delivery. ACS nano, 7(1), 438-446.

---

[90] Lee, N., Yoo, D., Ling, D., Cho, M. H., Hyeon, T., Cheon, J. (2015). Iron oxide-based nanoparticles for multimodal imaging and magnetoresponsive therapy. Chemical reviews, 115(19), 10637-10689.

[91] Fang, Z., Shen, Y., Gao, D. (2021). Stimulus-responsive nanocarriers for targeted drug delivery. New Journal of Chemistry, 45(10), 4534-4544.

[92] Fang, Z., Li, X., Xu, Z., Du, F., Wang, W., Shi, R., Gao, D. (2019). Hyaluronic acid-modified mesoporous silica-coated superparamagnetic Fe_3O_4 nanoparticles for targeted drug delivery. International journal of nanomedicine, 5785-5797.

[93] Ghosh, S. C., Neslihan Alpay, S., Klostergaard, J. (2012). CD44: a validated target for improved delivery of cancer therapeutics. Expert opinion on therapeutic targets, 16(7), 635-650.

[94] Schroeder, A., Honen, R., Turjeman, K., Gabizon, A., Kost, J., Barenholz, Y. (2009). Ultrasound triggered release of cisplatin from liposomes in murine tumours. Journal of controlled release, 137(1), 63-68.

[95] Kheirolomoom, A., Mahakian, L. M., Lai, C. Y., Lindfors, H. A., Seo, J. W., Paoli, E. E., ..., Ferrara, K. W. (2010). Copper− doxorubicin as a nanoparticle cargo retains efficacy with minimal toxicity. Molecular pharmaceutics, 7(6), 1948-1958.

[96] Sirsi, S. R., Borden, M. A. (2014). State-of-the-art materials for ultrasound-triggered drug delivery. Advanced drug delivery reviews, 72, 3-14.

[97] Husseini, G. A., Abdel-Jabbar, N. M., Mjalli, F. S., Pitt, W. G. (2011). Optimizing the use of ultrasound to deliver chemotherapeutic agents to cancer cells from polymeric micelles. Journal of the Franklin Institute, 348(7), 1276-1284.

[98] Zhou, X., Guo, L., Shi, D., Duan, S., Li, J. (2019). Biocompatible chitosan nanobubbles for ultrasound-mediated targeted delivery of doxorubicin. Nanoscale Research Letters, 14, 1-9.

[99] Vivero-Escoto, J. L., Slowing, I. I., Wu, C. W., Lin, V. S. Y. (2009). Photoinduced intracellular controlled release drug delivery in human cells by gold-capped mesoporous silica nanosphere. Journal of the American Chemical Society, 131(10), 3462-3463.

---

[100] Tong, R., Hemmati, H. D., Langer, R., Kohane, D. S. (2012). Photoswitchable nanoparticles for triggered tissue penetration and drug delivery. Journal of the American Chemical Society, 134(21), 8848-8855.

[101] Yen, H. C., Cabral, H., Mi, P., Toh, K., Matsumoto, Y., Liu, X., ..., Kataoka, K. (2014). Light-induced cytosolic activation of reduction-sensitive camptothecin-loaded polymeric micelles for spatiotemporally controlled in vivo chemotherapy. ACS nano, 8(11), 11591-11602.

[102] Luo, D., Li, N., Carter, K. A., Lin, C., Geng, J., Shao, S., ..., Lovell, J. F. (2016). Rapid light-triggered drug release in liposomes containing small amounts of unsaturated and porphyrin–phospholipids. Small, 12(22), 3039-3047.

[103] Khatun, Z., Nurunnabi, M., Nafiujjaman, M., Reeck, G. R., Khan, H. A., Cho, K. J., Lee, Y. K. (2015). A hyaluronic acid nanogel for photo–chemo theranostics of lung cancer with simultaneous light-responsive controlled release of doxorubicin. Nanoscale, 7(24), 10680-10689.

[104] Yang, G., Sun, X., Liu, J., Feng, L., Liu, Z. (2016). Light-responsive, singlet-oxygen-triggered on-demand drug release from photosensitizer-doped mesoporous silica nanorods for cancer combination therapy. Advanced Functional Materials, 26(26), 4722-4732.

[105] Tong, R., Chiang, H. H., Kohane, D. S. (2013). Photoswitchable nanoparticles for in vivo cancer chemotherapy. Proceedings of the National Academy of Sciences, 110(47), 19048-19053.

[106] Zhou, Z., Song, J., Nie, L., Chen, X. (2016). Reactive oxygen species generating systems meeting challenges of photodynamic cancer therapy. Chemical society reviews, 45(23), 6597-6626.

[107] Wang, Z., Huang, P., Jacobson, O., Wang, Z., Liu, Y., Lin, L., ..., Chen, X. (2016). Biomineralization-inspired synthesis of copper sulfide–ferritin nanocages as cancer theranostics. ACS nano, 10(3), 3453-3460.

[108] Zhou, M., Wei, W., Chen, X., Xu, X., Zhang, X., Zhang, X. (2019). pH and redox dual responsive carrier-free anticancer drug nanoparticles for targeted delivery and

---

synergistic therapy. Nanomedicine: Nanotechnology, Biology and Medicine, 20, 102008.

[109] Chen, P., Qiu, M., Deng, C., Meng, F., Zhang, J., Cheng, R., Zhong, Z. (2015). pH-responsive chimaeric pepsomes based on asymmetric poly (ethylene glycol)-b-poly (l-leucine)-b-poly (l-glutamic acid) triblock copolymer for efficient loading and active intracellular delivery of doxorubicin hydrochloride. Biomacromolecules, 16(4), 1322-1330.

[110] Fang, W., Yang, J., Gong, J., Zheng, N. (2012). Photo-and pH-triggered release of anticancer drugs from mesoporous silica-coated Pd@ Ag nanoparticles. Advanced Functional Materials, 22(4), 842-848.

[111] Baeza, A., Guisasola, E., Ruiz-Hernandez, E., Vallet-Regí, M. (2012). Magnetically triggered multidrug release by hybrid mesoporous silica nanoparticles. Chemistry of Materials, 24(3), 517-524.

[112] Han, D., Tong, X., Zhao, Y. (2012). Block copolymer micelles with a dual-stimuli-responsive core for fast or slow degradation. Langmuir, 28(5), 2327-2331.

[113] Nahire, R., Paul, S., Scott, M. D., Singh, R. K., Muhonen, W. W., Shabb, J., ..., Mallik, S. (2012). Ultrasound enhanced matrix metalloproteinase-9 triggered release of contents from echogenic liposomes. Molecular pharmaceutics, 9(9), 2554-2564.

[114] Carregal-Romero, S., Guardia, P., Yu, X., Hartmann, R., Pellegrino, T., Parak, W. J. (2015). Magnetically triggered release of molecular cargo from iron oxide nanoparticle loaded microcapsules. Nanoscale, 7(2), 570-576.

[115] Guo, C., Wang, J., Dai, Z. (2011). Selective content release from light-responsive microcapsules by tuning the surface plasmon resonance of gold nanorods. Microchimica Acta, 173, 375-382.

[116] Cheng, R., Feng, F., Meng, F., Deng, C., Feijen, J., Zhong, Z. (2011). Glutathione-responsive nano-vehicles as a promising platform for targeted intracellular drug and gene delivery. Journal of controlled release, 152(1), 2-12.

[117] Yi, Q., Sukhorukov, G. B. (2014). UV-induced disruption of microcapsules with azobenzene groups. Soft Matter, 10(9), 1384-1391.

---

[118] Jing, J., Szarpak-Jankowska, A., Guillot, R., Pignot-Paintrand, I., Picart, C., Auzély-Velty, R. (2013). Cyclodextrin/paclitaxel complex in biodegradable capsules for breast cancer treatment. Chemistry of Materials, 25(19), 3867-3873.

[119] Kanamala, M., Wilson, W. R., Yang, M., Palmer, B. D., Wu, Z. (2016). Mechanisms and biomaterials in pH-responsive tumour targeted drug delivery: a review. Biomaterials, 85, 152-167.

[120] Yatvin, M. B., Kreutz, W., Horwitz, B. A., Shinitzky, M. (1980). pH-sensitive liposomes: possible clinical implications. Science, 210(4475), 1253-1255.

[121] Bhattacharya, B., Mohd Omar, M. F., Soong, R. (2016). The Warburg effect and drug resistance. British journal of pharmacology, 173(6), 970-979.

[122] Cassim, S., Vučetić, M., Ždralević, M., Pouyssegur, J. (2020). Warburg and beyond: the power of mitochondrial metabolism to collaborate or replace fermentative glycolysis in cancer. Cancers, 12(5), 1119.

[123] He, Q., Chen, J., Yan, J., Cai, S., Xiong, H., Liu, Y., Liu, Z. (2020). Tumour microenvironment responsive drug delivery systems. Asian Journal of Pharmaceutical Sciences, 15(4), 416-448.

[124] Bae, Y., Fukushima, S., Harada, A., Kataoka, K. (2003). Design of environment-sensitive supramolecular assemblies for intracellular drug delivery: Polymeric micelles that are responsive to intracellular pH change. Angewandte Chemie, 115(38), 4788-4791.

[125] Ding, H., Tan, P., Fu, S., Tian, X., Zhang, H., Ma, X., ..., Luo, K. (2022). Preparation and application of pH-responsive drug delivery systems. Journal of Controlled Release, 348, 206-238.

[126] Devnarain, N., Osman, N., Fasiku, V. O., Makhathini, S., Salih, M., Ibrahim, U. H., Govender, T. (2021). Intrinsic stimuli-responsive nanocarriers for smart drug delivery of antibacterial agents—An in-depth review of the last two decades. Wiley Interdisciplinary Reviews: Nanomedicine and Nanobiotechnology, 13(1), e1664.

[127] Hassan, D., Omolo, C. A., Fasiku, V. O., Mocktar, C., Govender, T. (2020). Novel chitosan-based pH-responsive lipid-polymer hybrid nanovesicles (OLA-LPHVs) for

---

delivery of vancomycin against methicillin-resistant Staphylococcus aureus infections. International journal of biological macromolecules, 147, 385-398.

[128] Raza, A., Rasheed, T., Nabeel, F., Hayat, U., Bilal, M., Iqbal, H. M. (2019). Endogenous and exogenous stimuli-responsive drug delivery systems for programmed site-specific release. Molecules, 24(6), 1117.

[129] Pola, C. C., Moraes, A. R., Medeiros, E. A., Teófilo, R. F., Soares, N. F., Gomes, C. L. (2019). Development and optimization of pH-responsive PLGA-chitosan nanoparticles for triggered release of antimicrobials. Food chemistry, 295, 671-679.

[130] Wang, X., Song, L., Zhao, J., Zhou, R., Luan, S., Huang, Y., Khan, A. (2018). Bacterial adaptability of enzyme and pH dual-responsive surface for infection resistance. Journal of Materials Chemistry B, 6(46), 7710-7718.

[131] Yang, Y., Jiang, X., Lai, H., Zhang, X. (2022). Smart Bacteria-Responsive Drug Delivery Systems in Medical Implants. Journal of Functional Biomaterials, 13(4), 173.

[132] Doelle, H. W. (2014). Bacterial metabolism. Academic Press.

[133] Canaparo, R., Foglietta, F., Giuntini, F., Della Pepa, C., Dosio, F., Serpe, L. (2019). Recent developments in antibacterial therapy: Focus on stimuli-responsive drug-delivery systems and therapeutic nanoparticles. Molecules, 24(10), 1991.

[134] Lin, X., Wu, X., Chen, X., Wang, B., Xu, W. (2021). Intellective and stimuli-responsive drug delivery systems in eyes. International Journal of Pharmaceutics, 120591.

[135] Xing, L., Zheng, H., Che, S. (2011). A pH-responsive cleavage route based on a metal–organic coordination bond. Chemistry–A European Journal, 17(26), 7271-7275.

[136] Schattling, P., Jochum, F. D., Theato, P. (2014). Multi-stimuli responsive polymers–the all-in-one talents. Polymer Chemistry, 5(1), 25-36.

[137] Kanamala, M., Wilson, W. R., Yang, M., Palmer, B. D., Wu, Z. (2016). Mechanisms and biomaterials in pH-responsive tumour targeted drug delivery: A review. Biomaterials, 85, 152-167.

[138] Reyes-Ortega, F. (2014). pH-responsive polymers: properties, synthesis and applications. In Smart polymers and their applications (pp. 45-92). Woodhead Publishing.

---

[139] Yan, X., Gemeinhart, R. A. (2005). Cisplatin delivery from poly (acrylic acid-co-methyl methacrylate) microparticles. Journal of controlled release, 106(1-2), 198-208.

[140] Sun, Q., Bi, H., Wang, Z., Li, C., Wang, X., Xu, J., ..., Yang, P. (2019). Hyaluronic acid-targeted and pH-responsive drug delivery system based on metal-organic frameworks for efficient antitumour therapy. Biomaterials, 223, 119473.

[141] Hariyadi, D. M., Islam, N. (2020). Current status of alginate in drug delivery. Advances in pharmacological and pharmaceutical sciences, 2020.

[142] Shariatinia, Z., Ziba, M. (2022). Smart pH-responsive drug release systems based on functionalized chitosan nanocomposite hydrogels. Surfaces and Interfaces, 29, 101739.

[143] Boddu, S. H., Bhagav, P., Karla, P. K., Jacob, S., Adatiya, M. D., Dhameliya, T. M., ..., Tiwari, A. K. (2021). Polyamide/poly (amino acid) polymers for drug delivery. Journal of Functional Biomaterials, 12(4), 58.

[144] Richard, A., Margaritis, A. (2001). Poly (glutamic acid) for biomedical applications. Critical reviews in biotechnology, 21(4), 219-232.

[145] Zheng, M., Pan, M., Zhang, W., Lin, H., Wu, S., Lu, C., ..., Cai, J. (2021). Poly (α-l-lysine)-based nanomaterials for versatile biomedical applications: Current advances and perspectives. Bioactive Materials, 6(7), 1878-1909.

[146] Hall, A., Wu, L. P., Parhamifar, L., Moghimi, S. M. (2015). Differential modulation of cellular bioenergetics by poly(L-lysine)s of different molecular weights. Biomacromolecules, 16(7), 2119-2126.

[147] Marin, E., Tiwari, N., Calderón, M., Sarasua, J. R., Larrañaga, A. (2021). Smart layer-by-layer polymeric microreactors: pH-triggered drug release and attenuation of cellular oxidative stress as prospective combination therapy. ACS Applied Materials & Interfaces, 13(16), 18511-18524.

[148] Shen, H. J., Shi, H., Ma, K., Xie, M., Tang, L. L., Shen, S., ..., Jin, Y. (2013). Polyelectrolyte capsules packaging BSA gels for pH-controlled drug loading and release and their antitumour activity. Acta biomaterialia, 9(4), 6123-6133.

---

[149] Li, K., Zang, X., Cheng, M., Chen, X. (2021). Stimuli-responsive Nanoparticles Based on Poly Acrylic Derivatives for Tumour Therapy. International Journal of Pharmaceutics, 120506.

[150] Kocak, G., Tuncer, C. A. N. S. E. L., Bütün, V. J. P. C. (2017). pH-Responsive polymers. Polymer Chemistry, 8(1), 144-176.

[151] Roma-Luciow, R., Sarraf, L., Morcellet, M. (2001). Complexes of poly (acrylic acid) with some divalent, trivalent and tetravalent metal ions. European polymer journal, 37(9), 1741-1745.

[152] Kitaeva, M. V., Melik-Nubarov, N. S., Menger, F. M., Yaroslavov, A. A. (2004). Doxorubicin− Poly(acrylic acid) Complexes: Interaction with Liposomes. Langmuir, 20(16), 6575-6579.

[153] Liu, H., Chen, H., Cao, F., Peng, D., Chen, W., Zhang, C. (2019). Amphiphilic block copolymer poly (acrylic acid)-b-polycaprolactone as a novel pH-sensitive nanocarrier for anti-cancer drugs delivery: In-vitro and in-vivo evaluation. Polymers, 11(5), 820.

[154] Wu, W., Aiello, M., Zhou, T., Berliner, A., Banerjee, P., Zhou, S. (2010). In-situ immobilization of quantum dots in polysaccharide-based nanogels for integration of optical pH-sensing, tumour cell imaging, and drug delivery. Biomaterials, 31(11), 3023-3031.

[155] Lee, H. S., Dastgheyb, S. S., Hickok, N. J., Eckmann, D. M., Composto, R. J. (2015). Targeted release of tobramycin from a pH-responsive grafted bilayer challenged with S. aureus. Biomacromolecules, 16(2), 650-659.

[156] Escobar, A., Muzzio, N. E., Andreozzi, P., Libertone, S., Tasca, E., Azzaroni, O., ..., Moya, S. E. (2019). Antibacterial layer-by-layer films of poly (acrylic acid)–gentamicin complexes with a combined burst and sustainable release of gentamicin. Advanced Materials Interfaces, 6(22), 1901373.

[157] Kasprzak, M. M., Erxlebenb, A., Ochockia, J. Properties and applications of flavonoid metal complexes, RSC Adv., 2015, 5, 57, 45853-45877. DOI, 10, C5RA05069C.

---

[158] Cushnie, T. P. Tim and Lamb, Andrew J. 2011. “Recent Advances in Understanding the Antibacterial Properties of Flavonoids.” International Journal of Antimicrobial Agents, 38(2), 99-107.

[159] Kost, B., Svyntkivska, M., Brzeziński, M., Makowski, T., Piorkowska, E., Rajkowska, K., ... ,Biela, T. (2020). PLA/β-CD-based fibres loaded with quercetin as potential antibacterial dressing materials. Colloids and Surfaces B: Biointerfaces, 190, 110949.

[160] Penalva, R., González-Navarro, C. J., Gamazo, C., Esparza, I., Irache, J. M. (2017). Zein nanoparticles for oral delivery of quercetin: Pharmacokinetic studies and preventive anti-inflammatory effects in a mouse model of endotoxemia. Nanomedicine: Nanotechnology, Biology and Medicine, 13(1), 103-110.

[161] Hatahet, T., Morille, M., Hommoss, A., Devoisselle, J. M., Müller, R. H., Begu, S. (2018). Liposomes, lipid nanocapsules and smartCrystals®: A comparative study for an effective quercetin delivery to the skin. International journal of pharmaceutics, 542(1-2), 176-185.

[162] Batra, P., Sharma, A. K. (2013). Anti-cancer potential of flavonoids: recent trends and future perspectives. 3 Biotech, 3, 439-459.

[163] Kumar, S., Pandey, A. K. (2013). Chemistry and biological activities of flavonoids: an overview. The scientific world journal, 2013.

[164] Procházková, D., Boušová, I., Wilhelmová, N. (2011). Antioxidant and prooxidant properties of flavonoids. Fitoterapia, 82(4), 513-523.

[165] Samsonowicz, M., Regulska, E. (2017). Spectroscopic study of molecular structure, antioxidant activity and biological effects of metal hydroxyflavonol complexes. Spectrochimica Acta Part A: Molecular and Biomolecular Spectroscopy, 173, 757-771.

[166] Wu, Q., Needs, P. W., Lu, Y., Kroon, P. A., Ren, D., Yang, X. (2018). Different antitumour effects of quercetin, quercetin-3′-sulfate and quercetin-3-glucuronide in human breast cancer MCF-7 cells. Food & function, 9(3), 1736-1746.

[167] García-Mediavilla, V., Crespo, I., Collado, P. S., Esteller, A., Sánchez-Campos, S., Tuñón, M. J., González-Gallego, J. (2007). The anti-inflammatory flavones quercetin

---

and kaempferol cause inhibition of inducible nitric oxide synthase, cyclooxygenase-2 and reactive C-protein, and down-regulation of the nuclear factor kappaB pathway in Chang Liver cells. European journal of pharmacology, 557(2-3), 221-229.

[168] Jun, T., Bochu, W., Liancai, Z. (2007). Hydrolytic cleavage of DNA by quercetin manganese (II) complexes. Colloids and Surfaces B: Biointerfaces, 55(2), 149-152.

[169] Scambia, G., Ranelletti, F. O., Panici, P. B., De Vincenzo, R., Bonanno, G., Ferrandina, G., Mancuso, S. (1994). Quercetin potentiates the effect of adriamycin in a multidrug-resistant MCF-7 human breast-cancer cell line: P-glycoprotein as a possible target. Cancer chemotherapy and pharmacology, 34(6), 459-464.

[170] Nguyen, T. L. A., Bhattacharya, D. (2022). Antimicrobial activity of quercetin: an approach to its mechanistic principle. Molecules, 27(8), 2494.

[171] Osonga, F. J., Akgul, A., Miller, R. M., Eshun, G. B., Yazgan, I., Akgul, A., Sadik, O. A. (2019). Antimicrobial activity of a new class of phosphorylated and modified flavonoids. ACS omega, 4(7), 12865-12871.

[172] Wu, T., Li, H., Chen, J., Cao, Y., Fu, W., Zhou, P., Pang, J. (2017). Apigenin, a novel candidate involving herb-drug interaction (HDI), interacts with organic anion transporter 1 (OAT1). Pharmacological Reports, 69(6), 1254-1262.

[173] Wu, T., He, M., Zang, X., Zhou, Y., Qiu, T., Pan, S., Xu, X. (2013). A structure–activity relationship study of flavonoids as inhibitors of E. coli by membrane interaction effect. Biochimica et Biophysica Acta (BBA)-Biomembranes, 1828(11), 2751-2756.

[174] Daglia, M. (2012). Polyphenols as antimicrobial agents. Current opinion in biotechnology, 23(2), 174-181.

[175] Li, K., Xing, S., Wang, M., Peng, Y., Dong, Y., Li, X. (2012). Anticomplement and antimicrobial activities of flavonoids from Entada phaseoloides. Natural product communications, 7(7), 1934578X1200700715.

[176] Amin, M. U., Khurram, M., Khattak, B., Khan, J. (2015). Antibiotic additive and synergistic action of rutin, morin and quercetin against methicillin resistant Staphylococcus aureus. BMC complementary and alternative medicine, 15, 1-12.

---

[177] Pal, A., Tripathi, A. (2020). Quercetin inhibits carbapenemase and efflux pump activities among carbapenem-resistant Gram-negative bacteria. Apmis, 128(3), 251-259.

[178] Ahmad, A., Kaleem, M., Ahmed, Z., Shafiq, H. (2015). Therapeutic potential of flavonoids and their mechanism of action against microbial and viral infections—A review. Food Research International, 77, 221-235.

[179] Yang, D., Wang, T., Long, M., Li, P. (2020). Quercetin: its main pharmacological activity and potential application in clinical medicine. Oxidative Medicine and Cellular Longevity, 2020.

[180] Wang, S., Yao, J., Zhou, B., Yang, J., Chaudry, M. T., Wang, M., ... ,Yin, W. (2018). Bacteriostatic effect of quercetin as an antibiotic alternative in vivo and its antibacterial mechanism in vitro. Journal of Food Protection, 81(1), 68-78.

[181] Ouyang, J., Sun, F., Feng, W., Sun, Y., Qiu, X., Xiong, L., ... Chen, Y. (2016). Quercetin is an effective inhibitor of quorum sensing, biofilm formation and virulence factors in Pseudomonas aeruginosa. Journal of Applied Microbiology, 120(4), 966-974.

[182] Bukhari, S. B., Memon, S., Mahroof-Tahir, M., Bhanger, M. I. (2009). Synthesis, characterization and antioxidant activity copper–quercetin complex. Spectrochimica Acta Part A: Molecular and Biomolecular Spectroscopy, 71(5), 1901-190

[183] De Souza, R. F., Sussuchi, E. M., De Giovani, W. F. (2003). Synthesis, electrochemical, spectral, and antioxidant properties of complexes of flavonoids with metal ions. Synthesis and reactivity in inorganic and metal-organic chemistry, 33(7), 1125-1144.

[184] Tan, J., Wang, B., Zhu, L. (2009). DNA binding and oxidative DNA damage induced by a quercetin copper(II) complex: potential mechanism of its antitumour properties. JBIC Journal of Biological Inorganic Chemistry, 14, 727-739.

[185] Durgo, K., Halec, I., Šola, I., Franekić, J. (2011). Cytotoxic and Genotoxic Effects of the Quercetin/Lanthanum Complex on Human Cervical Carcinoma Cells. Archives of Industrial Hygiene and Toxicology, 62(3), 221-227.

---

[186] Tan, J., Zhu, L., Wang, B. (2009). DNA binding and cleavage activity of quercetin nickel (II) complex. Dalton Transactions, (24), 4722-4728.

[187] Janjua, N. K., Siddiqa, A., Yaqub, A., Sabahat, S., Qureshi, R., ul Haque, S. (2009). Spectrophotometric analysis of flavonoid–DNA binding interactions at physiological conditions. Spectrochimica Acta Part A: Molecular and Biomolecular Spectroscopy, 74(5), 1135-1137.

[188] Zhang, L., Liu, Y., Wang, Y., Xu, M., Hu, X. (2018). UV–Vis spectroscopy combined with chemometric study on the interactions of three dietary flavonoids with copper ions. Food chemistry, 263, 208-215.

[189] Ni, Y., Du, S., Kokot, S. (2007). Interaction between quercetin–copper (II) complex and DNA with the use of the Neutral Red dye fluorophor probe. Analytica Chimica Acta, 584(1), 19-27.

[190] Hajji, H. E., Nkhili, E., Tomao, V., Dangles, O. (2006). Interactions of quercetin with iron and copper ions: complexation and autoxidation. Free radical research, 40(3), 303-320.

[191] Cherrak, S. A., Mokhtari-Soulimane, N., Berroukeche, F., Bensenane, B., Cherbonnel, A., Merzouk, H., Elhabiri, M. (2016). In vitro antioxidant versus metal ion chelating properties of flavonoids: A structure-activity investigation. PloS one, 11(10), e0165575.

[192] Primikyri, A., Mazzone, G., Lekka, C., Tzakos, A. G., Russo, N., Gerothanassis, I. P. (2015). Understanding zinc(II) chelation with quercetin and luteolin: a combined NMR and theoretical study. The Journal of Physical Chemistry B, 119(1), 83-95.

[193] Corrente, G. A., Malacaria, L., Beneduci, A., Furia, E., Marino, T., Mazzone, G. (2021). Experimental and theoretical study on the coordination properties of quercetin towards aluminum(III), iron(III) and copper(II) in aqueous solution. Journal of Molecular Liquids, 325, 115171.

[194] Kalinowska, M., Lewandowska, H., Pruszyński, M., Świderski, G., Gołębiewska, E., Gryko, K., ..., Lewandowski, W. (2021). Co(II) complex of quercetin–spectral, anti-/pro-oxidant and cytotoxic activity in HaCaT cell lines. Applied Sciences, 11(19), 9244.

---

[195] de Castilho, T. S., Matias, T. B., Nicolini, K. P., Nicolini, J. (2018). Study of interaction between metal ions and quercetin. Food Science and Human Wellness, 7(3), 215-219.

[196] Massaro, M., Cina, V., Labbozzetta, M., Lazzara, G., Meo, P. L., Poma, P., Noto, R. (2016). Chemical and pharmaceutical evaluation of the relationship between triazole linkers and pore size on cyclodextrin–calixarene nanosponges used as carriers for natural drugs. RSC advances, 6(56), 50858-50866.

[197] Rubini, K., Boanini, E., Menichetti, A., Bonvicini, F., Gentilomi, G. A., Montalti, M., Bigi, A. (2020). Quercetin loaded gelatin films with modulated release and tailored anti-oxidant, mechanical and swelling properties. Food Hydrocolloids, 109, 106089.

[198] Kim, E. S., Lee, J. S., Lee, H. G. (2021). Quercetin delivery characteristics of chitosan nanoparticles prepared with different molecular weight polyanion cross-linkers. Carbohydrate Polymers, 267, 118157.

[199] Ramasamy, T., Ruttala, H. B., Chitrapriya, N., Poudal, B. K., Choi, J. Y., Kim, S. T., ..., Kim, J. O. (2017). Engineering of cell microenvironment-responsive polypeptide nanovehicle co-encapsulating a synergistic combination of small molecules for effective chemotherapy in solid tumours. Acta biomaterialia, 48, 131-143.

[200] Samadi, A., Pourmadadi, M., Yazdian, F., Rashedi, H., Navaei-Nigjeh, M. (2021). Ameliorating quercetin constraints in cancer therapy with pH-responsive agarose-polyvinylpyrrolidone-hydroxyapatite nanocomposite encapsulated in double nanoemulsion. International Journal of Biological Macromolecules, 182, 11-25.

[201] Zaborniak, I., Macior, A., Chmielarz, P. (2021). Smart, naturally-derived macromolecules for controlled drug release. Molecules, 26(7), 1918.

[202] Darvishan, S., Pourmadadi, M., Abdouss, M., Mazinani, S., Yazdian, F., Rahdar, A., Díez-Pascual, A. M. (2023). Gamma alumina coated-PAA/PVP hydrogel as promising quercetin nanocarrier: Physiochemical characterization and toxicity activity. Journal of Drug Delivery Science and Technology, 84, 104500.

[203] Carrillo-Castillo, T. D., Castro-Carmona, J. S., Luna-Velasco, A., Zaragoza-Contreras, E. A. (2020). pH-responsive polymer micelles for methotrexate delivery at tumour microenvironments. e-Polymers, 20(1), 624-635.

---

[204] Nagaj, J., Kołkowska, P., Bykowska, A., Komarnicka, U. K., Kyzioł, A., Jeżowska-Bojczuk, M. (2015). Interaction of methotrexate, an anticancer agent, with copper (II) ions: coordination pattern, DNA-cleaving properties and cytotoxic studies. Medicinal Chemistry Research, 24(1), 115-123.

[205] Nodiţi, G., Fuliaş, A., Ledeţi, I. (2014). Methotrexate as coordination complex ligand: study of interaction with Zn(II). Digest Journal of Nanomaterials & Biostructures (DJNB), 9(1).

[206] Pontinha, A. D. R., Jorge, S. M. A., Diculescu, V. C., Vivan, M., Oliveira-Brett, A. M. (2012). Antineoplasic drug methotrexate redox mechanism using a glassy carbon electrode. Electroanalysis, 24(4), 917-923.

[207] Casillas-Popova, S. N., Bernad-Bernad, M. J., Gracia-Mora, J. (2022). Modeling of adsorption and release kinetics of methotrexate from thermo/magnetic responsive $CoFe_2O_4$–$BaTiO_3$, $CoFe_2O_4$–$Bi_4Ti_3O_{12}$ and Fe_3O_4–$BaTiO_3$ core-shell magnetoelectric nanoparticles functionalized with PNIPAm. Journal of Drug Delivery Science and Technology, 103121.

[208] Tian, H., Cronstein, B. N. (2007). Understanding the mechanisms of action of methotrexate. Bull NYU Hosp Jt Dis, 65(3), 168-173.

[209] Hagner, N., Joerger, M. (2010). Cancer chemotherapy: targeting folic acid synthesis. Cancer management and research, 2, 293.

[210] Singka, G. S. L., Samah, N. A., Zulfakar, M. H., Yurdasiper, A., Heard, C. M. (2010). Enhanced topical delivery and anti-inflammatory activity of methotrexate from an activated nanogel. European Journal of Pharmaceutics and Biopharmaceutics, 76(2), 275-281.

[211] Zia, M. K., Siddiqui, T., Ali, S. S., Ahsan, H., Khan, F. H. (2019). Understanding the binding interaction between methotrexate and human alpha-2-macroglobulin: Multi-spectroscopic and computational investigation. Archives of biochemistry and biophysics, 675, 108118.

[212] Tu, L., Fan, Z., Zhu, F., Zhang, Q., Zeng, S., Chen, Z., Li, Y. (2020). Self-recognizing and stimulus-responsive carrier-free metal-coordinated nanotheranostics

---

for magnetic resonance/photoacoustic/fluorescence imaging-guided synergistic photo-chemotherapy. Journal of Materials Chemistry B, 8(26), 5667-5681.

[213] Roberts, G. C. K., Feeney, J., Birdsall, B., Charlton, P., Young, D. (1980). Methotrexate binding to dihydrofolate reductase. Nature, 286(5770), 309-309.

[214] Mizusawa, K., Takaoka, Y., Hamachi, I. (2012). Specific cell surface protein imaging by extended self-assembling fluorescent turn-on nanoprobes. Journal of the American Chemical Society, 134(32), 13386-13395.

[215] Chibber, S., Hassan, I., Farhan, M., Naseem, I. (2012). Light-mediated interaction of methotrexate with transition metal Cu (II). Medicinal Chemistry Research, 21, 2379-2387.

[216] Çeşme, M., Gölcü, A. (2019). Metal-Based Molecular Compounds: Structure, Analytical Properties, dsDNA Binding Studies and In vitro Antiproliferative Activity on Selected Cancer Cell Lines. Pharmaceutical Chemistry Journal, 53, 392-410.

[217] Fernández-Villa, D., Ramírez-Jiménez, R. A., Aranaz, I., Acosta, N., Vázquez-Lasa, B., Rojo, L. (2022). Development of Methotrexate Complexes Endowed with New Biological Properties Envisioned for Musculoskeletal Regeneration in Rheumatoid Arthritis Environments. International Journal of Molecular Sciences, 23(17), 10054.

[218] Cerra, S., Matassa, R., Beltrán, A. M., Familiari, G., Battocchio, C., Pis, I., ..., Fratoddi, I. (2020). Insights about the interaction of methotrexate loaded hydrophilic gold nanoparticles: Spectroscopic, morphological and structural characterizations. Materials Science and Engineering: C, 117, 111337.

[219] Abolmaali, S. S., Tamaddon, A. M., Mohammadi, S., Amoozgar, Z., Dinarvand, R. (2016). Chemically crosslinked nanogels of PEGylated poly ethyleneimine (l-histidine substituted) synthesized via metal ion coordinated self-assembly for delivery of methotrexate: cytocompatibility, cellular delivery and antitumour activity in resistant cells. Materials Science and Engineering: C, 62, 897-907.

[220] Bernaczek, K., Mielańczyk, A., Mielańczyk, Ł., Neugebauer, D., Grzywna, Z. J. (2019). Self-assembling water-soluble polymethacrylate–MTX conjugates: The significance of macromolecules architecture on drug conjugation efficiency, the final

---

shape of particles, and drug release. Journal of Biomedical Materials Research Part B: Applied Biomaterials, 107(8), 2476-2487.

[221] Bogusz, K., Zuchora, M., Sencadas, V., Tehei, M., Lerch, M., Thorpe, N., Konstantinov, K. (2019). Synthesis of methotrexate-loaded tantalum pentoxide–poly (acrylic acid) nanoparticles for controlled drug release applications. Journal of colloid and interface science, 538, 286-296.

[222] Pooresmaeil, M., Namazi, H. (2018). Surface modification of graphene oxide with stimuli-responsive polymer brush containing β-cyclodextrin as a pendant group: Preparation, characterization, and evaluation as controlled drug delivery agent. Colloids and Surfaces B: Biointerfaces, 172, 17-25.

[223] Ding, C., Wu, H., Yin, Z. Z., Gao, J., Wu, D., Qin, Y., Kong, Y. (2020). Disulfide-cleavage-and pH-triggered drug delivery based on a vesicle structured amphiphilic self-assembly. Materials Science and Engineering: C, 107, 110366.

[224] Meena, P., Kishore, N. (2021). Thermodynamic and mechanistic analytical effect of albumin coated gold nanosystems for antibiotic drugs binding and interaction with deoxyribonucleic acid. Journal of Molecular Liquids, 339, 116718.

[225] Bouchemal, K. (2008). New challenges for pharmaceutical formulations and drug delivery systems characterization using isothermal titration calorimetry. Drug discovery today, 13(21-22), 960-972.

[226] Tunçer, S., Gurbanov, R., Sheraj, I., Solel, E., Esenturk, O., Banerjee, S. (2018). Low dose dimethyl sulfoxide driven gross molecular changes have the potential to interfere with various cellular processes. Scientific reports, 8(1), 1-15.

[227] Pękal, A., Biesaga, M., Pyrzynska, K. (2011). Interaction of quercetin with copper ions: complexation, oxidation and reactivity towards radicals. Biometals, 24(1), 41-49.

[228] Ferreira, C. M., Pinto, I. S., Soares, E. V., Soares, H. M. (2015). (Un) suitability of the use of pH buffers in biological, biochemical and environmental studies and their interaction with metal ions–a review. RSC Advances, 5(39), 30989-31003.

[229] Guo, M., Perez, C., Wei, Y., Rapoza, E., Su, G., Bou-Abdallah, F., Chasteen, N. D. (2007). Iron-binding properties of plant phenolics and cranberry's bio-effects. Dalton Transactions, (43), 4951-4961.

---

[230] Pietta, P. G. (2000). Flavonoids as antioxidants. Journal of natural products, 63(7), 1035-1042.

[231] Jovanovic, S. V., Steenken, S., Tosic, M., Marjanovic, B., Simic, M. G. (1994). Flavonoids as antioxidants. Journal of the American Chemical Society, 116(11), 4846-4851.

[232] Irving, H. M. N. H., Williams, R. (1953). 637. The stability of transition-metal complexes. Journal of the Chemical Society (Resumed), 3192-3210.

[233] Xu, Y., Yang, J., Lu, Y., Qian, L. L., Yang, Z. Y., Han, R. M., Skibsted, L. H. (2019). Copper (II) coordination and translocation in luteolin and effect on radical scavenging. The Journal of Physical Chemistry B, 124(2), 380-388.

[234] Malešev, D., Kuntić, V. (2007). Investigation of metal-flavonoid chelates and the determination of flavonoids via metal-flavonoid complexing reactions. Journal of the Serbian chemical society, 72(10), 921-939.)

[235] Henry *Freiser,* Quintus Fernando. (1963) Ionic Equilibria in Analytical Chemistry. Wiley

[236] Rekharsky, M. V., Inoue, Y. (1998). Complexation thermodynamics of cyclodextrins. Chemical reviews, 98(5), 1875-1918.

[237] Satake, A. (2020). The Solvent Effect on Weak Interactions in Supramolecular Polymers: Differences between Small Molecular Probes and Supramolecular Polymers. ChemPlusChem, 85(7), 1542-1548.

[238] Rivas, B. L., Seguel, G. V. (1999). Poly (acrylic acid-co-maleic acid)–metal complexes with copper (II), cobalt (II), and nickel (II): Synthesis, characterization and structure of its metal chelates. Polyhedron, 18(19), 2511-2518.

[239] Tarabukina, E. B., Fatullaev, E. I., Filippov, A. P., Abzaeva, K. A. (2019). Behavior of metal complexes of polyacrylic acid in solutions. International Journal of Polymer Analysis and Characterization, 24(1), 10-17.

[240] Gregor, H. P., Luttinger, L. B., Loebl, E. M. (1955). Metal–polyelectrolyte complexes. I. The polyacrylic acid–copper complex. The Journal of Physical Chemistry, 59(1), 34-39.

---

[241] Tomida, T., Hamaguchi, K., Tunashima, S., Katoh, M., Masuda, S. (2001). Binding properties of a water-soluble chelating polymer with divalent metal ions measured by ultrafiltration. Poly (acrylic acid). Industrial & engineering chemistry research, 40(16), 3557-3562.

[242] Roma-Luciow, R., Sarraf, L., Morcellet, M. (2001). Complexes of poly (acrylic acid) with some divalent, trivalent and tetravalent metal ions. European polymer journal, 37(9), 1741-1745.

[243] De Vasconcelos, C. L., Bezerril, D. P., Dos Santos, D. E. S., Dantas, D. T., Pereira, M. R., Fonseca, J. L. C. (2006). Effect of molecular weight and ionic strength on the formation of polyelectrolyte complexes based on poly (methacrylic acid) and chitosan. Biomacromolecules, 7(4), 1245-1252.

[244] Khan, N., Brettmann, B. (2019). Intermolecular interactions in polyelectrolyte and surfactant complexes in solution. Polymers, 11(1), 51.

[245] Wang, C., Liu, M., Yuan, L., Wang, L., Sun, D., Wang, Z., Han, J. (2016). Calorimetric and spectroscopic studies on temperature-and pH-dependent interactions of stimuli-responsive poly (N-isopropylacrylamide) with piceatannol. The Journal of Chemical Thermodynamics, 98, 186-192.

[246] Termühlen, F., Kuckling, D., Schönhoff, M. (2017). Isothermal titration calorimetry to probe the coil-to-globule transition of thermoresponsive polymers. The Journal of Physical Chemistry B, 121(36), 8611-8618.

[247] Ross, P. D., Subramanian, S. (1981). Thermodynamics of protein association reactions: forces contributing to stability. Biochemistry, 20(11), 3096-3102.

[248] Archer, W. R., Schulz, M. D. (2020). Isothermal titration calorimetry: practical approaches and current applications in soft matter. Soft Matter.

[249] Migliore, R., Grasso, G. I., Milana, P., Cusmano, S., Santonoceta, G. D., Sgarlata, C. (2021). Adsorption of calixarene-based supramphiphiles at the solid–liquid interface monitored by QCM-D. Supramolecular Chemistry, 33(8), 475-486.

[250] Aykut, D. Y., Yolaçan, Ö., Deligöz, H. (2020). pH stimuli drug loading/release platforms from LbL single/blend films: QCM-D and in-vitro studies. Colloids and Surfaces A: Physicochemical and Engineering Aspects, 602, 125113.

---

[251] Deligoez, H., Tieke, B. (2014). QCM-D study of layer-by-layer assembly of polyelectrolyte blend films and their drug loading-release behavior. Colloids and Surfaces A: Physicochemical and Engineering Aspects, 441, 725-736.

[252] Karlsson, J., Atefyekta, S., Andersson, M. (2015). Controlling drug delivery kinetics from mesoporous titania thin films by pore size and surface energy. International journal of nanomedicine, 4425-4436.

[253] Notley, S. M., Eriksson, M., Wågberg, L. (2005). Visco-elastic and adhesive properties of adsorbed polyelectrolyte multilayers determined in situ with QCM-D and AFM measurements. Journal of colloid and interface science, 292(1), 29-37.

[254] Easley, A. D., Ma, T., Eneh, C. I., Yun, J., Thakur, R. M., Lutkenhaus, J. L. (2022). A practical guide to quartz crystal microbalance with dissipation monitoring of thin polymer films. Journal of Polymer Science, 60(7), 1090-1107.

[255] Ebara, Y., Okahata, Y. (1994). A kinetic study of concanavalin A binding to glycolipid monolayers by using a quartz-crystal microbalance. Journal of the American Chemical Society, 116(25), 11209-11212.

[256] Okahata, Y., Kawase, M., Niikura, K., Ohtake, F., Furusawa, H., Ebara, Y. (1998). Kinetic measurements of DNA hybridization on an oligonucleotide-immobilized 27-MHz quartz crystal microbalance. Analytical chemistry, 70(7), 1288-1296.

[257] Vogt, S., Kelkenberg, M., Nöll, T., Steinhoff, B., Schönherr, H., Merzendorfer, H., Nöll, G. (2018). Rapid determination of binding parameters of chitin binding domains using chitin-coated quartz crystal microbalance sensor chips. Analyst, 143(21), 5255-5263.

[258] Zhou, D., Porter, W. R., Zhang, G. G. (2017). Drug stability and degradation studies. In Developing solid oral dosage forms (pp. 113-149). Academic Press.

[259] Ansel, H. C. (2012). Pharmaceutical calculations. Lippincott Williams & Wilkins.

[260] Qin, L., Li, L., Sha, Y., Wang, Z., Zhou, D., Chen, W., Xue, G. (2018). Conformational transitions of polymer chains in solutions characterized by fluorescence resonance energy transfer. Polymers, 10(9), 1007.

---

[261] Swift, T., Swanson, L., Geoghegan, M., Rimmer, S. (2016). The pH-responsive behaviour of poly (acrylic acid) in aqueous solution is dependent on molar mass. Soft matter, 12(9), 2542-2549.

[262] Dash, S., Murthy, P. N., Nath, L., Chowdhury, P. (2010). Kinetic modeling on drug release from controlled drug delivery systems. Acta Pol Pharm, 67(3), 217-223.

[263] Korsmeyer, R. W., Gurny, R., Doelker, E., Buri, P., Peppas, N. A. (1983). Mechanisms of solute release from porous hydrophilic polymers. International journal of pharmaceutics, 15(1), 25-35.

[264] Bruschi, M. L. (2015). Strategies to modify the drug release from pharmaceutical systems. Woodhead Publishing.

[265] H. Flaschka, in EDTA Titrations, Pergamon Press, London, UK, 1959.

[266] Gans, P., Sabatini, A., Vacca, A. (1996). Investigation of equilibria in solution. Determination of equilibrium constants with the HYPERQUAD suite of programs. Talanta, 43(10), 1739-1753.

[267] Hansen, L. D., Fellingham, G. W., Russell, D. J. (2011). Simultaneous determination of equilibrium constants and enthalpy changes by titration calorimetry: Methods, instruments, and uncertainties. Analytical biochemistry, 409(2), 220-229.

[268] Sgarlata, C., Zito, V., Arena, G. (2013). Conditions for calibration of an isothermal titration calorimeter using chemical reactions. Analytical and bioanalytical chemistry, 405, 1085-1094.

[269] Arena, G., Gans, P., Sgarlata, C. (2016). HypCal, a general-purpose computer program for the determination of standard reaction enthalpy and binding constant values by means of calorimetry. Analytical and bioanalytical chemistry, 408, 6413-6422.

[270] Reviakine, I., Johannsmann, D., Richter, R. P. (2011). Hearing what you cannot see and visualizing what you hear: interpreting quartz crystal microbalance data from solvated interfaces.

[271] Alanazi, N., Almutairi, M., Alodhayb, A. N. (2023). A Review of Quartz Crystal Microbalance for Chemical and Biological Sensing Applications. Sensing and Imaging, 24(1), 10.

---

[272] Rodahl, M., Kasemo, B. (1996). Frequency and dissipation-factor responses to localized liquid deposits on a QCM electrode. Sensors and Actuators B: Chemical, 37(1-2), 111-116.

[273] Rodahl, M., Kasemo, B. (1996). A simple setup to simultaneously measure the resonant frequency and the absolute dissipation factor of a quartz crystal microbalance. Review of Scientific Instruments, 67(9), 3238-3241.

[274] Meloun, M., Ferenčíková, Z., Vrána, A. (2010). The thermodynamic dissociation constants of methotrexate by the nonlinear regression and factor analysis of multiwavelength spectrophotometric pH-titration data. Central European Journal of Chemistry, 8(3), 494-507.

[275] Poe, M. (1977). Acidic dissociation constants of folic acid, dihydrofolic acid, and methotrexate. Journal of Biological Chemistry, 252(11), 3724-3728.

[276] Poe, M. (1973). Proton magnetic resonance studies of folate, dihydrofolate, and methotrexate: Evidence from pH and concentration studies for dimerization. Journal of Biological Chemistry, 248(20), 7025-7032.

[277] Olmo, F., Rodriguez, A., Colina, A., Heras, A. (2022). UV/Vis absorption spectroelectrochemistry of folic acid. Journal of Solid State Electrochemistry, 26(1), 29-37.

[278] Maali, N. A. E., Ghandour, M. A., Vire, J. C., Patriarche, G. J. (1989). Voltammetric determination of the stability constants of copper (II) complexes with folic acid. Electroanalysis, 1(4), 341-345.

[279] Enyedy, É. A., Farkas, E., Dömötör, O., Santos, M. A. (2011). Interaction of folic acid and some matrix metalloproteinase (MMP) inhibitor folate-γ-hydroxamate derivatives with Zn (II) and human serum albumin. Journal of Inorganic Biochemistry, 105(3), 444-453.

[280] Kohzuma, T., Odani, A., Morita, Y., Takani, M., Yamauchi, O. (1988). Pteridine-containing ternary copper (II) complexes as pterin cofactor-metal binding models. Structures, solution equilibria, and redox activities. Inorganic Chemistry, 27(21), 3854-3858.

---

[281] Sigel, H., Griesser, R. (2005). Nucleoside 5′-triphosphates: self-association, acid–base, and metal ion-binding properties in solution. Chemical Society Reviews, 34(10), 875-900.

[282] Mitchell, P. R., Siegel, H. (1978). A proton nuclear-magnetic-resonance study of self-stacking in purine and pyrimidine nucleosides and nucleotides. European Journal of Biochemistry, 88(1), 149-154.

[283] Dunger, A., Limbach, H. H., Weisz, K. (1998). NMR Studies on the Self-Association of Uridine and Uridine Analogues. Chemistry–A European Journal, 4(4), 621-628.

[284] Ojha, H., Mishra, K., Hassan, M. I., Chaudhury, N. K. (2012). Spectroscopic and isothermal titration calorimetry studies of binding interaction of ferulic acid with bovine serum albumin. Thermochimica Acta, 548, 56-64.

[285] Li, X., Yang, Z. (2015). Interaction of oridonin with human serum albumin by isothermal titration calorimetry and spectroscopic techniques. Chemico-Biological Interactions, 232, 77-84.

[286] M. Neagu, Z. Piperigkou, K. Karamanou, A- B. Engin, A-O. Docea, C. Constantin, C. Negrei, D. Nikitovic, A. Tsatsakis. Archives of Toxicology, 2017, 91, 1031–1048;

[287] M. Mahmoudi, I. Lynch, M.R. Ejtehadi, M.P. Monopoli F.B. Bombelli, S. Laurent. Chemical Reviews, 2011, 111(9), 5610–5637;

[288] J. Shah, S. Singh. Nanoparticle–Protein Corona: Biophysics to Biology, 2019, 1, 1-30;

[289] L. Vroman, Materials (Basel), 2009, 2 (4), 1547–1557

[290] D. Prozeller, S. Morsbach, K. Landfester. Nanoscale, 2019, 11, 19265-19273;

[291] Panja, S., Khatua, D. K., Halder, M. (2018). Simultaneous binding of folic acid and methotrexate to human serum albumin: insights into the structural changes of protein and the location and competitive displacement of drugs. ACS omega, 3(1), 246-253.

[292] Shalbafan, M., Rezaei Behbehani, G. (2018). Docking studies on the binding properties of methotrexate to human serum albumin. Biomacromolecular Journal, 4(2), 114-117.

---

[293] Maciążek-Jurczyk, M., Sułkowska, A., Równicka-Zubik, J. (2016). Alteration of methotrexate binding to human serum albumin induced by oxidative stress. Spectroscopic comparative study. Spectrochimica Acta Part A: Molecular and Biomolecular Spectroscopy, 152, 537-550.

[294] Preisz, Z., Kunsági-Máté, S. (2021). Effect of methotrexate and its photodegradation products on the temperature induced denaturation of human serum albumin. Spectrochimica Acta Part A: Molecular and Biomolecular Spectroscopy, 245, 118905.

[295] Coassolo, P., Valentin, M., Bourdeaux, M., Briand, C. (1980). Modification of human serum albumin binding of methotrexate by folinic acid and certain drugs used in cancer chemotherapy. European Journal of Clinical Pharmacology, 17, 123-127.

[296] Cheng, L. Y., Fang, M., Bai, A. M., Ouyang, Y., Hu, Y. J. (2017). Insights into the interaction of methotrexate and human serum albumin: A spectroscopic and molecular modeling approach. Luminescence, 32(5), 873-879.

[297] Zhang, N., He, H., Zhang, M., Lv, X., Li, W., Wang, R., Chang, J. (2022). Investigation of the interactions between three flavonoids and human serum albumin by isothermal titration calorimetry, spectroscopy, and molecular docking. New Journal of Chemistry, 46(26), 12814-12824.

[298] Jha, N. S., Kishore, N. (2011). Thermodynamic studies on the interaction of folic acid with bovine serum albumin. The Journal of Chemical Thermodynamics, 43(5), 814-821.

[299] Yu, S., Xu, X., Yigit, C., van der Giet, M., Zidek, W., Jankowski, J., ..., Ballauff, M. (2015). Interaction of human serum albumin with short polyelectrolytes: a study by calorimetry and computer simulations. Soft Matter, 11(23), 4630-4639.

[300] Simón-Vázquez, R., Lozano-Fernández, T., Peleteiro-Olmedo, M., González-Fernández, Á. (2014). Conformational changes in human plasma proteins induced by metal oxide nanoparticles. Colloids and Surfaces B: Biointerfaces, 113, 198-206.

[301] Guo, M., Li, H., Zhang, Y., Shao, S., Wang, X. (2015). Study on the interaction of zinc ion binding with human serum albumin using isothermal titration calorimetry. J. Chem. Soc. Pakistan, 37(3), 452-457.

---

[302] Dixon, M. C. (2008). Quartz crystal microbalance with dissipation monitoring: enabling real-time characterization of biological materials and their interactions. Journal of biomolecular techniques: JBT, 19(3), 151.

[303] Alhankawi, A. R., Al-Husseini, J. K., Spindler, A., Baker, C., Shoniwa, T. T., Ahmed, M., ..., Johal, M. S. (2022). The relationship between hydrophobicity and drug-protein binding in human serum albumin: A quartz crystal microbalance study. Biophysica, 2(2), 113-120.

[304] Wang, X., Ho, C. T., Huang, Q. (2007). Investigation of adsorption behavior of (−)-epigallocatechin gallate on bovine serum albumin surface using quartz crystal microbalance with dissipation monitoring. Journal of agricultural and food chemistry, 55(13), 4987-4992.

[305] Gagliardi, M., Colagiorgio, L., Cecchini, M. (2023). A Fast and Reliable Method Based on QCM-D Instrumentation for the Screening of Nanoparticle/Blood Protein Interactions. Biosensors, 13(6), 607.

[306] Adamczyk, Z., Pomorska, A., Nattich-Rak, M., Wytrwal-Sarna, M., Bernasik, A. (2018). Protein adsorption mechanisms at rough surfaces: Serum albumin at a gold substrate. Journal of colloid and interface science, 530, 631-641.

[307] Hampitak, P., Melendrez, D., Iliut, M., Fresquet, M., Parsons, N., Spencer, B., ..., Vijayaraghavan, A. (2020). Protein interactions and conformations on graphene-based materials mapped using a quartz-crystal microbalance with dissipation monitoring (QCM-D). Carbon, 165, 317-327.

[308] Yousefi, N., Tufenkji, N. (2016). Probing the interaction between nanoparticles and lipid membranes by quartz crystal microbalance with dissipation monitoring. Frontiers in chemistry, 4, 46.

[309] Molino, P. J., Higgins, M. J., Innis, P. C., Kapsa, R. M., Wallace, G. G. (2012). Fibronectin and bovine serum albumin adsorption and conformational dynamics on inherently conducting polymers: a QCM-D study. Langmuir, 28(22), 8433-8445.

[310] Yu, B., Lang, X., Wang, X., Ding, L., Han, M., Guo, Y., Dong, Z. (2023). Effects of different conformations of polylysine on the anti-tumour efficacy of methotrexate nanoparticles. Biomedicine & Pharmacotherapy, 162, 114662.

---

[311] Chen, S. T., Kramer, P. A., Kildsig, D. O. (1978). Interaction of methotrexate with polycationic carriers. Life Sciences, 23(4), 365-374.

[312] Peters Jr, T. (1985). Serum albumin. Advances in protein chemistry, 37, 161-245.

[313] Li, Q. L., Sun, Y., Sun, Y. L., Wen, J., Zhou, Y., Bing, Q. M., ..., Yang, Y. W. (2014). Mesoporous silica nanoparticles coated by layer-by-layer self-assembly using cucurbit [7]uril for in vitro and in vivo anticancer drug release. Chemistry of Materials, 26(22), 6418-6431.

[314] Hermal, F., Frisch, B., Specht, A., Bourel-Bonnet, L.,Heurtault, B. (2020). Development and characterization of layer-by-layer coated liposomes with poly (L-lysine) and poly (L-glutamic acid) to increase their resistance in biological media. International Journal of Pharmaceutics, 586, 119568.

[315] Lengert, E. V., Koltsov, S. I., Li, J., Ermakov, A. V., Parakhonskiy, B. V., Skorb, E. V., Skirtach, A. G. (2020). Nanoparticles in polyelectrolyte multilayer layer-by-layer (LbL) films and capsules - Key enabling components of hybrid coatings. Coatings, 10(11), 1131.

[316] Chen, X., Zhang, Q., Li, J., Yang, M., Zhao, N., Xu, F. J. (2018). Rattle-structured rough nanocapsules with in-situ-formed gold nanorod cores for complementary gene/chemo/photothermal therapy. ACS nano, 12(6), 5646-5656.

[317] Zhou, J., Yu, G., Huang, F. (2017). Supramolecular chemotherapy based on host–guest molecular recognition: a novel strategy in the battle against cancer with a bright future. Chemical Society Reviews, 46(22), 7021-7053.

[318] Hu, X. Y., Gao, J., Chen, F. Y., Guo, D. S. (2020). A host-guest drug delivery nanosystem for supramolecular chemotherapy. Journal of Controlled Release, 324, 124-133.

[319] Della Sala, P., Del Regno, R., Talotta, C., Capobianco, A., Hickey, N., Geremia, S., Gaeta, C. (2020). Prismarenes: a new class of macrocyclic hosts obtained by templation in a thermodynamically controlled synthesis. Journal of the American Chemical Society, 142(4), 1752-1756.

[320] Biedermann, F., Vendruscolo, M., Scherman, O. A., De Simone, A., Nau, W. M. (2013). Cucurbit [8]uril and blue-box: high-energy water release overwhelms

---

electrostatic interactions. Journal of the American Chemical Society, 135(39), 14879-14888.

[321] Schneider, H. J. (2009). Binding mechanisms in supramolecular complexes. Angewandte Chemie International Edition, 48(22), 3924-3977.

[322] Schneider, H. J., Yatsimirsky, A. K. (2008). Selectivity in supramolecular host–guest complexes. Chemical Society Reviews, 37(2), 263-277.

[323] St-Jacques, A. D., Wyman, I. W., Macartney, D. H. (2008). Encapsulation of charge-diffuse peralkylated onium cations in the cavity of cucurbit[7]uril. Chemical communications, (40), 4936-4938.

[324] Escobar, L., Ballester, P. (2021). Molecular Recognition in Water Using Macrocyclic Synthetic Receptors. Chemical Reviews, 121(4), 2445-2514.

[325] Sgarlata, C., Mugridge, J. S., Pluth, M. D., Zito, V., Arena, G., Raymond, K. N. (2017). Different and often opposing forces drive the encapsulation and multiple exterior binding of charged guests to a M4L6 supramolecular vessel in water. Chemistry–A European Journal, 23(66), 16813-16818.

[326] Yao, H., Ke, H., Zhang, X., Pan, S. J., Li, M. S., Yang, L. P., ... Jiang, W. (2018). Molecular recognition of hydrophilic molecules in water by combining the hydrophobic effect with hydrogen bonding. Journal of the American Chemical Society, 140(41), 13466-13477.

[327] Hanayama, H., Yamada, J., Tomotsuka, I., Harano, K., Nakamura, E. (2021). Rim Binding of Cyclodextrins in Size-Sensitive Guest Recognition. Journal of the American Chemical Society, 143(15), 5786-5792.

[328] Rekharsky, M. V., Mori, T., Yang, C., Ko, Y. H., Selvapalam, N., Kim, H., Inoue, Y. (2007). A synthetic host-guest system achieves avidin-biotin affinity by overcoming enthalpy–entropy compensation. Proceedings of the National Academy of Sciences, 104(52), 20737-20742.

[329] Schönbeck, C., Holm, R. (2019). Exploring the origins of enthalpy–entropy compensation by calorimetric studies of cyclodextrin complexes. The Journal of Physical Chemistry B, 123(31), 6686-6693.

---

[330] Moghaddam, S., Yang, C., Rekharsky, M., Ko, Y. H., Kim, K., Inoue, Y., Gilson, M. K. (2011). New ultrahigh affinity host-guest complexes of cucurbit[7]uril with bicyclo[2.2.2]octane and adamantane guests: Thermodynamic analysis and evaluation of m2 affinity calculations. Journal of the American Chemical Society, 133(10), 3570-3581.